PRELIMINARY STUDY OF THE SCENT PROJECT

L. Calabretta, G. Cuttone, D. Battaglia, D. Campo, L. Celona
S. Gammino, D. Garufi, P. Lojacono, L. Piazza
G. Raia, M. Re, D. Rifuggiato, M. G. Sabini
INFN-LNS

P. Fabbricatore, S. Farinon, R. Musenich
INFN-GENOVA

M. Maggiore
Università di Catania, INFN-LNS

Carlo Greco
Università della magna Grecia, Catanzaro

PRELIMINARY STUDY OF THE SCENT PROJECT

L. Calabretta, G. Cuttone, D. Battaglia, D. Campo, L. Celona
S. Gammino, D. Garufi, P. Lojacono, L. Piazza
G. Raia, M. Re, D. Rifuggiato, M. G. Sabini
INFN-LNS

P. Fabbricatore, S. Farinon, R. Musenich
INFN-GENOVA

M. Maggiore
Università di Catania, INFN-LNS

Carlo Greco
Università della magna Grecia, Catanzaro

TABLE OF CONTENT

Introduction

The study of the SCENT (Superconducting Cyclotron for Exotic Nuclei and Therapy) project here was triggered by the need at LNS-Catania to build a facility for radioactive ions and for radiotherapy at the same time [1]. Although this proposal was not chosen as a development plan of the laboratory, it was supported as a project study for a new independent radiotherapy centre by the 5th INFN Scientific Board.

We want to underline that the cyclotron described in the present report is able to accelerate both protons and Carbon ions to be used in radiotherapy. Although low beam intensities are generally required for therapy, we also evaluated the stripper extraction which allows the cyclotron to deliver beam power up to 20 kW. Such high beam power can be useful in feeding a facility for the production of new medical radioisotopes [2,3]. Despite the fact that at the beginning of the project the goal was that of an accelerator capable of operating both for therapy and for radioisotope production, in the last year and half the interest has mainly been focused on the therapy alone. In particular, the interest of companies like ACCEL and IBA in establishing a cooperation agreement with INFN to develop the SCENT project, was the main reason for this specific objective. Recently INFN, ACCEL and ANSALDO have established an agreement to investigate the feasibility of, and the market interest in this project, with a view to building it as a therapy centre in Italy and/or in the world.

The SCENT project is a contribution to the hadrontherapy development for the treatment of tumours and benign malformations placed close to high risk organs and/or for particularly radioresistent tumour treatments.

At present hadrontherapy, the most advanced technique for treatment with external radiation beams, is considered the most effective approach in this particular field of medicine.

This technique consists in employing protons or light ions beams (Carbon ions typically) with enough energy to guarantee water penetration at less than 25 cm. For this reason, proton beams must have at least an energy of 230 MeV (250 MeV is the optimum), while the Carbon ions must have an energy of about 400 AMeV.

Both particles, protons and Carbon ions, have a special feature: their interaction with matter produces a limited energy release in the first part of their path, where the beam has more energy. In addition, the energy release increases when the beam energy decreases, and in the final part of the trajectory there is a sudden and strong energy release with a precise and sharp decrease to zero energy release in a few millimetres. This feature produces the well-known Bragg Peak in the curve of the relative dose vs. trajectory length, Fig. 1.

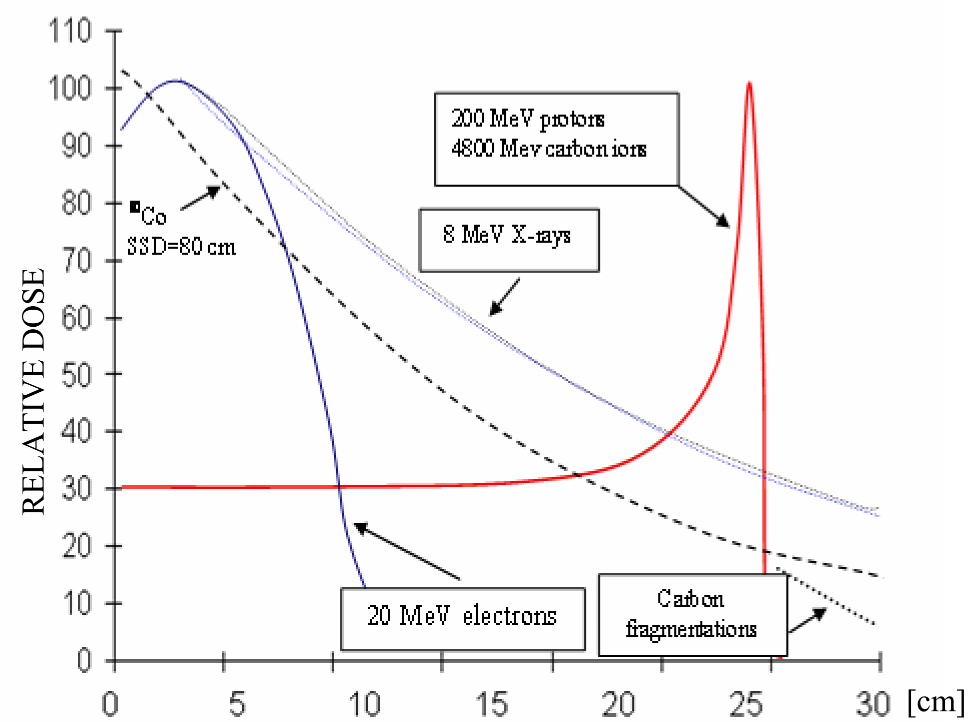

Fig. 1: Relative dose deposition for ^{60}Co radiation, electrons, X-rays, protons and Carbon ions vs. path length across the target.

This physical behaviour makes protons and Carbon ions the most suitable particles among those used as radiotherapy external beams (photons, electrons), to obtain the best dose conformation to the target volume with the maximum sparing of organs at risk close to the tumour. This ballistic advantage of hadrons compared to photons and electrons, is emphasized by better RadioBiological Effectiveness (in particular light ions have a higher RBE than protons). These considerations have led to the clinical use of ions above all in particularly radioresistent tumour pathologies; in fact, in this case the radiation treatment with high RBE beams may become the golden standard treatment.

All the above-mentioned clinical, physical and radiobiological considerations have led to the study, development and realization of a new generation of accelerators dedicated to the production of proton and/or ion beams in tumour radiation therapy.

Two kinds of accelerator are mainly employed world wide to produce protons and light ion beams for hadrontherapy: cyclotrons and synchrotrons.

Cyclotrons are generally characterized by their small size and by their ability to produce particle beams with a practically continuous temporal structure and a fixed, invariable energy.

Synchrotrons are characterized by their large size and by their ability to produce particle beams with their own temporal structure and energy. The energy of particle delivered by the synchrotron can be varied quite easily during treatment. Despite the fact that some studies for superconducting cyclotrons able to deliver Carbon beams at an energy of up to 400 AMeV were carried out in the past [4,5], up to now room temperature and superconducting cyclotrons have been built only to deliver proton beams at energies of 230-250 MeV. The main disadvantages of the previous design of the 400 AMeV cyclotron are either the size of the machine [4], or the high value of the spiral angle of the cyclotron's hills [5].

Moreover, the great advances made by cryogenic technology offer the opportunity to design superconducting cyclotrons that have a really low cryogenic consumption, and on the other hand compact and relatively small Helium relyquefiers, which are available today. These two technical developments allow the cyclotron user to avoid the problem of driving a plant for liquid Helium, which was one of the disadvantages of the previous project.

It is important to note that the continuous temporal structure of cyclotron beams allows the feedback and dose delivering control systems to perform more efficiently, than in synchrotrons.

To avoid this problem, or at least to reduce it, the new generation of synchrotrons for therapy are designed to perform a so-called "slow extraction". Despite this method allowing for a quasi-continuous beam the mean current is lower than for the synchrotron with a fast extraction. Moreover the current ripple of synchrotron beam delivered with the "slow extraction" is not as low as for the cyclotron beam.

On the other hand, the therapy facilities which use cyclotrons also need an energy selector which allows the facility to select and transport particles with the desired energy and energy spread. The energy selector consists of the energy degrader target and of a fully achromatic double-bend spectrometer. The energy selection with the desired energy and angular spread are performed by a selection slit placed on the symmetry plane of the spectrometer. The second half of the spectrometer is used to deliver an achromatic beam to the entrance of a treatment beam line.

The use of an energy degrader to change the beam energy also produces light particles caused by projectile fragmentation on the material, of which the energy modulator is made. A fraction of these secondary particles has the same magnetic rigidity as the main beam. If these light particles reach the patient, they can release an amount of their energy beyond the Bragg peak. To remove these light particles from the main beam, or at least to reduce this effect strongly, one simply has to insert a thin degrader on the symmetry plane of the spectrometer.

The thin degrader produces an energy loss on the particles which depends on their Z. Therefore, by scaling the second part of the spectrometer for the new magnetic rigidity of the main beam only, the main beam will then be refocused in the right position on the beam axis line, whilst the lighter particles produced inside the main degrader will be removed from the main beam.

In the current international market the general, unvarying tendency is to use cyclotrons in radiotherapy centres that only employ proton beams (thanks to the better characteristics of extracted beams and to the possibility of a highly efficient control of dose delivering), and to use synchrotrons in all radiotherapy centres that also perform treatment with ion beams, or that plan to do so in the future.

SCENT, as a proposal from LNS and the INFN Sezione Genova for the period 2002-2005, originates from the above considerations, taking the specific INFN experience in the fields of the superconducting cyclotron R&D, operation and maintenance, superconductivity R&D and protontherapy development into account.

The basic idea in addressing our study towards a superconducting cyclotron for proton and light ions at 250 AMeV, is that from a general point of view the installation and maintenance of a cyclotron in a hospital environment is less complex and cheaper compared to that of a synchrotron. Moreover, we believe that light ions will play a more important role than protons in the future, once the radiation oncologist's trust has been gained. Considering the lack of a superconducting cyclotron with these features on the market, our study has addressed the evaluation of the physical and technological limitations of installing one in a hospital-based centre.

Looking at the clinical experience gained in Japan, the country with major experience in Carbon ions treatment, it seems perfectly clear that the maximum useful depth for the tumour with a clear clinical advantage from Carbon, is around 15 cm (on the head and neck, lung, brain), Fig 2. The initial goal of the preliminary design study was to verify the feasibility of a reliable superconducting cyclotron with a maximum energy of 250 AMeV. After our study, as described in the conclusion as well, we are confident that the present design study can be upgraded to 300 AMeV, which is a good compromise considering the request for higher energy, the size and cost of the accelerator, the simplicity and minimisation of operational and maintenance costs.

We believe that this solution represents a good clinical compromise for centres which would now like to exploit the clinical use of protons, and to start research activity in the field of therapy with light ions with a view to gradually increasing the use of Carbon ions, without having to face the complexity of the synchrotron's installation and maintenance.

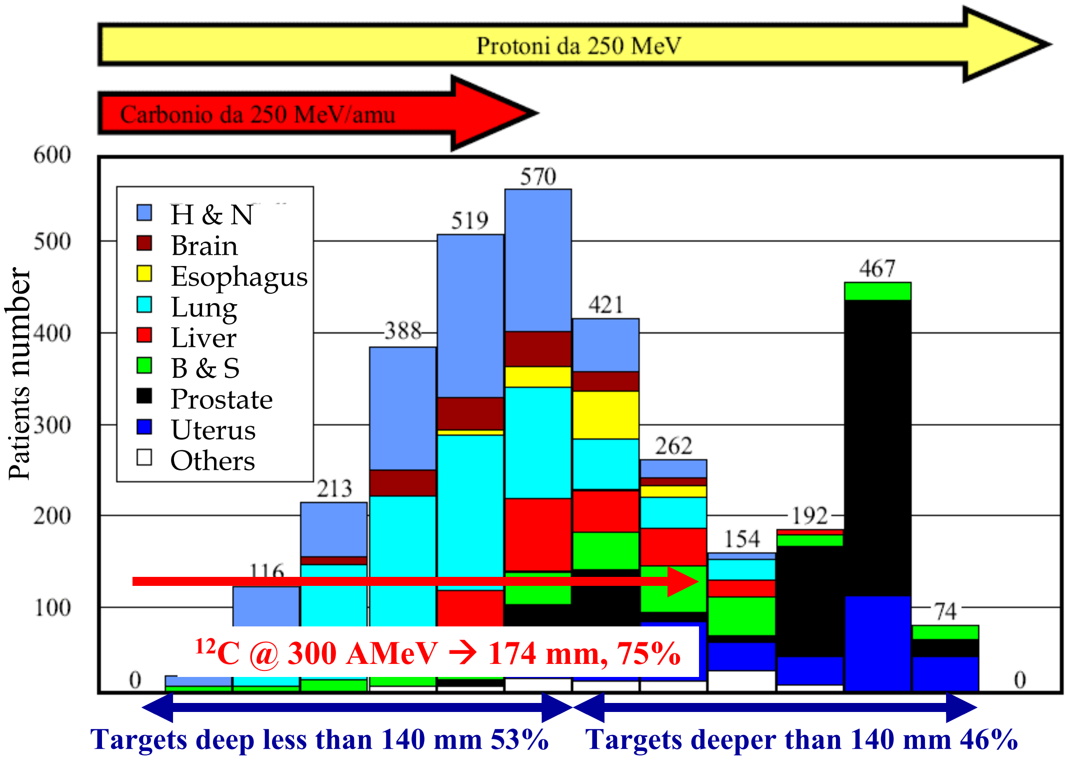

Fig. 2.

The first two sections of the report are dedicated to describe first of all the tumours treatable with Carbon ions, and the matters related to the production of the beams and to their injection inside the cyclotron. The description of the cyclotron is presented in section 3. While in section 4 is described the RF system. Section 5 is dedicated to the extraction problem and the cyclotron's vacuum plant is discussed in section 6.

References

[1] L. Calabretta et al., Nuclear Physics (2004) Nuclear Physics A734 (C) (2004), pp. 378-381.

[2] Brookhaven Linac Isotope Producer (BLIP).

[3] Isotope Production and Distribution Program, http://isotopes.lanl.gov/.

[4] P. Mandrillon et al., XII Int. Conf. On Cyclotrons and Their Applications, Berlin (1989), p.152.

[5] J. Kim, F. Marti and H. Blosser, *“Design Study of a Superconducting Cyclotron for Heavy Ion Therapy”*, XVI Int. Conf. On Cyclotrons and Their Applications, East Lansing (2001), p.324.

[6] Y. Hirao, *“Results from HIMAC centre”*, XVI Int. Conf. On Cyclotrons and Their Applications, East Lansing (2001), p.8.

Chapter 1. Assessment of tumours treatable with a 3 GeV Carbon ion beam

1.1 Introduction

Clinical experience using ion beams started in 1957 and it is estimated that more than 4000 patients have been treated thus far with encouraging results.

Recent technological developments in the construction of dedicated accelerators and improvements in dose-calculation software for particle therapy, have stimulated a new clinical interest for hadrontherapy, especially for ions. Carbon ions, in particular, apart from the inherent a high level of ballistic precision, may have a considerable clinical advantage in terms of their high relative biological efficiency (RBE).

Clinical experience with Carbon ions began in 1994 when the Chiba facility (HIMAC), in Japan, was activated. More recently, two other facilities, Darmstadt in Germany (GSI) and Hyogo in Japan (HIBMC) have started treating patients, and clinical data, although preliminary, is accruing.

1.2 Physical and radiobiological properties of Carbon ions

Several kinds of ions have been tested clinically. Helium ions, with atomic number Z=2 and mass number A=4, and Neon ions, with Z=10 and A=20, were the first to be used. Helium ions are, however, relatively light and their RBE value is 1.2-1.4. The RBE value for Neon ions, on the other hand, is about 3.5. Neon ions, however, present some negative characteristics, such as fragmentation in smaller ions having a longer range that creates a tail beyond the Bragg peak and damages the ballistic properties of the beam. From a clinical point of view, therefore, the atomic number must be chosen carefully, in order to obtain the best compromise between RBE (that improves with increasing Z) and ballistic characteristics (that worsens with increasing Z). Carbon ions have long been considered as optimal particles for clinical purposes, since they fulfil the above-mentioned requirements. Indeed, the depth-dose curve for Carbon ions has a tail, at the end of the Bragg peak (see Fig.1), because of the fragmentation in smaller ions (Boron, Lithium and mainly Helium and protons) created by collisions with the nuclei of crossed matter. However, this is not so large to significantly alter the beam ballistic properties. Carbon ions have high LET (Linear Energy Transfer) that increases significantly near the Bragg peak. It has been calculated that the LET of Carbon ions for the last 5 cm of their range is 200 MeV/cm, that is about 50 times greater than the LET of photons. High LET increases the RBE markedly and makes Carbon ions relatively insensitive to Oxygen levels (OER, Oxygen Enhancement Ratio) and thus radiobiologically more efficacious than photons in hypoxic tissues.

Carbon ions with energy of 4.5 GeV can cross a tissue thickness of about 25 cm before stopping. If their energy loss is constant, a LET value of 180 MeV/cm may be considered. However, LET increases significantly with depth, with values ranging between 100 and 150 MeV/cm for the first half of its range and increases to 200 MeV/cm in the last 5 cm of its range (at a depth about 20 cm) and may reach 1 GeV/cm in close proximity to the Bragg peak. The corresponding RBE, at such high LET, is further increased by the production of secondary electrons.

1.3 Clinical indications

So far, about 4000 treatments with ion beams have been reported in the medical literature. The facility at Berkeley University has treated 1314 patients between 1975 and 1993 with Helium ions and about 1400 with Carbon ions. Most clinical indications for ion therapy coincide with those generally recognized for proton beams (ocular pathologies, head and neck tumours and paraspinal tumours), taking into account the excellent ballistic characteristics of the beam. The availability of ion beams with high RBE, however, encouraged their clinical application in radio-resistant pathologies. About 15% of tumours that benefit from radiotherapy may be defined as radio-resistant and are potential candidates to Carbon ion therapy.

Typical radio-resistant tumours include:

- salivary glands tumours (locally-advanced or recurrent);
- paranasal sinuses adenocarcinomas and adenoid-cystic carcinomas;
- locally-advanced head and neck tumours;
- soft-tissue sarcomas;
- osteosarcomas;
- low grade chondrosarcomas;
- locally-advanced tumours of the uterine cervix (FIGO stage III b and IV);
- locally-advanced prostate tumours;
- rectal carcinoma (inoperable or recurrent);
- selected cases of medically-inoperable NSCLC (non small cell lung cancer);

- melanomas;
- selected cases of epatocarcinoma.

These clinical indications are confirmed by on-going phase I/II trials at the Chiba facility involving more than 1200 cases treated with Carbon ions since inception of clinical activity in 1994 for the following pathologies:

- uterine cervix (FIGO IIIb and IV);
- prostate tumours (stage cT2b and cT3);
- locally-advanced head and neck cancer;
- selected cases of medically-inoperable NSCLC;
- selected cases of epatocarcinoma.

A particularly interesting promising modality of Carbon ion therapy is the possibility of using it as a boost dose prior to photon irradiation with IMRT (Intensity Modulated Radiation Therapy) techniques. With this approach, recently proposed by Brahme (Karolinska Hospital, Stockholm), a preliminary dose of about 5-10 Gy with Carbon ions is administered (corresponding to a dose of approximately 10-30 GyE, Gray Equivalent, obtained by the product of physical dose and RBE), followed by a X-ray IMRT technique that completes the treatment. The advantage of a preliminary treatment with ions is that high LET particles are not sensitive to Oxygen and may be more efficacious during the starting phase of the treatment when the tumour comprises an higher component of hypoxic cells, whereas, during the ensuing treatment phase with photons, the disease should have shrunk and reoxygenated.

It appears obvious that the number of patients amenable to ion therapy with this short, initial approach, is significantly higher than the number of patients treatable exclusively with ions.

1.4 Clinical results

1.4.1 Base of skull

About 200 patients tumours of the base of skull have been treated at Berkeley with Helium and Neon ions with doses in the order of 65 Gy. At 5 years, reported local tumour control is 78% for chondrosarcomas, 63% of chordomas and 85% for meningiomas. GSI of Darmstaadt has recently reported similar results albeit with a shorter follow-up.

1.4.2 Salivary gland an paranasal sinuses

These tumours represent the ideal indication for ion treatment. Especially in the light of the encouraging results obtained with neutrons in this clinical context. Published data from the Berkeley Laboratory on 18 cases of inoperable or recurrent salivary glands tumours, indicate a 50% local control rate at 5 years. Recently, the Chiba facility has reported on 130 patients treated with Carbon ions indicating a local tumour control rate of 80%-85% at one year and 58%-80% at three years, with doses between 48.6 and 70.2 GyE in 16-18 fractions. The excellent local tumour control for adenoid-cystic tumours is confirmed by GSI data where a 18 GyE Carbon ions boost following conventional radiotherapy at 54 Gy was administered. Local tumour control at a median follow-up 12 months was 80% at one year and 65% at three years; moreover, no late toxicity above grade 2 was observed.

1.4.3 Bone and soft tissues sarcomas

A dose-escalation study with Carbon ions performed at Chiba involved doses between 52.8 and 73.6 Gy in 16 fractions of 3.3-4.6 GyE in four weeks to 57 patients with inoperable soft tissues sarcomas. At the highest dose level a grade 3 skin toxicity was observed in 41% patients and the dose-escalation program was interrupted. Actuarial local tumour control at 5 years was 72% with a 46% overall survival.

1.4.4 Medically-inoperable lung cancer

In a dose-escalation program performed at Chiba, 81 patients with medically-inoperable stage I (non small cell lung cancer, NSCLC) were treated with doses ranging between 59.4 GyE in 18 fractions in 6 weeks and 95.4 GyE in 9 fractions in 3 weeks. Overall survival and cause-specific survival at 5 years were 42% and 60%, respectively. Local tumour control improved significantly using total doses above 86.4 GyE. However, significant pulmonary toxicity observed as a function of increasing irradiated volume. This experience was the starting point of a new study with a lower number of fractions whose purpose was the reduction of the overall treatment time with a similar local control rate.

1.4.5 Epatocarcinoma

A study including 106 patients with advanced or recurring epatocarcinoma was performed at Chiba. Different fractionation schemes ranging from 15 fractions in 5 weeks to 4 fractions in one week were utilized. No severe side effects or treatment-related deaths have been reported. Local tumour control at 3 years was 87% for patients with longer fractionation schemes and 84% for patients with accelerated fractionation. Overall survival for patients with a single lesion, not treated before, was 90%, 70% and 57% at 1, 2 and 3 years, respectively. Carbon ions radiotherapy, which is non-invasive, appears to yield treatment outcomes comparable to surgery.

1.4.6 Prostate tumours

At Chiba patients with clinical stage T2b – T3 have been treated with a dose level of 66 GyE and delivered in 20 fractions of 3.3 GyE each over a period of 5 weeks. Biochemical recurrence free survival was 90.5% at 3 years and 87.2% at 7 years. However, these results ought to be compared with the excellent outcomes obtained using IMRT with photons at doses in the order of 80 Gy. In theory, there is a hypothetic advantage in using hadrontherapy because of the lower irradiated volume at low dose, reducing the risk of stochastic radiation-induced tumours, possible with IMRT. During past years radiobiological models comparing these two treatment techniques have been developed. To date, however, comparisons are not feasible due to lack of epidemiological data.

1.5 Epidemiological assessment of the potentially treatable cases in Italy

Epidemiological data on incidence of potentially treatable cases with Carbon ions are summarized in Table 1.1.

It is noteworthy that epidemiological data in Italy are lacking; moreover, percentages of patients who could potentially benefit from high RBE treatment have been derived from data about locally-advanced/hypoxic tumours with outcomes from conventional treatment. For these reasons, data summarized in the above table must be considered with great caution and could change significantly over time.

1.6 Beam characteristics evaluation, 3 GeV vs. 4.8 GeV

The maximum range of 3 GeV Carbon ions is approximately 130 mm and appears suitable for the treatment of head and neck, base of skull and paraspinal lesions. Most of soft tissues sarcomas may be within this range, as well. Most of deep tumours of the thorax, abdomen and pelvic regions are also easily reachable with ion beams that penetrate as far as 130 mm. Nevertheless, obese patients (less than 20% in our population) with deep-seated tumours in the abdomen or pelvic regions may need ion beams with higher energy with a range of at least 200 mm such as those obtainable with 4.8 GeV.

Table 1.1

Clinical indications	**Expected number per year in Italy**	**Treatable with ions**	**Patient number per year treatable with ions**
Salivary gland tumours	340	≈ 50%	≈ 170
Soft tissues sarcomas	420	≈ 30%	≈ 120
Epatocarcinomas	3400	≈ 10%	≈ 340
Prostate tumours	9000	≈ 10%	≈ 900
Head and neck tumours	2700	≈ 25%	≈ 670
Base of skull tumours	210	≈ 50%	≈ 100
Lung tumours (NSCLC)	15000	≈ 5%	≈ 750
Total			≈ 3460

1.7 Bibliography

[1] A. Brahme, R. Lewenshon, U. Ringborg, et al., *"Design of a centre for biologically optimised light ion therapy in Stockholm"*. Internal Report MSF (2001-01), TERA 1/2 GEN 30.

[2] JR. Castro, *"Results of heavy ion radiotherapy"*. Radiat. Environ Biophys. (1995), 34, pp. 45-48.

[3] JR. Castro *"Clinical programmes: a review of past and existing hadron protocols"*. In: Amaldi U, Larsson B, Lernoigne Y. eds, Advances in Hadrontherapy, Elsevier Science BV (1997).

[4] JD. Cox, *"Dose escalation by proton irradiation for adenocarcinoma of the prostate"*. Int. J. Radiat. Oncol. Biol. Phys. (1995), 32, pp. 265-266.

[5] J. Debus, O. Jackel, G. Kraft, M. Wannenmacher, *"Is there a role for heavy ion beam therapy"*, *"Recent results cancer Therapy" (*1998), 150, pp. 170-182.

[6] J. Debus, T. Haberer, D. SchuIz-Ertner et al. *“Carbon ion irradiation of skull base tumours at GSI. First clinical results and future perspectives”*. Strahienther Onkol (2000), 176, pp. 211-216.

[7] M.A. Fagundes, E.B. Hug, N.J. Liebsch, W. Daly, J. Efird, J.E. Munzenrider, *“Radiation therapy for chordomas of the base of the skull and cervical spine: patterns of failure and outcome after relapse”*. Int. J. Radiat. Oncol. Biol. Phys. (1995), 33, pp. 579-584.

[8] Gademann G, Wannenmacher M. *“Charged particle therapy to pediatrie tumour of the retroperitoneal region: a possible indication”*. Int. J. Radiat. Oncol. Biol. Phys. (1992), 22, pp. 375-381.

[9] E.B. Hug, M.M. Fitzek, N.J. Liebsch, J.E. Munzenrider, *“Locally challenging osteo and chondrogenic tumours of the axial skeleton: results of a combined proton and photon radiation therapy using three-dimensional treatment planning”*. Int. J. Radiat. Oncol. Biol. Phys. (1995), 31, pp. 467-476.

[10] O. Jakel, M. Kramer, C.P. Karger, J. Debus, *“Treatment planning for heavy ion radiotherapy: clinical implementation and application”*. Phys. Med. Biol. (2001), 46, Vol. II 06.

[11] T. Kamada, H. Tsujii, T. Yanagi et al., *“Efficacy and Safety of Carbon Ion Radiotherapy in Bone and Soft Tissue Sarcomas”*. Journal of Clinical Oncology (2002), 20, pp. 4466-4471.

[12] K. Kagawa, M. Murakami,Y. Hishikawa et al., *“Preclinical biological assessment of proton and Carbon ion beams at Hyogo Ion Beam Medical Center”*. Int. J. Radiat. Oncol. Biol. Phys. (2002), 54, pp. 928-938.

[13] M. Kramer, *“Treatment planning for heavy-ion radiotherapy: biological optimisation of multiple beam ports”*. J. Radiat. Res. (2001), 42, pp. 39-46.

[14] U. Isacsson, A. Montelius, B. Jung et al., *“Comparative treatment planning between proton and X-rays therapy in locally advanced rectal cancer”*. Radiother. Oncol (1996), 41, pp. 263-272.

[15] G.E. Laramore, J.M. Krall, T.W. Griffin et al., *“Neutron versus photon irradiation for unresectable salivary gland tumours”*. Final report of an RTOG-MRC randomised clinical trial. Int. J. Radiat. Oncol. Biol. Phys. (1993), 27, pp. 235-240.

[16] C.V. Levin *"Potential for gain in the use of proton beam boost to the para-aortic lymph nodes in carcinoma of the cervix"*. Int. J. Radiat. Oncol. Biol. Phys. (1992), 22, pp. 355-359.

[17] D.E. Linstadt, J.R. Castro, T.L. Phillips, *"Neon ion radiotherapy: results of a phase I/Il clinical trial"*. Int. J. Radiat. Oncol. Biol. Phys. (1991), 20, pp. 761-769.

[18] V.A. Nowakowski, J.R. Castro, P.L. Peti et al., *"Charged particle radiotherapy of paraspinal tumours"*. Int. J. Radiat. Oncol. Biol. Phys. (1992), 22, pp. 295-303.

[19] R. Miralbell, C. Crowell, HD. Suit, *"Potential improvement of three-dimensional treatment planning and proton therapy in the outcome of maxillary sinus cancer"*. Int. J. Radiat. Oncol. Biol. Phys. (1992), 22, pp. 305-310.

[20] R. Orecchia, M. Krengli, *"Number of potential patients to be treated with proton therapy in Italy"*. Tumori (1998), 84, pp. 205-209.

[21] CL. Rossi, JD. Slater, N. Reyes-Molyneux et al., *"Particle beam radiation therapy in prostate cancer: is there an advantage?"*. Semin. Radiat. Oncol. (1998), 8, pp. 115-123.

[22] H.W. Sandler, D.L. McShan, A.S. Lichter, *"Potential improvement in the results of irradiation for prostate carcinoma using improved dose distribution*". Int. J. Radiat. Oncol. Biol. Phys. (1992), 22, pp. 361-367.

[23] R. Schoenthaler, J.R. Castro, P.L. Petti, K. Baken-Broen, T.L. Phillips, *"Charged particle irradiation of sacral chordomas"*. Int. J. Radiat. Oncol. Biol. Phys. (1993), 26, pp. 291-298.

[24] W.U. Shipley, L.J. Verhay, J.E. Munzenrider et al., *"Advanced prostate cancer: the results of a randomised comparative trial of high dose irradiation boosting with conformal protons compared with conventional dose irradiation using photons alone"*. Int. J. Radiat. Oncol. Biol. Phys. (1995), 32, pp. 2-12.

[25] D. Schulz-Ertner, B. Didinger, A. Nikoghosyan, O. Jakel, I. Zuna, M. Wannenmacher, J. Debus, *"Optimisation of radiation therapy for locally advanced adenoid cystic carcinomas with infiltration of the skull base using photon intensity-modulated radiation therapy (IMRT) and a Carbon ion boost"*. Stahienther. Onkol. (2003), 179, pp. 345-351.

[26] J.M. Slater, J.O. Archambeau, D.W. Willer, M.I. Notarus, W. Preston, J.D. Slater, *"The proton treatment center at the Loma Linda University Medical Center:*

rationale and description of its development". Int. J. Radiat. Oncol. Biol. Phys. (1992), 22, pp. 383-389.

[27] J.D. Slater, J.M. Slater, S. Wahien, *"The potential for proton beam therapy in locally advanced carcinoma of the cervix"*. Int. J. Radiat. Oncol. Biol. Phys. (1992), 22, pp. 343-347.

[28] L.D. Skarsgard, *"Radiobiology with heavy charged particles: a historical review"*. Phys. Med (1998), 14, pp.1-19.

[29] H.D. Suit, *"The scope of the problem of primary tumour control"*. Cancer (1988), 61, pp. 2141-2147.

[30] H. Tsujii, T. Inada et al., *"Clinical results of fractionated proton therapy"*. Int. J. Radiat. Oncol. Biol. Phys (1993), 25, pp. 49-60.

[31] H. Tsunemoto, T. Ishikawa, S. Merita, *"Indication of particle radiation therapy in the treatment of carcinoma of the esophagus*". Int. J. Radiat. Oncol. Biol. Phys. (1992), 22, pp. 321- 324.

[32] M.M. Urie, B. Fullerton, H. Tatsuzaki et al., *"A dose-response analysis of injury to cranial nerves and/or nuclei following proton beam radiation therapy"*. Int. J. Radiat. Oncol. Biol. Phys. (1992), 23, pp. 27-39.

[33] L.T. Yonemoto, J.D. Slater, E.J. Friedrichsen et al., *"Phase I/II study of proton beam irradiation for the treatment of subfoveal choroidal neovascularisation in age-related macular degeneration: treatment techniques and preliminary results"*. Int. J. Radiat. Oncol. Biol. Phys. (1996), 36, pp. 867-871.

[34] L.T. Yonemoto, J.D. Slater, C.J. Rossi et al., *"Combined proton and photon conformal radiation therapy for locally advanced carcinoma of the prostate: preliminary results of a phase I/II study"*. Int. J. Radiat. Oncol. Biol. Phys. (1997), 37, pp. 21-29.

Chapter 2. Injection

2.1 Source

In order to feed the cyclotron with beams like H_2^+ and $^{12}C^{6+}$, and other ions like $^{10}B^{5+}$ and $^{6}Li^{3+}$, an ECR source is the natural choice. Despite the ECR source and the cyclotron also being able to deliver both $^{6}Li^{3+}$ and $^{10}B^{5+}$, we will only consider the two beams H_2^+ and $^{12}C^{6+}$ in the following chapter so as to simplify the evaluation. Moreover, the possible users of this kind of cyclotron are mainly interested in these two ion beams because the treatments planning for protons and Carbon ions already exists and are accepted by the radiotherapist world.

The main requirements that an ion source has to satisfy are:

- high reliability;
- good current stability;
- easy operation;
- low maintenance.

The ECR source meets these requirements.

Said Kantas for the Pantechnik company reported the latest results for their ECR source, called “SUPERNANOGAN” at the recent ECPM (European Cyclotron Progress Meeting) in Belgrade.

The most relevant feature of this source is that the radial and axial beams are produced by permanent magnets and it is able to produce enough $^{13}C^{6+}$. The main features of the source are:

- beam intensity: 3 eμA ($3x10^{12}$ pps) for $^{13}C^{6+}$;
- low ripple < 3%;
- good stability over time < 2%;
- low emittance < 30 π mm.mrad;
- acceleration Voltage 30 kV.

In Fig. 2.1.2 the plot of current vs. time of this source for the $^{13}C^{6+}$ is shown. The mean value is 3 μA and the fluctuation is between 2.95 and 3.05 μA (red lines). The test shown here was carried out using $^{13}C^{6+}$ to avoid the problem of contamination of the 6+ state of charge by other contaminants with Q/A=0.5, like $^{16}O^{8+}$. The results achieved for $^{13}C^{6+}$ can however be extrapolated to $^{12}C^{6+}$. This problem will be discussed further in session 2.1.2.

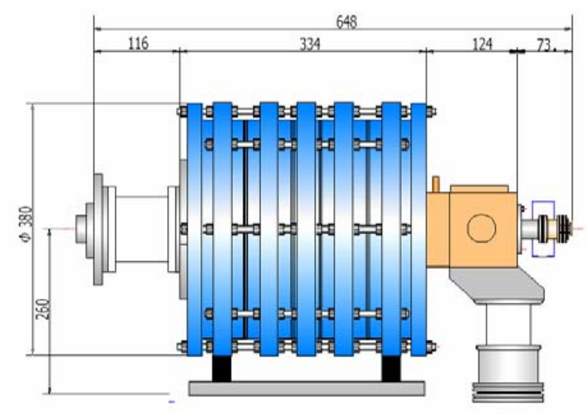

Fig. 2.1.1: The ECR source supernanogan of the Pantechnik company.

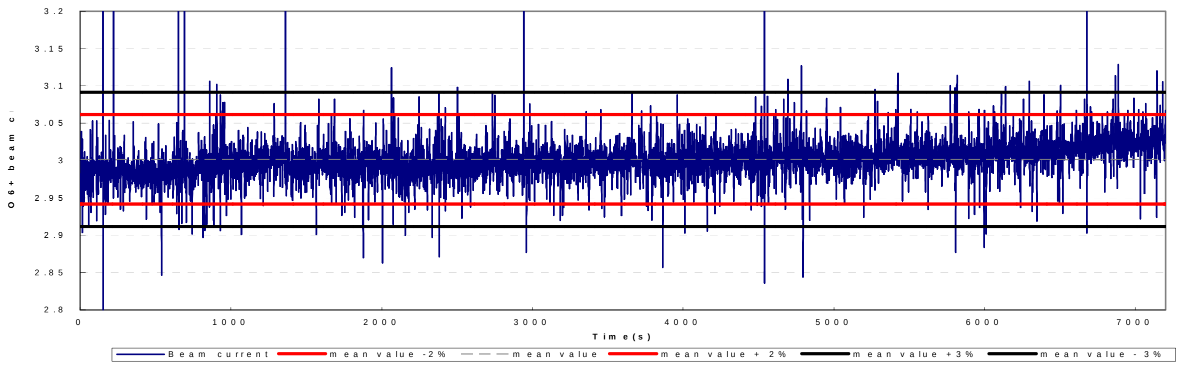

Fig. 2.1.2: Current vs. time for $^{13}C^{6+}$ produced by the supernanogan ECR source.

The same source is also able to deliver a lot of H_2^+, 1 mA with an emittance of 180 π mm.mrad. By scaling to a smaller emittance of 30 π mm.mrad, a beam current of about 150 μA should be feasible.

This beam current is enough for the production of a proton beam for therapy. Commercial cyclotrons used for proton therapy in hospitals deliver beam currents in the range of 300-500 nA, for the IBA and ACCEL cyclotrons respectively.

For the SCENT cyclotron with a beam extracted at 250 AMeV, we require an extracted beam current of 500 nA for protons, and of 100 nA for $^{12}C^{6+}$. The design of the IBA C-400 requires a current of 60 nA as extracted current for a Carbon beam (Y. Jongen, private communication). The lower current for a Carbon beam is the consequence of the smaller angular spread produced by the target degrader of the energy selector system after the cyclotron. This is due to the Carbon mass which is higher than the proton mass. The expected beam current to be delivered to the treatment room is lower than 1 nA as consequence of the higher RBE of Carbon compared with proton.

The expected efficiencies for the different steps of transport and acceleration from the source to the energy selector are:

- ε_t: transport from the ECR source to the central region → 50%;
- ε_{inj}: phase acceptance of cyclotron without buncher → 10%;
- ε_{inj_b}: phase acceptance of cyclotron with buncher → 40%;
- ε_a: acceleration from the central region to the extraction radius → 100%;
- ε_e: extraction from the cyclotron → 50%.

According to these values, in order to deliver the required beam current of $^{12}C^{6+}$ from the cyclotron, the ECR source has to deliver:

- $I_{source} = I_f / (\varepsilon_t \cdot \varepsilon_{inj} \cdot \varepsilon_a \cdot \varepsilon_e) = I_f / 0.025 = 40 I_f = 40 \cdot 100 = 4$ μA without Buncher;
- $I_{source} = I_f / (\varepsilon_t \cdot \varepsilon_{inj\_b} \cdot \varepsilon_a \cdot \varepsilon_e) = I_f / 0.1 = 10 I_f = 10 \cdot 100 = 1$ μA with Buncher.

Therefore, the existing ECR Supernanogan sources of the Pantechnik company are able to deliver enough beam current to operate the cyclotron. By using a simple drift tube buncher, presented in session 2.2.3, a security margin of factor 3 in current is available.

Despite the fact that other sources could deliver more beam current, there are some key parameters which show that the SUPERNANOGAN is probably the right source for the proposed therapy cyclotron:

- limited weight → 200 kg;
- limited RF power, about 500 W at 14.5 GHz;
- only permanent magnets are used to produce the radial and hexapole fields.

The extraction voltage of the ECR source has effects on many of the parameters of the cyclotron and of the beam transport, like the size of the spiral inflector and of the first orbit in the central region of the cyclotron, the sensitivity of the beam to the stray field of the cyclotron, the space charge and aberrations of the transport system. For these reasons, we proposed to operate with a beam accelerated by an extraction voltage of 40 kV. Despite the fact that the SUPERNANOGAN source is usually built with an extraction voltage of 30 kV, upgrading this value to 40 kV is feasible and not much expensive. Once again the advantage of this source is the use of a permanent magnet, which simplifies the insulation. As shown in

Fig. 2.1.2 just two H.V. breakers are used to insulate the source vs. ground. S. Kantas of Pantechnik confirmed that this voltage upgrading is feasible and cheap.

The choice to use particles with Q/A=0.5 is a good choice for the cyclotron, but it creates some problems at source level. Indeed, inside the ECR source a lot of ions are ionized with a charge state Q/A=0.5, so it is impossible to select just one atomic species. Particles that have the same Q/A and are accelerated with the same voltage, have the same magnetic and electric rigidity, so it is impossible to select one or the other through the usual electromagnetic devices. It is only the cyclotron, with its high resolving power in mass, that is able to select the different ions.

This problem does not exist for the H_2^+ beam which is produced with such a low RF power that the other species are not ionized.

There are however some tricks to reduce the contaminant of $^{12}C^{6+}$. The gas generally injected inside the ECR chamber to produce the $^{12}C^{6+}$ ions is CO_2. In this way, only $^{16}O^{8+}$ is a serious contaminant of $^{12}C^{6+}$. To avoid this problem, the gas injected inside the plasma chamber of the ECR source at LNS is often CH_4. ^{3}He gas is then used as a support gas. In this way $^{12}C^{6+}$ is produced without any significant contaminants except for some H_2^+ (decreasing with the microwave power) and all the ions with Q/A=0.5 can be injected inside the cyclotron.

2.2 Injection line

To transport the beam from the source to the cyclotron we studied two possible beam line. The first is very simple and consist of an axial injection line with one ECR source, the second beam line has two ECR sources, one dedicated to the H_2^+, the other to C and use a double arm 90° bending magnet to switch from one source to the other.

2.2.1 One source, axial line

The function of the injection line is to transfer the beam delivered by the source to the center of the cyclotron, and to achieve matching between the source emittance and the cyclotron acceptance. A typical layout of the injection line is shown in Fig. 2.2.1. It consists of the source coupled to a Solenoid lens, which focus the beam at the object point of a bending magnet. This allows us to perform the charge state analysis. After the analysis, the beam is focused at the entrance of the cyclotron’s inflector by a second solenoid lens.

Faraday cups have to be installed at the object and image points of the analyzing magnet and just at the entrance of the cyclotron yoke to check the injected beam current.

In the present case, the beams delivered to the cyclotron will only be H_2^+ and C^{6+}. The H_2^+ beam will probably be quite free of contaminants, whilst the C^{6+} beam could be delivered together with other contaminants like H_2^+, N^{7+}, O^{8+} and so on. These contaminants have the same Q/A ratio so it is impossible to clean the beam through the analyzing magnet. For this reason, we do not consider the use of the magnetic analyzer necessary. Fortunately, the isochronous magnetic field of the cyclotron is able to select the required beam. Therefore, in order to reduce the cost and simplify the injection line, we propose installing the source directly along the cyclotron axis, as shown in Fig. 2.2.1 B.

Only if it is considered useful to plan the installation of two sources, it will be necessary to install a small ± 90° bending magnet to allow to sweep from one source to the other in a short space of time. The final decision of whether to install 1 or 2 sources depends very much on the treatment centre's working plan. It is not crucial to the design of the whole facility. As a result, this decision has been postponed.

In the configuration without analyzing magnet just one solenoid lens is necessary to focus the beam at the entrance of the cyclotron's inflector. It might not be possible to achieve a good emittance matching, and 50% of the injected beam could be lost due to the mismatch.

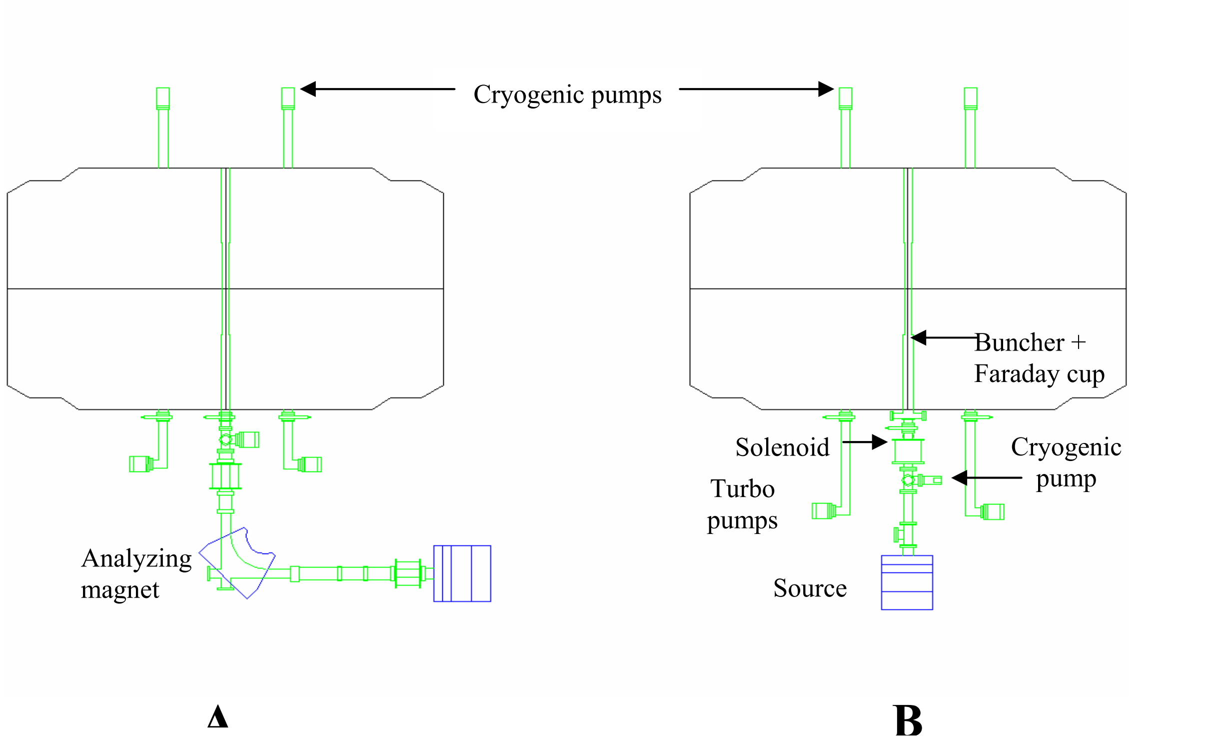

Fig. 2.2.1: A): with analyzing magnet; B): without analyzer, the position of the buncher is also shown.

This will be dealt with later. Fortunately, the ability of the source to deliver beam current in excess of the amount required allows us to tolerate a large amount of beam losses. Just one Faraday cup will be installed before the entrance of the axial hole of the cyclotron.

The position and the characteristics of the solenoid have been selected to minimize the beam spot at the entrance of the inflector.

To evaluate the beam dynamic along the axial line, the cyclotron's magnetic field along the vertical axis of the machine was evaluated by the code OPERA 2D, so reducing a 3-dimensional problem to a 2-dimensional one. A description of this simulation can be found in section 3.5. The beam envelope was then simulated by the transport code which simulates the cyclotron's magnetic field by a stack of thin solenoids equal in length to the OPERA mesh steps on the axis and the evaluated magnetic field.

This simulation method, despite its simplicity, is quite accurate as we have already verified during our previous simulation of K800 cyclotron axial injection [3].

In Fig. 2.2.2 the beam envelope along the axial injection axis is shown. The solenoid lens is placed at 1.1 m after the ion source and at 40 cm from the bottom of the cyclotron. Its effective length is about 40 cm. By using the magnetic field along the axial axis of the cyclotron achieved by the 2D simulation code TOSCA, it is possible to focus the beam at the entrance of the inflector with a solenoid's magnetic field of about 1.64 kGauss. With this geometry and assuming an emittance of 100 π mm.mrad (x=5 mm, ϑ=20 mrad), the beam spot at the inflector entrance is 1.55 mm.

The effect of misalignments between the cyclotron axis and the solenoid/source axis was evaluated too. Fig. 2.2.3 shows the effect of a misalignment of 3 mrad in both the axis X and Y of the solenoid lens. Fig. 2.2.4 shows that this misalignment could be compensated by a steerer installed before the solenoid lens (correction required x'=-0.36 mrad and y'=-4.26 mrad). In addition, if a source displacement of x=y=2 mm, x'=y'=3 mrad is introduced, the residual off axis of the beam centroid is only that of x_c=-0.14 mm and y_c=0.44mm.

So we believe that the proposed geometry is feasible and reliable[1].

---

[1] Simulation file: AxialLine_Scent_1.pbol; file with beam envelopes: Directory \Scent\report\axial injection, file Beam envelope.xls).

As already mentioned, focusing the beam at the entrance of the spiral inflector does not guarantee good matching between the beam emittance and cyclotron acceptance.

It is well known that the spiral inflector produces mixing between the two spaces (*x,x'* and *y,y'*), so it is practically impossible to solve this problem in analytical form. The only possible way therefore, is to simulate the beam injection line including the spiral inflector to find a solution which minimizes the mismatch. It has been shown [4] that the use of a quadrupole doublet with a free rotation angle is a useful device to achieve this goal. The next paragraph details the results of our simulations.

The layout of the injection line and of the beam envelope along it, does not change significantly if we replace the solenoid lens with an electrostatic quadrupole doublet.

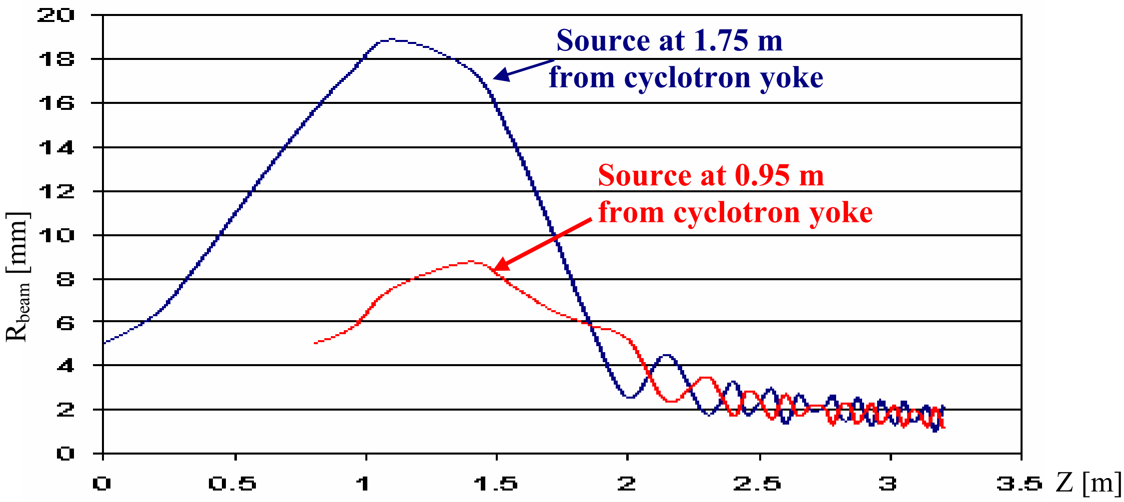

Fig. 2.2.2: Beam envelope along the axial injection line. Beam emittance $\varepsilon_x=\varepsilon_y=5\cdot 20\ \pi$ mm.mrad. Solenoid at 0.35 m from the bottom of the cyclotron. Solenoid field +fringing field 1.4372 kGauss (blu line). Solenoid field+fringing field 2.1483 kGauss (red line). Beam radius at entrance of inflector and along the last 12 cm is smaller than 2.5 mm.

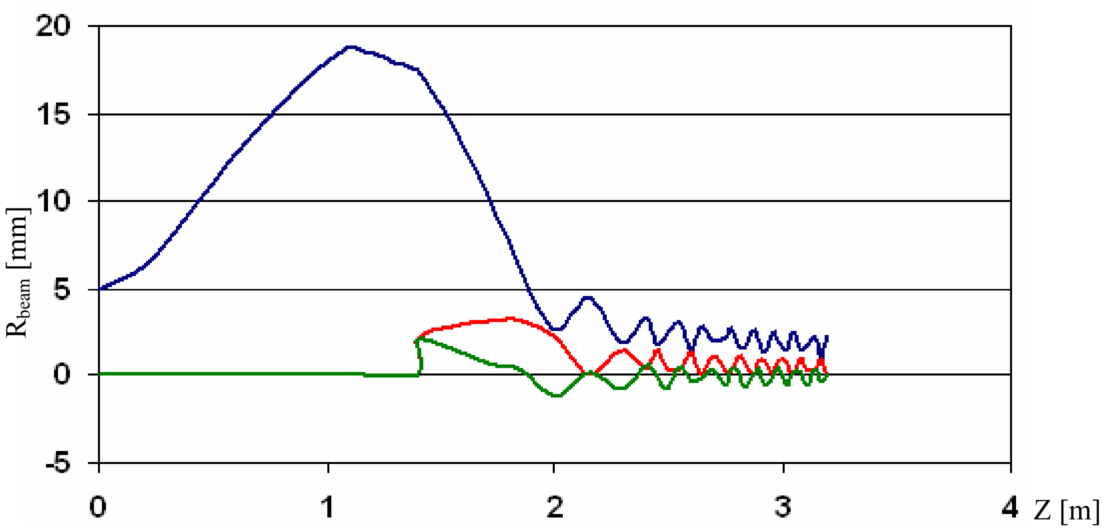

Fig. 2.2.3: Beam envelope along the axial injection line. Effect of the solenoid misalignment: $x_c=y_c=2$ mm; x'=y'=2 mrad. Residual oscillation 1 mm.

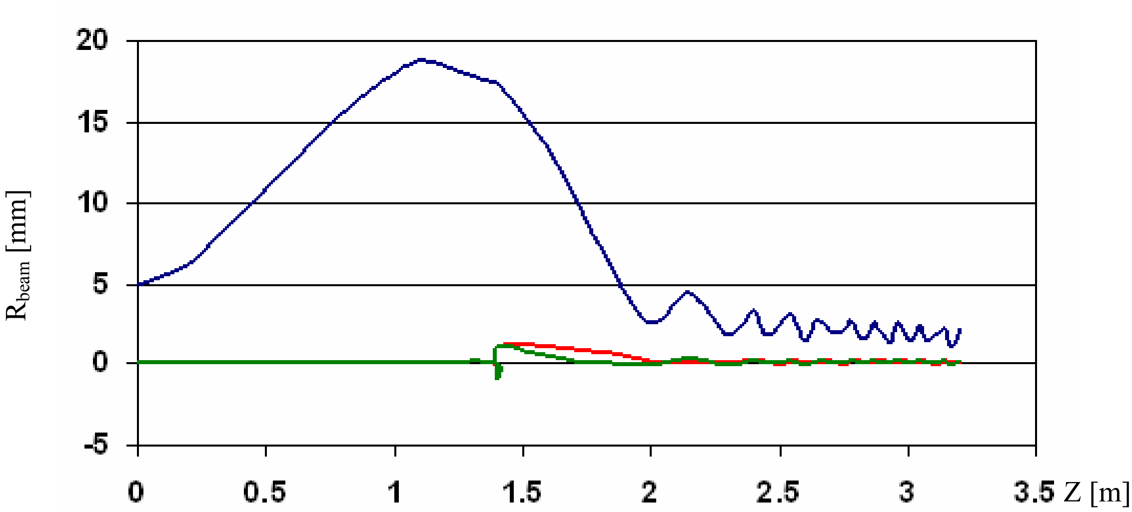

Fig. 2.2.4: Beam envelope along the axial injection line. Effect of the solenoid misalignment compensated by a correction steerer: $x_c=y_c=2$ mm; x'=y'=2 mrad. Residual oscillation 0.2 mm.

There are some advantages to using an electrostatic quadrupole versus a magnetic solenoid. The E.Q. is lighter and cheaper than the solenoid magnet, it is not influenced by the magnetic field of the cyclotron, and its rotation along the axis of the beam line allows control of the radial and vertical mixing after the spiral inflector. Of course, it is necessary to shield the electrodes to prevent possible impact on them from the halo and spurious beams.

In Fig. 2.2.5 the beam envelope produced using a quadrupole triplet is shown. Figs. 2.2.6a and 2.2.6b show the (*x,y*) mixing effect produced by the triplet rotation.

In the present simulation this is not completely exact because the region of the triplet is simulated to be free of the axial stray field of the cyclotron.

Moreover, our triplet is assumed to be magnetic. We have to perform a simulation using TOSCA.

However, before this last step we have to evaluate the following:

- find the right spiral inflector;
- find out for the real spiral inflector the *(x,y)* mixing produced in one direction and in the other;
- see if a shape of the beam with an (*x,y*), correlation which minimizes the (*x,x'*) and *(y,y')* emittances after the spiral inflector exists (try to transport *(x,y)* beam with different values of correlation).

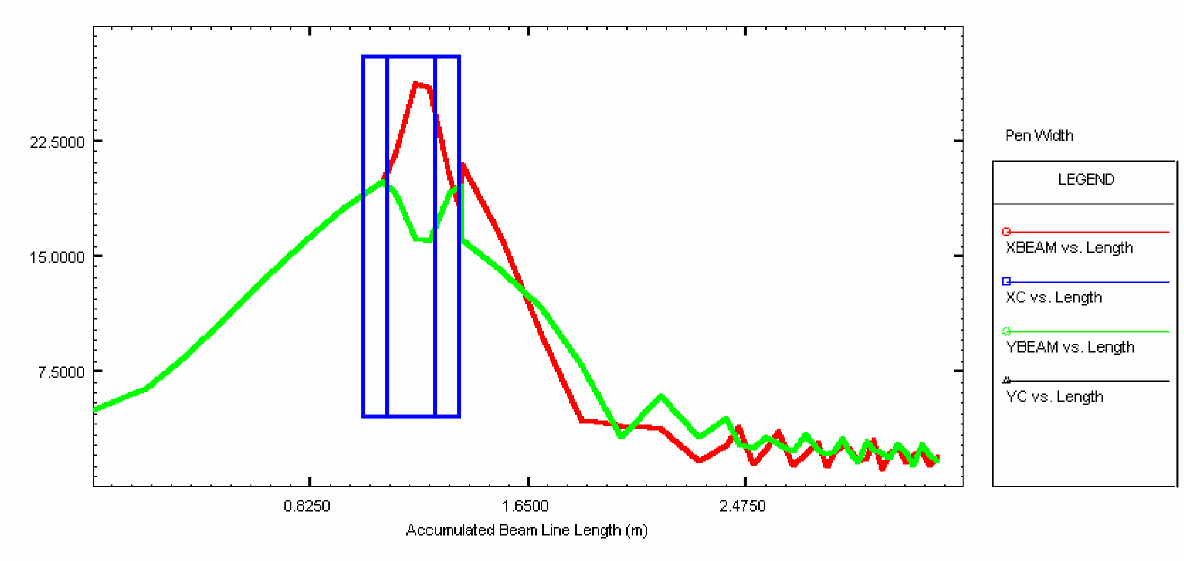

Fig. 2.2.5: Beam envelope achieved by quadrupole triplet[2].

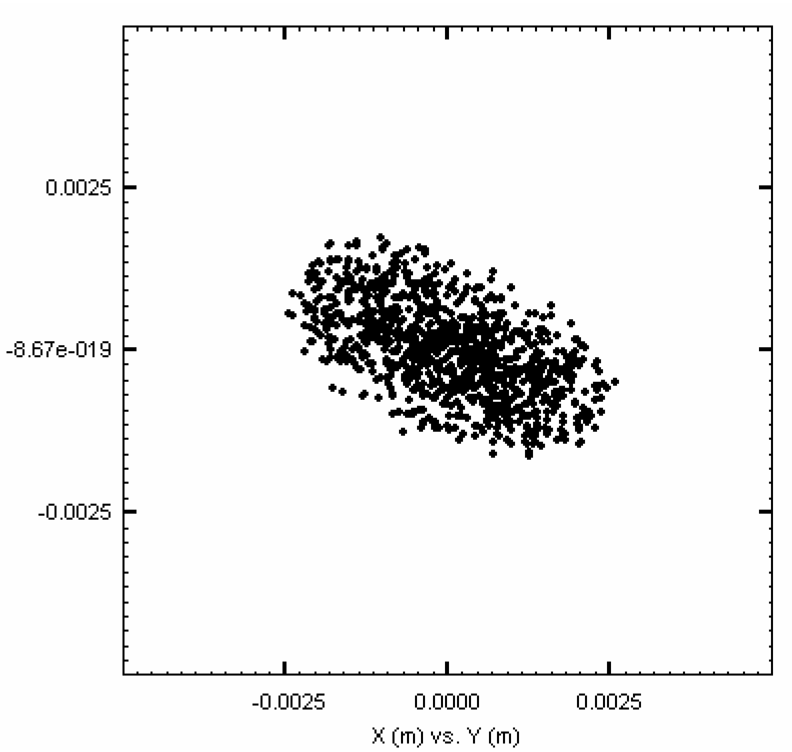

Fig. 2.2.6a: Correlation in the x-y plane, at 15 cm before the entrance of the spiral inflector, produced by a 45° rotated quadrupole triplet[3].

[2] File: \scent\report\axial Injection \axialLine_scent3.pbo.

[3] File: \scent\report\axial injection\axialLine_scent3.pbo, Turtle.

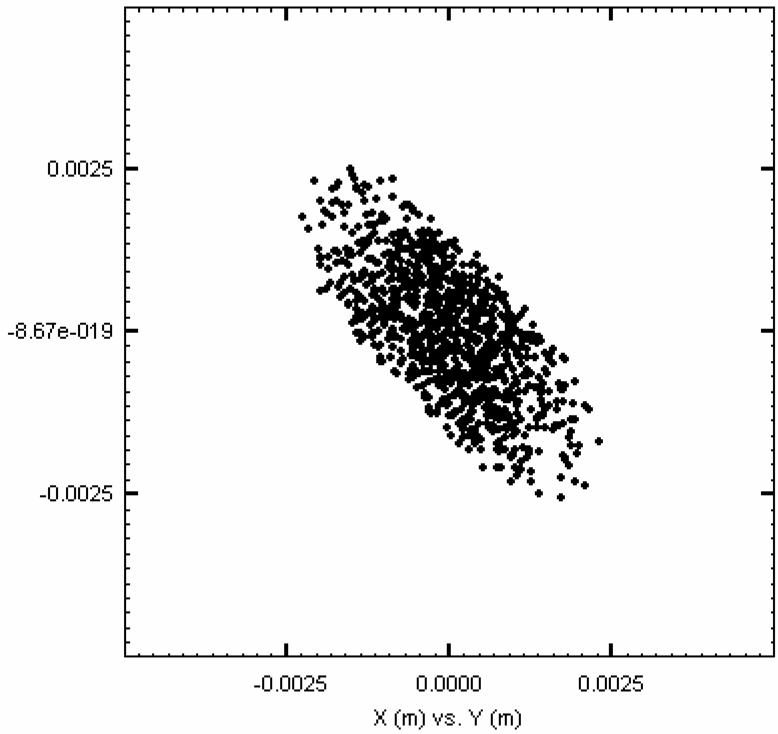

Fig. 2.2.6b: As in previous figure but after 15 cm, just at the entrance of the spiral inflector[4].

2.2.2 Two sources, injection line

The layout of the beam line with two ECR sources is shown in Fig. 2.2.7. The advantages of this more expensive solution are:

- inside the cyclotron only particles with Q/A=0.5 are injected;
- the tuning of the ECR source can be checked properly;
- the beam changing from proton to Carbon is faster.

The beam produced by the ECR source is focused by a solenoid in front of a 90° bending magnet, then focused at the entrance of the inflector by a second solenoid placed between the 90° dipole and the bottom of the cyclotron. A description of the beam injection line can be found in table 2.II. The beam line was simulated with the Transport code and Turtle code at the 3rd order using the PBO code (the input file being AxialLine_soluz_1.pbol).

The cyclotron field inside the axial hole and outside the cyclotron was simulated by a set of solenoids. The field inside each solenoid has the same value as the cyclotron axis field at the corresponding distance from the cyclotron median plane (see Fig. 2.2.8).

[4] File: \scent\report\axial injection \axialLine_scent3.pbo, Turtle.

An evolution of the previous axial injection line design is there to replace the second solenoid with a quadrupole doublet (simulation file: AxialLine_soluz_2.pbol).

As for the previous axial line, the use of a quadrupole doublet allows us to produce a correlation in the space (*x*,*y*).

The parameters of the quadrupole doublet which replace the second solenoid are:

- Quadrupole 1: effective length=5 cm, magnetic field=807 Gauss, ∅=60 mm.
- Drift length: 10 cm.
- Quadrupole 2: effective length=5 cm, magnetic field=-647 Gauss, ∅=60 mm.

Table 2.2: Parameters of the 2 source injection line.

Drift length	22 cm
Solenoid 1	Eff. length=20 cm, Axial field=3.344 kGauss, ∅=60 mm
Drift length	40 cm
90° Analyzing Dipole	Bending radius=300 mm, pole's gap=40 mm entrance angle=27°, exit angle=0°, B=1.36 kG
Drift length	97 cm
Solenoid 2	Eff. length=20 cm, axial field=1.90 kGauss, ∅=80 mm
Drift to the Cyclotron	70 cm

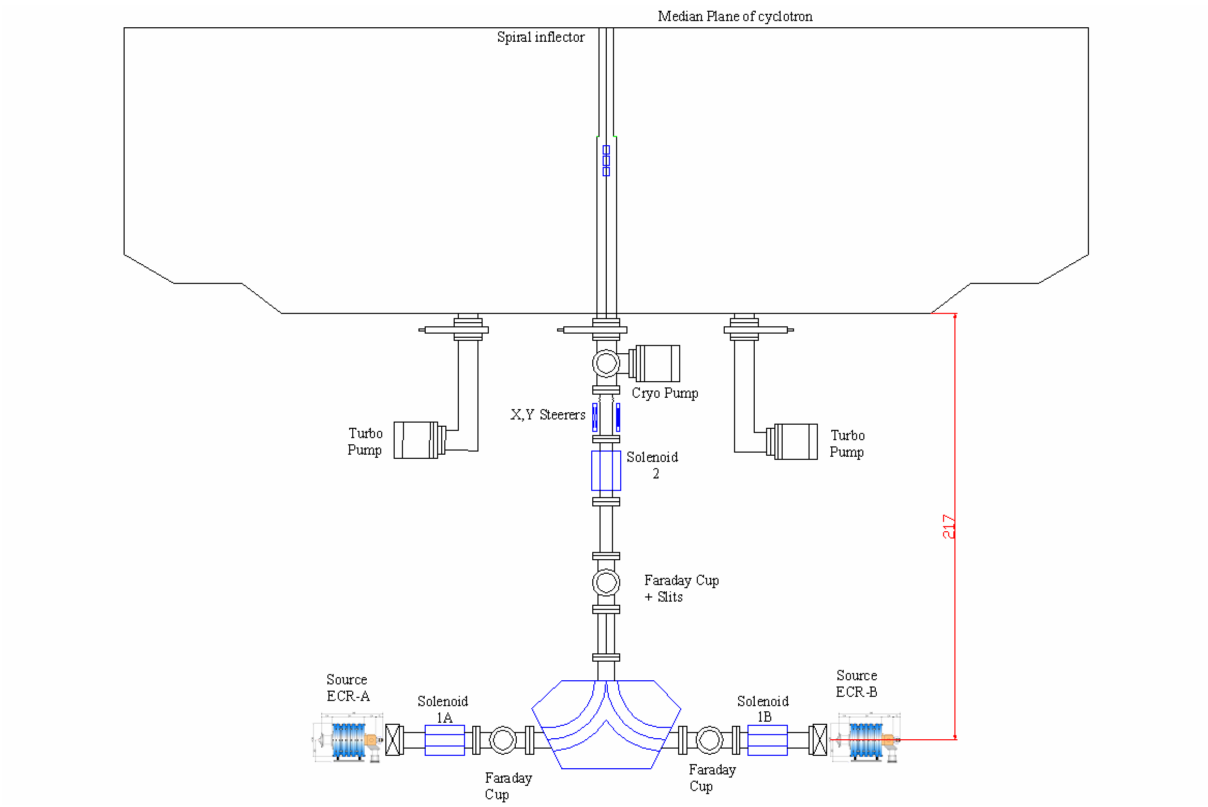

Fig. 2.2.7: Two source, injection line.

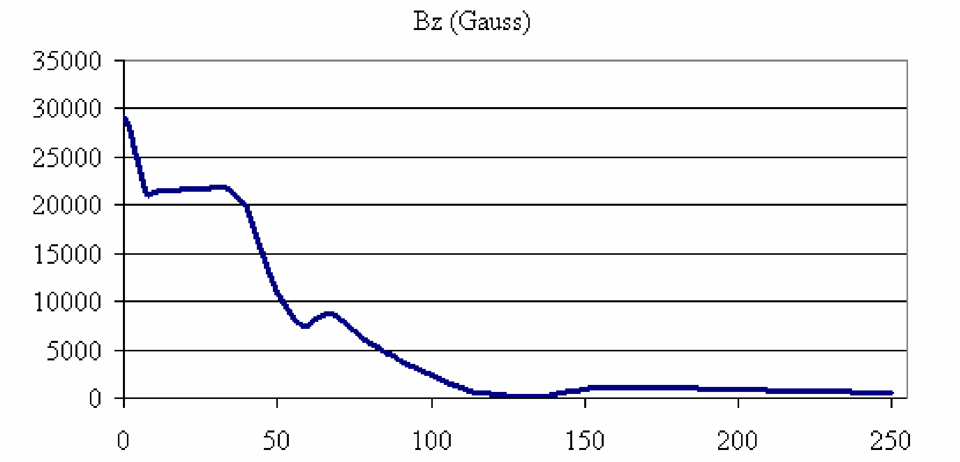

Fig. 2.2.8: Cyclotron fields along the axis vs. distance from the median plane (cm).

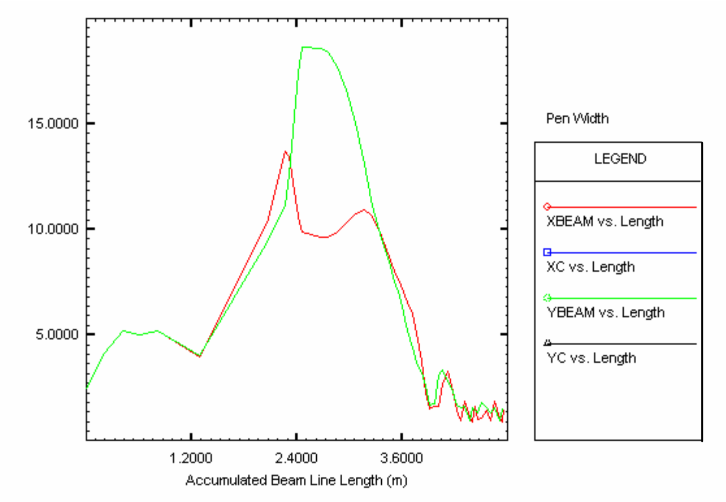

Fig. 2.2.9: Beam envelope for a beam delivered by the ECR source with an extraction voltage of 40 kV, with emittance of 2.5·15 π mm.mrad, simulation performed with transport code (PBO) at first order. Beam line parameter according to Table 2.2.

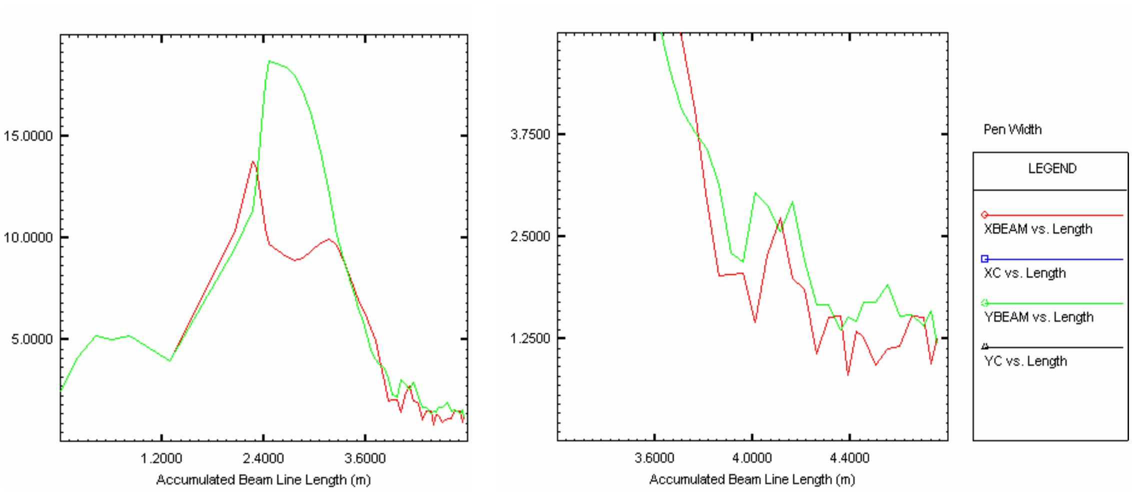

Fig. 2.2.10: Beam envelope, like the previous figure, but including third order effects. On the left side is the zoom of the beam envelope inside the axial hole of the cyclotron.

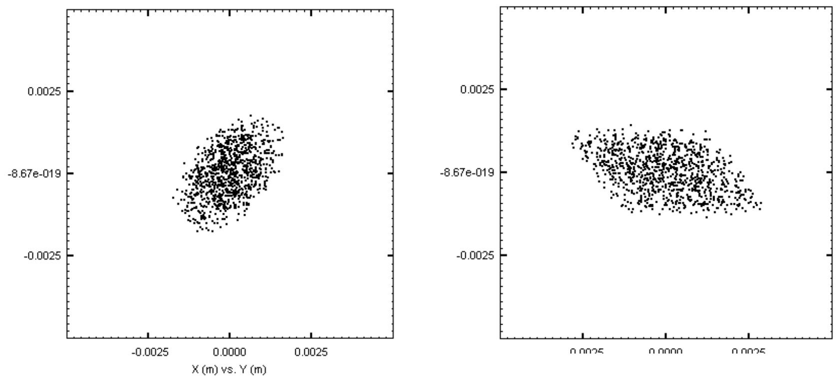

Fig. 2.2.11: Beam spot at median plane of cyclotron. 3° order Turtle code. Left side, effect of 45° rotation of quadrupole doublet.

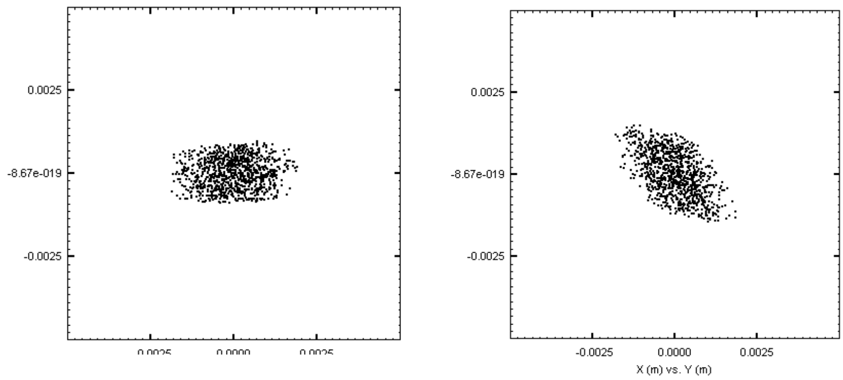

Fig. 2.2.12: Beam spot at 2.5 cm from the median plane of cyclotron. 3° order Turtle code. Left side, effect of 45° rotation of quadrupole doublet.

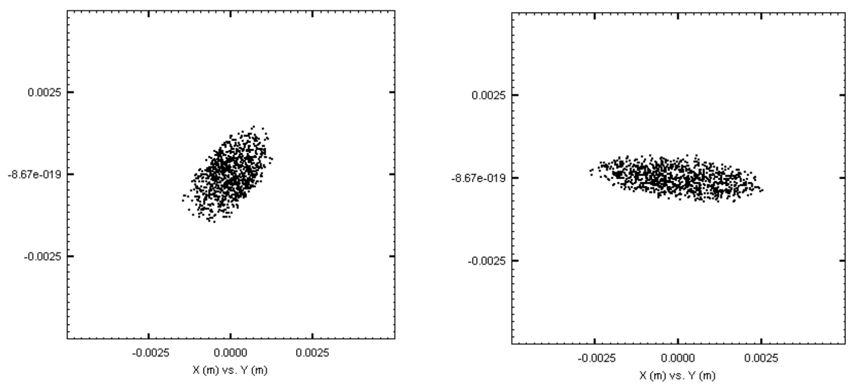

Fig. 2.2.13: Beam spot at 5 cm from the median plane of cyclotron. 3° order Turtle code. Left side, effect of 45° rotation of quadrupole doublet.

2.3 Axial buncher

The installation of a buncher might also not be necessary to increase beam intensity, but could reduce beam losses at the extraction and along the acceleration, with a significant reduction in the accelerator's activation.

In particular, a drift buncher system similar to the device developed for AGOR and for our K800 cyclotron [5], would be very useful, simple and cheap. It consists of a matching box, which is the main component of the system, connected to the electrode by a coaxial cable, Fig. 2.3.1.

The buncher will be driven at the same frequency as the RF cavities (about 93 MHz), and it will be located just 0.6 m from the median plane, see Fig. 2.2.1. Alternatively, it would be possible to install the device outside the cyclotron yoke just to simplify handling.

The voltage required to drive the buncher should be lower than 150 V and the power lower than 20 W.

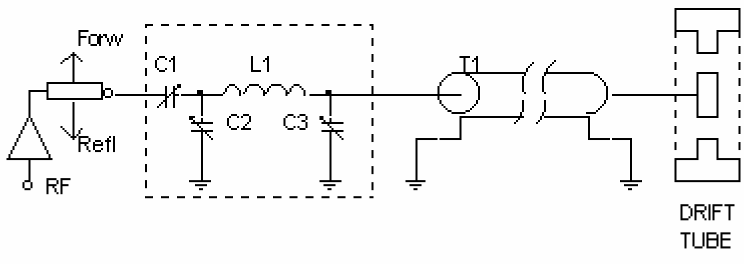

Fig. 2.3.1: Block diagram of the axial buncher system.

2.4 Low energy chopper

The low energy chopper is a useful device which can be used as a variable attenuator of the injected beam [6]. A section of the beam line could hosts a pair of deflecting electrodes as shown in Fig. 2.4.1. Here we describe the characteristics of the device used at LNS.

The distance between the plates is 50 mm, the length is 100 mm and the width is 70 mm, the total capacitance is about 43 pF. With this simple apparatus we are able to modify the duty cycle of the continuous beam from the ECR sources. The layout of the system is shown in Fig. 2.4.1. The core is a compact pulse generator module producing fast, high voltage wave forms to 1500 V; that is the switch in the layout. It is driven by a remote controlled TTL frequency generator. Through this generator it is easy to change the frequency and the duty cycle. We can also change the amplitude of the pulse voltage applied to the deflecting plates. We have tested the system on different continuous particle beams. The duty cycle setting of the pulse generator was followed with the same rate of attenuation by the accelerated beam current. Repetitive tests have been carried out from 1 to 90% of attenuation. This device is very useful in setting the cyclotron parameters with high peak current to investigate space charge effects, but with a low duty cycle in order to avoid activation inside the accelerator chamber and on the walls of the electrostatic deflector. The performances of the chopper are linked to the main parameters of the pulse generator. The maximum voltage delivered is ±1500 V, the rise/fall time is 25 ns (10% to 90%), and the pulse recurrence frequency is 75 kHz at a single shot. These specifications are valid if a 50 pF load connected with 2 feet of RG-62 cable are used. In our case we have tested the system at 850 V, measuring the same or better performances with a pulse recurrence frequency in the range of 1-10 kHz.

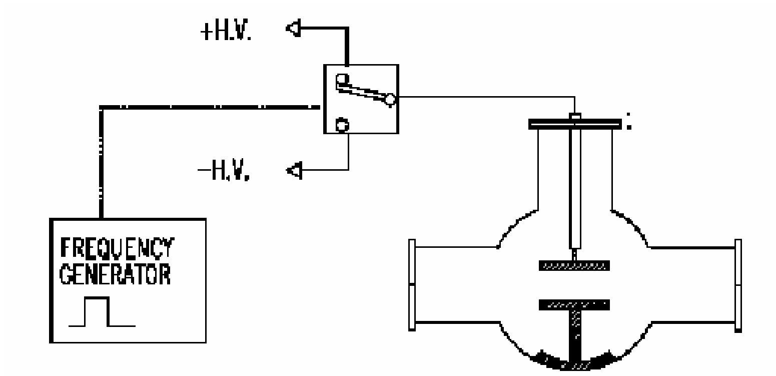

Fig. 2.4.1: Layout of the low energy chopper.

2.5 Inflector design

The properties of the spiral inflectors are described in historical references [7-9]. Here we will repeat them briefly.

We will first define a radius of curvature A and a radius of curvature R_m. A is the radius of the ion if it was acted upon by an electric field in the absence of any magnetic field, it is also the height of the spiral infector. R_m is the radius of the ion if it was acted upon by a magnetic field in the absence of any electric field. They are defined by the following equations:

$$A = \frac{T}{qE_e} \qquad R_m = \frac{p}{qB}$$

where T is the kinetic energy of the ion, p the total momentum of the ion, B the magnetic field value, q the electric charge of the ion, and E_e the magnitude of the electric field.

In length units p is given by:

$$p = \frac{10^6 \cdot E_0}{\eta B c}\sqrt{\frac{T}{E_0}\left(2+\frac{T}{E_0}\right)}$$

where η is the specific charge of the ion, E_0 the rest energy of the ion per nucleon and c the speed of light. The total momentum of the ion through the inflector is constant.

The spiral inflector has two free parameters. One parameter is A, and the second one is k' (a parameter which is related to the direction of the electric field, called *tilt*). It is convenient to define a new parameter k as:

$$k = \frac{A}{2R_m} + \frac{k'}{2}$$

It is assumed that the direction of the electric force on an ion located at the entrance of the inflector is in the $\hat{u}$ direction. The versor $\hat{u}$ is one of the unit vectors of the so-called *optical coordinate system* (see Fig. 2.5.1) [10]. The other two unit vectors of this coordinate system are $\hat{h}$ and $\hat{v}$, where $\hat{v}$ is parallel at the particle's velocity and $\hat{h} = \hat{v} \times \hat{u}$.
Given that we wish to apply an electric field perpendicular to the direction of motion (so there is no energy gain for the central ray) then the electric field vector must lie in the $\hat{u} - \hat{h}$ plane. In the simplest inflector (i.e. no tilt) the appropriate direction for the electric force would be given by the vector $\hat{u}$, and the spacing between the two electrode surfaces (the gap width) is held constant and the magnitude of the electric field in the $\hat{u}$ direction is a constant. In the case of a tilted inflector, the idea is to use a component of the electric field to modify the beam centering. In this case, the direction of the electric force is the $\hat{u}_r$ direction. The $\hat{u}_r$ is one of the unit vectors of the so-called *rotated optical coordinate system*.

The other two unit vectors of this coordinate system are $\hat{h}_r$ and $\hat{v}$. In order to maintain a constant electric field in the $\hat{u}$ direction (Fig. 2.5.2) the gap width d is narrowed. The magnitude of the electric field in the $\hat{u}_r$ direction, E_{ur}, is raised as the ion proceeds along the trajectory in such a way described by:

$$E_{ur} = \frac{2T}{\eta A}\sqrt{1 + k'^2 \sin^2 b}$$

where $0<b<\pi/2$ is the angle of inflection, the instantaneous angle between the velocity vector and the vertical.

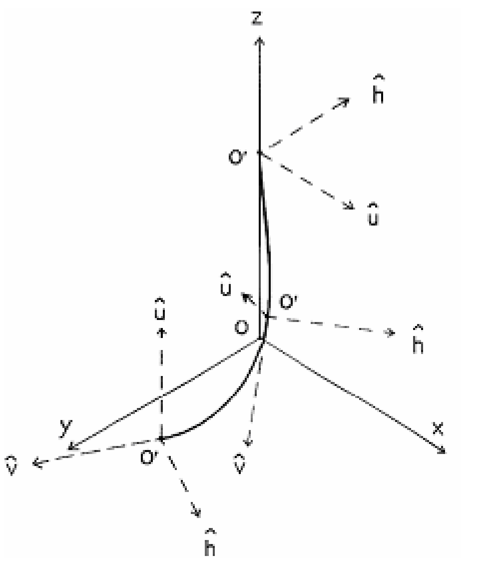

Fig. 2.5.1: The optical coordinate system.

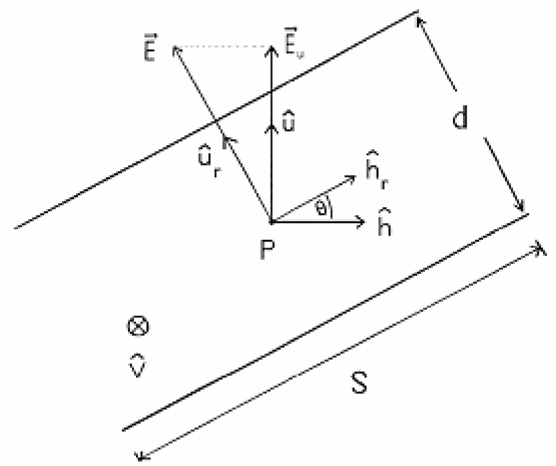

Fig. 2.5.2: The rotated optical coordinate system.

The relations shown have been founded assuming that the component of the electric field E_u follows the approximation *hard edge*. In fact the electric field distribution has *fringing effects* that increase the effective length of electrodes. The figure 2.5.3 shows the fringing effects. This study was realized by Toprek et. al. [10-13] [16-17] and shows the differences between analytical electric field and the result of simulator RELAX3D.

An important parameter of the inflector is the *aspect ratio* that is defined as:

$$a = \frac{s}{d}$$

Where s is the width and d is the gap of electrodes. The fringing effects depend on aspect ratio, as Fig. 2.5.4 shows.

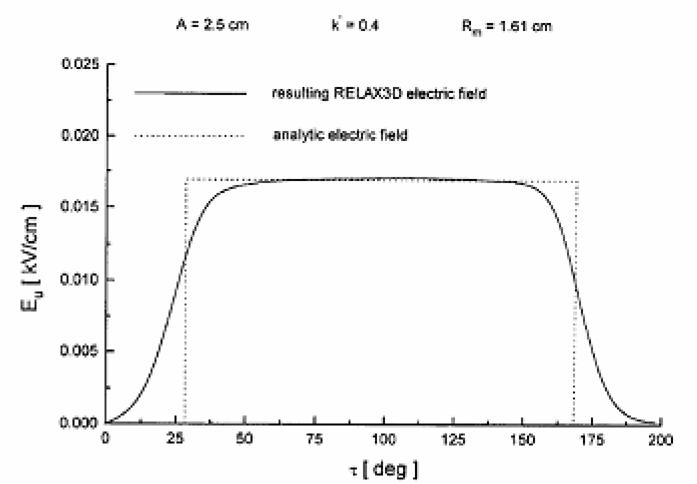

Fig. 2.5.3: Analytic electric field and RELAX3D simulated electric field vs. the angular position along the spiral inflector.

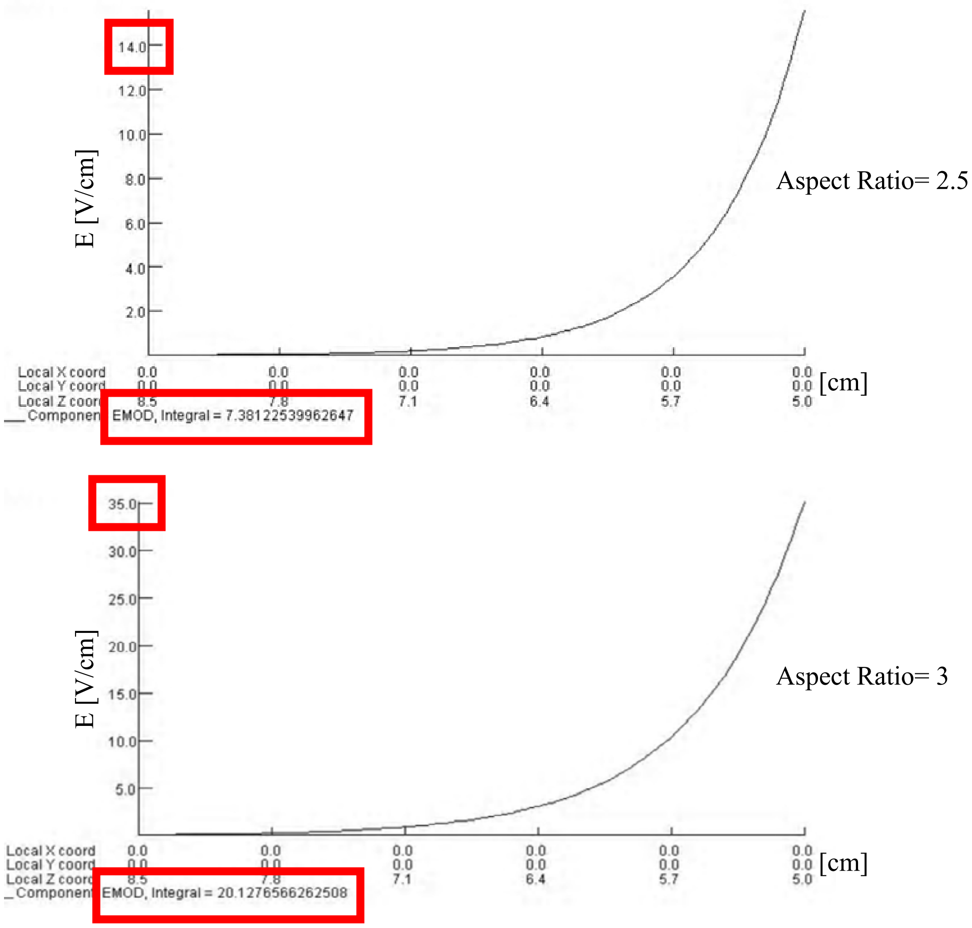

Fig. 2.5.4: Effects of different values of aspect ratio on the electric field of the inflector in the fringing field area.

The fringing effects change the beam dynamic and force the beam particles to oscillate along the central ideal trajectory. In particular at the end of the inflector, the beam trajectory further deviates from the ideal trajectory. The beam is deflected and goes to the electrode that has an attractive force. This effect is as big as small is the height of the inflector.

It is possible to compensate for the fringing effects in three ways:

1. decreasing the inflector length;
2. changing the electric field between electrodes;
3. inserting two collimators before and after the inflector.

In the first one, it is necessary to measure the real distribution of the electric field and calculate the effective length. So this length must be compared with the physical length and the difference should be reduced by cutting certain pieces of the electrodes.

The second alternative is much simpler. In order to change the electric field, it is only necessary to decrease the potential of the electrodes. Therefore, it is not necessary to modify the geometry of the inflector.

If we call V_{nom} the difference of potential that is calculated from the analytical model, we can defined χ, ratio of decrement, as:

$$\chi = (1-\chi_r)\cdot 100\% \text{ and } \chi_r = \frac{V_{\inf}}{V_{norm}}$$

where V_{inf} is the potential that minimizes the fringing effects. Figs. 2.5.5 and 2.5.6 show the influence of parameter χ on the velocity and position of the central particle outside the inflector.

Another method is to insert two collimators near the beginning and the end of the inflector. These collimators are grounded and allow for a reduction in the length of the region where the fringing effects are present. The distance between the collimators, the inflector and the shape of hole, where the beam goes through, influence the trajectory so they should be optimized. Fig. 2.5.7 shows that the fringing effects are greatly reduced when the collimators are present (b).

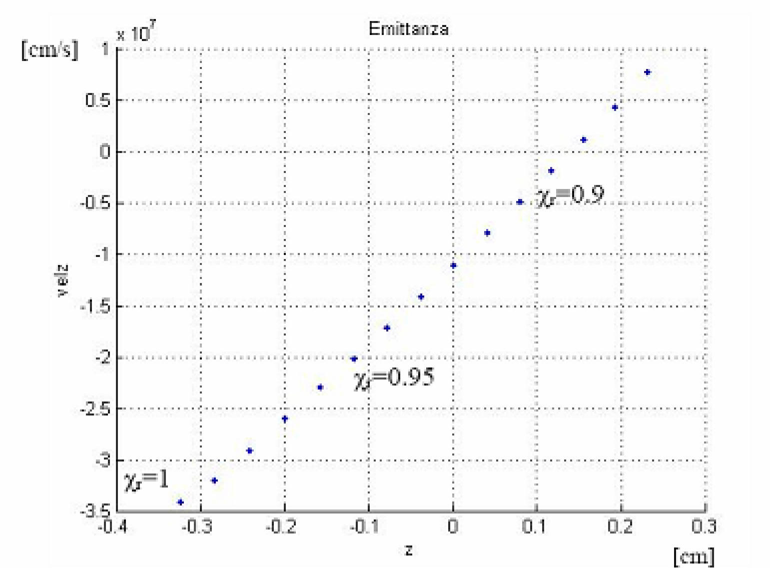

Fig. 2.5.5: Effects on the vertical position and velocity of the central particle due to different values of ratio of decrement χ.

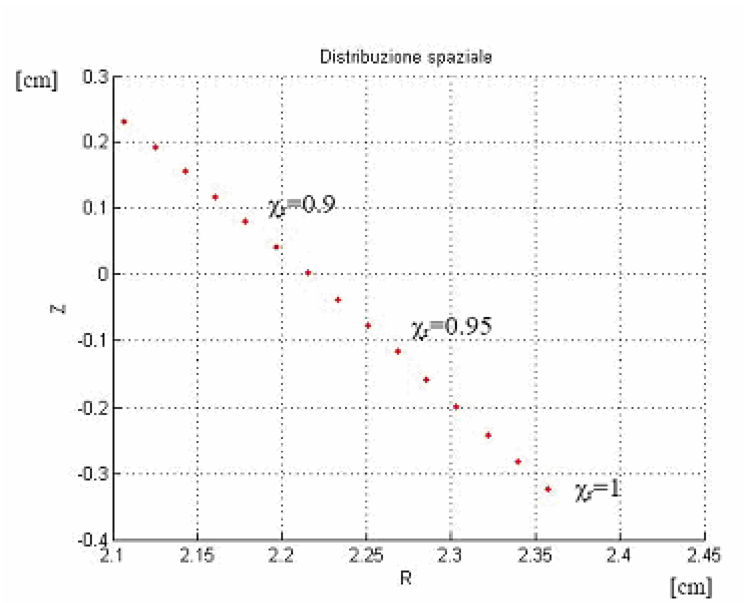

Fig. 2.5.6: Effects on the vertical and radial position of the central particle due to different values of ratio of decrement χ.

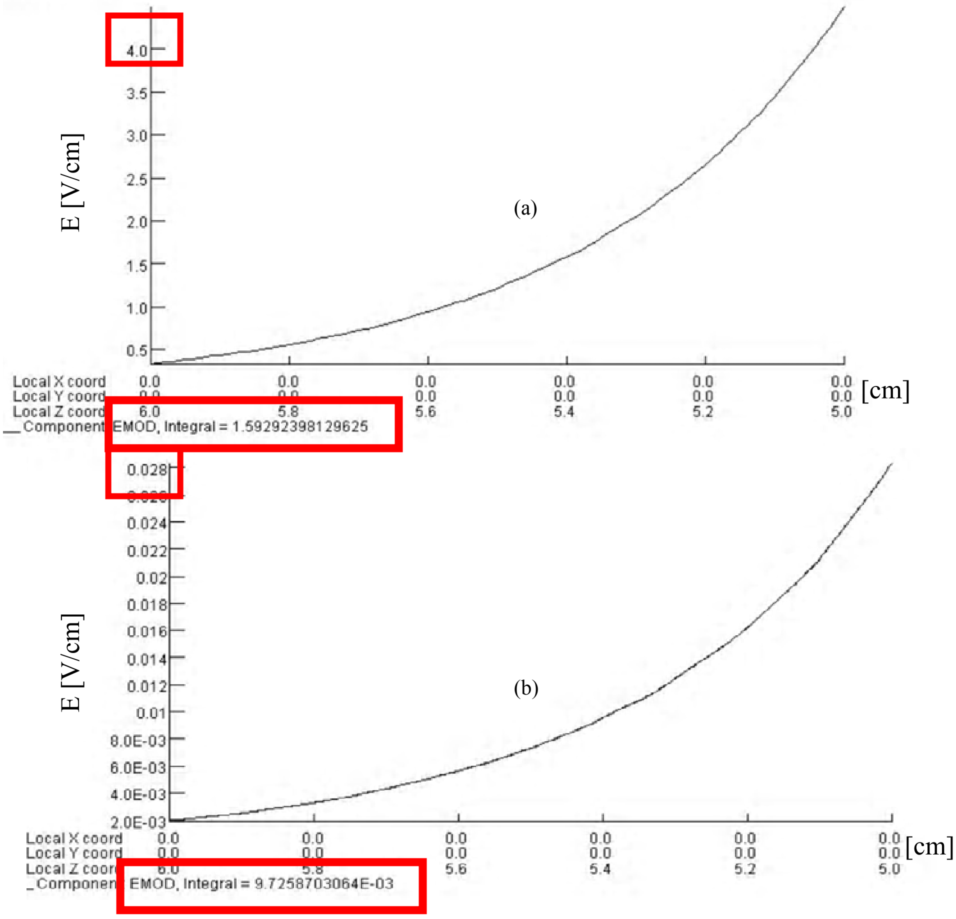

Fig. 2.5.7: Electric field in the fringing region without the collimators (a) and with collimators (b).

2.5.1 Numerical results

The preliminary calculations have been done by analytical approximations described above by means of MATLAB code [18]. Once the geometrical structure was determined, the inflector was designed and simulated by means of the 3D code OPERA to calculate the effective electric field distribution. The trajectory of the ions inside the inflector was analyzed by using the tracking code of OPERA itself.

We have selected, preliminarily, the spiral inflector with:

$$R_m=1.356 \text{ cm} \qquad A=3.42 \text{ cm} \qquad k'=0$$

the electrode spacing at its entrance is d=0.6 cm, and the width of its electrodes is s=1.2 cm (aspect ratio of 2). Different configurations of the injected beam were considered in order to analyze the behaviour of the beam at the inflector exit.

In our calculations of the paraxial ion trajectory through the spiral inflector, we considered the case when the following three requirements should be satisfied:

- the maximal size of the beam emittance at the inflector entrance should be 30 π mm.mrad;
- the beam envelopes through the spiral inflector have to be contained within a small volume to prevent the beam being affected by the bad field quality in the fringing field;
- the size of the beam emittance at the inflector exit should be reasonable for the acceptance of the central region of the cyclotron.

During the simulation of the trajectory, the magnetic field was considered too, due to the presence of the magnet.

To obtain the required parameters, we optimized some variables. First of all, we chose the positions of the collimators. Then we translated the inflector vertically to allow the beam to leave the inflector in the plane z=0. Finally, we changed the potential and the start position of the beam to achieve the required emittance. The change of the beam position is feasible by using magnetic steerer placed at the entrance, as also shown in subsection 2.2. Figure 2.5.8 shows the final inflector; it is important to note that the collimators will be part of the housing.

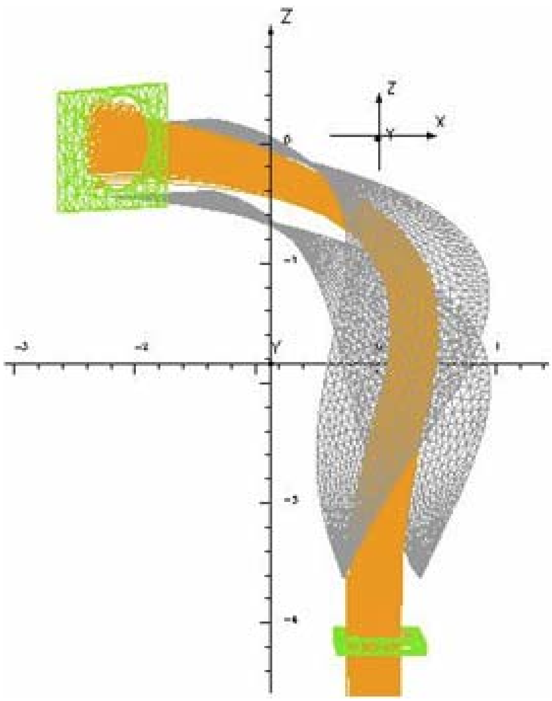

Fig. 2.5.8: Layout of the spiral inflector with beam. The electrodes surface are in grey, the collimator are green and the beam particles in yellow.

When a good result with the central trajectory was achieved, we studied the transport of a uniform spatial distribution. The beam radius was 2 mm and every particle has random velocity around the theoretical value with a difference of 1.5%.

Fig. 2.5.9 shows the distribution in a section located at the first collimator; the red dots are the contour of the hole. The particles travel through the inflector and the distribution shown in Fig. 2.5.10 is achieved. The beam loss is about 1.5%.

The final parameters are shown in Table 2.5.1.

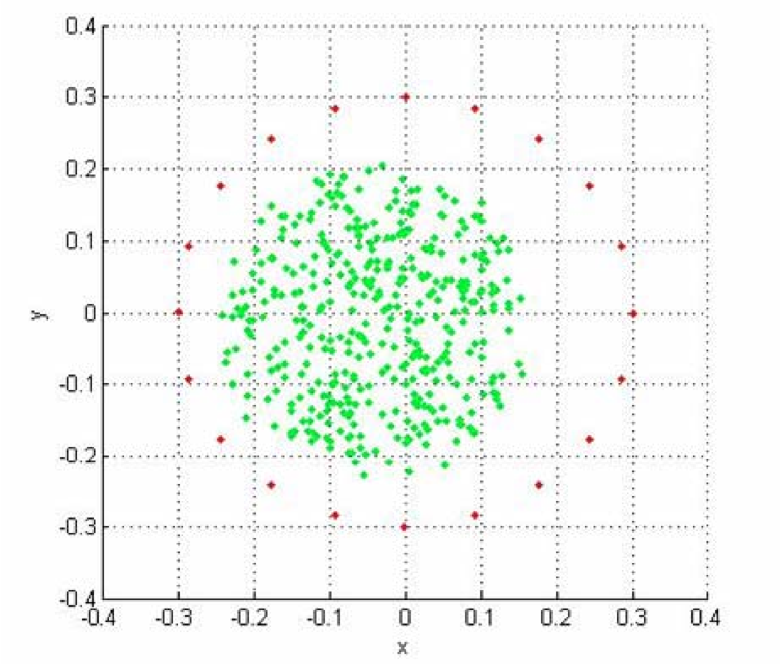

Fig. 2.5.9: Beam particle's distribution at the position of the first collimator. The red dots are the collimator boundary.

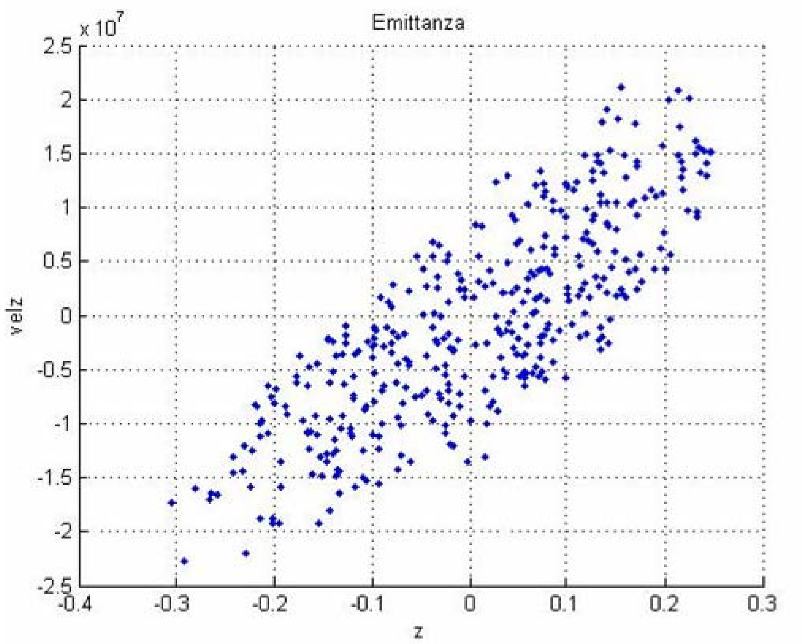

Fig. 2.5.10: Beam axial emittance at the exit of the spiral inflector.

Table. 2.5.1

Type	Spiral inflector
V_{nom}	±7 KV
Electrode spacing	6 mm
Aspect ratio	2
Tilt parameter	0
A	3.42
K	1.26
R_m	1.356
χ (electrodes potential decreasing parameter)	9%

2.6 Central region

Once the inflector shape was determined, a central region was designed [14-15]. The accelerating structures in the SCENT machine consist of four Dees occupying the valley region of the magnet gap. These Dees extend radially from some centimetres out to extraction radius. The space at the center of the machine (up to 5 cm) is used for the central region. The central region itself consists of a set of specially-shaped electrodes attached to the Dees, which accelerate the particles from the inner region out to the main, electrode-free Dee structures. The central region electrodes consist of posts mounted on the center plug and electrodes mounted on the tips of the Dees (and thus called Dee tips). The placements and shape of the various posts and electrodes define a range of starting conditions for the ions which can be accelerated out of the region. Furthermore, the electrodes are positioned so as to place the beam as close to its accelerated equilibrium orbit, upon exiting the central region, as possible. These electrodes then limit the amount of beam which the machine can accelerate and define the quality of the beam. All electrode shapes and positions had to accommodate the inflector housing and guide the beam through the central region leaving it reasonably well-centred. This placement, orientation and shape of the posts, inflector and Dee tips need to satisfy the following conditions:

- the inflector orientation must provide good vertical focusing for the emerging ions. Since the first few gaps will provide the critical vertical focusing, the inflector exit must be placed to ensure that the ions will pass through the first few gaps with the proper late phase required for electric focusing.
- each Dee must be isolated; that is, the field produced by a Dee must be restricted to the area immediately surrounding that structure and not allowed to bleed into the fields of neighbouring Dees. This forbids cross-talk between the RF amplifiers and prevents the formation of destructive radial fields along the beam path.
- the size and position of the Dees electrodes must provide the required structural support at the Dee tips as well as preventing the creation of radial fields in the beam path. By placing posts at the tips of each Dee and larger secondary posts at a larger radial distance along the Dee, the radial fields are excluded from the ion orbit and the structural strength of the Dee is enhanced.

- the beam should be placed along the existing central region so that during acceleration through the machine, it is well-centred (a beam is well-centred if it exhibits no coherent radial oscillations). In this way, any small centering errors produced by misplacements in the mechanical construction of the central region should be correctable through the use of a possible first harmonic magnetic bump. To achieve such beam placement, the shape and position of the aforementioned posts are adjusted to misshape the accelerating gaps during the first turn. The resulting distortion of the gap shapes can be chosen to correctly place the beam at the end of the first turn.

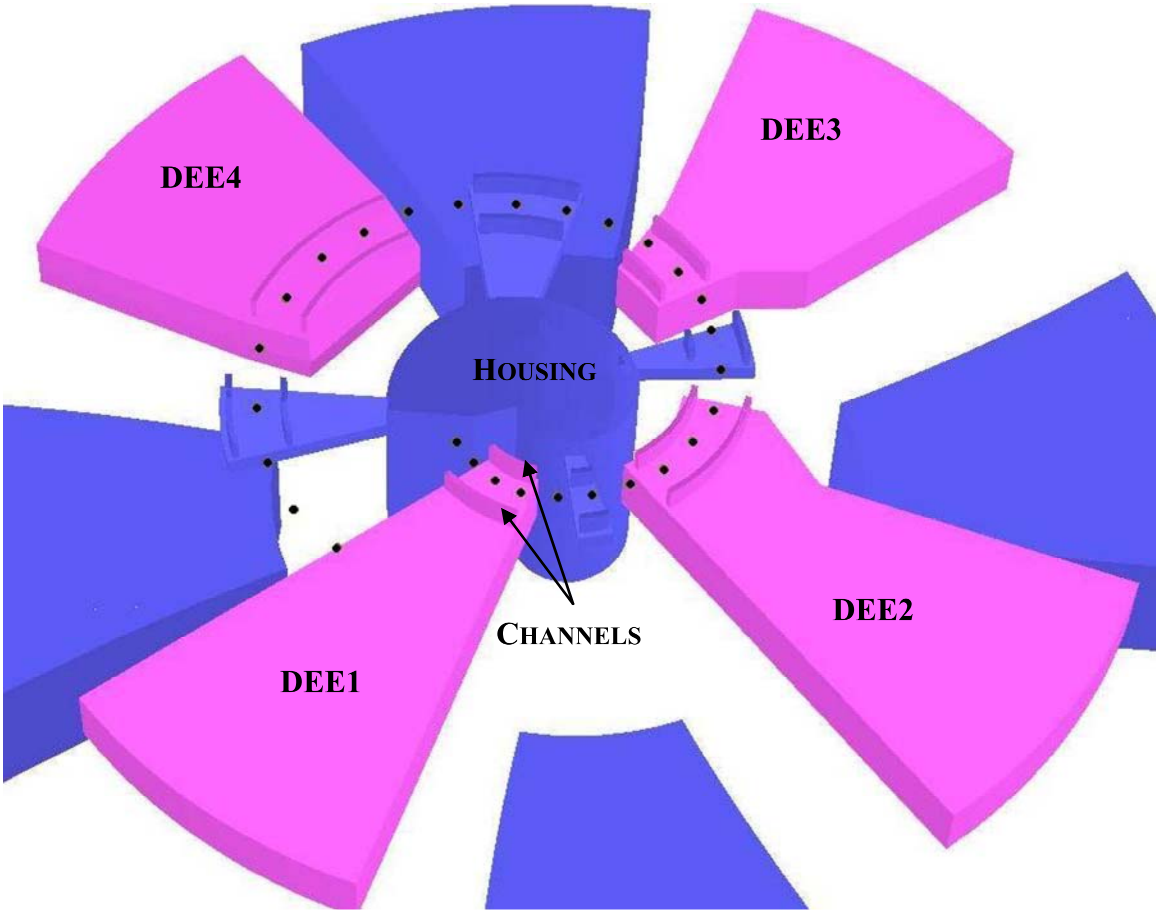

Fig. 2.6.1: Layout of the central region of SCENT.

Added to all the above conditions, there are the constraints that the electric fields are kept as low as possible to limit sparking (Kilpatrick limit [19]), and that the transmitted current is as large as possible. Since the Dee voltage will be 70 kV for ions injection, an electrode separation of 8 mm at least was chosen, limiting fields to 88 kV/cm.

With these considerations in mind, a preliminary central region was designed (Fig. 2.6.1), which produced a well-centred beam (Fig. 2.6.2) with good vertical focusing properties.

A code to calculate the trajectory of the beam was written in MATLAB environment. This code evaluates the beam dynamics integrating the Lorentz's equation $\vec{F} = q(\vec{E} + \vec{v} \times \vec{B})$ using the cartesian coordinates and time as variables of integration (the step Δt is a small fraction of the RF period):

$$\begin{aligned} v_x &= \frac{\partial \xi}{\partial x} = \frac{Z}{A} \cdot \frac{q}{m} \cdot \left[E_x \cos\left(h\omega_0 t + \phi\right) + v_y B_z - v_z B_y \right] \\ v_y &= \frac{\partial \xi}{\partial y} = \frac{Z}{A} \cdot \frac{q}{m} \cdot \left[E_y \cos\left(h\omega_0 t + \phi\right) - v_x B_z + v_z B_x \right] \\ v_z &= \frac{\partial \xi}{\partial z} = \frac{Z}{A} \cdot \frac{q}{m} \cdot \left[E_z \cos\left(h\omega_0 t + \phi\right) + v_x B_y - v_y B_x \right] \end{aligned} \quad (2.6.1)$$

where $\vec{v}(t)$ and $\vec{\xi}(t)$ are velocity and the position of the particle at instant *t*, ω_0 is the cyclotron's frequency, *h* is the harmonic number and in our case it is *h*=4. The electric and magnetic field maps were evaluated by the OPERA code. The initial conditions of these differential equations are the parameters derived from the study of the injection region.

A general procedure for the design of the central region, once the accelerating structure (number and extension of the Dees, harmonic number mode, gap width and height) has been defined, will be schematized. When the particle through the gap between liner and Dee increases its kinetic energy, since the revolution frequency ω_0 is constant and $v = \omega_0 r$, it involves an increase of the radius of the curve. This increase is continuous along the path of the particle into the gap, but we concentrate this variation in the middle of the gap. The new radius should be founded as follows:

$$\begin{cases} \frac{1}{2} m \left[\omega_0 (r + \Delta r) \right]^2 = E_c + \Delta E_c \\ \frac{1}{2} m \left[\omega_0 r \right]^2 = E_c \end{cases} \quad (2.6.2)$$

So:

$$1 + \frac{\Delta r}{r} = \sqrt{1 + \frac{\Delta E_c}{E_c}} \quad (2.6.3)$$

The energy gain ΔE_c depends on the transit time of the particle through the gap, τ, on the electric field distribution on the gap at those distances from the centre, and on the arrival phase. If it is possible, the angular amplitude of the Dee should be 45° (because *h*=4). In this way, the particle that crosses the first gap on the maximum of the electric field, finds the opposite peak at the second gap. So the particle was "pulled" into the Dee at the first gap and "pushed" out at the second gap. It is usually impossible to impose the angular amplitude for all the Dees, so the gain of energy should not be maximized. A good approximation is that maximum ΔE_c is about 25 AkeV. When the gains of kinetic energy are fixed, it is possible to draw the trajectory of the reference particle. The first radius and the first center are given by the study of the inflector, so with some iterations the particle path should be designed.

In the first turn, to improve the effects of the accelerating electric field, it is convenient to insert two channels for each Dee. These channels allow us to confine the electric field near the gaps and this effect is bigger if the distance between both channels is narrow. Besides, the space between these channels must be large enough to allow the beam to cross. We chose a distance of 8 mm.

In Figs. 2.6.2-2.6.4 the results of the code are shown.

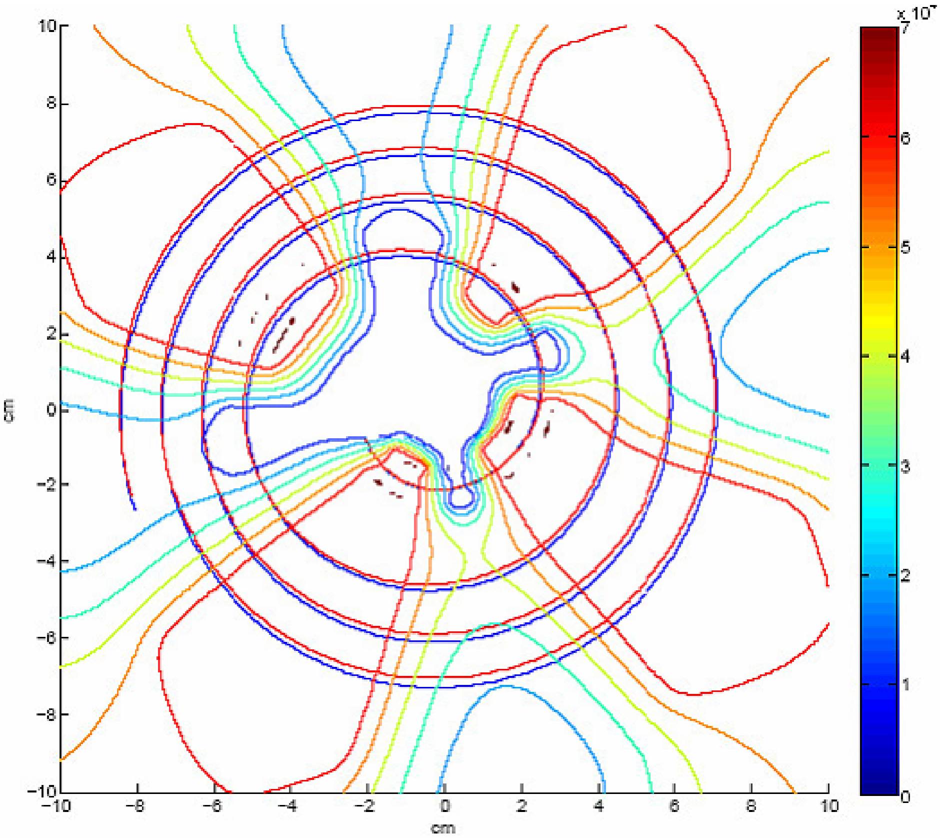

Fig. 2.6.2: Trajectory of two particles with different phase.

In Fig. 2.6.2 the central trajectories with starting times 110° to 120° are plotted. In Fig. 2.6.3, instead, the gain of energy for nucleon vs. angle is shown. Figure 2.6.4 shows the coordinates of a particle curvature's center for the first five turns. After a few turns, the beam seems to converge towards the magnetic center.

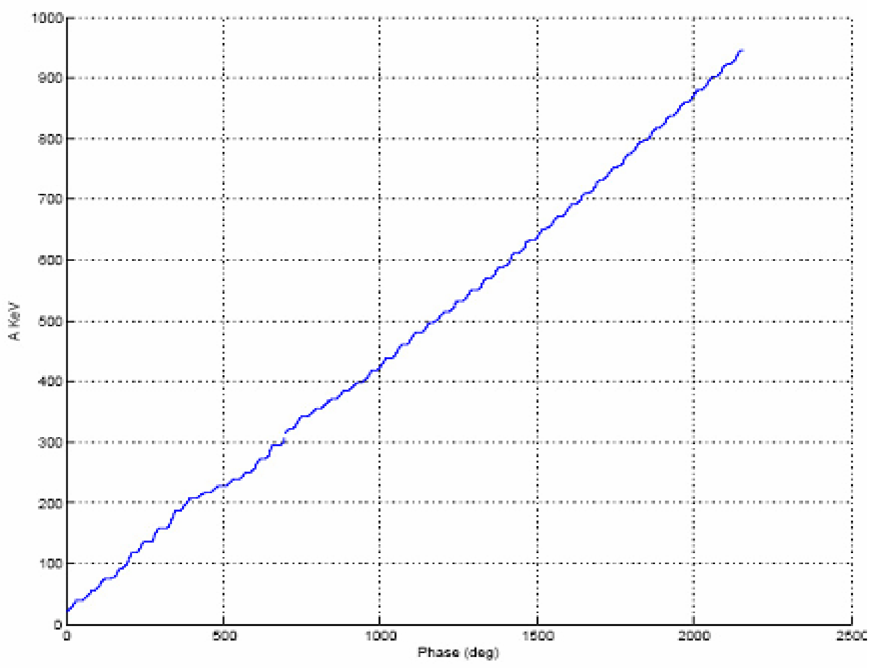

Fig. 2.6.3: Energy gain for the first turns.

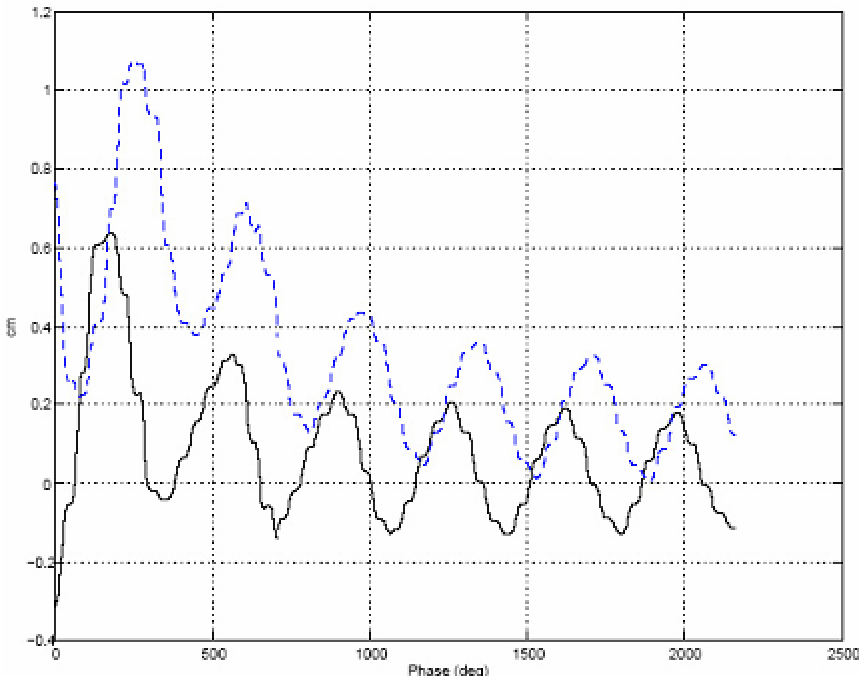

Fig. 2.6.4: The plot shows the X (solid line) and Y (dashed line) coordinates of the curvature's center.

2.7 References

[1] S. Kantas, *"A dedicated ECRIS for Hadron and Proton Therapies"*, XXXIV European Cyclotron Progress Meeting, Belgrade (2005).

[2] A. Geisler at al., XVII International Conference on Cyclotron and their applications, Tokyo (2004), p. 178.

[3] L. Calabretta, D. Rifuggiato, V.A. Shchepounov, *"The Final Section of the CS Axial Injection Beam Line"*, Report LNS, 01 April 1998.

[4] T. Kuo et al., proc. XIVth I.C.C.A., CapeTown (1995), p. 177.

[5] A. Caruso et al., XVI International Conference on Cyclotron and their applications, Lansing (2001), p. 297.

[6] L. Calabretta et al., *"The Low Energy Chopper"*, Activity report LNS (2001), p. 145.

[7] L. Belmont and J.L. Pabot. IEEE Trans. Nucl. Sci., (NS-13): p.191, (1966).

[8] L.W. Root, Master's thesis, Univ. Of British Columbia (1972).

[9] L.W. Root, PhD thesis, Univ. Of British Columbia (1974).

[10] D. Toprek, *"Theory of the central ion trajectory in the spiral inflector"*. NIM A 440 (2000), pp. 285-295.

[11] D. Toprek, *"Some optical properties of the spiral inflector"*. NIM A 431 (1999), pp. 38-45.

[12] D. Toprek, "*Comment on Theory of the central ion trajectory in the spiral inflector"*. NIM A 510 (2003), pp. 399-400.

[13] D. Toprek, *"Design of the central region in Gustaf Werner cyclotron at the Uppsala university"*. NIM A 486 (2002), pp. 539-544.

[14] D. Toprek, *"Beam orbit simulation in the central region of the RIKEN AVF cyclotron"*. NIM A 425 (1999), pp. 409-414.

[15] L. Milinkovic, *"Design of the central region for axial injection in the VINCY cyclotron"*. NIM A 370 (1996), pp. 287-296.

[16] L. Milinkovic. RELAX3D Spiral Inflector. TRI-DN-89-21.

[17] Y. Zhang, D. Alton, *"Electric field distribution in a spiral inflector for Cyclotron injection applications"*. Proceedings of the 2003 Particle Accelerator Conference.

[18] The MathWorks, Inc. Matlab ver. 7, http://www.mathworks.com.

[19] S.O.Schriber et al. "*Factors limiting the operations of structures under high gradient*". In LINAC 98 (1998).

Chapter 3. Magnet system

3.1 Introduction and magnetic field design

In this section the analytical and computational tools to design the cyclotron are presented. The design guidelines of such a machine are based on the existing K1200 superconducting cyclotron operating at MSU (Michigan State University, USA) [1]. The key differences are that there are four sectors instead of three, and the size of the radius is higher due to the higher extraction energy of the accelerated ions (250 AMeV instead of 200 AMeV), which causes an increase in the dimensions of the whole machine.

The pole radius has been fixed at 1.3-1.33 m in order to keep the overall weight of the machine acceptable. Consequently, the maximum average value of the isochronous magnetic field $\langle B(R_{EXTR}) \rangle$ at the extraction region will be about 3.75 Tesla.

The K bending parameter [2,3] for this machine should be:

$$K_{BEND} = \frac{e^2 \cdot c^2 \cdot \langle B(R_{EXTR}) \rangle^2 \cdot R_{EXTR}^2}{(1+\gamma) \cdot E_o} \approx 1000 \text{ MeV}$$

e: electron charge

c: light speed

E_o: rest energy

which gives, from the relation $\frac{T}{A} \leq \left(\frac{Q}{A}\right)^2 \cdot K_{BEND}$, the maximum theoretical energy achievable (T) of 250 AMeV by accelerating the ions with Q/A=0.5.

Assuming the isochronous field shape along the radius, we can determine the magnetic field at the center of the cyclotron as B_o=2.96 Tesla and the revolution frequency of the ions inside the machine as f_o≈23 MHz.

The gap between the magnet poles in the hills has been fixed at 5 cm. A small gap reduces the required number of ampere-turns in the cyclotron main coils and allows the last orbit of accelerated particles to be brought closer to the pole edge, in order to simplify the extraction operation with the electrostatic deflectors.

Table 3.1.1: Cyclotron's Main Parameters.

K_{BEND}	1000 MeV
Particles Accelerated	Q/A=0.5, H_2^+, $^{12}C^{6+}$
Extraction Energy	250 AMeV
Extraction Radius	1.3 m
Average magnetic field at extraction	3.75 Tesla[5]
Magnetic Field at center	2.96 Tesla
Frequency fundamental	23 MHz
Minimum Gap size	5 cm

3.1.1 Analytical magnetic field design

A fourfold symmetric compact magnetic structure has been chosen to produce the required azimuthal varying magnetic field.

The magnetic field has to guide the particles on isochronous trajectories and provide the required focusing in order to maintain good internal beam characteristics. These properties are the results of two effects:

- The azimuthal field variations due to the shape of four spiral sectors.
- The positive radial gradient of the isochronous field which is required to maintain the isochronism despite the consistent relativistic mass increase of the ions due to the increasing energy. This gradient is obtained by adjusting the angular span of the sectors and by an adequate position of the superconducting coils.

Once the main parameters are set, it is necessary to establish the dimensions of the machine. As our first approximation, it is possible to scale the dimensions of the K1200 superconducting cyclotron in order to set the radial width of the flux return yoke. To validate the scaling law, the total magnetic flux in the cyclotron is also estimated using the average magnetic field and the pole radius, in order to make the magnetic flux through the pole area and the return yoke equal:

$$\Phi\left(\langle B\rangle_{POLE}\right) = \Phi\left(\langle B\rangle_{YOKE}\right)$$

$$\pi \cdot R_{EXT}^2 \cdot \langle B_{ISO}(r)\rangle_\theta = Area_{YOKE} \cdot B_{SATURATION}$$

A value of yoke radius $R_{YOKE}=2\times R_{POLE}$ should be a conservative choice.

[5] The magnetic field will be fixed, with a narrow tuning range (±0.4%) to allow for acceleration of different light ions with Q/A≈0.5.

The chosen average magnetic field depends upon the magnetic field value in the hill $B_{hill}(r)$, in the valley $B_{valley}(r)$ and of the fraction of the hill α on one symmetry period according to the following equation:

$$\langle B(r)\rangle = \alpha \cdot \langle B_{hill}(r)\rangle + (1-\alpha)\cdot\langle B_{valley}(r)\rangle$$

The values of B_{hill} and B_{valley} are determined by using a sinusoidal shape of the magnetic field along the azimuthal direction:

$$B(r,\theta) = \langle B(r)\rangle(1 + f\cdot\sin(4\cdot\theta))$$

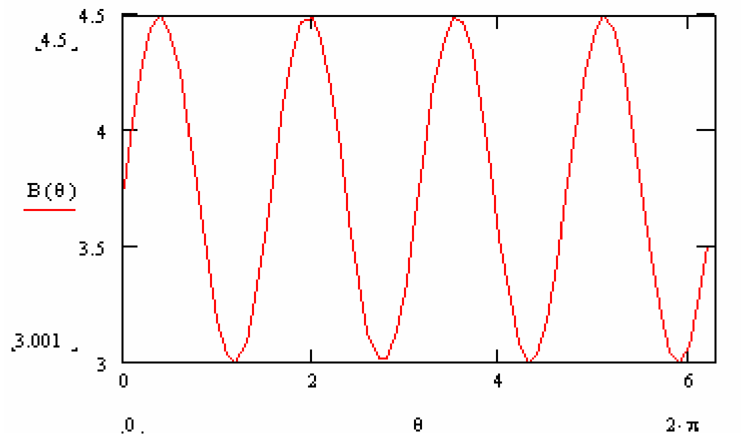

Fig. 3.1.1

On the previous graph, the analytical approximation of the magnetic field at the extraction radius is plotted, where the main value is 3.75 Tesla and the peak values are B_{hill}=4.5 Tesla and B_{valley}=3 Tesla respectively. In this case, if f=0.2, the flutter, which we assume to be constant as our first approximation, gets the following value [2]:

$$F = \frac{\langle B^2\rangle - \langle B\rangle^2}{\langle B\rangle^2} = \frac{f^2}{2} = 0.02$$

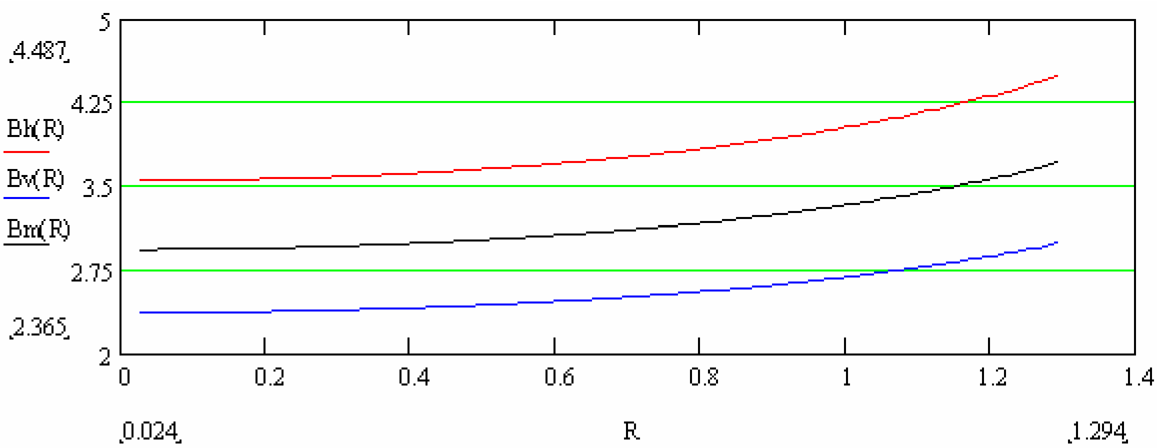

Fig. 3.1.2: First approximation of the average value of the magnetic field along the radius (m).

3.1.2 Stability conditions and spiral definition (matrix method)

In order to ensure the axial stability of the beam during acceleration, it is necessary to shape the edges of the sectors as spirals. To define the spiral angle, the matrix method was applied for an approximate description of the beam dynamics inside the cyclotron without considering the acceleration phase. Taking the previously shown magnetic field design, the transfer matrix of the radial and axial phase space of the beam was defined. Then the stability condition (|Tr(M)|≤2, where M is the transfer matrix) was applied [2].

The following results were produced after the preliminary analysis:

R	E(R)	Bm(R)	ξ1(R,ζ)
m	MeV·A	tesla	deg
0.024	0.06	2.933	1.013
0.152	2.393	2.94	10.998
0.279	8.192	2.959	23.264
0.407	17.657	2.989	35.042
0.534	31.124	3.031	44.996
0.662	49.105	3.088	52.87
0.79	72.348	3.162	58.949
0.917	101.928	3.255	63.64
1.045	139.414	3.374	67.298
1.172	187.15	3.525	70.194
1.3	248.774	3.72	72.522

where R is the average radius of several equilibrium orbits calculated for given energy E(R). Bm(R) is the average isochronous field and ξ1(R,ζ) is the spiral angle needed for the stability of the orbit.

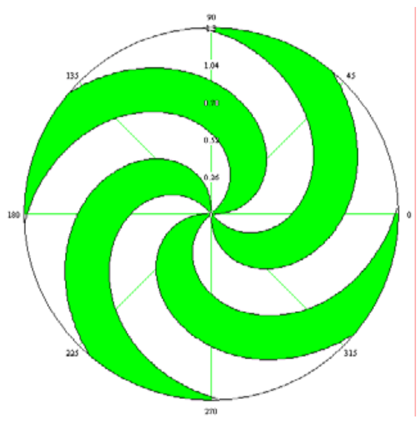

Fig. 3.1.3: Preliminary layout of the spiral sector of the cyclotron.

3.1.3 Preliminary design with 3D code

The calculations described above are simple, analytical and allow for an initial layout of the cyclotron magnet. More sophisticated tools are required for further optimisation of the cyclotron magnet.

The overall structure is being designed with CAD code [4] and several variables have been parameterised in order to optimise the magnetic field.

The first step is to define the angular width of the sectors for a preliminary matching of the isochronous field. For this reason, the coordinates of the points positioned on the edge of the spiral sectors can be changed. In addition, the vertical coordinates of eventual valley shims and their extension radius will be parameterised.

The 3D model is restricted to 1/8 of the cyclotron, imposing the constraints of tangential and normal boundaries to achieve the symmetry conditions.

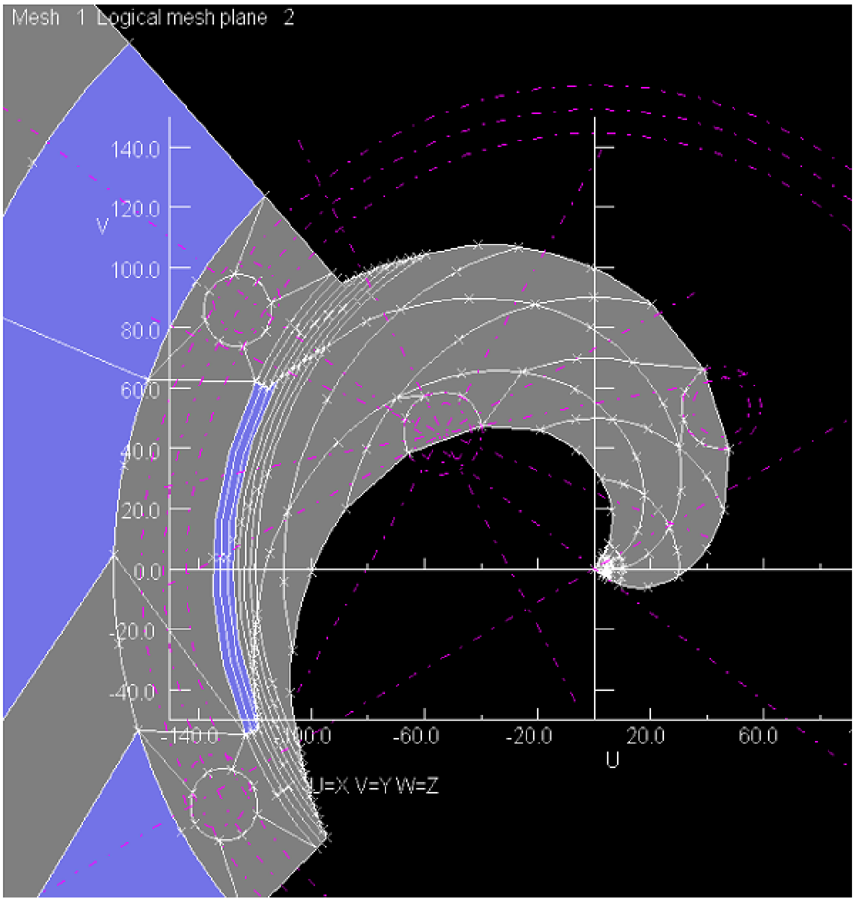

Fig. 3.1.4: The 1/8 symmetric model simulated.

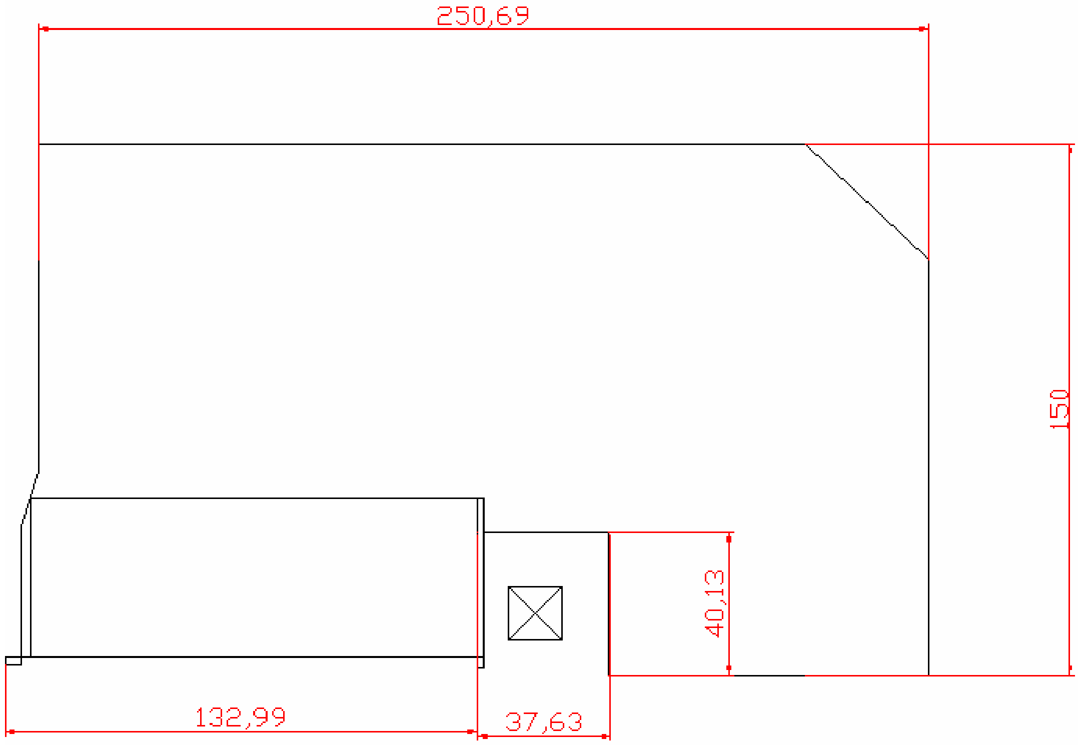

Fig. 3.1.5: Preliminary side view (1/8 of the model) of the cyclotron with the positioning of the coils.

The size of the coils has been fixed preliminarily as follows:

Table 3.1.2: Preliminary coil parameters.

Number	2
Internal radius	142 cm
External radius	157 cm
Height	20 cm
Distance to the median plane	10 cm
Current density	< 45 A/mm^2
Total current per coil	~1.1MA

After the first simulations, the preliminary results are shown in Fig. 3.1.6. Any discrepancy between the average cyclotron magnetic field and the isochronous magnetic field results in a shift of accelerated particles with respect to the isochronous phase of the cyclotron RF system. The following equation gives a relation between the phase shift and the magnetic field imperfection [5,6]: $d(\sin\phi)=N_t \cdot h \cdot 2\pi \cdot \Delta B/B$

Where:

- ϕ is the phase shift of the reference particle that is of about 20°;

- N_t is the number of turns of the particles inside the cyclotron;
- h=4 is the harmonic of the RF frequency;
- B is the mean value of the isochronous magnetic field along the acceleration orbit;
- ΔB is the required accuracy of the mean field.

According to this equation the phase shift depends on the type of particle extraction, the geometry of the accelerating electrodes and the harmonic mode of operation. The multiturn extraction allows a phase shift as large as 20°-30°. Hence a tolerance of the magnetic field as $\Delta B/B \approx 5\cdot 10^{-5}$ is acceptable. Therefore small and local variations of the isochronous magnetic field around the right values can be accepted, especially if their overall effects produce a d(sinϕ)=0. Integral of d(sinϕ)=0 minimize the energy spread and allow us to achieve a higher extraction efficiency. Local field variations which produce gradient of the magnetic field resulting in imaginary values of the ν_z are of course not acceptable.

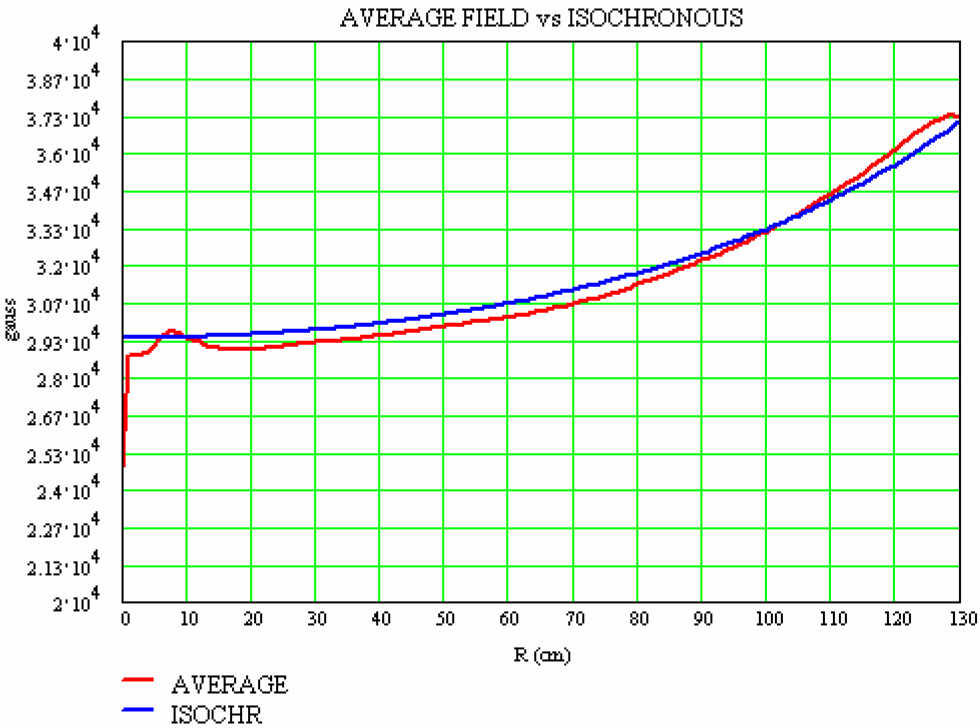

Fig. 3.1.6: Average field obtained by 3D simulations and the required isochronous field.

According to the following equation, the flutter and the main harmonic coefficient of the Fourier envelope of the magnetic field have also been calculated.

$$B(r,\theta) = B_0(r) + \sum_{n=1}^{\infty} B_n(r)\cdot\cos\left[n(\theta-\phi_n(r))\right]$$

B_n are the Fourier coefficients, where n=0 is the average magnetic field, and n=4 is the main harmonic.

$$F(R) = \frac{1}{B_o^2(R)} \cdot \sum_{n=1}^{\infty} B_n^2(R)$$

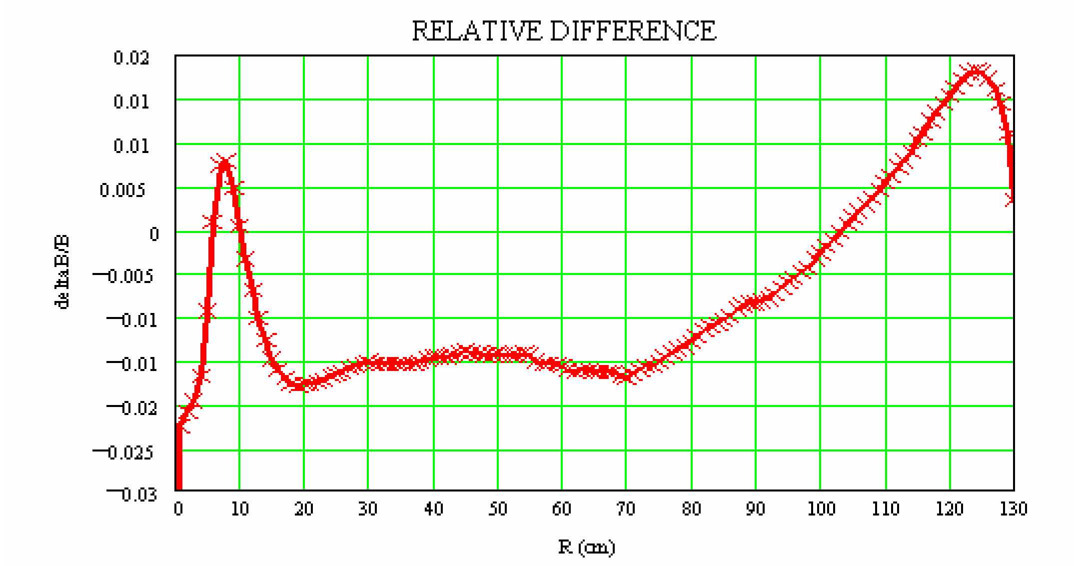

Fig. 3.1.7: Relative difference between the average magnetic field simulated and the isochronuos.

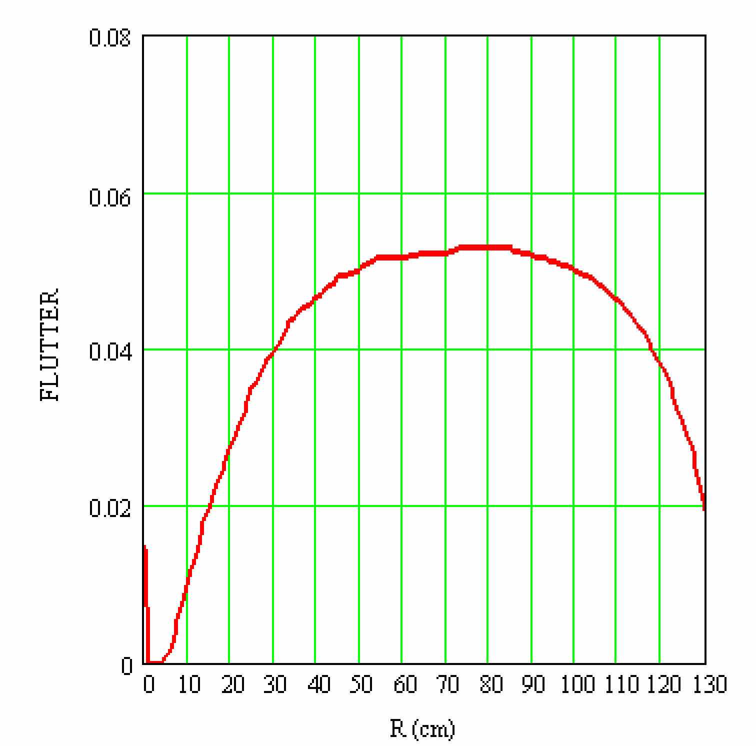

Fig. 3.1.8: Flutter of simulated cyclotron vs. R.

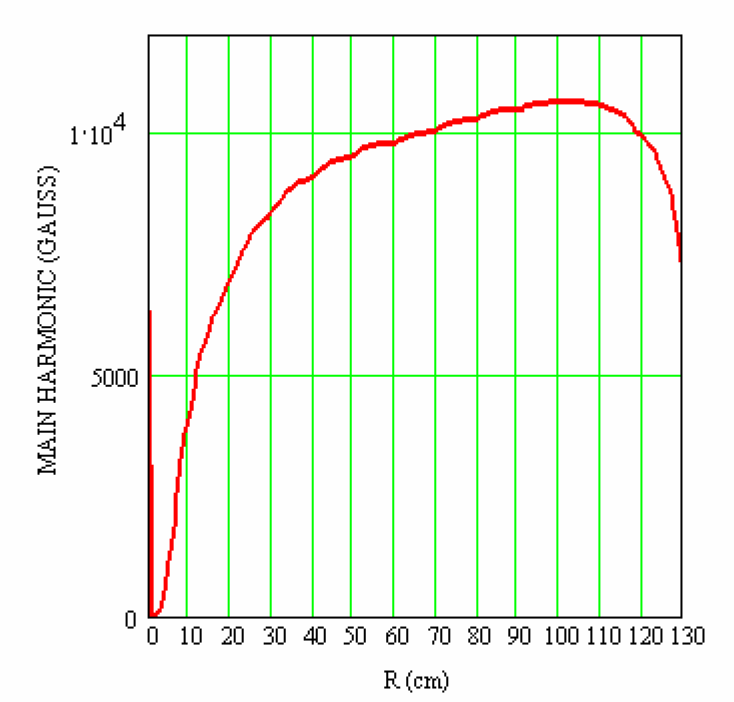

Fig. 3.1.9: Main harmonic coefficient of the simulated field vs. R.

The knowledge of the main harmonic coefficient is necessary to calculate the preliminary focusing limit (K_{FOC}) of the cyclotron.

$$K_{FOC} = \frac{Q}{A}\frac{e \cdot c \cdot R}{2}\sqrt{C^2 \cdot [1 + 2 \cdot \tan^2(\xi)]}$$

R : radius

C : main harmonic coefficient

ξ : spiral angle

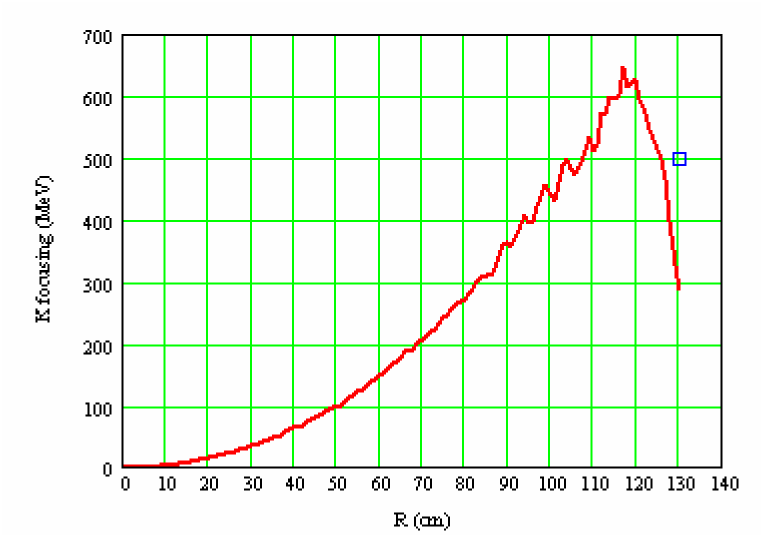

Fig. 3.1.10: Focusing limit of the cyclotron vs. radius. The point corresponding to K_{FOC}=500 limit is marked by a box.

The solid line shows the upper limit of the machine described here. The decreasing above 120 cm is compensated by the negative gradient of the field (this term does not appear in the previous K_{FOC} equation), resulting in an increase in the focusing frequency ν_Z.

In order to control the radial and vertical stability, the betatron oscillations have been evaluated by means of the GENSPE code [7,8].

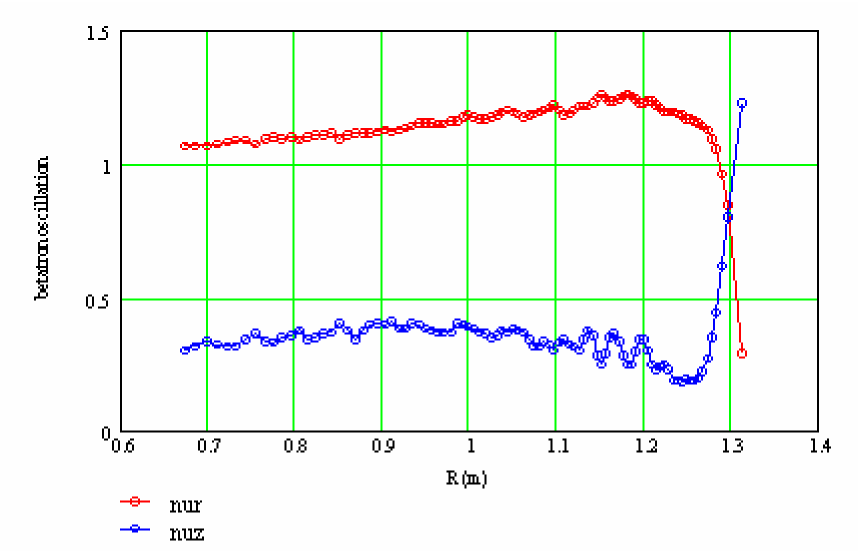

Fig. 3.1.11: Evaluated radial and axial betatron oscillation frequencies.

3.2 Main parameters of the machine

In this section the main parameters of a superconducting cyclotron able to deliver ion beams with Q/A=0.5, in particular the H_2^+ molecule and $^{12}C^{6+}$ ion (but in general it should be also able to accelerate all fully stripped light ions up to Neon) up to the maximum energy of 250 AMeV, are presented. Such a machine is a compact cyclotron whose magnetic field is generated by means of a pair of superconducting coils, symmetrically placed above and below the median plane, whose maximum current density should be less than 50 A/mm^2. The coils should also provide a rather sharp fringing field fall-off to facilitate the beam extraction. This requirement again calls for coils placed as close as possible to the pole and to the mid-plane and for a high aspect ratio height/width of the coils cross-section. The selected values, compatible with all the constraints of the coil construction, are a cross section of 150×210 mm^2, with a distance to the median plane (MP) of 75 mm.

Four sectors are expected in order to avoid harmful resonance of ν_r=N/2 (N is the number of sectors). The primary goal of the sector design is however to ensure an adequate axial focusing for the accelerated beam.

In the previous section the bending limit of the machine was preliminarily set as $K_{BEND}\approx 1000$ MeV (see subsection 3.1) corresponding to a maximum average field of 3.75 Tesla (such a value in the final design should be higher) and to a pole radius of approximately 1325 mm. The focusing limit of the machine was previously (see subsection 3.1) calculated at the value of $K_{FOC}\approx 500$ MeV.

The operating RF harmonic mode should be the 4^{th}. This choice needs a very precise isochronous magnetic field. The fine tuning of the magnetic field will be performed by means of the passive magnetic elements like the trim rods (TR) discussed in subsection 3.6.

The extraction system is composed of a stripper foil, appropriately positioned inside the cyclotron in order to extract the proton beam by breaking the H_2^+ molecule and two electrostatic deflectors for light ions extraction. This system should be followed by a set of passive magnetic channels, in order to optimize the extraction efficiency.

The Table 3.2.1 summarizes the main parameters of the cyclotron.

The general structure of all aspects of the machine relevant to the magnetic field design, like the iron geometry or the superconducting coils, is outlined in subsection 3.2.1.

The description of the physics model with the assumptions made for the simulation is outlined in subsection 3.2.2.

The design techniques employed are discussed in subsection 3.2.3, whilst the results of the 3D simulations and magnetic field calculation are outlined in subsection 3.2.4.

Table 3.2.1: SCENT main parameters.

K bending (K_{BEND})	1000 MeV
K focusing (K_{FOC})	500 MeV
Particle accelerated	H_2^+, $^{12}C^{6+}$, Q/A≈0.5
Maximum energy	250 AMeV
Injection energy	20÷30 AMeV
Extraction radius ($\overline{R}_{ext}$)	1276 mm
Max Average Magnetic field	3.86 Tesla
Magnetic field at center (B_0)	~ 3 Tesla
Frequency fundamental	~ 23 MHz
RF harmonic operating mode	4
RF frequency	92÷93 MHz
Number of cavities	4
Max and min voltage expected	70÷120 kV
Extraction system	Stripper foil (H_2^+) + E.D. (light ions)+M.C.
Coils type	Superconducting
Number of coils	2 (one pair)
Coils size	150×210 mm^2
Max density current expected	< 45 A/mm^2
Tuning System Magnetic field	Trim rods
Estimated weight	<360 tons

3.2.1 Magnet structure

The whole magnet is mainly a cylinder with a radius of 2450 mm and a height of 2900 mm. A sketch of the magnet tops are shown in Fig. 3.2.1, while a side view of the whole structure is shown in Fig. 3.2.3.

The magnet structure can be separated into three different regions:

1. the sectors region;
2. the poles region;
3. the return yoke region.

The first region includes the spiralled sectors and the plug of the central region designed for the axial injection of the beam in order to compensate the hole effect on the magnetic field at the mid plane. This region extends up to z=525 mm from the median plane (valley floor) and radially up to 1325 mm, where the sectors end. The height of the sectors (hills) is 500 mm, in order to keep a half gap of 25 mm (the height of the gap is set at 50 mm).

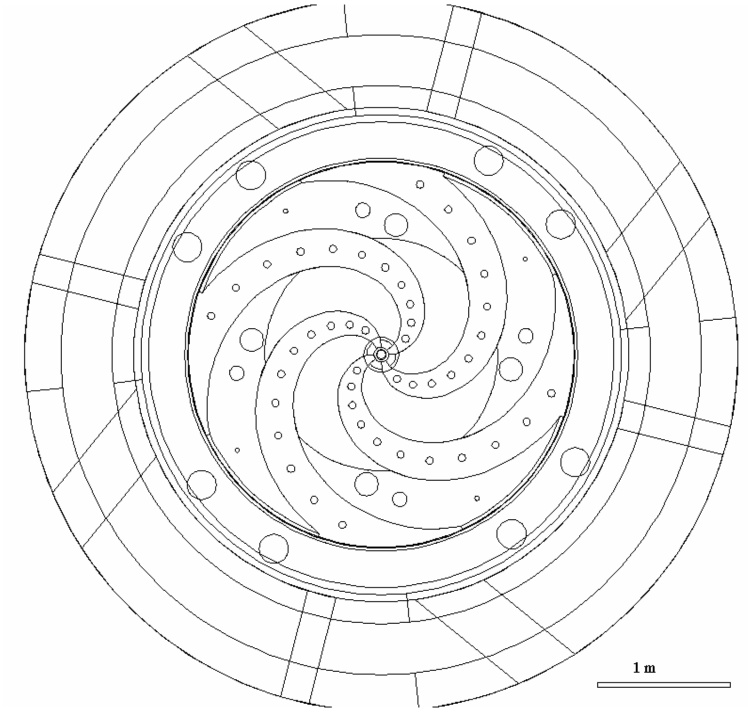

Fig. 3.2.1: Top view of the cyclotron.

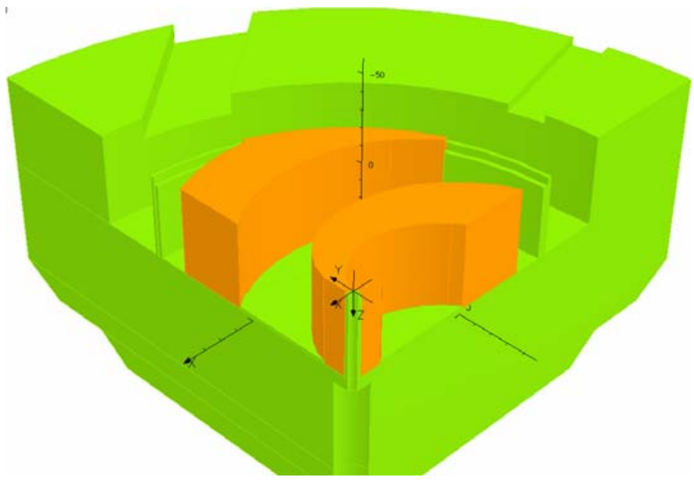

Fig. 3.2.2: Spiralled sectors highlighted in the model.

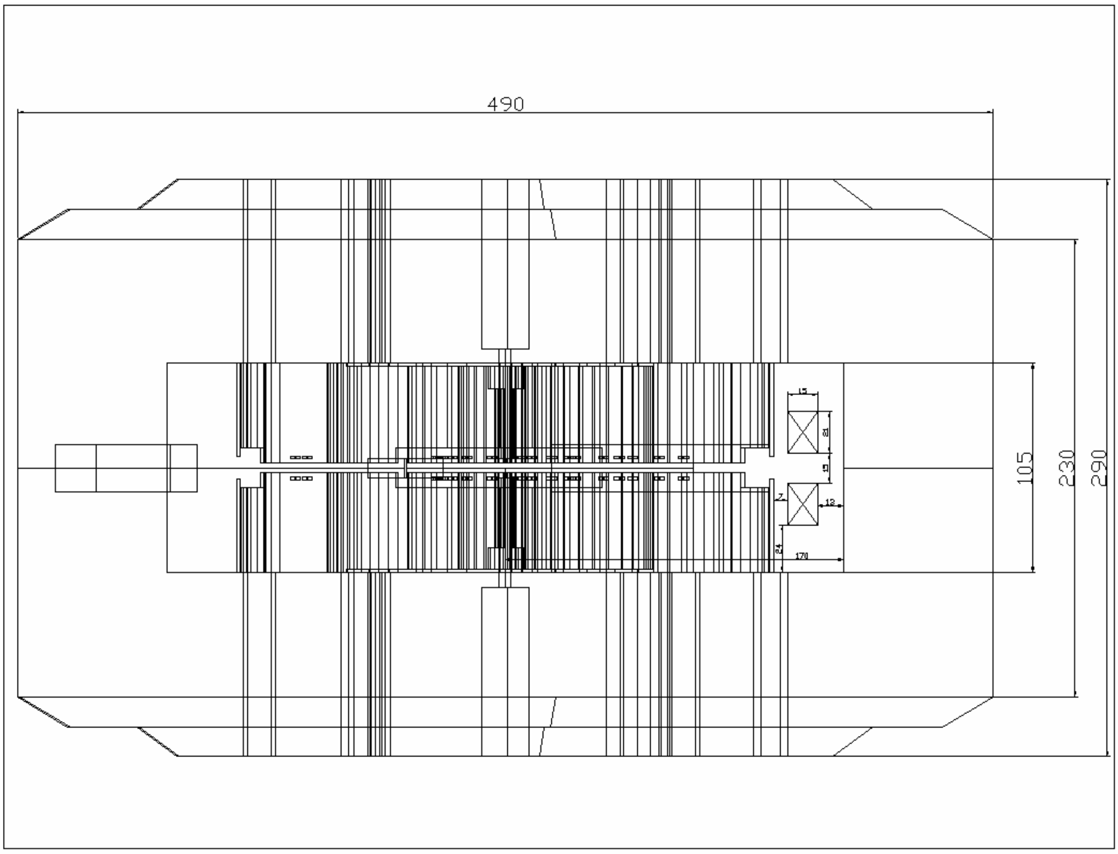

Fig. 3.2.3: A side view of the cyclotron with the quota (cm).

Table 3.2.2 shows the azimuthal hill width as a function of the radius, while Table 3.2.3 shows the parameters used for defining the spiral angles (as shown in Fig. 3.2.4).

Table 3.2.2: Sector (hill) width.

R (cm)	**Width** (deg)	**R** (cm)	**Width** (deg)	**R** (cm)	**Width** (deg)
5	34	55	37.6	105	41
10	34	60	38.1	110	41.2
15	35.1	65	38.6	115	41.3
20	35.6	70	39	120	41.8
25	35.8	75	39.5	125	43
30	36	80	40	130	44
35	36.2	85	40.3		
40	36.5	90	40.5		
45	36.8	95	40.7		
50	37.1	100	40.9		

Table 3.2.3: Spiral angle vs. radius.

R (cm)	**PHI** (deg)	**Spiral angle** (deg)	**R** (cm)	**PHI** (deg)	**Spiral angle** (deg)
10	5.01	6.5	80	74.79	59.5
20	12.33	15.6	90	87.16	63.2
30	20.89	25.4	100	99.96	66.2
40	30.37	34.6	110	113.15	68.7
50	40.59	42.6	120	126.7	70.8
60	51.45	49.4	130	140.59	72.6
70	62.87	55			

On the valley floor, there is a shim which increases the height of the valley up to z=510 mm and it extends radially from the center to R=800 mm, for producing the desired field shape. In the rest of the valley, from R=800 to R=1300, the valley's height is z=525 mm.

Another shim is placed between R=1300 mm and R=1325 mm and extends vertically up to 100 mm from the median plane. This shim together with the inner wall of the vacuum chamber (which extends up to 60 mm from the median plane) are necessary to gain a magnetic field in the extraction region, shifting the peak average value towards the geometric limit of the pole. This feature provides an higher bending limit and helps to bring the fall-off of magnetic field closer to the pole's geometrical radius.

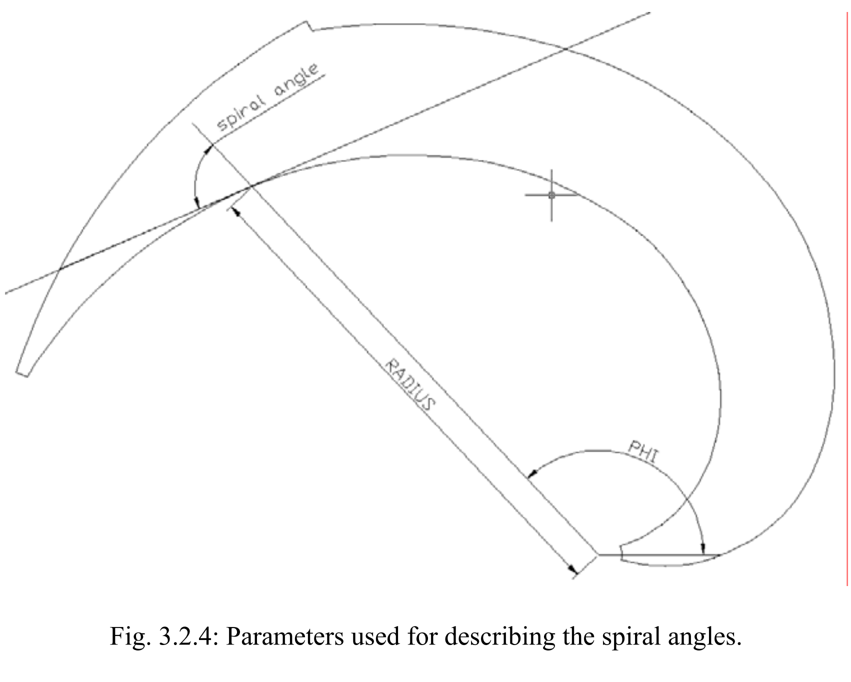

Fig. 3.2.4: Parameters used for describing the spiral angles.

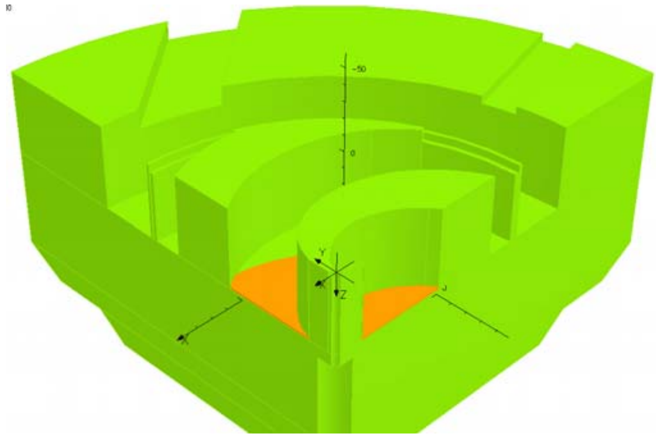

Fig. 3.2.5: Valley shim highlighted in the model.

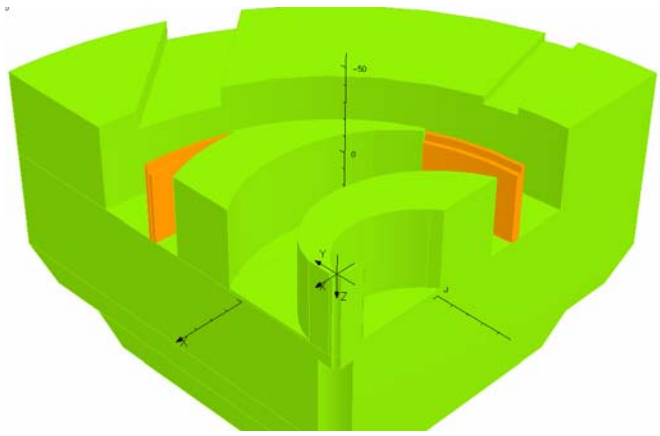

Fig. 3.2.6: Inner wall and second valley shim are highlighted in the model.

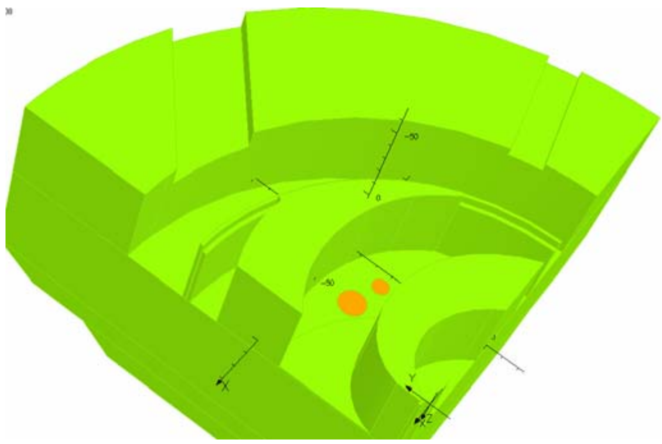

Fig. 3.2.7: RF holes highlighted in the model.

The poles are characterized by the presence of the holes provided for cooling systems, cryogenic insertions (the biggest) and the trimming and coupling capacitors (the smallest), Fig. 3.2.7. In Table 3.2.4 the coordinates and size of the holes are shown.

Table 3.2.4: Holes pole parameters. R is the distance from the center.

R (cm)	**Diameter** (cm)
90	16
100	10

The yoke region has to guide the return magnetic flux. The design was performed looking at two parameters:

1. the fringing field in the area around the cyclotron and mainly in the control room;
2. the shape of the fringing field around the cyclotron.

By means of EM codes, the magnet yoke has been shaped in order to minimize the leakage of the magnetic flux at 10 Gauss at a distance of 10 m from the cyclotron and 500 Gauss at 1 m from the pole caps (see Fig. 3.2.8).

Symmetric holes have been made across the median plane of the yoke in order to simulate the apertures for the beam exit and for radial support of the superconducting coils.

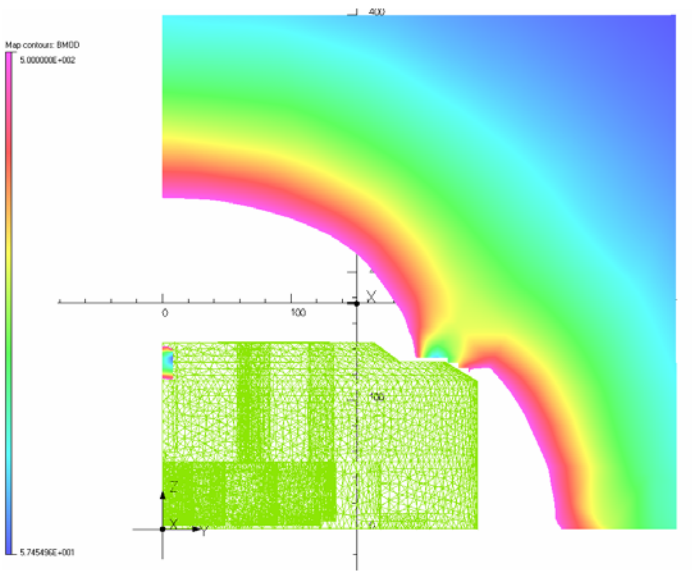

Fig. 3.2.8: Leakage magnetic flux outside the cyclotron (Gauss).

As for the coils, a set of 8 holes (diameter=100 mm) has been designed vertically across the yoke for the axial coil supports, the currents leads and liquid Helium feeder, Fig. 3.2.9.

A cross section of the main coils is shown in Fig. 3.2.10 where their geometrical parameters are also defined (see also Table 3.2.5).

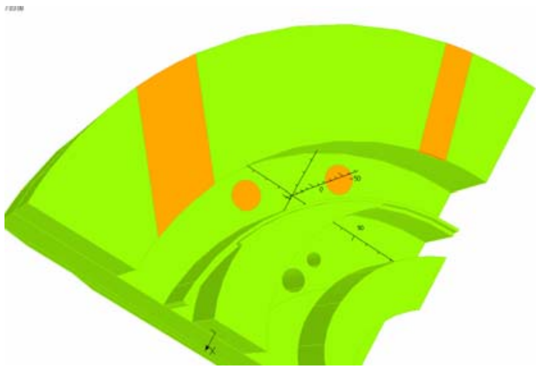

Fig. 3.2.9: Extraction and coil support holes highlighted in the model.

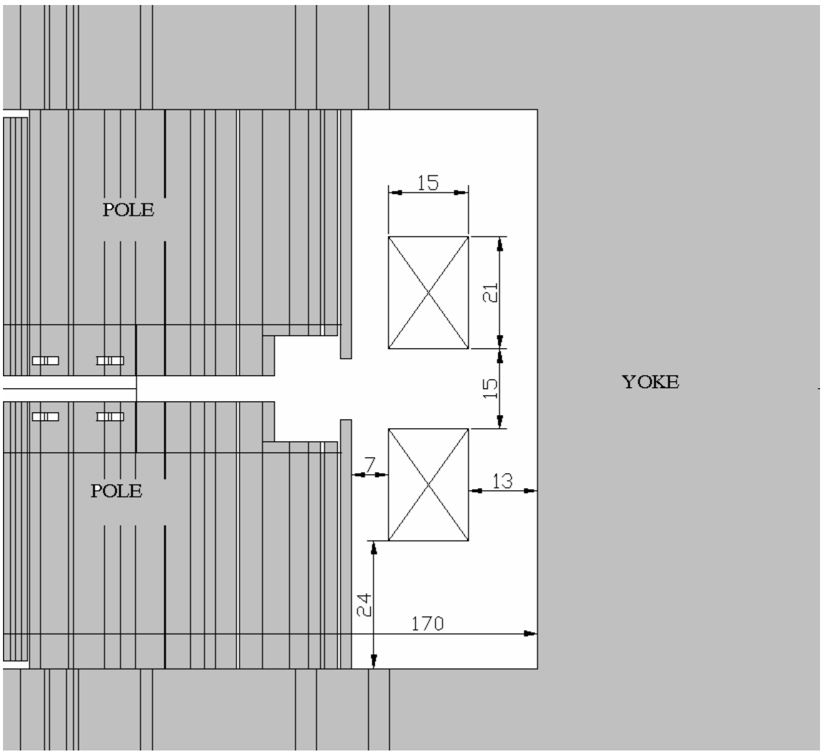

Fig. 3.2.10: Cross section of the main coils.

The total energy stored in the two coils should not exceed 15 MJ. Since the maximum field strength on the coil conductors and the current density is not too high (see subsection 3.6), we suggest an NbTi multifilamentary multistrand conductor with rectangular cross section in a copper matrix. Such a coil could operate in the persistent mode, then the magnet system could be disconnected from the grid. Therefore, any noise on power lines should not affect the magnetic field. As a consequence, the safety and reliability are increased while reducing the overall Helium consumption.

Table 3.2.5: Coil parameters.

Coil inner radius	1420 mm
Coil outer radius	1570 mm
Coil axial height	210 mm
Gap between coils	150 mm
Overall current density	< 45 A/mm^2
Maximum nominal current	~1500 A
Ampere per turns per coil	~1.4 MA

3.2.2 The magnetic model

The final structure of the cyclotron was built step by step, starting from the simplest model shown in previous subsection 3.1. Computational limitations, finite boundary conditions and material property are all possible limitations to the accuracy of the “paper” design.

Considerable effort was put into refining computer calculations as the design progressed to obtain reproducible convergence to very high accuracy.

The 3D model was designed just for 1/8 of the machine (see subsection 3.1.3). The complete model could be defined with eventual asymmetry, but this would be unnecessarily expensive for CPU time analysis.

The boundary conditions have been set as:

1. normal magnetic on the median plane;
2. periodic boundaries on the lateral sides of the box air enclosing the model;
3. tangential magnetic on upper and external sides of the box air.

Generally, the iron used for the magnets have a low Carbon content. In our experience with 3D simulations, for iron specifications ranging from very high to normal commercial quality Carbon content, no major effects should be found on any important parameter. We have, therefore, chosen a high quality steel whose B-H curve used for the analysis is shown in Fig. 3.2.11.

The air box limit was set at $3\times R_{YOKE}$ along R and $3\times H_{YOKE}$ along z. In practice, at long distances from the device producing field, the distribution will be modified by the local environment (tangential or open boundaries), but this will not affect the field close to the orbit plane of the cyclotron.

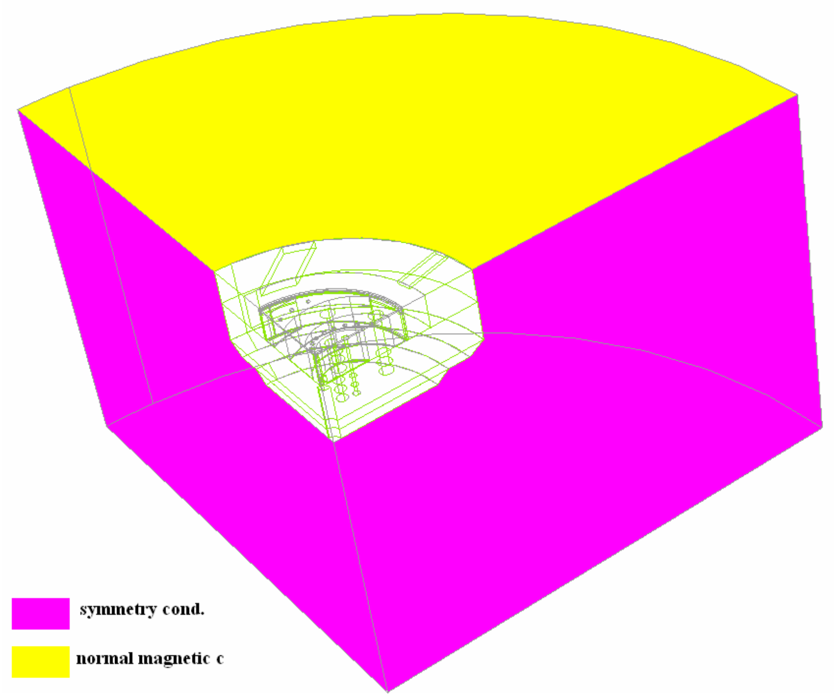

Fig. 3.2.11: Overview of the simulated model with air box surrounding the magnet structure.

The first model was meshed with hexahedral elements in order to speed up the analysis time. The number of cells during the first simulations didn't exceed 300'000.

The last model was simulated with tetrahedral meshing in order to increase the geometrical accuracy. In this case the simulations achieved more than 1 million mesh cells and nodes.

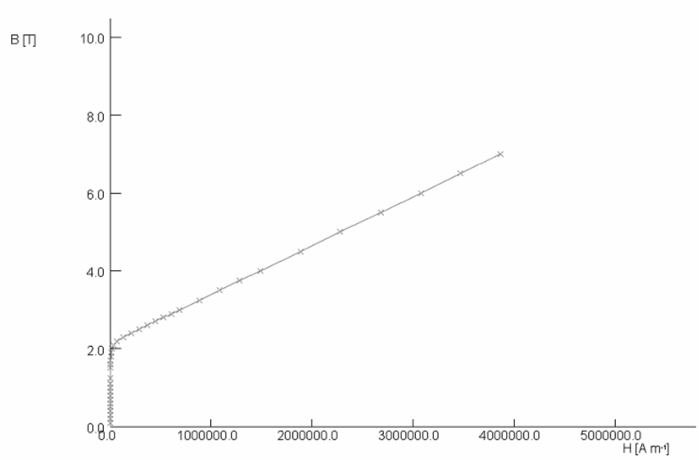

Fig. 3.2.12: B-H magnetization curve.

3.2.3 Magnetic field design

The corresponding optimal iron field was calculated and the sector geometry shaped in order to meet this field as close as possible to the isochronous one. The sector shape which produces the best magnetic field was obtained in different steps. The layout of such an iterative process is presented in Fig. 3.2.13.

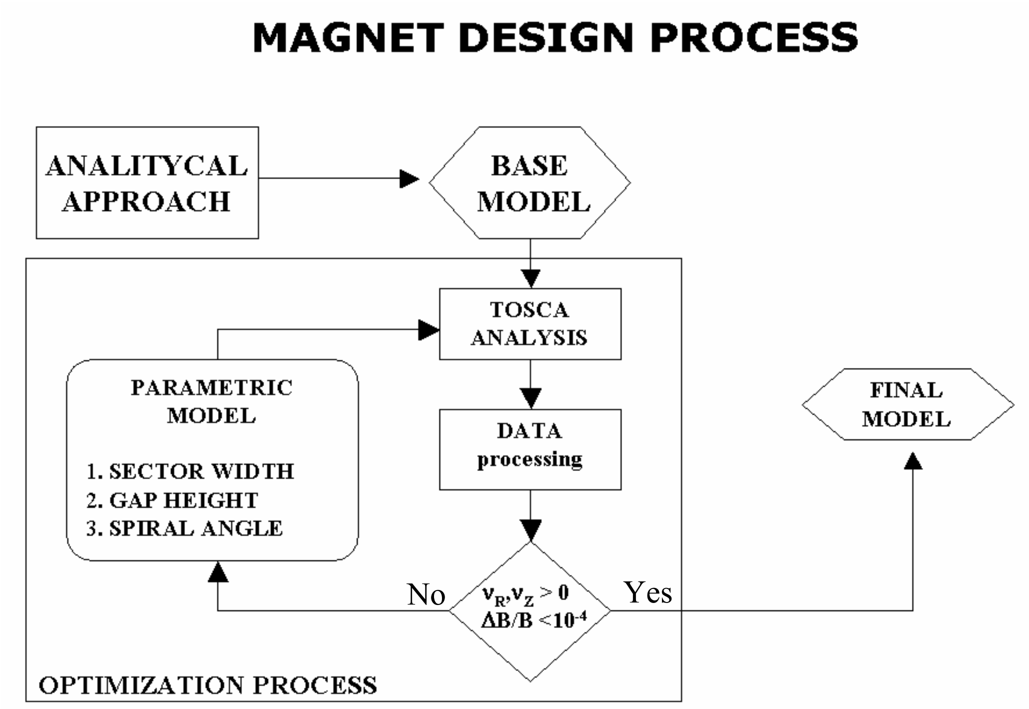

Fig. 3.2.13.

From the analytical approach we have designed the preliminary model of the machine, assuming the width angle of the sectors to be constant along the radius. The matrix method (discussed in subsection 3.1) was applied to define the spiral angle in order to ensure the axial stability of the beam. Once the dimensions of the structure were fixed, the simulations with 3D dedicated codes were carried out, to refine the magnetic field. Several of the magnetic circuit model's variables were parameterized in order to meet the best field design. In the first model, the edge spiral line on the sector was parameterized as shown in Fig. 3.2.14.

By means of this parameterization it was possible to change the sector width in order to vary the magnetic field value locally and at the same time, if necessary, it allowed us to modify the spiral angle of the sector in order to increase the axial focusing effect. The focusing limit is therefore mainly dependent on the spiral term and increases almost linearly with the spiral constant.

A limit is set however by the reduced spiral efficiency since in reality, the magnetic focusing term does not increase like the geometric one for high value of the spiral constant.

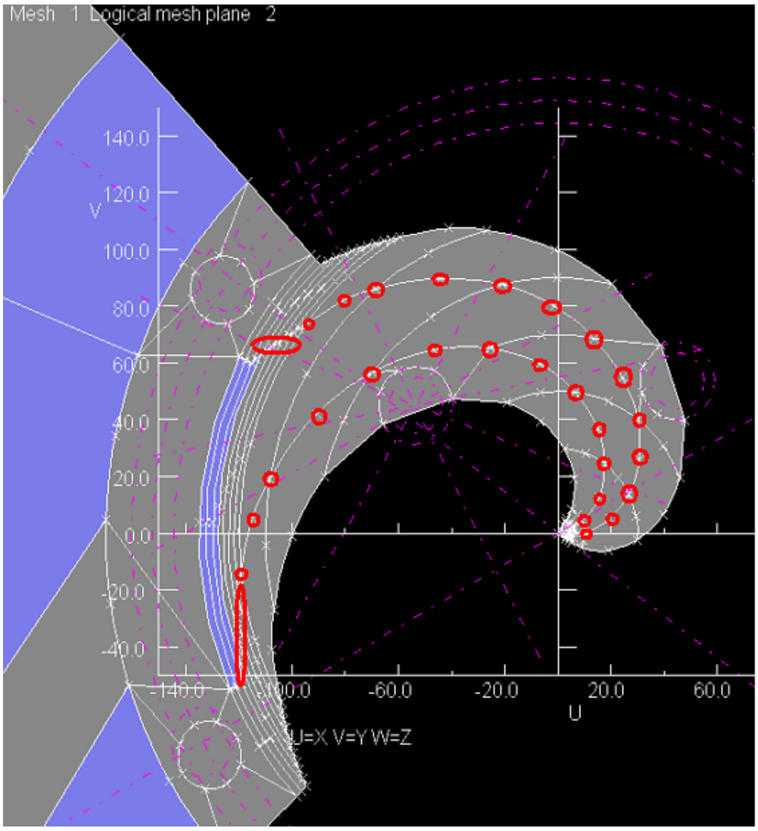

Fig. 3.2.14: Preliminary model of the magnetic structure. The hill-edge points, which we have parameterized, are pointed out with red circles.

The difference between the geometric and magnetic spiral can be better appreciated by considering the respective spiral focusing terms, which are presented in Fig. 3.2.15.

The closeness of the two curves, up to R=120 cm, shows that the magnetic spiral depends mostly on the hill shape with negligible effect from either the valley shims or the holes drilled in the poles. Differences exist in the central region but they are not relevant since the spiral focusing is negligible there. The two curves are instead quite different near the extraction region because of the radial shape of the sector and the last valley shims positioned between the R=130 cm and 132.5 cm. This discrepancy points out that in the extraction region, where the axial focusing, the isochronism and the fringing field fall-off simultaneously play a role in limiting the machines performances, a satisfactory design of the sector geometry can be reached only by trial and error.

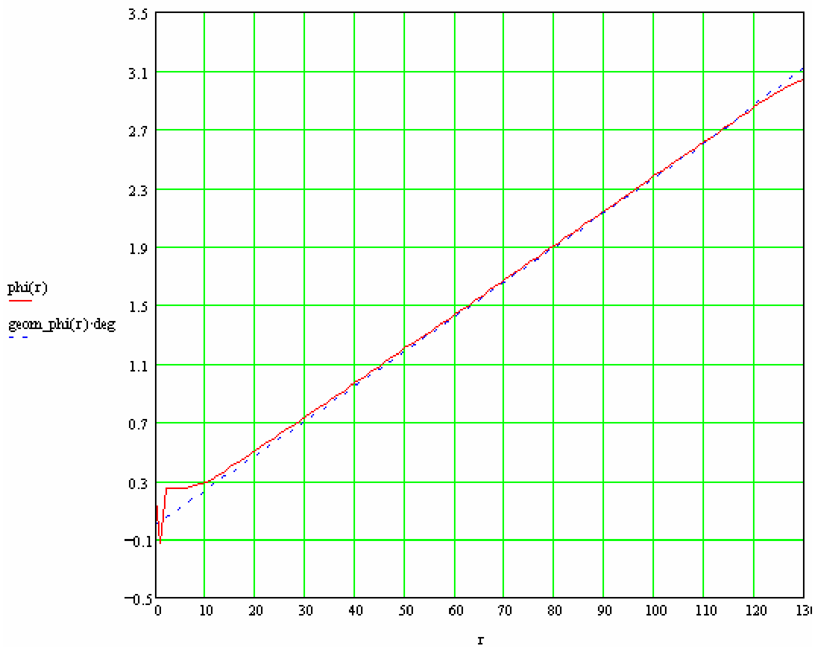

Fig. 3.2.15: Geometric spiral function (dashed blue line) compared with the magnetic spiral function (solid red line), along the radius in cm.

For example, at radius R=125 cm, where the axial focusing frequency reaches the minimum value, the magnetic spiral focusing term is 15% lower than the corresponding geometric term. This discrepancy had to be compensated by increasing the spiral angle and shaping the sector width. The Fig. 3.2.16 shows the results after the preliminary modifications of the spiral had been carried out in order to meet the required axial focusing.

In order to decrease the number of ampere-turns in the main coils and to allow for the last orbit of the accelerated particles to be brought closer to the pole edge and simplify the extraction operation, the gap hill size was reduced to 5 cm. Such a modification already allows us to increase the flutter and generally, to raise the axial focusing effect. Compared to the previous value of 7 cm, the new flutter curve is shown in Fig. 3.2.17. An increase of almost 20% of the focusing properties of the machine allows us to reduce the spiral angle. In fact, the vertical focusing tune is usually set to be greater than 0.15. The previously chosen spiral line was rather prudent in that the tune was over 0.4. The hill-edge line is thus unspiraled, which is beneficial when reducing capacitive load to lower RF power losses.

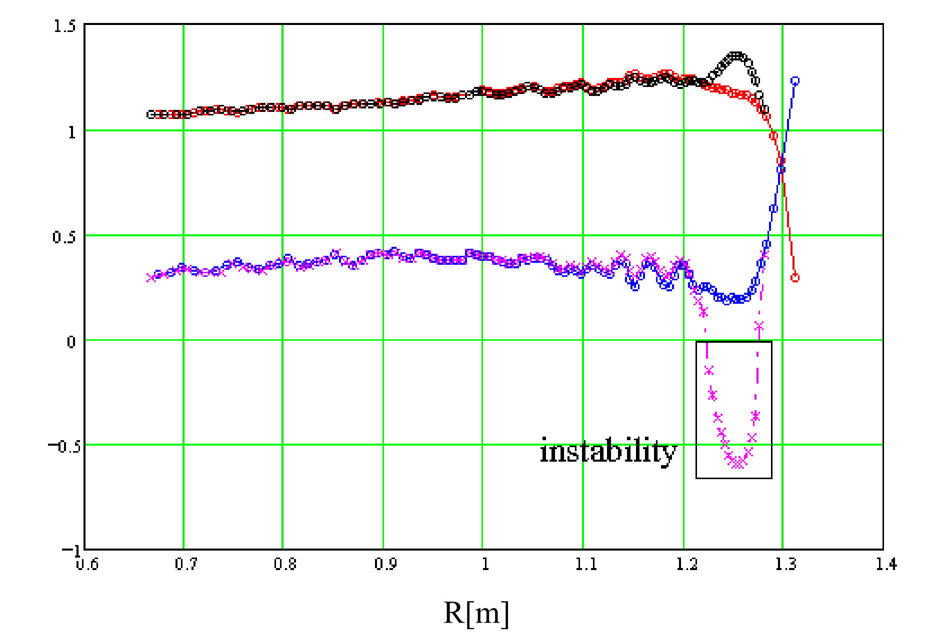

Fig. 3.2.16: Frequency tunes comparison. ν_r and ν_z during an unstable configuration (black and magenta lines) and after some modification in order to meet the dynamic stability (red and blue lines).

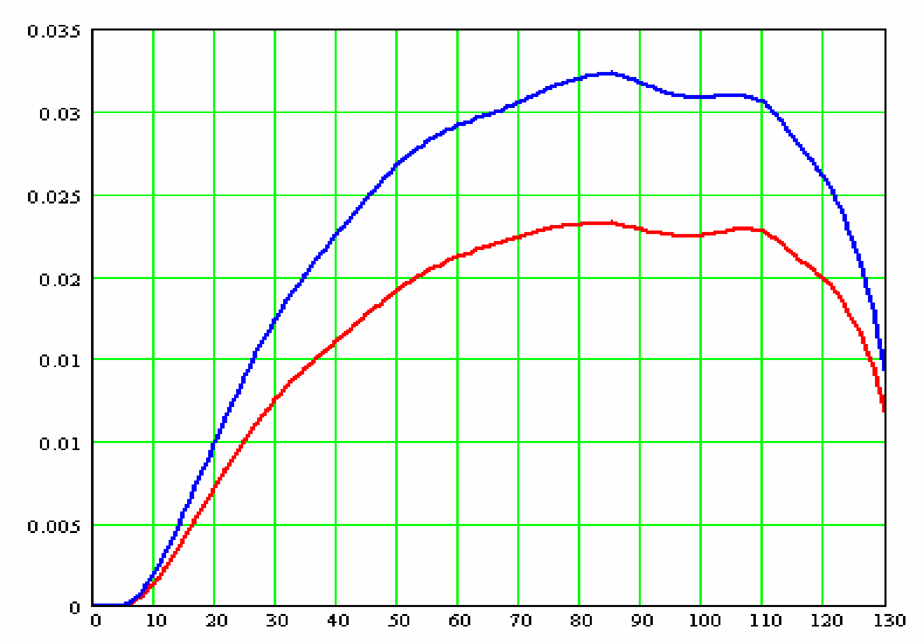

Fig. 3.2.17: Flutter vs. radius (cm) plot. The flutter function before the gap was reduced (red line) and afterwards (blue line).

The hill-spiral lines of the two designs and their corresponding focusing tunes are shown in Figs. 3.2.18 and 3.2.19 respectively.

Once the spiral hill edge and the angular width of the sector have been set, it is possible to refine the magnetic field by means of the shims located on the valley.

A second model of the magnet was built, in which more parameters can be set in order to fulfil the magnetic field requirements.

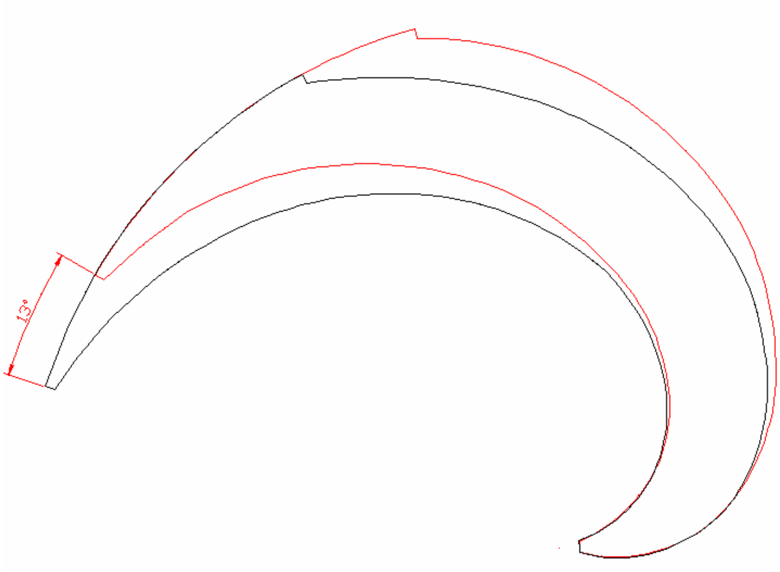

Fig. 3.2.18: Comparison between two different sectors with the spiral shape modified. As shown in the plot the new spiral (red sector) reduces the angular span of the sector by 13 deg. The length of the hill-edge is reduced by 6 % compared to the old shape.

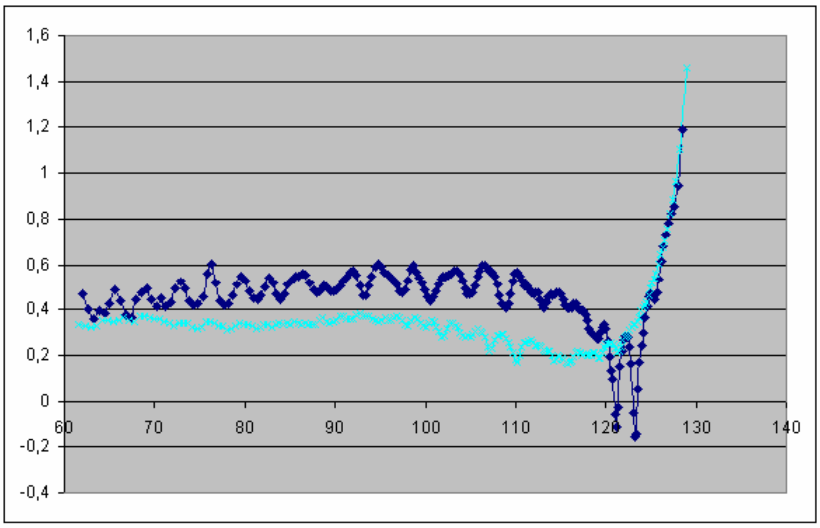

Fig. 3.2.19: Vertical focusing tunes comparison before (blue line) and after (cyclamen line) introducing the new spiral.

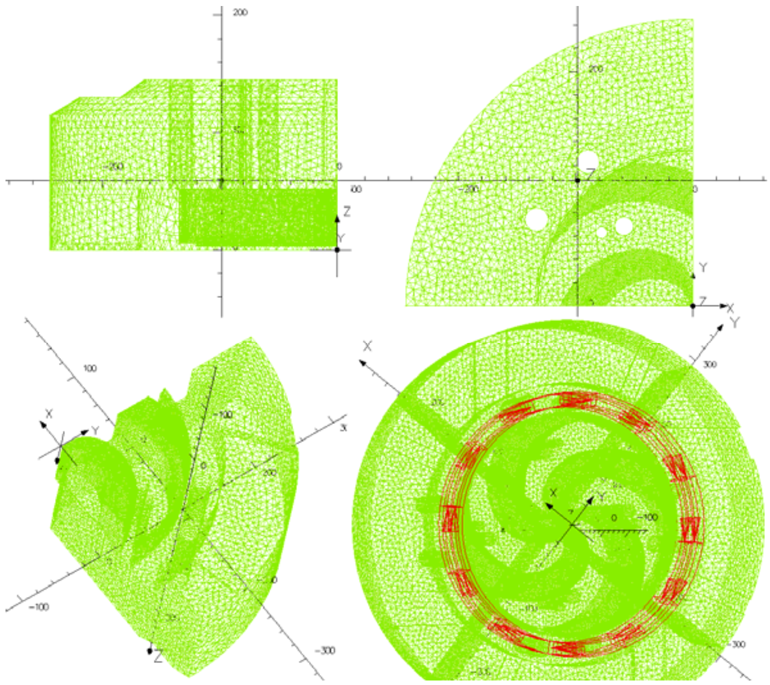

Fig. 3.2.20: Final model of the superconducting cyclotron.

A file, containing the parameterized structure, was written in ASCII format.

Part of this file, concerning the design of the valley shims, is shown in detail and explained in the following:

```
/
/       shims valley definition whit air
/
$ cons #r_shim_1 10
$ cons #r_shim_2 80
$ cons #h_shim_1 40
$ cons #h_shim_2 45+6

CYLINDER Name=SHIM_VALLEY_EXT X0=0 Y0=0 Z0=#h_shim_1 X1=0 Y1=0 Z1=52.5 MAJORRADIUS=#r_shim_1 MINORRADIUS=#r_shim_1 T
CYLINDER Name=SHIM_VALLEY_INT X0=0 Y0=0 Z0=#h_shim_1 X1=0 Y1=0 Z1=52.5 MAJORRADIUS=5 MINORRADIUS=5 TOPRADIUS=5
PICK OPTION=ADD,   | PICK PROPERTY=Name LABEL='SHIM_VALLEY_EXT'
PICK OPTION=ADD,   | PICK PROPERTY=Name LABEL='SHIM_VALLEY_INT'
COMBINE OPERATION=SUBTRACT +REGULAR
PICK OPTION=ADD,   | PICK PROPERTY=Name LABEL='SHIM_VALLEY_EXT'
PICK OPTION=ADD,   | PICK PROPERTY=Labels LABEL='spirale_new5'
COMBINE OPERATION=SUBTRACT +REGULAR
LOAD OPTION=INSERT FILE=g:\scent_last\spirale_new5.sat
PICK OPTION=ADD,   | PICK PROPERTY=Labels LABEL='spirale_new5'
TRANSFORM OPTION=COPY KEEP=YES TYPE=ROTATE COUNT=3 ROTU=0 ROTV=0 ROTW=1 ANGLE=90
PICK OPTION=ADD,   | PICK PROPERTY=Labels LABEL='spirale_new5'
TRANSFORM OPTION=APPLY TYPE=DISPLACE DU=0 DV=0 DW=2.5
CYLINDER Name=SHIM_VALLEY2_EXT X0=0 Y0=0 Z0=#h_shim_2 X1=0 Y1=0 Z1=52.5 MAJORRADIUS=#r_shim_2 MINORRADIUS=#r_shim_2
CYLINDER Name=SHIM_VALLEY2_INT X0=0 Y0=0 Z0=#h_shim_2 X1=0 Y1=0 Z1=52.5 MAJORRADIUS=#r_shim_1 MINORRADIUS=#r_shim_1
PICK OPTION=ADD,   | PICK PROPERTY=Name LABEL='SHIM_VALLEY2_EXT'
PICK OPTION=ADD,   | PICK PROPERTY=Name LABEL='SHIM_VALLEY2_INT'
COMBINE OPERATION=SUBTRACT +REGULAR
PICK OPTION=ADD,   | PICK PROPERTY=Name LABEL='SHIM_VALLEY2_EXT'
PICK OPTION=ADD,   | PICK PROPERTY=Labels LABEL='spirale_new5'
COMBINE OPERATION=SUBTRACT +REGULAR
/
```

Each section is introduced by a title describing the part of the machine. Then there are a set of parameters which it is possible to vary, in this case the radial span of the shims and their related heights.

The set-up conditions for the simulation and the meshing parameters are defined in another ASCII file.

```
MATERIAL UNPICK
MATERIAL PICK 'iron'
MATERIAL OPTION=MODIFY MULINEARITY=NONLINEAR MUANISOTROPY=ISOTROPIC BH=Default
EPSANISOTROPY=ISOTROPIC SIGANISOTROPY=ISOTROPIC KAPANISOTROPY=ISOTROPIC
BOUNDARY PICK 'NM'
BOUNDARY OPTION=MODIFY CONDITION=NORMMAGN
BOUNDARY UNPICK 'NM' | BOUNDARY PICK 'SYMM'
BOUNDARY OPTION=MODIFY CONDITION=SYMMETRY
IMPORT FILE='h:\sim_tosca\SCENT\conductors2.cond'
PERIODICITY NSETS=1 DX1=0 DY1=0 DZ1=0 ROTX1=0 ROTY1=0 ROTZ1=1 ANGLE1=90 TYPE1=POSITIVE
OPTION1=SYMMETRY
MODEL CREATE
MESH SIZE=200 NORMALTOL=30 SURFACETOL=0 TOLERANCE=1.0E-06
FILL TOL=1.0E-06
ANALYSIS OPTION=LOAD PROGRAM=TOSCAMAGN
ANALYSISDATA OPTION=SET PROGRAM=TOSCAMAGN LINEAR=NO NLITERTYPE=NEWTON NITERATIONS=21
TOLERANCE=1.0E-07 HX=0 HY=0 HZ=0 RHS=ADAPTIVE PERIODICITY=YES POTENTIALCUT=NO
COMMENT CLEAR=YES TYPE=DBTITLE
SOLVERS OPTION=NEW PROGRAM=TOSCAMAGN UNITS=CGS ELEMENT=MIXED SURFACE=CURVED
FILE='h:\sim_tosca\SCENT\prova3h_more_mesh.op3'
$OS OPERAANL WRD3=H:\sim_TOSCA\SCENT\prova3h_more_mesh.op3 WRD2=TOSCA WRD4=BACK
```

Once the file has been written, it is possible to run the code by means of a batch file containing only commands and calls to files where variables are defined.

3.3 3D simulation results

A good agreement between the isochronous field and the average field was achieved without the help of any correction system (trim coils or trim rods). The discrepancy is under 10 Gauss from the central and the extraction regions, see Figs. 3.3.1-2.

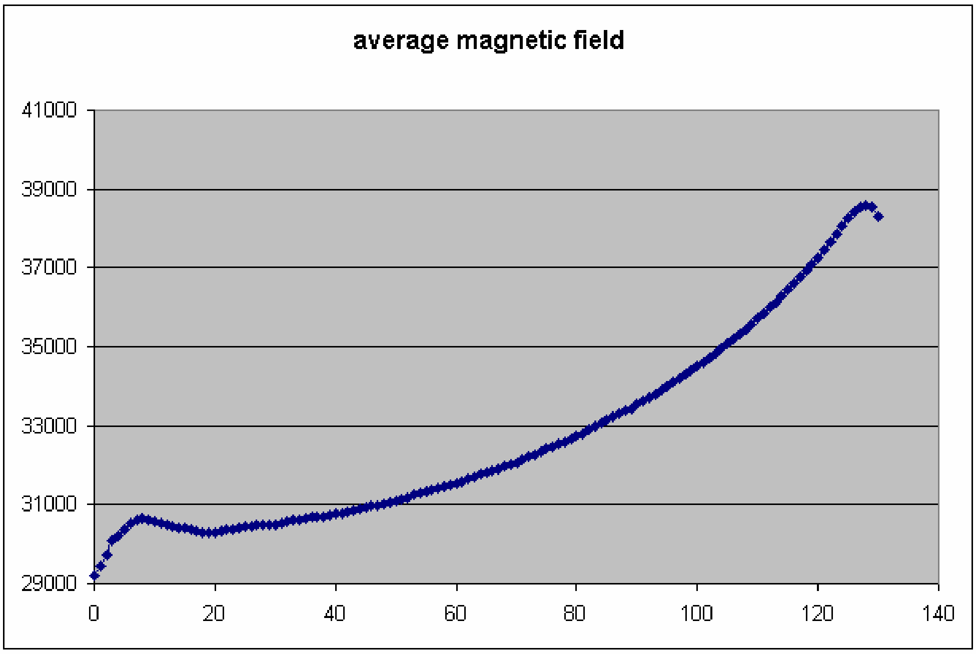

Fig. 3.3.1: Average magnetic field (Gauss) simulated along the radius (cm).

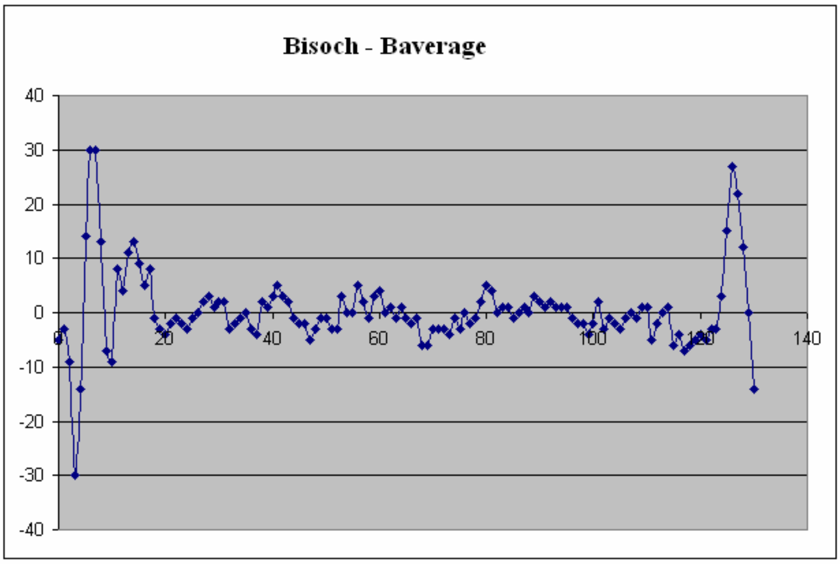

Fig. 3.3.2: Difference between the average isochronous magnetic field and average magnetic field simulated.

A cone field in the central region is necessary to provide axial magnetic focusing and an appropriate starting phase for the beam, so as to ensure axial electric focusing.

The amplitude of the main harmonics of the field as a function of the radius is plotted in Fig. 3.3.3. The peak value of the fourth harmonic C_4 is in excess of more than 10 kGauss around R=100 cm and in the extraction region drops to about 7 kGauss. The amplitude of the other harmonics is much lower.

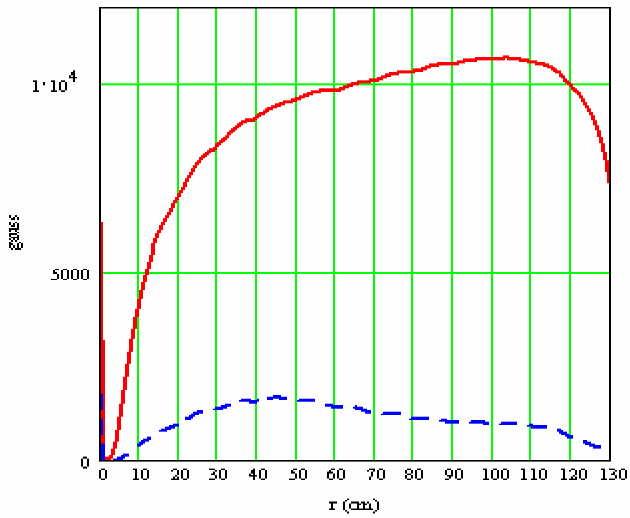

Fig. 3.3.3: Harmonics amplitude of the C_4 coefficient (red line) and C_8 (blue line).

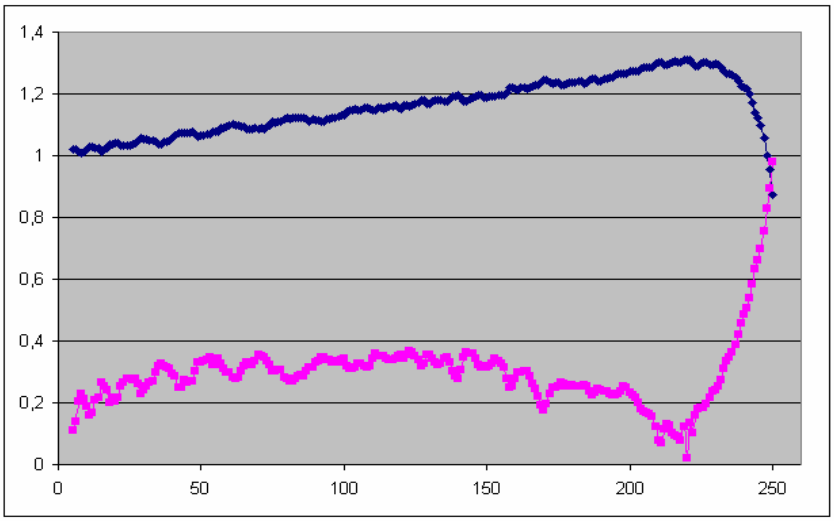

Fig. 3.3.4: Focusing frequency (ν_r blue line and ν_z magenta line) versus the energy of the ions (AMeV).

The validity for beam acceleration of the computed field is tested with codes [7,8] calculating the equilibrium orbit which provides the phase curve and the focusing frequency, plotted in Figs. 3.3.4 and 3.3.5.

The working path in the (ν_r, ν_z) plane is shown in Fig. 3.3.6, where the major resonance lines are plotted. Examination of the curve shows that the extraction, via the excitation of the ν_r=1 resonance with a first harmonic coil (eventually), takes place in proximity to the $\nu_r+2\nu_z=0$ resonance which, however, should not be crossed. The second dangerous resonance $\nu_r=2\nu_z$ (Walkinshaw resonance) should not be a problem, because it is crossed during the final turns.

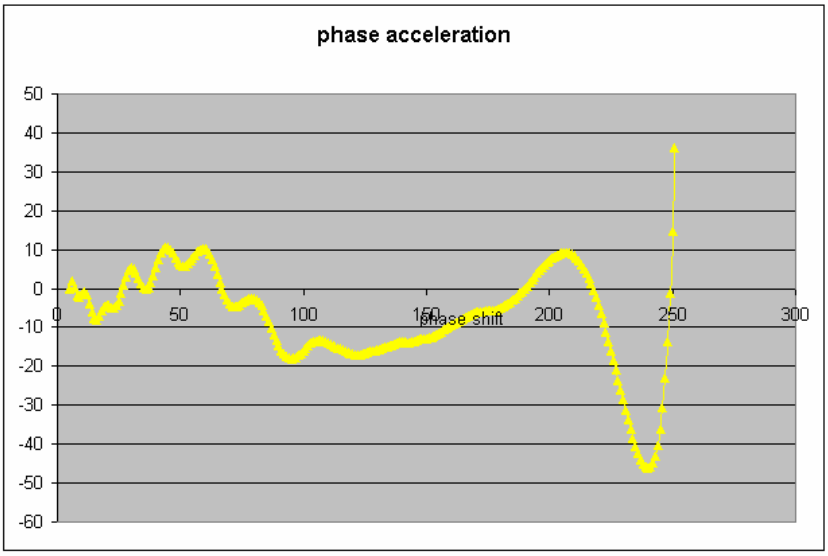

Fig. 3.3.5: Phase history (deg) versus the energy of the ions (AMeV).

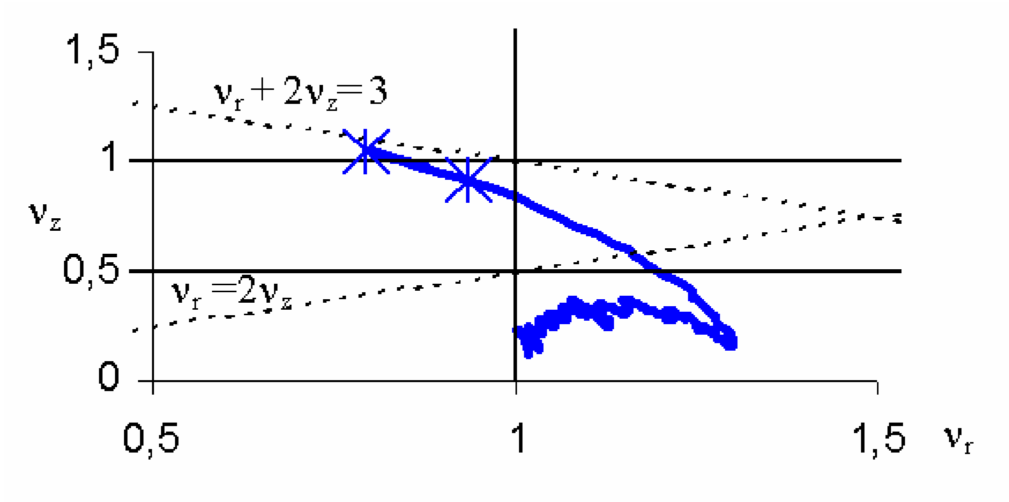

Fig. 3.3.6: Working path in (ν_r,ν_z) plane. The energy corresponding to the two points marked by asterisk are 250 and 251 AMeV.

On the median plane, the maximum magnetic field of 4.6 Tesla is located in proximity to the hills, whilst the magnetic field does not exceed the 5.4 Tesla on the structure as shown in the Figs. 3.3.7-8.

This magnetic field was achieved by setting a coil current density of 40.5 A/mm^2. Such a low value of current crossing the coils allows us to maintain the maximum strength on the coils quite moderate as shown in Table 3.3.1.

The isochronization of the magnetic field, as previously mentioned, must be obtained through the independent excitation of two coils and through the shape of the sectors, since the correction capability of whatever system is limited to a few hundred Gauss.

Table 3.3.1

MAGNETIC VALUES		**COIL VALUES**	
B hill peak	4.64 Tesla	Size	150×210 mm^2
B valley min	2.37 Tesla	Internal radius	142 cm
B peak	5.4 Tesla	Distance to the median plane	7.5 cm
B min	0.24 Tesla	Current density	40.5 A/mm^2
Energy stored	28 MJ	Max Strength	11 MN (axial)
			24 MN (radial)
		Max magnetic field	3 Tesla

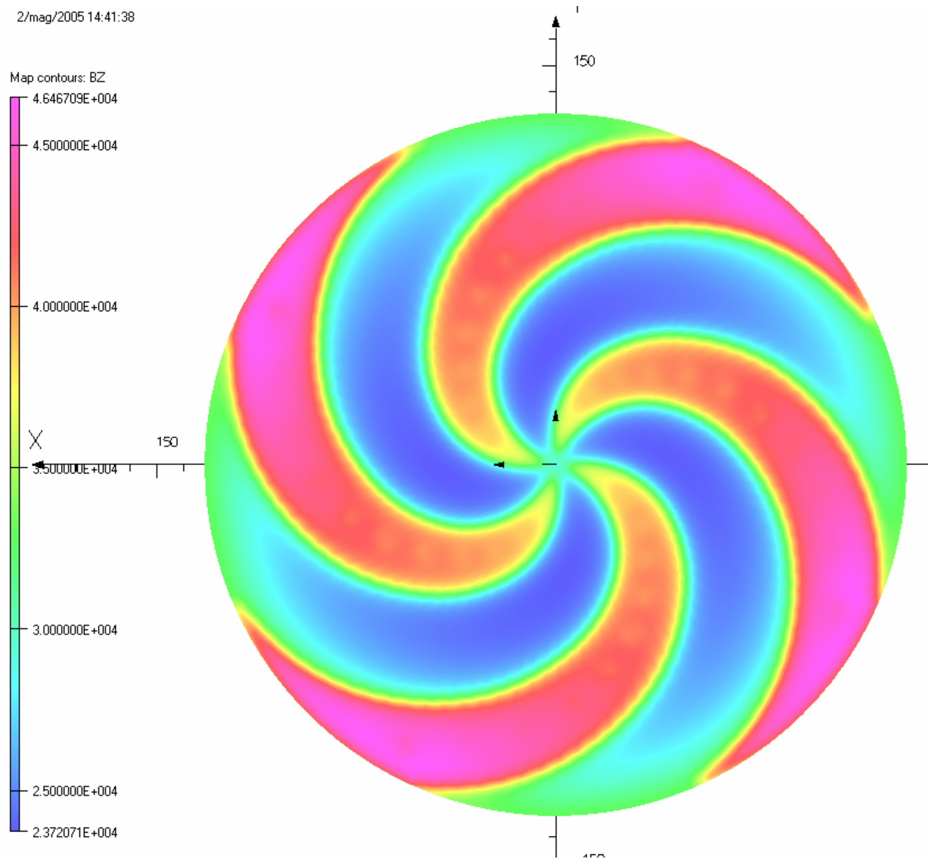

Fig. 3.3.7: Magnetic field map (Gauss) on the median plane of the cyclotron.

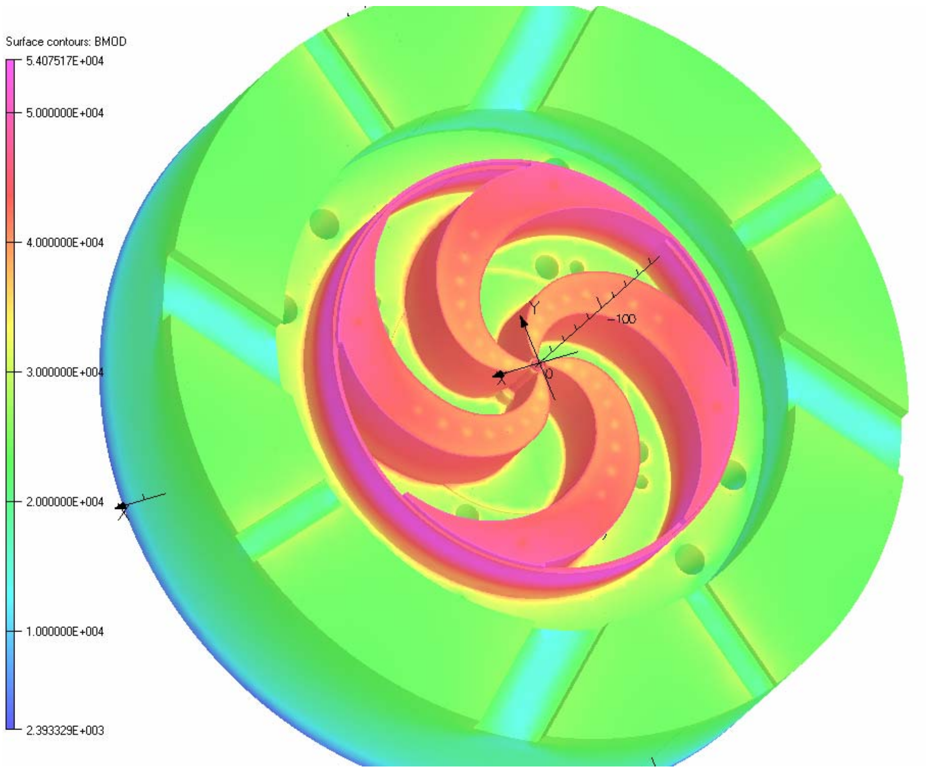

Fig. 3.3.8: Magnetic field (Gauss) distribution on the surface of the cyclotron.

Because the cyclotron is able to accelerate one set of ions[6], in our opinion it is better to make the fine tuning of the magnetic field by means of a few moveable mechanical iron shims instead of trim coils. The advantage of using the Trim Rods (TR) vs. the trim coils is to avoid to installing coils all around the hills and all the related negative effects like: a reduction in the useful vertical clearance for the Electrostatic deflector, feed through for the current leads, cooling for the coil, a set of power supplies and so on.

The trim rod consists of a cylindrical piece of iron which can be pulled out from the cyclotron. Therefore, maintaining the flexibility for adding to or subtracting from the field using the TR is mandatory to evaluate the field map of the cyclotron with empty space at the end position of each TR. The cylinder holes are drilled inside each sector, starting from 6 cm to the median plane up to 4.5 cm (height=1.5 cm) with a diameter of 5 cm, see Figs. 3.3.9 and 3.3.11. This solution allows us to increase or decrease the field pushing inside or pulling out the TR.

The final setting of the magnetic field was achieved by adding the contribution of a set of trim rods (TR). Eleven TRs per hill, placed along the center of the hill and with a radial distance of 10 cm between them, were simulated to obtain the individual magnetic field map and the respective form factor. According to the commercial requirement to switch from one beam to another in a very short space of time, it is mandatory to move the TR maintaining the magnetic field on. This means that in order to move the TR, it is necessary to counterbalance the magnetic force which acts on each TR. To reduce the magnetic force on the TR, we suggest a special TR design shown in Fig. 3.3.10. The TR only consists of a smaller cylinder, 30 cm tall, placed inside the cyclotron's hill. The magnetic force acting on the TR is then about 200 kg. The movement of the TR is performed through an inox steel bar, 10 mm in diameter, which crosses the pole and the yoke of the cyclotron. The TR is moved by pneumatic pistons. When the piston is switched on, it pulls out the TR. The inner position of the TR is fixed by a mechanical block bar, which has a proper profile and which stays outside the yoke. When the pneumatic pistons are switched on, the mechanical block bar can be moved into positions 1, 2 and 3, corresponding to the different heights of the block, see Fig. 3.3.10. Once the mechanical block is in position, the pneumatic piston is switched off and the

[6] The magnetic field will be fixed, with a narrow tuning range of 0.4 % to allow for acceleration of different light ions with Q/A=0.5

TR go to the desired position. This solution allows us to change the position of each TR without dismantling the system, but only re-machining the external mechanical block bar.

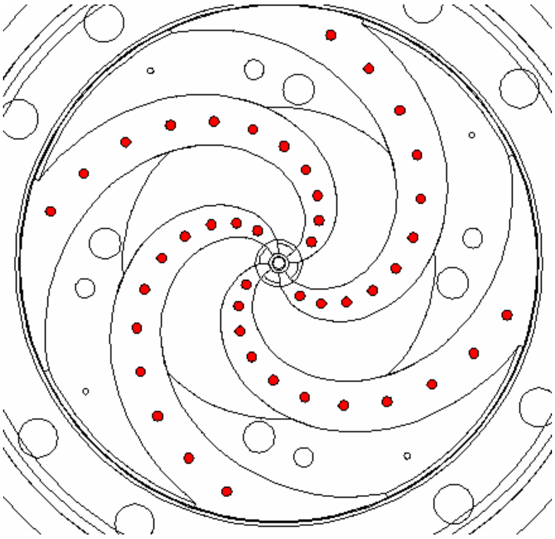

Fig. 3.3.9: Trim rods (red circles) configuration.

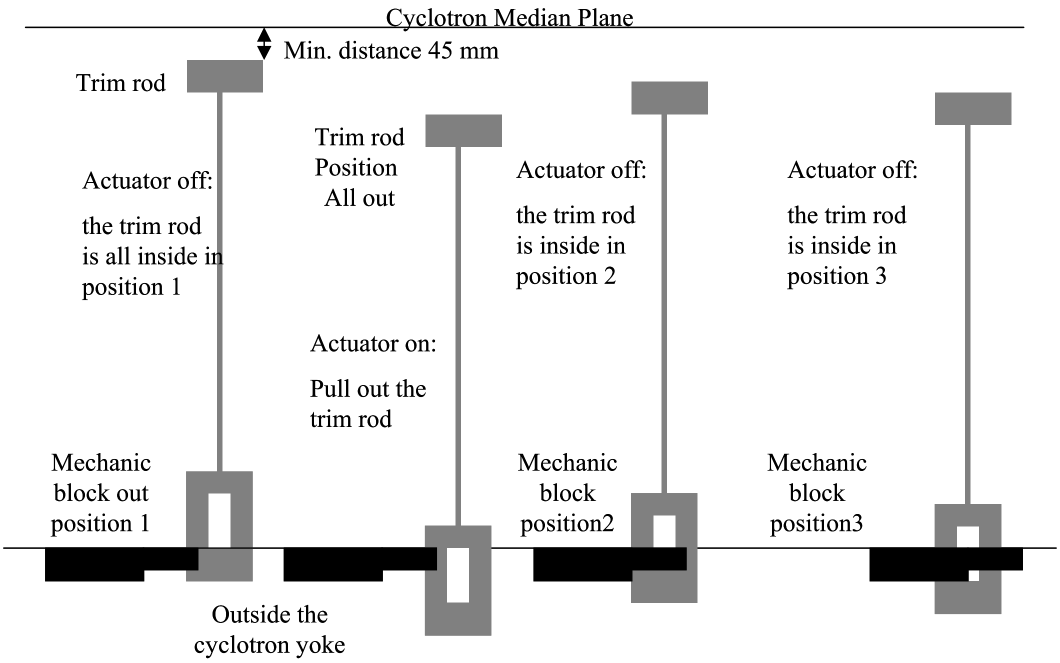

Fig. 3.3.10: Layout of a trim rod and of the movement bar. Four positions of the Trim rod are shown. Position 1 is for acceleration of H_2^+; position 2 the TR is pull out to allow us to move the mechanical block in position corresponding to acceleration of a different ion; position 2 and 3 are for acceleration of different ions, as Litium or Carbon.

Pneumatic devices able to develop a force in excess of 1 Ton, with a small size and cost of about 1 k€ are commercially available. Hence, a group of 5 TRs can be moved by a single pneumatic piston, reducing the cost and the complexity of the system.
Through the preliminary trimming of the field the phase growth has been reduced within ±10 deg as shown in the plot of Fig. 3.3.12.

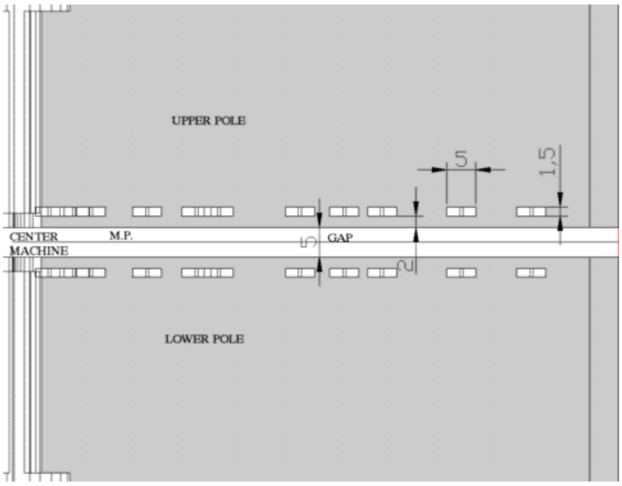

Fig. 3.3.11: Side view of trim rods configuration.

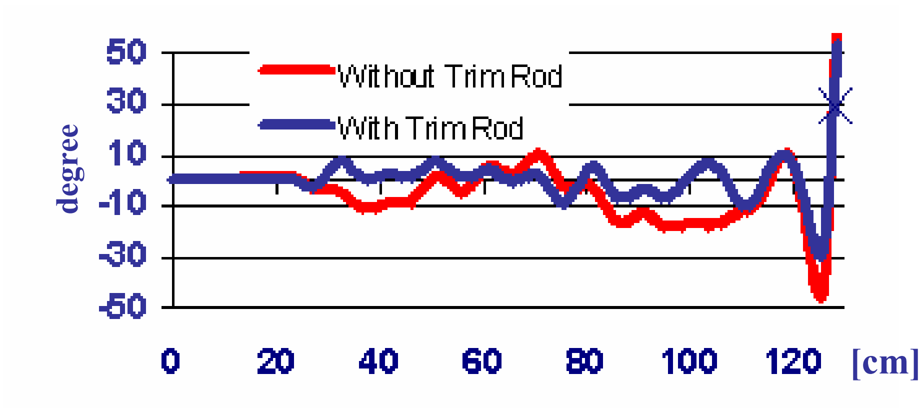

Fig. 3.3.12: Isochronous phase (deg) vs. radius, with and without Trim Rods optimisation.

3.4 Beam dynamics for H_2^+ and $^{12}C^{6+}$

In subsections 3.2 and 3.3 the study of the preliminary design of the magnetic circuit of the 250 AMeV superconducting cyclotron has been carried out under the assumption of accelerating particles with a mass to charge ratio equal to 2. In this section, the beam dynamic features for the acceleration of H_2^+ and Carbon ($^{12}C^{6+}$) beams are presented. Despite the fact that these two ions have charge to mass ratios of 2.0156 and 2.0086, with a difference of about 0.35%, this difference is large enough for the isochronous magnetic field of one not to allow for the acceleration of the other ion.

The Trim Rods allow us to perform a fine tuning of the magnetic field to achieve a good isochronism for both the ions H_2^+ and $^{12}C^{6+}$. In Fig. 3.4.1 the plots of the beam phase vs. the beam energy are shown. The plot was calculated through the GENSPE code [8] using the original magnetic field map in addition to the field map of a set of 26 TR and of two shims for each hill. The energy gain was assumed to be 0.43 AMeV per turn, and the points of the plot are evaluated with a step of 1 AMeV. As shown by the figures, the maximum phase slip of the beam is of 5° from the central region to the 210 AMeV. Fig. 3.4.2 is similar to the previous one, but this time the beam phase vs. orbit radius is shown. The large phase oscillation starts near R=120 cm. The large phase oscillation allows us to reduce the phase slip of the last orbit corresponding to the point marked by an asterisk in Fig. 3.4.2. Without the phase oscillation the last 3 points, corresponding roughly to the last 6 turns, will have about a 30° larger phase. Hence, the phase oscillation allows us to extract a beam with higher energy and with a larger radius, and the electric field required to push out the beam will be lower.

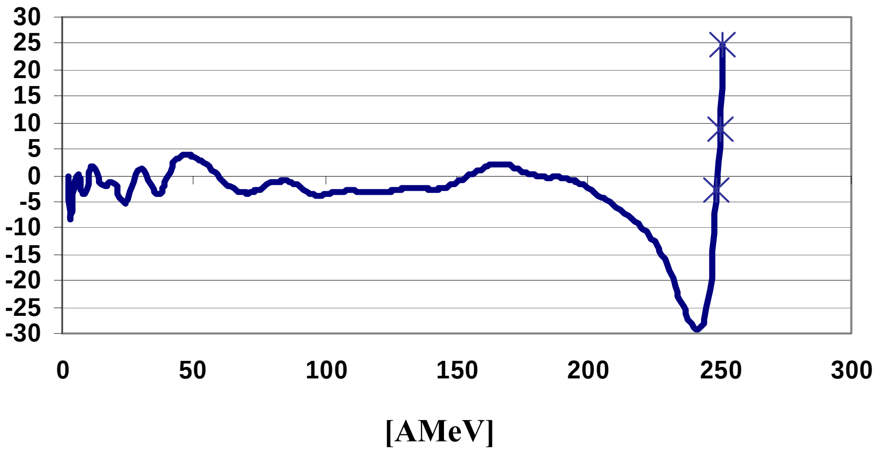

Fig. 3.4.1: Isochronous phase vs. beam energy, the last 3 points marked have a separation of 1 AMeV.

In Figs. 3.4.3 and 3.4.4 the beam phase vs. the beam energy and vs. the orbit mean radius are respectively shown. It is evident that the phase oscillation in this case is not as nice as in the previous case. This is a consequence of the magnetic field optimisation procedure, which was performed using the H_2^+ as the accelerated beam. This feature can be changed if the

Carbon beam will be used as the accelerated beam along the optimisation procedure. For the final design of the cyclotron the Carbon will be used as the reference beam. Moreover, as will be explained in the conclusion, the final design can be upgraded to 300 AMeV for Carbon, while the proton beam will be extracted at 250 MeV which correspond to an extraction radius of about 118 cm. This means that the field isochronization near the extraction region has to be adjusted only for the Carbon beam with great simplification.

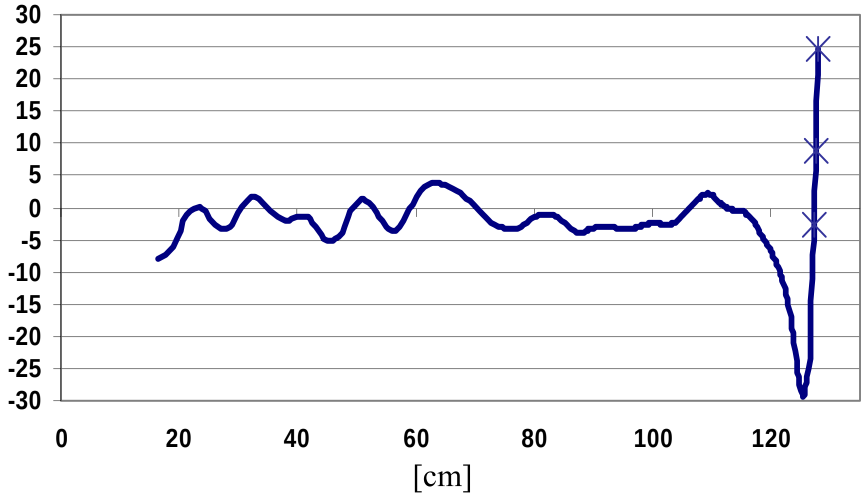

Fig. 3.4.1: Isochronous phase vs. orbit's mean radius, the last 3 points marked have a separation of 1 AMeV.

Table 3.4.1: Radial and vertical positions of 26 TR to optimise isochronism of magnetic field for the H_2^+ and $^{12}C^{6+}$ ions.

TR	R [cm]	$Z(H_2^+)$ [mm]	$Z(^{12}C^{6+})$ [mm]	TR	R [cm]	$Z(H_2^+)$ [mm]	$Z(^{12}C^{6+})$ [mm]
1	10	0.0	-1.22	14	75	-1.7	-12.9
2	15	-0.2	-2.52	15	80	-0.8	-10.4
3	20	-0.2	-3.0	16	85	-1.8	-10.8
4	25	-0.3	-5.72	17	90	-0.8	-7.9
5	30	-0.5	-5.5	18	95	-1.5	-7.6
6	35	-0.6	-8.4	19	100	-0.9	-4.8
7	40	-0.3	-7.4	20	105	-1.1	-3.2
8	45	-0.4	-9.3	21	110	-0.8	-0.6
9	50	-0.4	-10.4	22	116	-0.8	1.6
10	55	-0.8	-12.7	23	120	0.8	2.9
11	60	-0.4	-11.1	24	123	-1	1.99
12	65	-1.2	-13.0	25	126	-2.2	0.4
13	70	-0.2	-11.0	26	130	2.1	7.1

The radial and vertical positions of each TR, for the H_2^+ and Carbon setting, are reported in Table 3.4.1. A positive vertical position means that the TR is nearer to the median plane than its original position, resulting in more field, whilst a negative value means that the TR is farther away from the median plane, resulting in less field.

Of course, similar fine tuning is also possible for all the ions which have a mass to charge ratio value between 2.0156 and 2.0086. The vertical position of the TR shows that for the Carbon beam we have to pull out the TR to reduce the mean magnetic field according to the lower mass to charge ratio of Carbon vs. H_2^+. The magnetic field map used to evaluate the curves from Figs. 3.4.1 to 3.4.4 was achieved also including the effects of two magnetic shims.

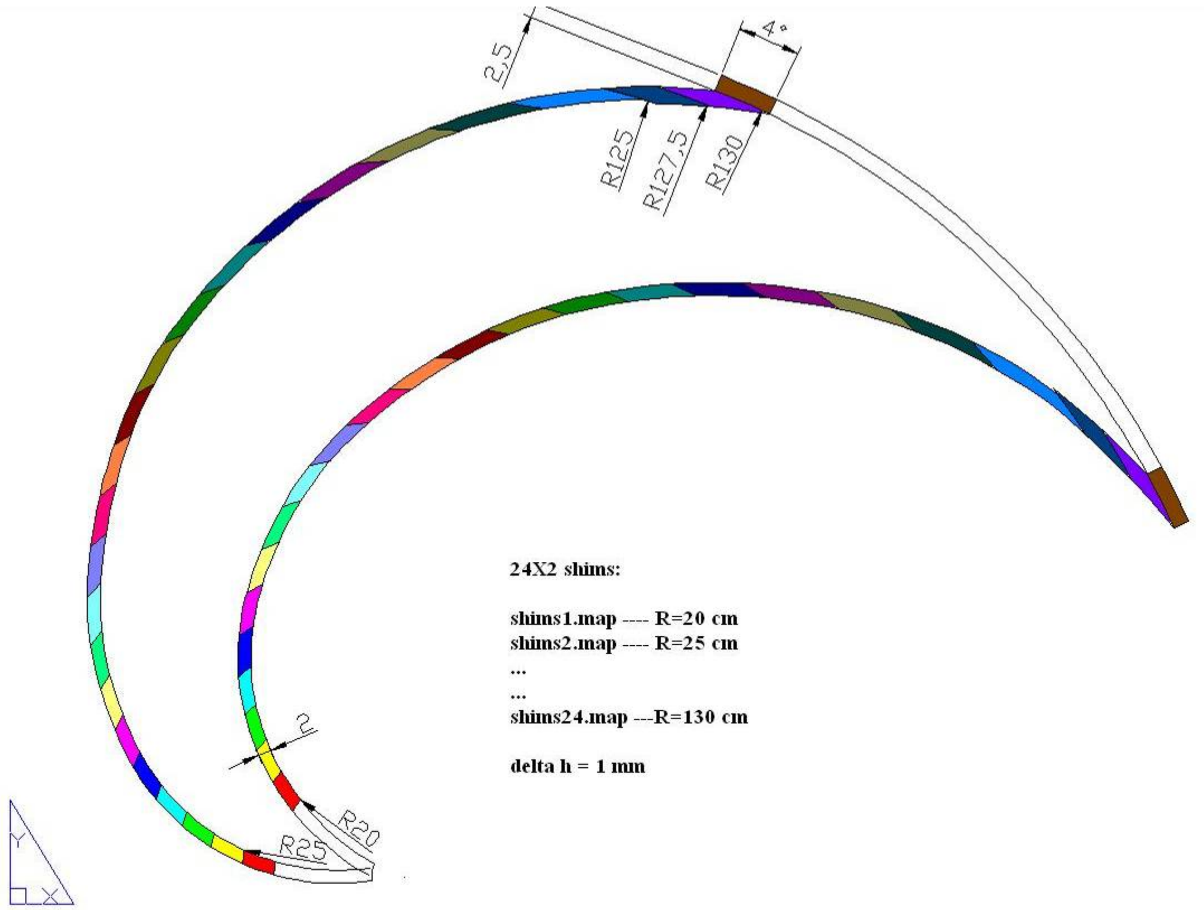

Fig. 3.4.5: Positions and sizes of 24 shims placed on the top of the hill. Of all these only the n.22 and 24 were used to evaluate the magnetic field map used to evaluate the beam dynamics for Carbon and H_2^+.

Fig. 3.4.5 shows the positions of the 24 shims that we simulated. They are located on the top of each hill. Of all these shims, we just used shim n. 22 and the last one, starting at radii 125 and 130 cm respectively. The thickness of these two shims are +3 and -5 mm respectively, and these values are the same for both the ions H_2^+ and Carbon. We used these shims in the attempt to reduce the electric field required to extract the beam, but the effect was negligible. For this reason, the final design of the cyclotron we plan does not use shims but only Trim Rods. In Fig. 3.4.6a and b, the working path in the (ν_r,ν_z) plane for the H_2^+ and Carbon ions is shown.

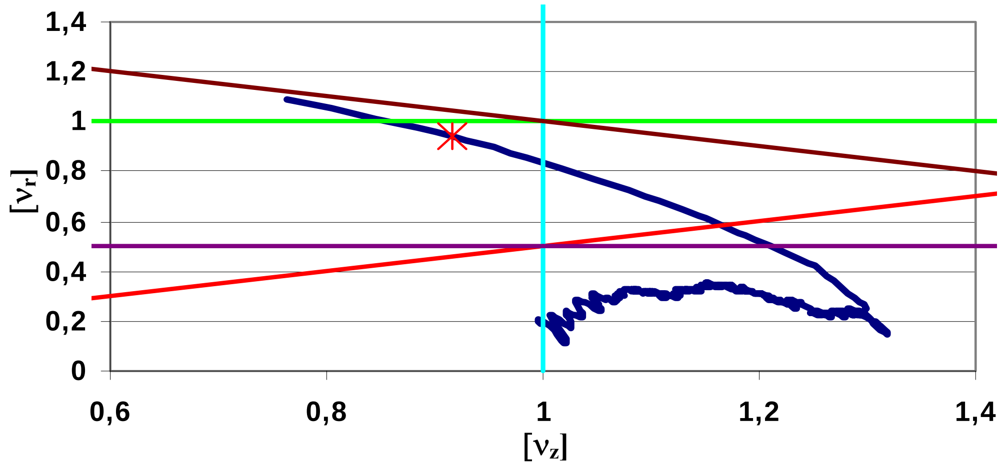

Fig. 3.4.6a: Working path in the (ν_r,ν_z) plane for the acceleration of H_2^+, the coloured lines are the resonances which have to be avoided.

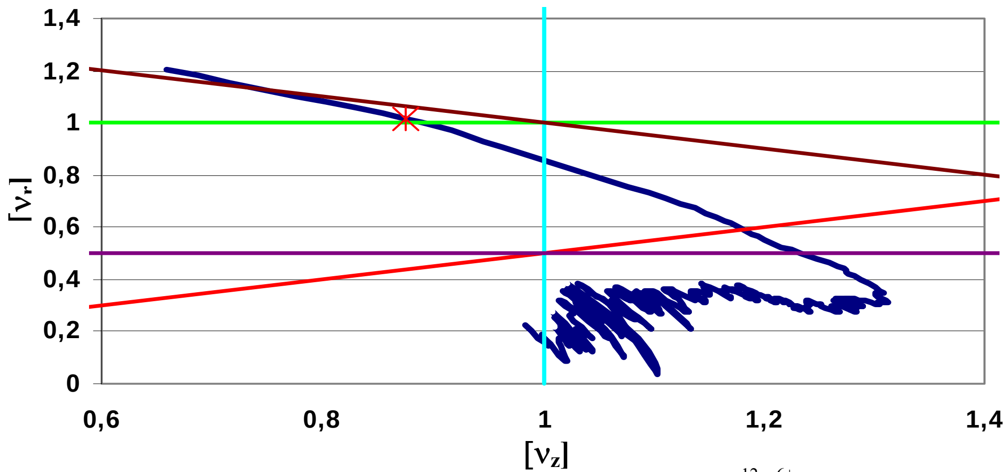

Fig. 3.4.6b: Working path in the (ν_r,ν_z) plane for the acceleration of $^{12}C^{6+}$, the coloured lines are the resonances which have to be avoided.

It is quite evident that the features of the H_2^+ beam are better than for the Carbon and in particular, that the orbit corresponding to the energy of 250 AMeV, marked by a red asterisk, has a ν_z value a little bit larger than 1. Both these features, like the difference in phase oscillations in the previous figures, are related to the optimisation procedure as we said before. The problem is the difficulty to scale the magnetic field at the extraction region properly. A better solution can be achieved if we also use an independent coil to adjust the main field of the cyclotron. In this case, a little fine tuning of the magnetic field for Carbon produces the beam phase and the working path in the (ν_r,ν_z) plane shown in Figs. 3.4.7 and

3.4.8 respectively. In particular in Fig. 3.4.8 the point at 250 AMeV is now in the same position as in the case of H_2^+, which means that the beam dynamic in the two cases H_2^+ and $^{12}C^{6+}$ is very similar. This solution was achieved reducing the current of the main coil to a value of 99.928% in the case of H_2^+, adjusting the TR set, but also powering an additional coil placed on the main coil with a density of -15.32 A/mm^2. The parameters of this additional coil are:

- Inner Radius 1420 mm.
- Outer Radius 1570 mm.
- Distance from the median plane 285 mm.
- Coil's height 10 mm.

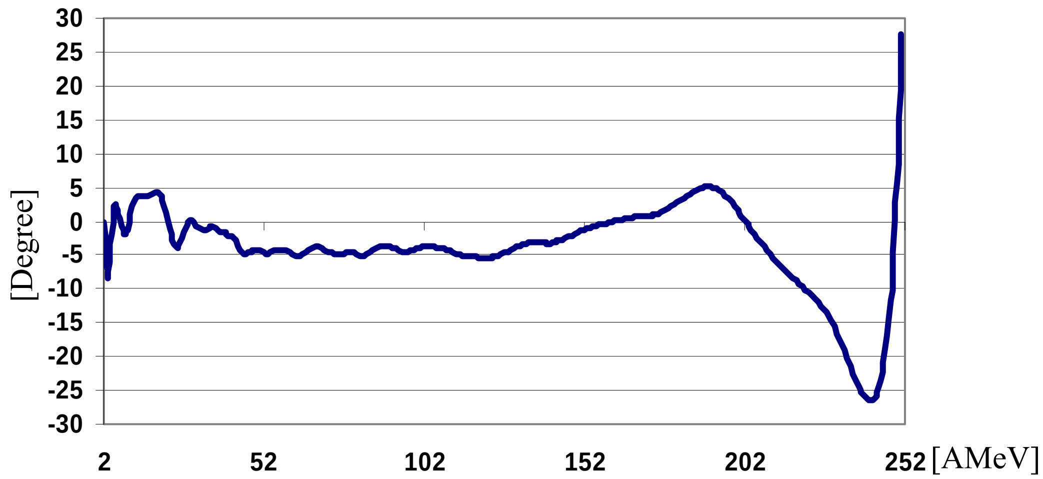

Fig. 3.4.7: Isochronous phase vs. beam energy for the $^{12}C^{6+}$. The magnetic field was optimised using also an additional coil.

The positions of the 26 TR for Carbon are shown in Fig. 3.4.9 together with the TR position of the H_2^+ case. The use of the additional coil allows us to maintain the positions of the last 3 TRs unchanged when the cyclotron setting is changed from H_2^+ to $^{12}C^{6+}$. The use of an additional coil also allows us to reduce the adjustments of the other TR. The positions of the TR for the H_2^+ case are the same as already shown in Table 3.4.1.

A common feature of the magnetic fields used to simulate the acceleration of H_2^+ and $^{12}C^{6+}$ is that it is possible to extract the beam just after the beam crosses the resonance ν_r=1. This feature allows us to excite a first harmonic radial oscillation to increase the inter turns separation. Moreover, the crossing of the Walkinshaw resonance is accomplished quickly, so we do not expect it to produce a significant deterioration of the accelerated beams.

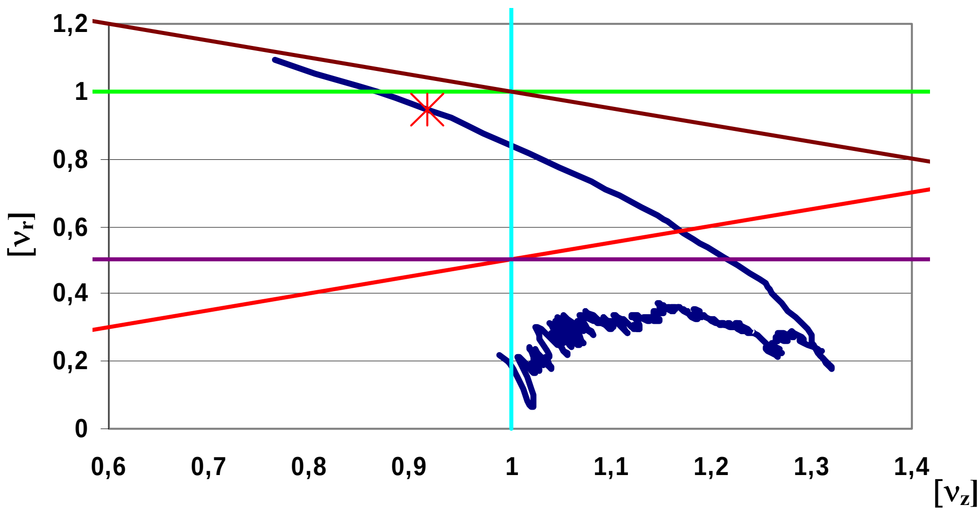

Fig. 3.4.8: Working path in the (ν_r,ν_z) plane for the acceleration of $^{12}C^{6+}$, the point corresponding to a 250 AMeV is marked by an asterisk. Isochronous field achieved by using also an additional coil.

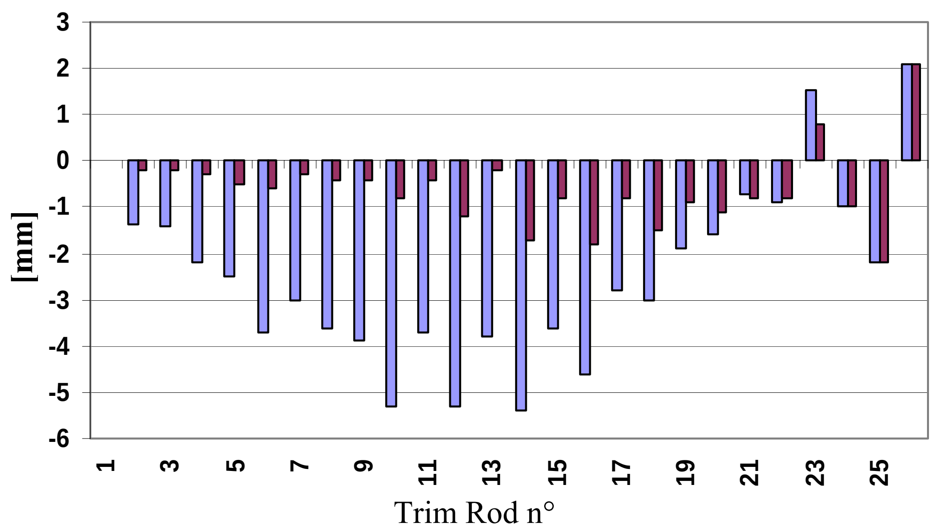

Fig. 3.4.9: vertical position of 26 TR to optimise isochronism of magnetic field for the H_2^+ and $^{12}C^{6+}$ ions.

Now we will look at figures 3.4.10 to 3.4.12, where the plots of the ν_z and ν_r vs. the orbit's mean radius are shown. Fig. 3.4.10 is obtained by the magnetic field map relative to the acceleration of H_2^+, while the other two are for the acceleration of $^{12}C^{6+}$. In particular, Fig. 3.4.11 is obtained by the magnetic field map optimised using only the TR, the positions of the TR being those shown in table 3.4.1. Fig. 3.4.12 is obtained by the magnetic field map optimised using the TR and also the above-mentioned correction coil. It is quite evident that Fig. 3.4.10 is the most regular of the three. This is due to the small correction and perturbation introduced by the TRs. At the same time, we can observe that Fig. 3.4.12 is more similar to

Fig. 3.4.10 than the Fig. 3.4.11, since the smooth contribution of the correction coil allows us to reduce the amount of correction introduced by TR. Hence, here we have an indication of how to optimise the magnetic field for H_2^+ and Carbon:

- we have to optimise the main magnetic field with respect to a beam having a mass to charge ratio equal to 2.0121 which is the intermediate value between the H_2 and $^{12}C^{6+}$ beams. In this way, the basic magnetic field map will be intermediate between the two ions and the required TR correction will be reduced.
- The use of a correction coil could help to optimise the procedure of field tuning, but it is neither a simple nor economic solution. Perhaps a bigger TR installed far from the median plane, at about 40 cm and at a radius of 65 cm, could produce a smooth form factor useful in reducing the contribution of the TR from 7 to 18, see figure 3.4.9 and Table 3.4.1, which are the TRs that have to produce the larger correction.

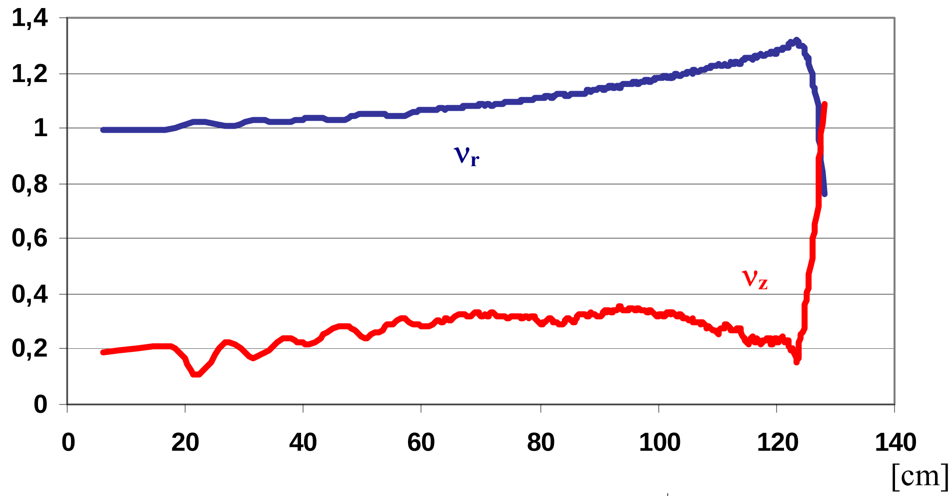

Fig. 3.4.10: ν_r and ν_z vs. orbit's mean radius, for H_2^+ acceleration.

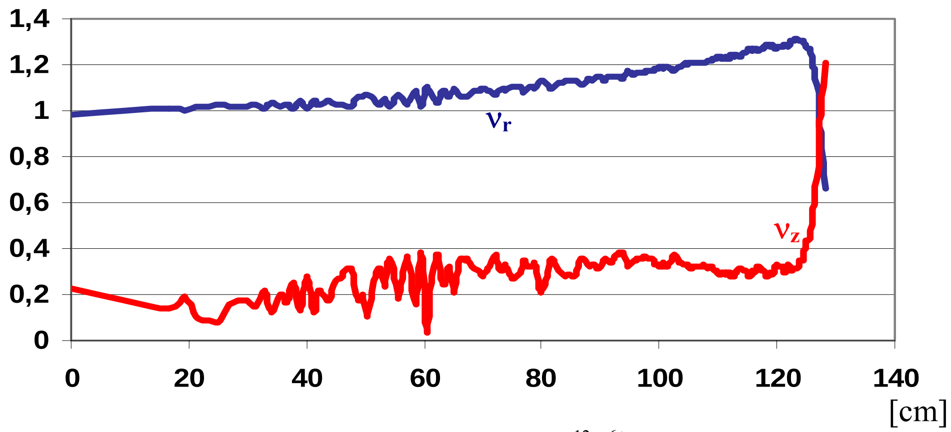

Fig. 3.4.11: ν_r and ν_z vs. orbit's mean radius, for $^{12}C^{6+}$ acceleration, magnetic field optimisation achieved using only TR.

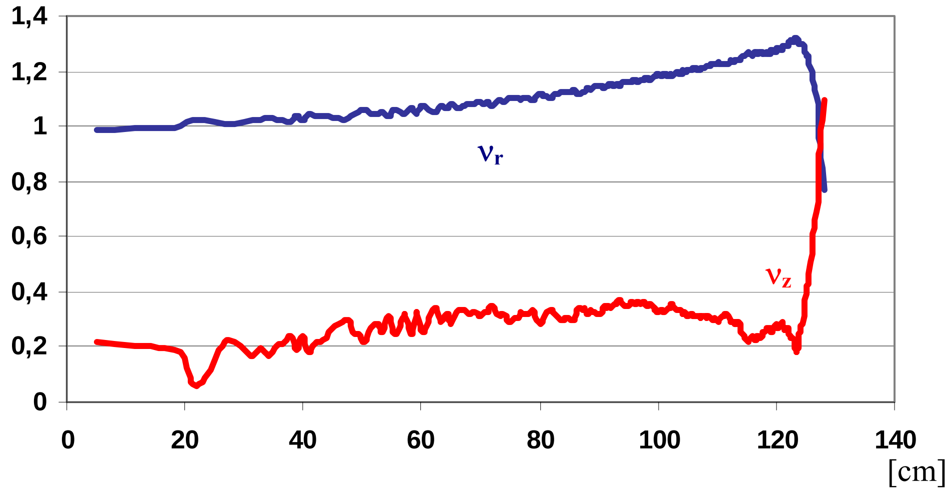

Fig. 3.4.12: ν_r and ν_z vs. orbit's mean radius, for $^{12}C^{6+}$ acceleration, magnetic field optimisation achieved using TR and a correction coil.

3.5 Magnet yoke and fringing field

Due to conflicting scientific research and a lack of international standards, establishing an acceptable level of magnetic field for human exposure is very perplexing and complex. A table reporting the guidelines from the International Commission on Non-Ionizing radiation is shown below [11]. Due to people's sensitivity to environmental radiation, the values here reported have to be considered as an upper limit. When possible and feasible, the values in this table have to be reduced by a factor of 10 in the perspective of possible future restrictions.

Table 3.5.1: International Commission on Non-Ionizing Radiation Protection Guidelines.

Occupational Workers:	**Electric Field**	**Magnetic Field**
Whole working day	10 kV/m	5,000 mG
Short term (2 hours)	30 kV/m	50,000 mG
For limbs	----	250,000 mG
General Public:		
Up to 24 hours per day	5 kV/m	1,000 mG
Few hours per day	10 kV/m	10,000 mG

To design the return yoke from the cyclotron magnet two parameters are important:

- the fringing field in the area around the cyclotron and mainly in the control room;
- the shape of the fringing field around the cyclotron.

The cyclotron return yoke was designed following the guideline of the fringing field of the existing cyclotron K800 at LNS. Our experience shows that to operate the K800 with a magnetic field over 4.2 T produces a fringing field of about 5 Gauss at a distance of 8 m from the cyclotron's center. For some devices like RF transmitters and computer controls, magnetic field values in excess of 5 Gauss could produce serious problems.

Moreover, at a distance of 15 m from the cyclotron's center, the fringing field values are lower than 2-3 Gauss but they are still high enough to produce serious disturbances to the computer monitors, the tilting of the screen and change in colours. This kind of disturbance could be minimized using LCD monitors, but we decided that the magnetic fringing field of the new cyclotron had to be lower than 2 Gauss at a distance of 10 m from the cyclotron's center. This value is low enough to allow the permanence of the cyclotron crew in the console area for the standard 8 hour day; the control room being located at an average distance of about 10 m from the cyclotron. To reduce the stray field at a lower value, the construction of a local magnetic shield could be a cheaper and feasible solution.

The shape of the fringing field was designed as smoothly as possible, similar to the fringing field shape of the K800. The starting point was a preliminary cyclotron design with a cross-shape box (see Fig. 3.5.1) which produces the required isochronous magnetic field at the center of the cyclotron, with values for the size of the iron pole and coils quite near to the final design.

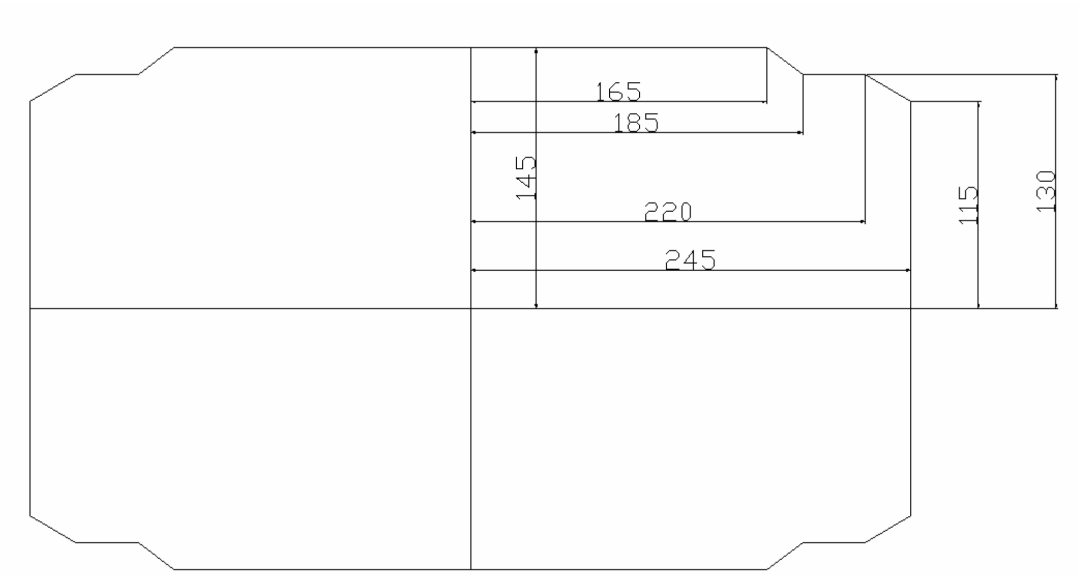

Fig. 3.5.1: Shape and outer size of SCENT. The units are in cm.

To achieve the final design of the return yoke, the computer code OPERA was used. In this case, the cyclotron iron shape had to be simulated taking on a circular symmetry. To do that, each section was simulated by inserting different values of magnetization iron corresponding to the stacking factor value. The stacking factors used for the 2D simulation of SCENT are in table 3.5.2. The area numbers are only of the upper half, the lower half being symmetric, see Fig. 3.5.2.

Table 3.5.2: Stacking factor.

Area	Stacking Factor	Area	Stacking Factor
3,5	0.5	48,39,40,36,33	1
49	0.972	34,41,42,43,50	1
51	0.979	52,53,54,56	1
55	0.843	11 valley skirt	0.75

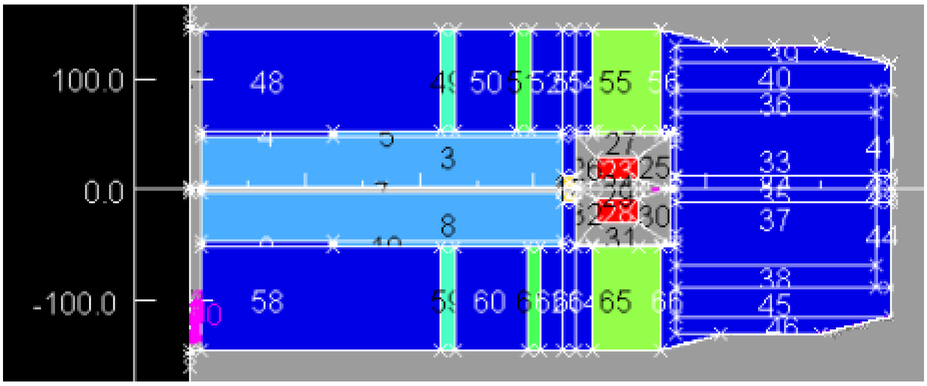

Fig. 3.5.2: Layout of SCENT cyclotron. The numbers of the different regions allow us to know the stacking factors value used in the present simulations, see table 3.5.2.

To evaluate the reliability of the previous simulations, we simulated the fringing field of the K800 cyclotron assuming a magnetic field at the center of 4.2 T (see Fig. 3.5.3) and we compared the simulated stray field of the K800 to the stray field measured (see Table 3.5.3).

It is evident that the simulated stray field must be lower than the real one at a long distance, due to the effect of the boundary. But at the present status of the design we will use the simulation just to evaluate the residual stray field and to understand how we can reduce it.

However, the comparison between the data extracted from Fig. 3.5.3 and the measured data, showed a satisfactory agreement.

Now we will report on some of the results of our simulations.

Table 3.5.3: Stray field of K800 vs. distance from cyclotron center.

Measured values		**Simulated values**	
Ia=1595,Ib=1155	B_0=4.2 T	Ia=1595, Ib=1155	B_0=4.2 T
R	B(R)	R	B(R)
4 m	115-120 Gauss	4 m	70 Gauss
5 m	50 Gauss	6.5 m	17 Gauss
7 m	25 Gauss	8 m	12 Gauss
11 m	6 Gauss	10 m	7 Gauss
17 m	2 Gauss		
20 m	1.3 Gauss		

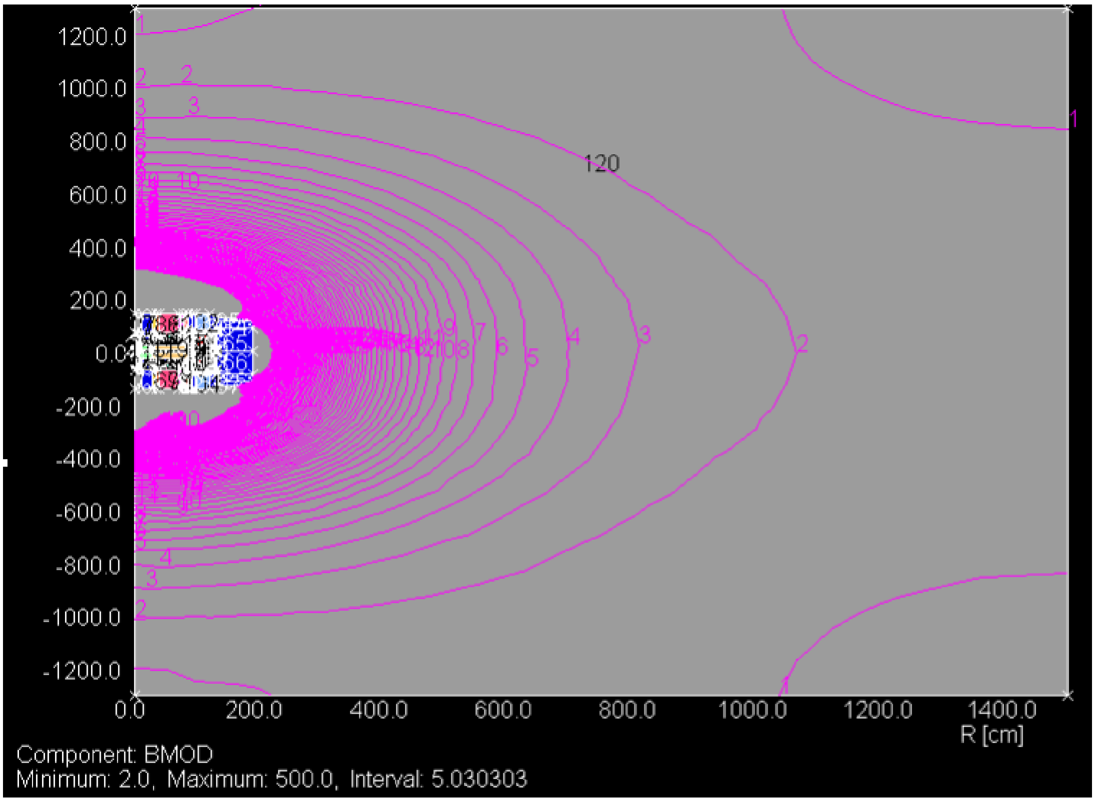

Fig. 3.5.3: Stray field of K800 simulated by TOSCA code. The magnetic field difference between the isofield line is about 5.03 Gauss. The isofield line n°1 is at 2 Gauss while n° 2 is at 7.03 Gauss.

Fig. 3.5.4 shows the stray field of the SCENT cyclotron; the density current in the coils being 43.3 A/mm^2. The pole sizes are R_{max}=250 cm and Z_{max}=140 cm. It is quite evident that the stray field does not match our previous specifications. The usual solution when decreasing the stray field is to increase the thickness of the iron yoke. But another solution is also feasible: a local shield placed near the control room and far away from the cyclotron can produce significant results with smaller amount of iron.

The use of a local shield could probably help to reduce the stray field. The local shield could consist of an iron bar placed inside the concrete shield.

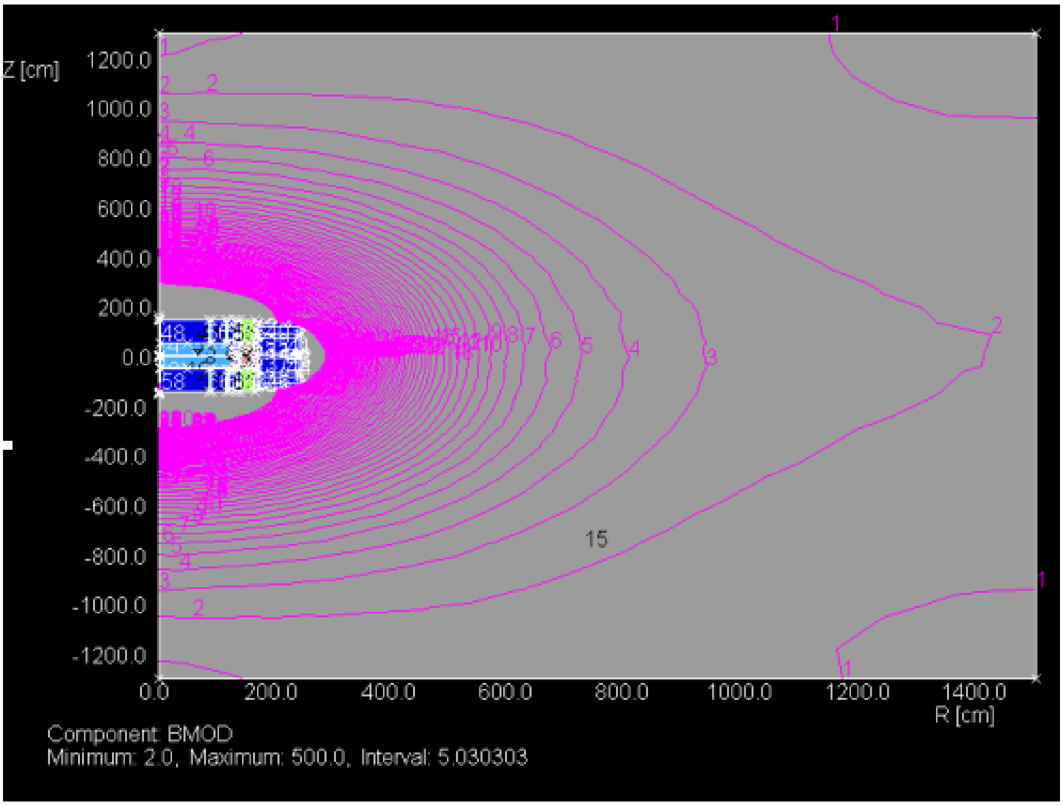

Fig. 3.5.4: Stray field of SCENT cyclotron: Pole size Z=145, R=245, J=43.3 A/mm^2. The isoline of 5 Gauss extends up to 14 m.

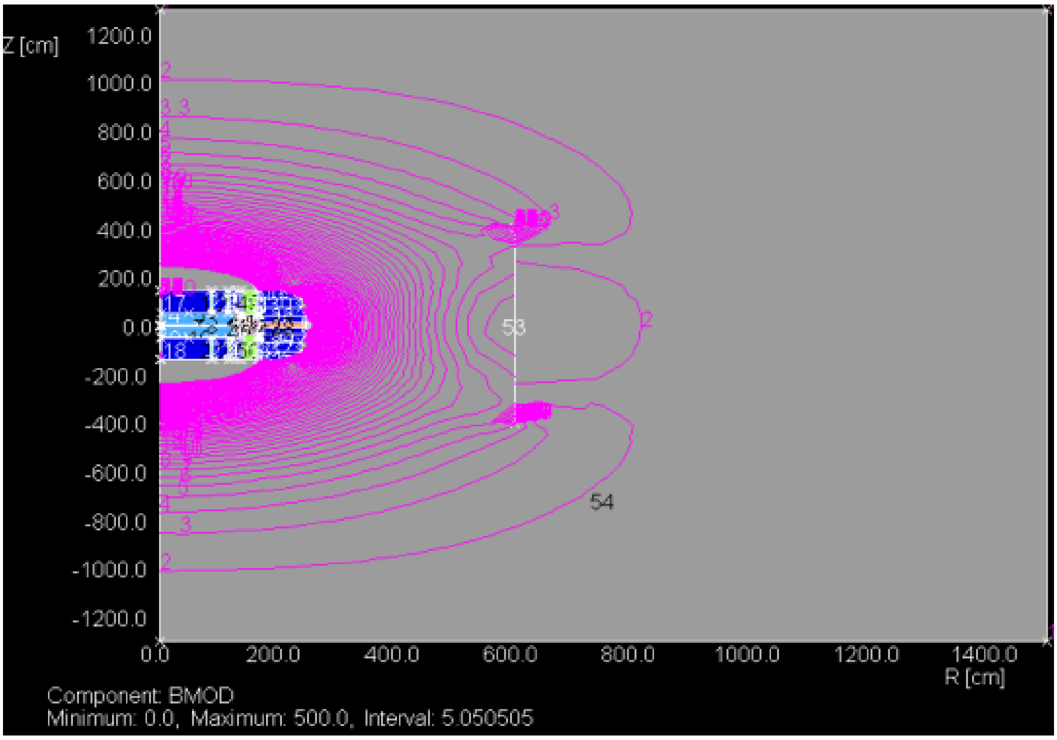

Fig. 3.5.5: Stray field of SCENT cyclotron. The cyclotron parameters are the same as in Fig. 3.5.4. A local shield at radius 6 m, 5 mm thick and ±4 m high, has been added. The isoline of 5 Gauss is stopped at radius 8 m.

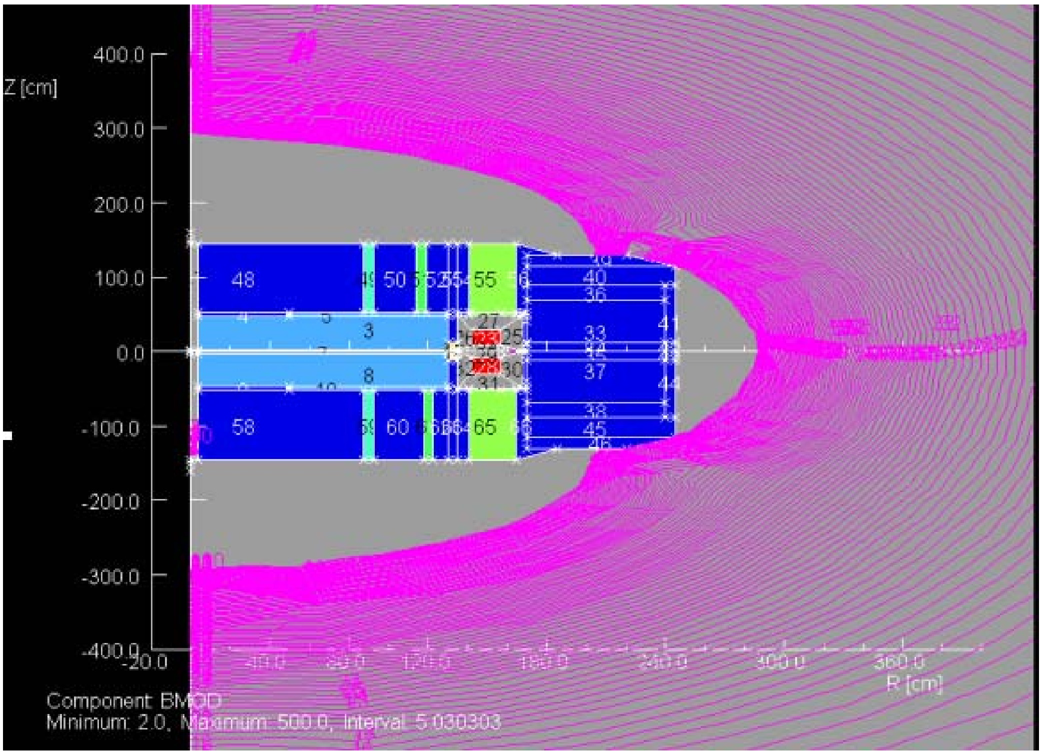

Fig. 3.5.6: Stray field around the SCENT cyclotron. The parameters are just the same as in Fig. 3.5.4.

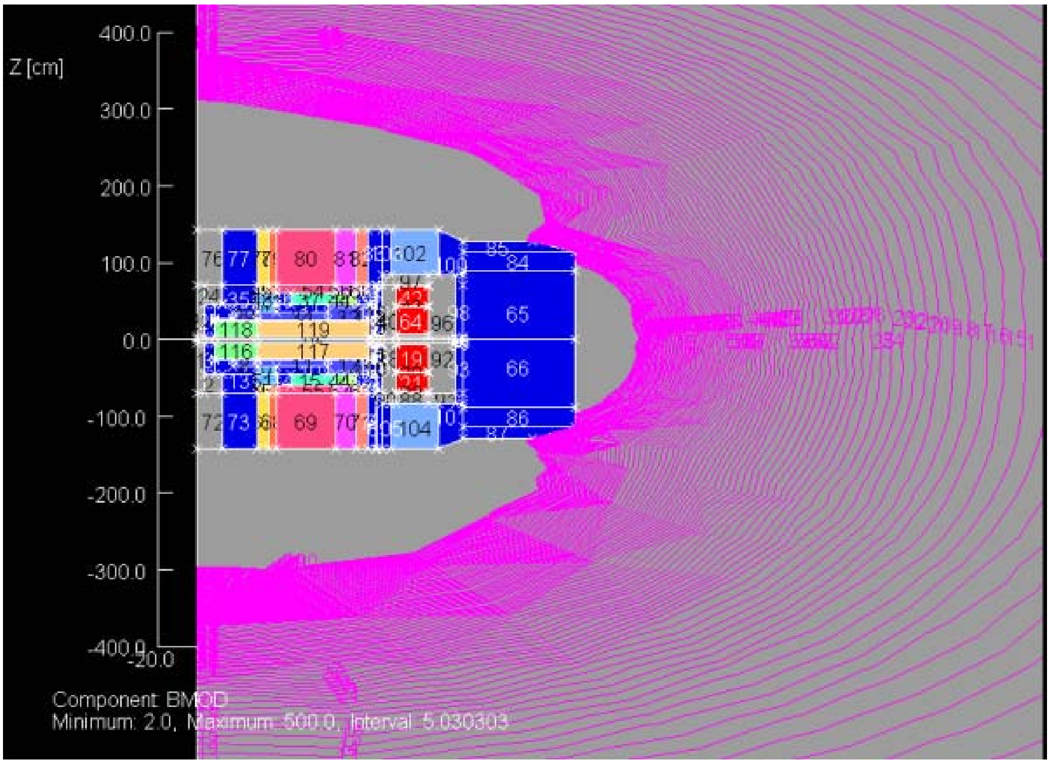

Fig. 3.5.7: Stray field around the K800 cyclotron. The magnetic field at the centre is 4.2 T.

If we compare the stray field around SCENT (see Fig. 3.5.6) isoline of 500 Gauss value, to the same isoline for the existing K800 (see Fig. 3.5.7), we see that SCENT has a lower stray field than K800. We have to remember that the simulations in Fig. 3.5.7 for the K800 are for a central magnetic field of 4.2 T and that this, in our experience, is the maximum field value that does not produce serious problems when operating all the other ancillary equipment.

Therefore, by installing turbo pumps and a compressor and by moving part of the cryo-pumps at a distance more than 3 m from the median plane, the stray field will be lower than 500 Gauss.

3.6 Superconducting coils

The useful text book for this subsection and for the following are [12,13].

3.6.1 Design guidelines

When performing the design of the cold mass of the superconducting cyclotron, we had to consider that the cooling system could not involve the use of cryogenic liquids (namely LHe), due to the negative impact they would have on the medical environment (because of the complexity of the operations). As a result, we have worked under the hypothesis of cooling the coil with 4-6 cryo-cooler, which can be operated very simply. Nevertheless, the impact on the magnet design is quite strong:

- due to the relatively low available cooling power at 4.5 K (a few Watts), we had to design a superconducting winding based on the method of indirect cooling. This means that the cooling system will be able to remove the limited heat loads (due to cryostat heat loss and to current leads), but it will not be able to protect the winding from thermal disturbances. The release of local energy for mechanical or electrical reasons will be recovered by the winding itself. This is not a new idea; the coils used in the detector for HEP are based on this criterion. In order to survive these localized disturbances, the winding will have a good enthalpy margin. Consequently, we had to keep the overall current density as low as the total temperature increase is within the limit. As a superconducting material, we chose NbTi because, in spite of the relatively low critical temperature (9.2 K), it is the most well-known material involved in superconducting magnets (Nb3Sn is too brittle, High Tc has not yet been developed at an industrial level);

- current leads are sources of dissipation. The maximum current was then set around 1 kA. This is also the minimum current to limit the number of turns and the coil inductance, which plays an important role in case of quench;
- since the winding is indirectly cooled, it is highly recommended to involve structural material with good transport thermal properties. As a consequence, aluminium alloy was implemented in the mechanical structure. In this case we can have a containing structure with high thermal conductivity (an advantage for the cooling) and thermal contraction not far from the winding (copper plus resin), so we can limit the mechanical stress. Of course, the aluminium will be a suitable alloy with excellent mechanical properties (high yield and tensile stress, good elongation).

3.6.2 Conductor definition

In order to choose the conductor, the protection criterion based on the hot spot temperature has been followed. Let us schematize the magnet as an inductance L_m protected by placing the resistance R_D in parallel. The current flowing in the circuit in operating conditions is I_{op}.

Let us consider that a small portion of the conductor becomes normal, with a resistance $r(T) << R_D$, and that the protection system opens the switch S in such a way that the magnet is disconnected from the power supply (see Fig. 3.6.1).

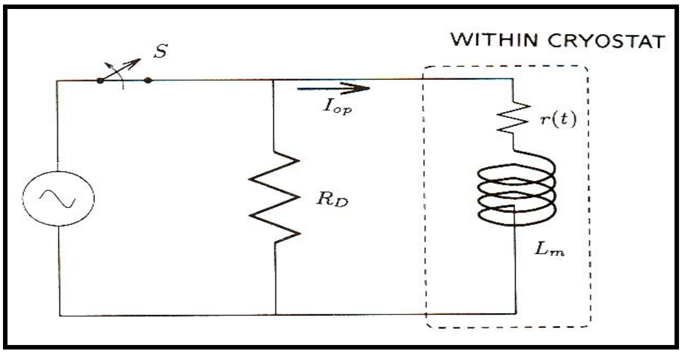

Fig. 3.6.1: Protection circuit of the magnet.

In these conditions, starting from a temperature T_i, the normal zone warms up to the temperature T_f, following the approximated relation:

$$\frac{1+\alpha}{2}\int_{T_i}^{T_f}\frac{C_p(T)}{\rho_m(T)}dT = Z(T_i,T_f) = \frac{1}{A_{Tot}A_m}\frac{I_{op}^2 L_m}{2R_D} \qquad (3.6.1)$$

where $C_p(T)$ e $\rho_m(T)$ are respectively the specific heat and the matrix resistivity as a function of the temperature, A_{sc} is the area of the superconductor, A_m is the area of the copper matrix, A_{iso} is the area of the insulation, $A_{tot}=A_m+A_{sc}+A_{iso}$ is the total area of the conductor and finally α is the ratio between the area of the conductor excluding the insulation and its total area.

Introducing the coefficients $\lambda=A_m/A_{sc}$ and $\lambda_1=A_{iso}/A_{sc}$, we find that $A_{tot}=A_{sc}(\lambda+\lambda_1+1)$. Finally:

$$\alpha = \frac{A_m + A_{sc}}{A_{tot}} = \frac{\lambda+1}{\lambda+\lambda_1+1}, \quad \text{so that} \quad \lambda_1 = (1+\lambda)\frac{1-\alpha}{\alpha} \qquad (3.6.2)$$

The $Z(T_i,T_f)$ function is shown in Fig. 3.6.2 for several materials.

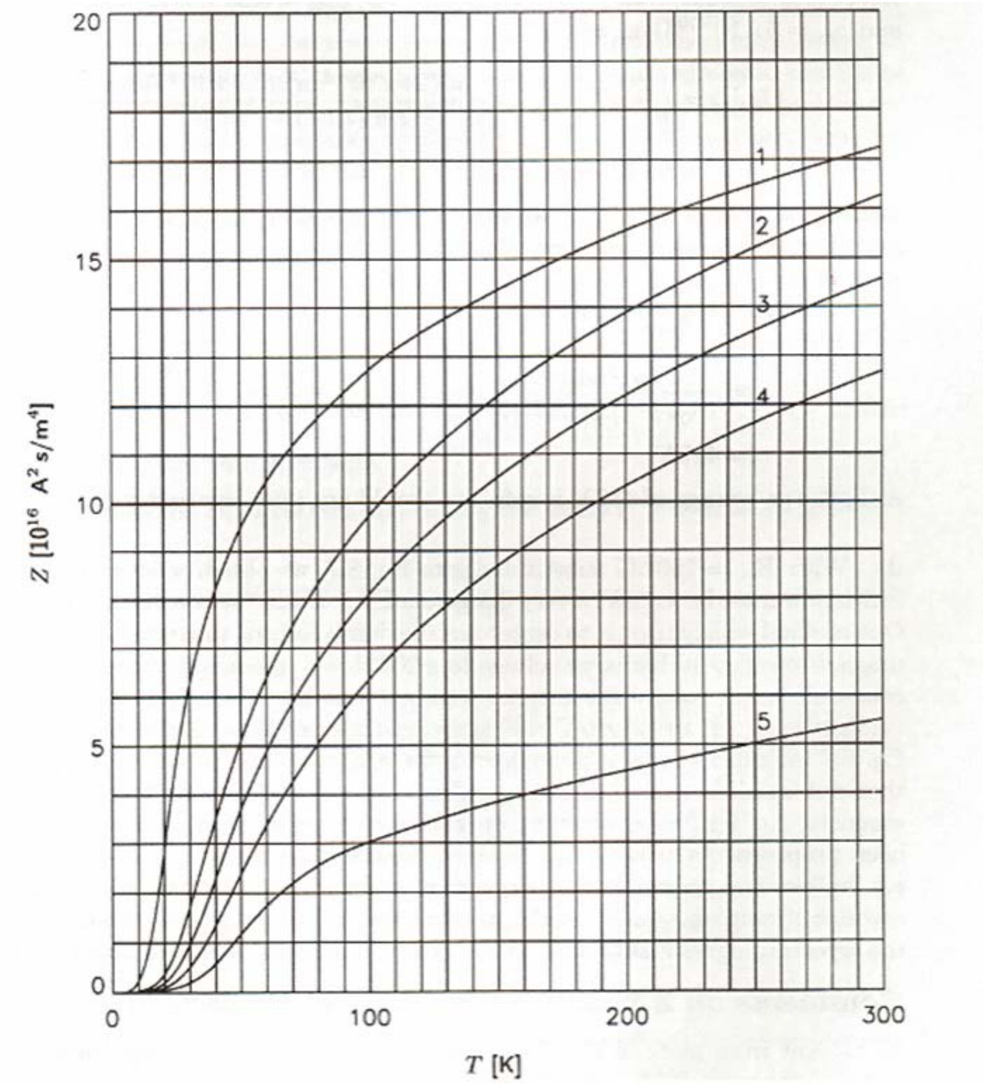

Fig. 3.6.2: $Z(4.2, T_f)$ function for several materials: 1) silver 99.99%; 2) copper RRR 200; 3) copper RRR 100; 4) copper RRR 50; 5) aluminium 99.99%.

Let us introduce some parameters: the magnetic energy $E=\frac{1}{2}LI_{op}^2$, the maximum voltage in case of quench $V=R_D I_{op}$, the critical current density at the maximum field on the conductor $J_c(B_{max})$ and the ratio between this last parameter and the current density in the superconductor in operating conditions $g=J_c(B_{max})/J_{op}$. Relation (3.6.1) can be rewritten as:

$$A_m=\frac{E}{VZ(T_i,T_f)}\frac{2\alpha}{g(1+\alpha)(1+\lambda)}J_c(B_{\max}) \qquad (3.6.3)$$

It is worth noting that the magnetic energy is determined by the dimensions of the magnet and the operating magnetic field, whilst the maximum voltage and the Z function are partially arbitrary and connected to the safety. The critical current density at the maximum field is fixed, so that only the parameter λ and the cross sectional area of the copper matrix will descend from the operating conditions of the system and from our choices.

As regards the overall current density, its value is typically less than 100 A/mm^2 (for instance, it is 31 for the CMS magnet and 45 for the Babar magnet). In order to have a satisfactory enthalpy margin (see introductory notes), let us set this value to 50 A/mm^2, so that:

$$J_{op}=\frac{I_{op}}{A_{tot}}=\frac{J_c(B_{\max})\alpha}{g(1+\lambda)}=50\ \text{A/mm}^2 \qquad (3.6.4)$$

Then we can choose to have a wide stability margin, for instance ¼ of the critical current, setting g=4. Knowing that B_{max}=3.8 T, Jc(B=3.8 T, T=4.5 K)≅3100 A/mm^2 (see Fig. 3.6.3) and typically α=0.73, we find λ=10.

Finally, we can choose a protection voltage V=1000 V and $Z(T_i=4.5,T_f=300)=$ $=1.25\cdot10^{17}$ A^2 s/m^4 (supposing we have an RRR 50 copper matrix and limiting the hot spot temperature to 300 K). Knowing that E=32 MJ, we obtain from the relation (3.6.3) A_m=15.22 mm^2.

It is now possible to calculate the area of the superconductor $A_{sc}=A_m/11$=1.38 mm^2 e and the operative current $I_{op}=A_{sc}\cdot$Jc(B=4.7 T, T=4.5 K)/g=1070 A.
The inductance is $L=2\ E/I_{op}^2$=56 H.

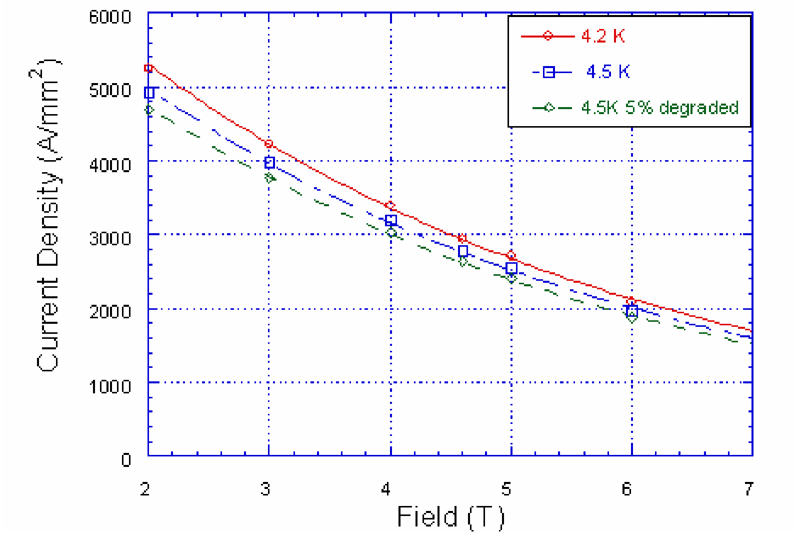

Fig. 3.6.3: NbTi critical current density.

3.6.3 Conductor layout

The total section of the conductor is $A_m+A_{sc}=15.22 +1.38=16.6$ mm^2.

A reasonable layout is a Rutherford cable composed of 14 filaments, 1.25 mm in diameter, leading to the overall dimensions 2.3 × 8.5 mm^2 (considering a packing factor of 87%).

The main characteristics of the conductor are summarized in the Table 3.6.1.

Table 3.6.1

Main characteristics of the conductor	
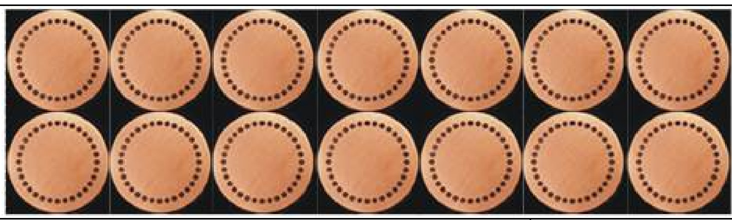	
Conductor overall dimensions (non-insulated)	2.3 × 8.5 mm^2
Conductor overall dimensions (insulated)	2.6×8.8 mm^2
Stabilizer	Copper
Strand diameter	1.25 mm
Filament diameter	50 μm
Number of strands	14 multifilamentary
Strand twist pitch	1.5 cm
Cable twist pitch	5 cm
Cu/Sc ratio	10
Cable Critical Current @ 4.2 K and 5 T	3250 A
Virgin Strand Critical current @4.2 K and 5 T	270 A
Sharing temperature @ 1070 A	6.9 K

3.6.4 Load line and stability

The magnet load line is shown in Fig. 3.6.4. At the maximum field 3.8 T, the critical current is 4280 A (=1070×4 as we set it). The sharing temperature, that is the temperature at which the current starts flowing in the copper matrix, is 6.9 K. This means that there is a temperature margin of 2.4 K with respect to disturbances or heating of the cold mass, corresponding to a heat input of 0.35 J/kg (43 mJ/m).

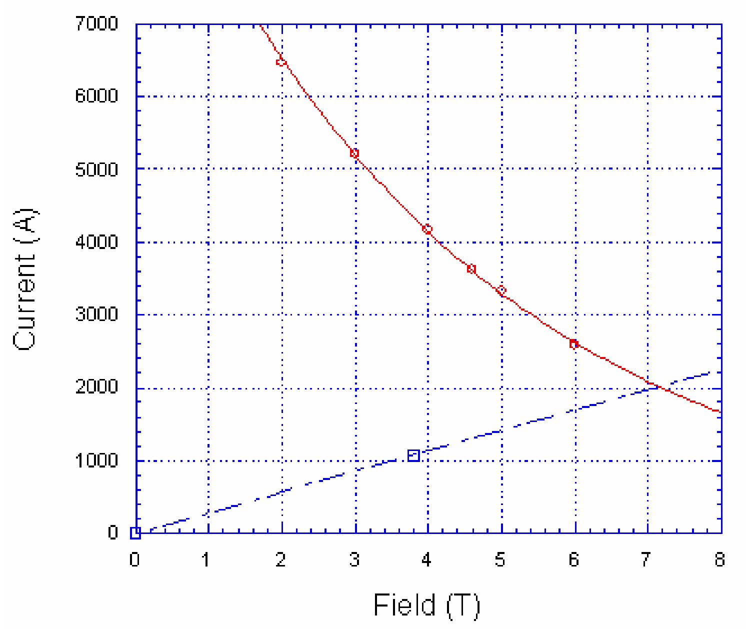

Fig. 3.6.4: Load line and critical current at the maximum field 3.8 T.

3.6.5 Magnet design

The designed dimensions of the two solenoids are the following:

R_i=1.42 m, R_e=1.57 m, h=0.21 m, d=0.85×2=1.7 m,

where R_i is the inner radium, R_e the outer radius, h the height and d the axial distance.

Considering that the coils have to be wound with a conductor 2.6×8.8 mm^2 in section, the real dimensions will be slightly different from the ones designed:

- number of layers=150/2.6=57.7→58.
- number of turns per layer=210/8.8=23.9→24.

The total length of conductor will be: 58×24×2π×1.495=13080 m.

This conductor can be reasonably supplied in 5 lengths, 2700 m each. As the joints cannot be immersed in the winding, it follows that the number of layers has to be divisible by 5. The result is a winding made up of 60 layers (156 mm in thickness), with 24 turns per layer (211.2 mm in height). The total length of the conductor is then 60×24×2π×1.498=13560 m (supplied in 5 lengths, 2.75 km each).

3.7 Forces on the coils

The magnetic analysis shows that on each coil there is a total radial force F_r=24.5 MN (corresponding to a radial pressure of 13 MPa), and a total axial force F_z=11.3 MN (in the sense that the coils get compressed one against the other). Let us consider the effects of these two forces separately.

3.7.1 Radial pressure

It can easily be shown that in a thin solenoid, radial pressure results in a circumferential stress given by $\sigma_T = \frac{\Pr \cdot R}{\Delta R}$, where Δ*R* is the winding thickness (156 mm). Replacing *R* with the outer radius (1.576 m), it can be found that σ_T=130 MPa. Obviously, this stress value cannot be self-sustained by the winding alone; an external supporting cylinder is necessary. The best material for this use is the aluminium alloy 5083, due to its good mechanical properties and for thermal reasons, as its high thermal conductivity allows for indirect cooling.

Let us try to find the minimum thickness of the supporting cylinder. If ε_W is the strain in the winding, $\varepsilon_W=\sigma_W/E_W$, where σ_W e E_W are respectively the stress and the Young modulus of the winding (E_W=11010^9 Pa). For symmetry reasons, the containing cylinder will have the same strain as the winding: $\varepsilon_c=\varepsilon_W$; the stress in the cylinder, σ_c, will then be given by: $\sigma_c = E_c \cdot \varepsilon_w = E_c \cdot \sigma_w / E_w$, where E_c is the Young modulus of the cylinder ($E_c=80\cdot10^9$ Pa).

On the other end, $T=\sigma_c \Delta R_c + \sigma_w \Delta R_w = \Pr \cdot R$ where ΔR_W and ΔR_c are, respectively, the thickness of the winding and of the cylinder. By imposing a maximum stress on the winding of 100 MPa, it can be found that:

$$\Delta R_C = \frac{E_W}{E_C}\left(\frac{\Pr}{\sigma_W} R - \Delta R_W\right) = 67\ mm \qquad (3.7.1)$$

Considering the limited room available for the whole magnet, ranging from 1.35 m to 1.7 m in radius, the best configuration is shown in Fig. 3.7.1: there is a 15 mm thick inner cylinder (where the magnet is wound), and a 40 mm thick outer cylinder leading to a total thickness of 55 mm. Using relation (3.7.1), it can be found that the corresponding stress on the winding increases up to 110 MPa, as is confirmed by the finite element calculation shown in Fig. 3.7.2.

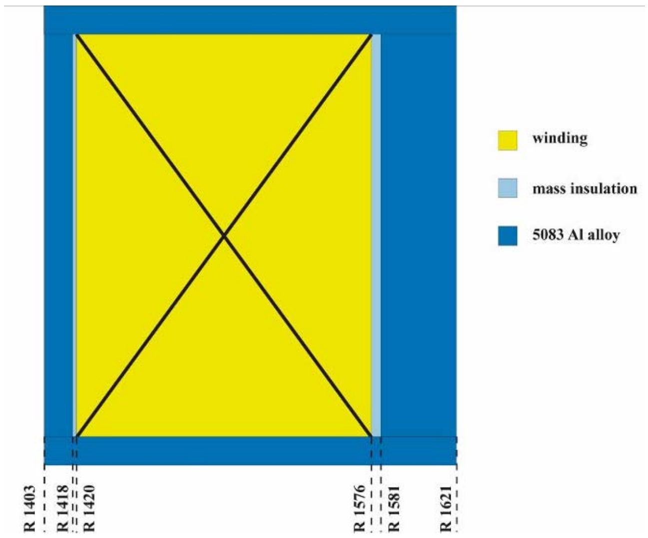

Fig. 3.7.1: Mechanical configuration of the coils.

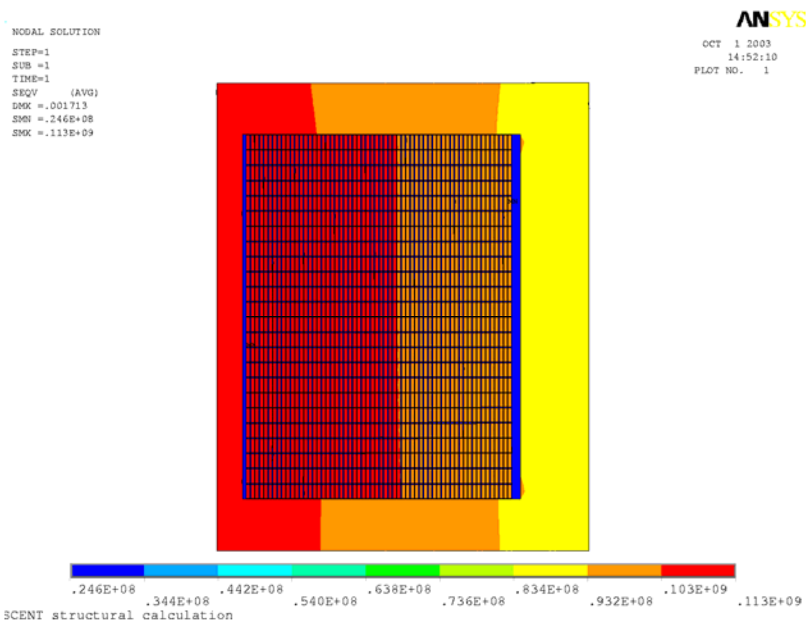

Fig. 3.7.2: Circumferential stress due to a radial pressure of 13 MPa.

3.7.2 Axial force

The axial force tends to compress the two coils one against the other with a force of about 1200 tons. We are considering the possibility of inserting a certain number of stainless steel supports between the two coils. However, it will be necessary to introduce an axial suspension system to be integrated with the suspension system of the coils inside the cryostat.

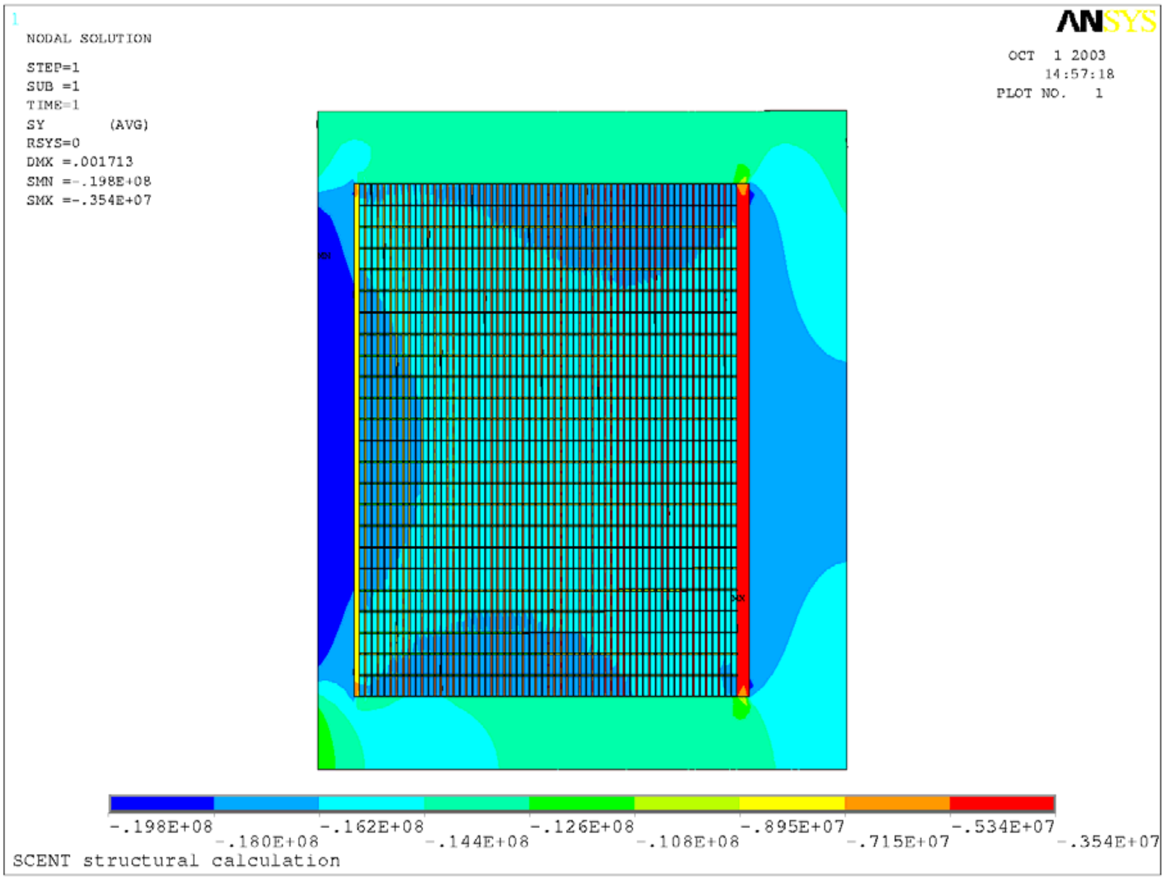

Fig. 3.7.3: Axial stress due to a force of 11.3 MN.

3.8 References

[1] H. Blosser et al., k1200 MSU, Proc. XI Int. Conf. on Cyc. and their Appl., Tokyo (1986), p. 157.

[2] J. J. Livingood, *"Principles of Cyclic Particle Accelerators"*, D. Van Nostrand Comp., (1961).

[3] W. Schaerf, *"Particle Accelerators and their Uses"*, Harwood Academic Publisher (1986).

[4] CAD CODE used to design, AUTOCAD version 2000, www.autodesk.it.

[5] T. Stambach, Cern Accelerator School 1996, LaHulpe, (1994) p. 113.

[6] Y. Jongen and S. Zaremba, Cern Accelerator School 1996, LaHulpe, (1994) p. 140.

[7] M. M. Gordon, *"Computational of Closed Orbits and Basic Focusing Properties for Sector-Focused Cyclotrons and the Design of CYCLOPS"*, Particle Accelerators, Vol. 16, p.39-62, (1984).

[8] GENSPE Code, NSCL-MSU.

[9] OPERA, Vector Fields http://www.vectorfields.com.

[10] G. Bellomo and F. Resmini, IEEE Trans. On Nuclear Sci. NS-26, (1979) p. 2095.

[11] Guide to solving AC power EMF problems, http://vitatech.net/eng_guide.htm.

[12] Martin N. Wilson, *"Superconducting Magnet"*, Oxford Science Publication.

[13] Yukikazu Iwasa, *"Case studies in superconducting magnets"*, Plenum editor.

Chapter 4. RF system

4.1 Dee shapes

Superconducting cyclotron RF systems typically work in the frequency range 10-50 MHz and need big apertures in the pole to house the vertical stems. The cavities are half-wave resonators, practically symmetric with respect to the median plane, characterised by strongly spiralled electrodes (Dees). In the case of the SCENT machine, whose pole diameter is 132.5 cm, the size of the Dees is large and we searched for a solution which allows us to house the resonators inside the valleys. The available depth in the valley is of ±45 cm respect to the median plane. For this reason and to maximize the energy gain per turn we chosen to drive the RF electrodes with the 4^{th} harmonic, which means about 93 MHz.

The energy gain ΔE per cavity in a cyclotron can be written as:

$$\Delta E(\phi, \Delta\theta) = qV_0\left[\sin(\phi) - \sin(\phi + h\Delta\theta)\right]$$

where $\Delta\theta$ is the geometrical width of the cavity's electrode, V_0 is the maximum voltage, q is the charge of the particle to be accelerated and h is the RF harmonic number respect to the revolution frequency of the particles. The sign minus in the second term takes account of the reversal direction of the electric field along the two accelerating gap of the cavity. For each value of the cavity width $\Delta\theta$ there is a particle with phase ϕ which gains a maximum of energy.

The maximum voltage gain through the cavity depends by $\Delta\theta$, and for the 2^{nd} or 4^{th} harmonic mode we have respectively:

$$V_{M2} = V_0\left[(\sin(\pi\text{-}\Delta\theta) - \sin(\pi+\Delta\theta)\right]$$

$$V_{M4} = V_0\left[(\sin(\pi\text{-}2\Delta\theta) - \sin(\pi+2\Delta\theta)\right]$$

In Fig. 4.1.1 the maximum voltage gain per cavity vs. $\Delta\theta$ for the two cases of a cavity driven in harmonic 2^{nd} and 4^{th} respectively is shown.

It is quite evident that if the geometrical width of an electrode is shorter than 60°, then the 4^{th} harmonic is advantageous over the 2^{nd}. This advantage is in general counterbalanced by the higher power losses which occur in a cavity driven at a higher frequency, and are scaled proportionally to the square root law of the frequency ($\sqrt{f}$).

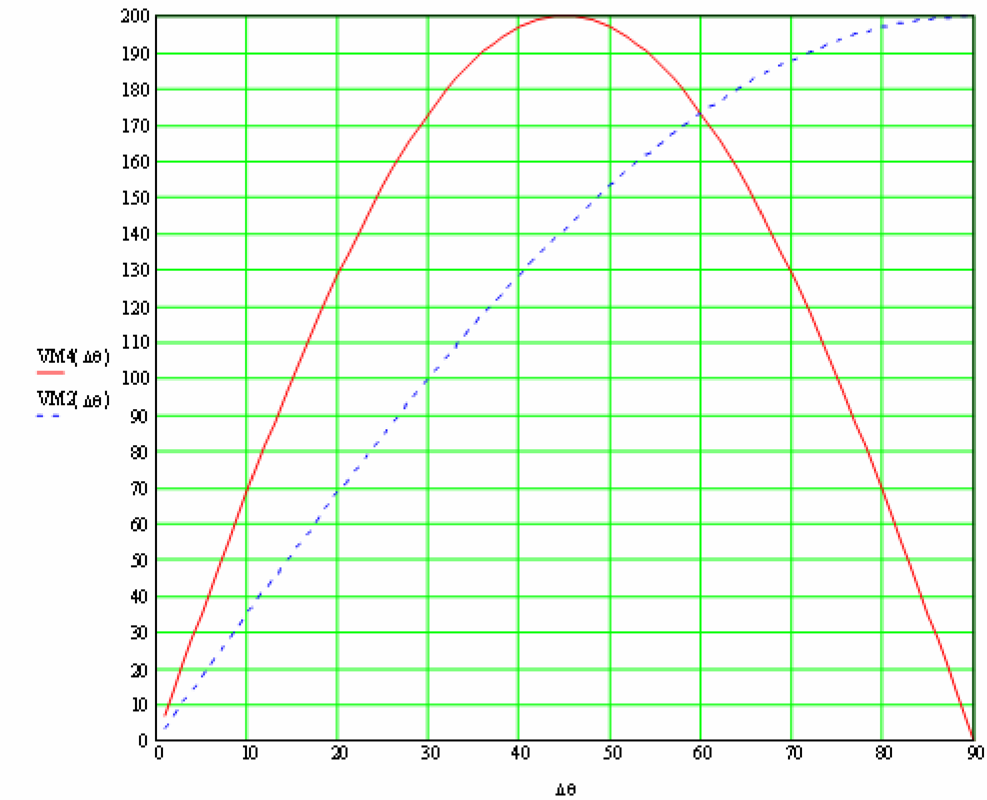

Fig. 4.1.1: Maximum voltage gain per cavity vs. Δθ, harmonic 2nd and 4th.

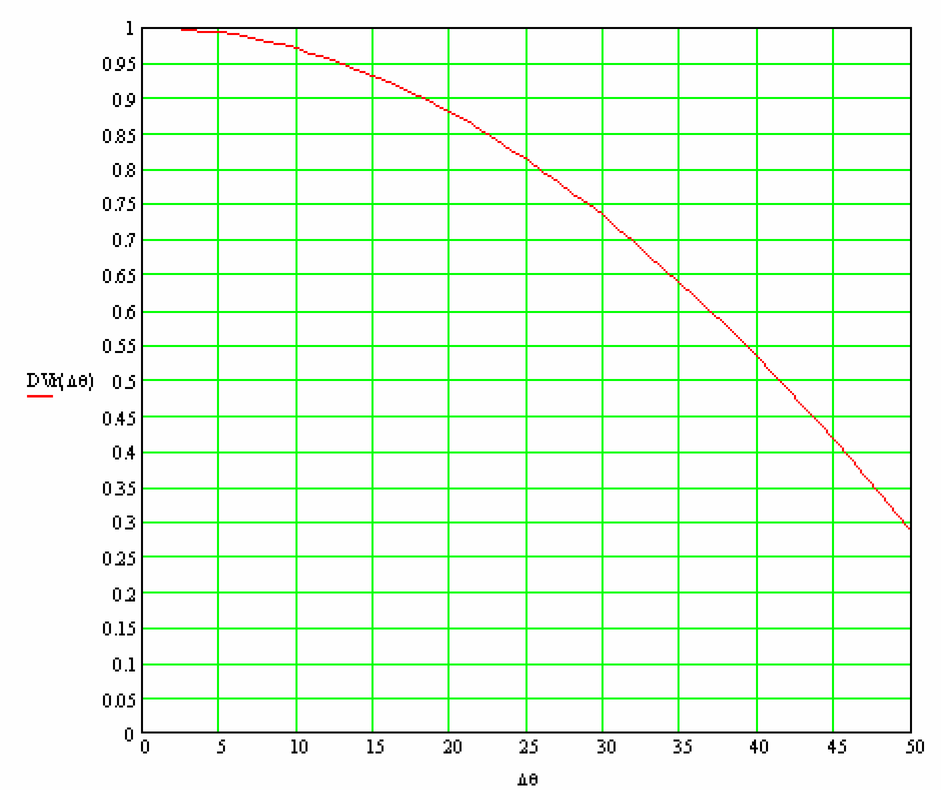

Fig. 4.1.2: Normalized difference between Maximum voltage gain per cavity of harmonic 4th and 2nd vs. Δθ.

In Fig. 4.1.2 the difference between V_{M4} and V_{M2} normalized to V_{M2} is shown, $DV_n(\Delta\theta)=[V_{M4}(\Delta\theta)-V_{M2}(\Delta\theta)]/V_{M2}(\Delta\theta)$.

While in Fig. 4.1.3 the ratio $Vr(\Delta\theta)=V_{M4}(\Delta\theta)/V_{M2}(\Delta\theta)$ is shown.

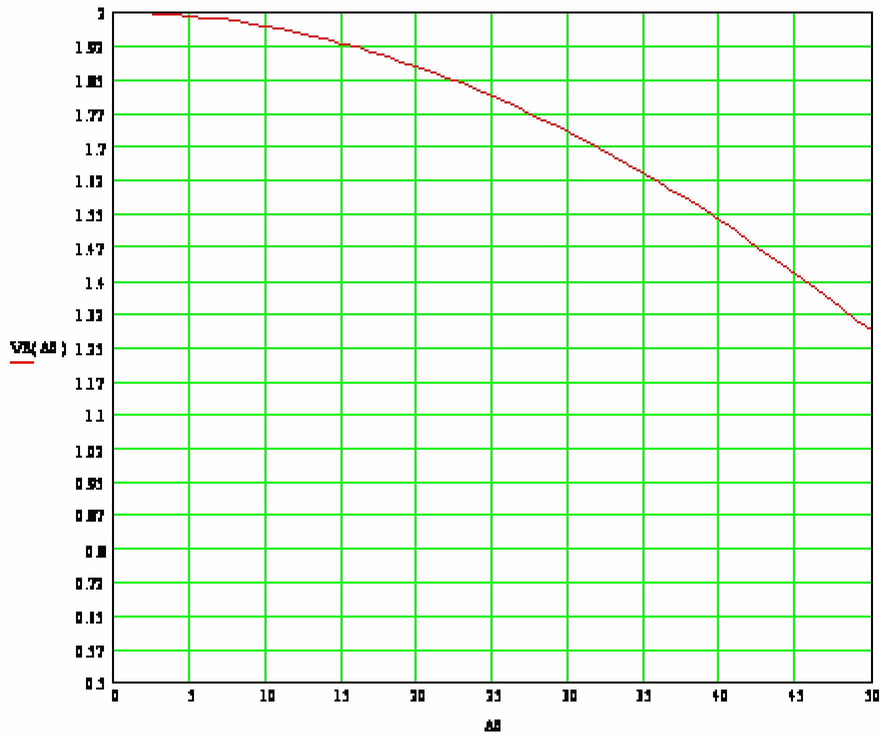

Fig. 4.1.3: Ratio $Vr(\Delta\theta)$ between maximum voltage gain per cavity of harmonic 4th and 2nd vs. $\Delta\theta$.

It is evident that in a 4-sector cyclotron the width of the valley is about 45°, but that the effective width of the electrode will be smaller than this value (as we will see later) and that this width also decreases to the shape of the electrodes, which present a large spiral angle. In our case, the mechanical width of the RF cavity electrode is about 23° at the extraction region. In accordance with the plot in Fig. 4.1.2. and assuming we can excite the cavity at the maximum voltage V_0, the use of the 4^{th} harmonic allows us to achieve an 82% energy gain more than in the case of the 2^{nd} harmonic. Indeed, the power losses are scaled to the square of the voltage, so this means a reduction in power loss higher than about factor 2.4 (the higher losses due to the law $\sqrt{f}$ have been considered). Moreover, the use of the 4^{th} harmonic allows us to drive the 4 cavities with the same phase.

The disadvantages of operating in the 4^{th} harmonic are:

- a more precise isochronisms requirement
- higher losses due to the law of $\sqrt{f}$

which means roughly 40% extra power required to achieve the same voltage. Moreover, as we shall see, the solution of the 4^{th} harmonic allows us to achieve voltage distribution along the acceleration gap increasing with the radius; this is very useful in minimizing the beam losses at the extraction.

To minimize the risk of discharges, voltages lower than 70 kV are required in the central area, while voltages around 120 kV or higher are required at the outer radius to achieve adequate separation among the particles as they orbit at the extraction region. Due to the strong spiral angle, the equivalent length of the electrode is around 2.5 m which results in an electric capacity of about 200 pF. In order to control the radial voltage distribution and to obtain the required resonant frequency then, a multi-stem configuration is the only feasible solution [1,2].

4.2 The modelling method: the multistem approach

For simplicity's sake, we will consider the median symmetry plane and talk about quarter-wave resonators (QWR). A multi-stem QW resonator can in principle be modelled as several parallel QWRs, each one having the same eigen-frequency whose field distribution stays almost unchanged if they are coupled in such a way that they do not interact with each other. This is feasible when the stems are far enough apart, and each QWR is simulated with the proper boundary conditions, as we shall see later.

Each QWR consists of one stem, charged on one section of the electrode. Such a structure usually has a voltage distribution with a minimum near the stem base, increasing towards the Dee extremities. In order to ensure that each QWR resonates at the same resonant frequency and to find an arrangement such that the whole structure remains electro-magnetically stable, the diameter and the position of the stem on the Dee have been parameterised and optimised separately. The best position was sought in order to maximize the local quality factor (Q) and minimize the magnetic interaction with the adjacent sub-systems. Once the position had been determined, the diameter of the stem was increased in order to attain the required resonant frequency. Because the coupling between sub-systems is very low, combining them produces an entire structure resonating at the fixed frequency; one that is optimised so that all of Q is maximized. Moreover, the combination of two or more sub-structures like this, gives a voltage distribution where the adjacent maxima join in a plateau as no current has to flow in either direction.

By cutting the Dee into sections of different length, it is possible to obtain several different profiles, where the lower voltage corresponds to the minimum of the section with higher capacity.

To simulate each section with the proper boundary conditions, we tested two different solutions, both giving comparable results. In the first case, a magnetic symmetry condition is set among two adjacent stems as shown in Fig. 4.2.1. This method greatly reduces the number of mesh cells. In the second case, tested on a simplified structure, each stem with its section of Dee is simulated in the whole cavity volume.

In both cases the stem position and diameter are adjusted in order to obtain the required voltage distribution and frequency. For this last adjustment, we know that, lowering the cut frequency of each portion arises the local voltage level. Then the whole structure is simulated using the geometry found in this way, and few local adjustments are done to compensate the effects of the method's approximations.

At least one simulation of the whole volume is required to check the position of other resonant modes that must be not too close. In the case of a 3-stem structure, for instance, the two nearest modes typically have voltages of opposite sign on the Dee extremities, or lower voltages on the extremities than on the central part.

By means of such a method it should be possible to optimise resonator with three or more stems. Increasing number of stems improves the control of the voltage distribution along the gap, but it could harm the performances of the cavities in terms of losses and power consumption. Indeed, increasing the number of stems, in order to maintain the frequency value, the diameter dimension will be smaller, reducing the lateral surface of the cylinder. Because of the currents flowing through the surfaces of the stems, the local power density could increase although the current value is reduced. The choice of two, three or more stems, depends on the geometric structure of the cavity and on the voltage profile desired.

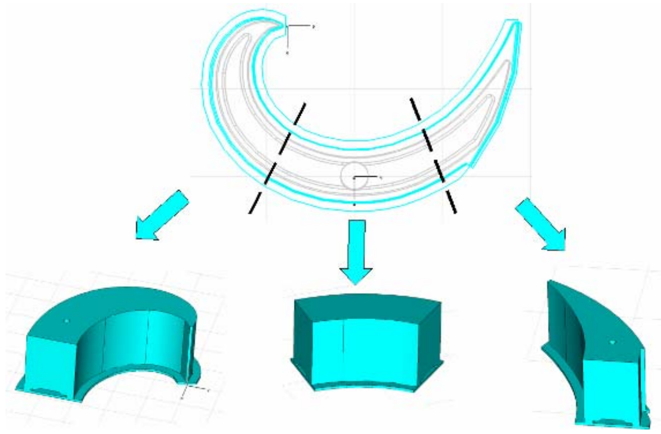

Fig. 4.2.1: Example of cavity subdivision. Normal magnetic boundaries are selected on the vertical surfaces.

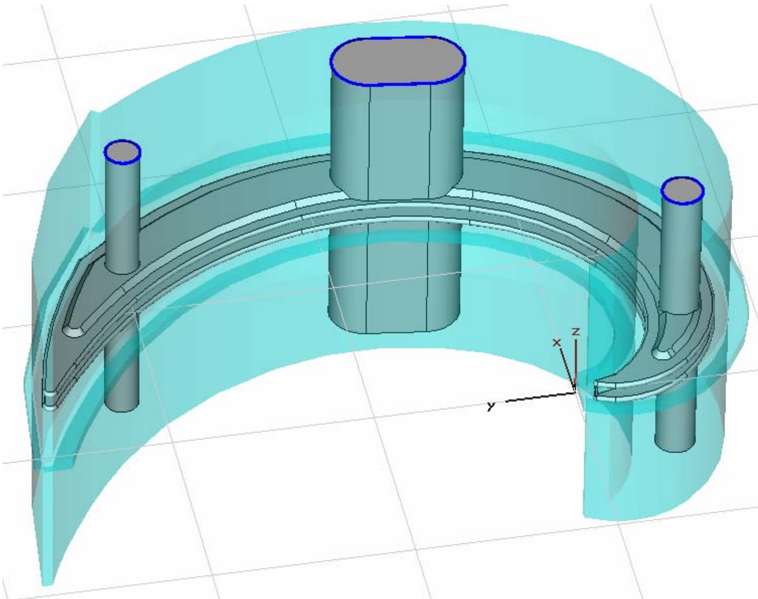

Fig. 4.2.2: Layout of the cavity.

4.3 The cavity geometry

As regards the cavities we expect to use in SCENT, in order to attain the high resonant frequency, we have been forced to insert at least three stems. Thus, we have chosen to have higher electrode voltages on the inner and outer extremities and to keep a lower voltage in most of the Dee, in order to optimise the shunt impedance. By applying the above-described method, we have obtained the resonator shown in Fig 4.2.2. The large central stem (low inductance) concentrates the currents coming from most of the electrode, while the two lateral ones (high inductance) resonate with the much smaller capacitances of the Dee extremities.

The total height of the half-wave cavity is 80 cm, while a vertical aperture of 30 mm along the median plane is left for the beam. In order to reduce the Dee capacity and the electric field, the acceleration gap size ranges from 1.5 cm at inner radii to 6 cm at the outer end. The electrode's angular width gradually increases up to 39 degrees near to the first stem, then it is rather constant in the proximity of the main stem and decrease down to 23 degrees at full radius (see Fig. 4.3.1).

The three stems are centered at radii 30, 90 and 120 cm. Their diameters being 8.6 cm for the external stem and 10 cm for the internal stem. The main stem extends 32 cm radially and 18 cm azimuthally.

To prevent sparking at regions of high surface electric field, we have adjusted the nose shape and gap length so that the surface electric fields do not exceed the Kilpatrick field limit.

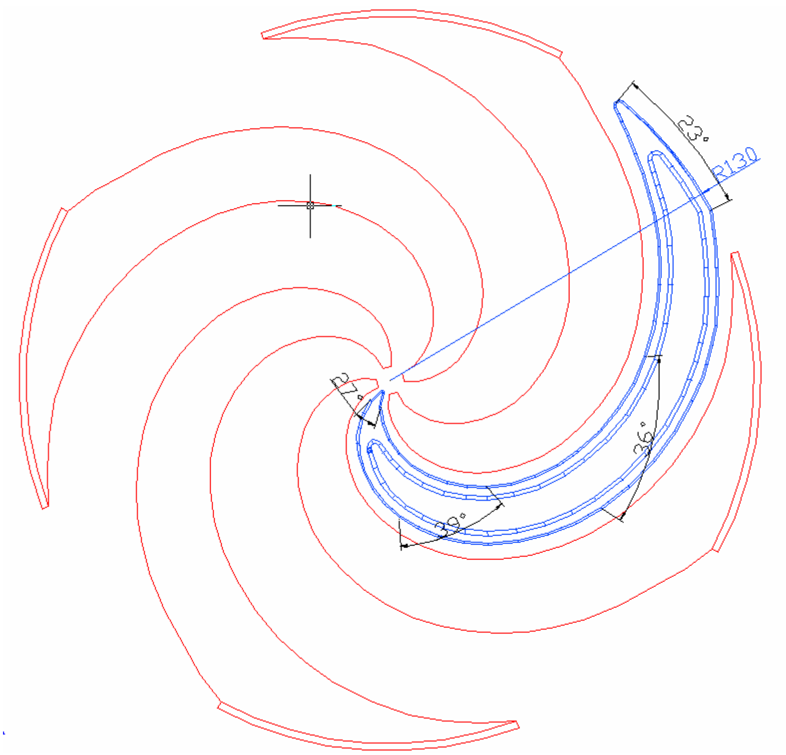

Fig. 4.3.1: Layout of a Dee between the poles.

4.4 RF simulation results

The simulations have mainly been performed with the eigenmode module of CST Microwave Studio (MWS) [3] and Table 4.4.1 reports the calculated parameters. The mean effective voltage distribution, going from 60 kV in the injection region to a peak value of

120 kV in the extraction region, is shown in figure 4.4.1. The values are obtained by integrating the electric field profiles across the gaps in the median plane of the cavity: it has to be noted that, due to the reduced width of the electrode in the injection region, the transit time factor is there very low.

Table 4.4.1

Parameters	**Value**
Resonance frequency	~ 93 MHz
Voltage range	30-160 KV
Quality factor	~ 8500
Max power density	16 W/cm^2
RF Power	~ 45 KW
E Max	10 MV/m
Mode 2	98 MHz

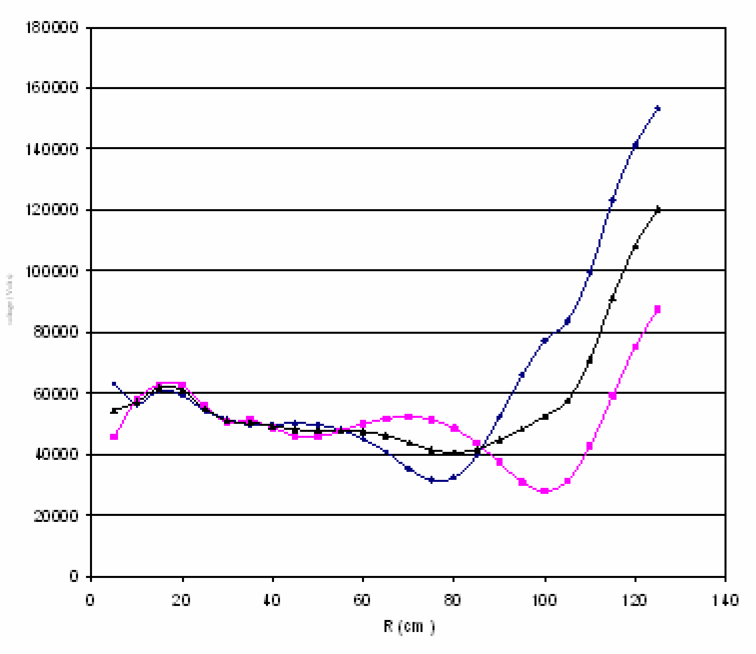

Fig. 4.4.1

Loss calculations were also carried out with the SOPRANO code [4] and compared with the MWS results in Table 4.4.2. The data did not show remarkable difference between the results of the two codes. Power losses did not exceed the 44 kW per cavity at 120 kV of maximum average voltage (160 kV of peak). To take into account the surface roughness and the average working temperature, the copper conductivity has been set as $5.0 \cdot 10^7$ S/m (instead of $5.8 \cdot 10^7$ S/m). We have neglected the quality of the contacts and the beam loading effect (the current of the beam accelerated is relatively low). The current distribution on the Dee surface is shown in Fig 4.4.2, which shows very clearly how the different sections interact with the stems and how the currents are well split next to the cuts previously made for optimising each sub-system. The currents, coming from the large radii, gather along the gaps towards the stem and heat the electrode along the gap. The maximum current density is about 69 A/cm and is located on the edges of the two gaps near the external stem. In this region the maximum power density is estimated at 16 W/cm^2, for an average maximum voltage of 120 kV (see Fig. 4.4.3). High currents are also visible at the base of the external stem, requiring special care for the connection to the electrode.

Table 4.4.2: Comparison between losses calculated with SOPRANO and MWS for different cavity elements.

	SOPRANO [kW]	**MWS** [kW]
LINER	7.50	7.60
DEE	4.40	7.33 (Dee + main stem)
INTERNAL STEM	2.14	1.87
EXTERNAL STEM	4.87	5.25
MAIN STEM	1.76	
TOT **for 120 kV@130 cm**	**20.67**	**22.05**
Total losses per cavity	**41.34**	**44.10**

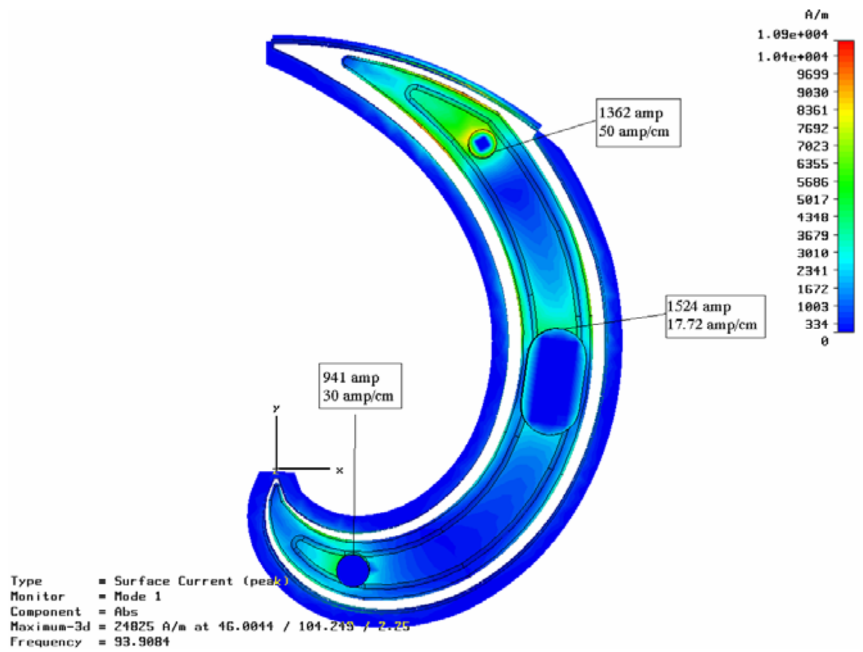

Fig. 4.4.2: Current distribution on the Dee; current values at the short-circuit plate are given in boxes.

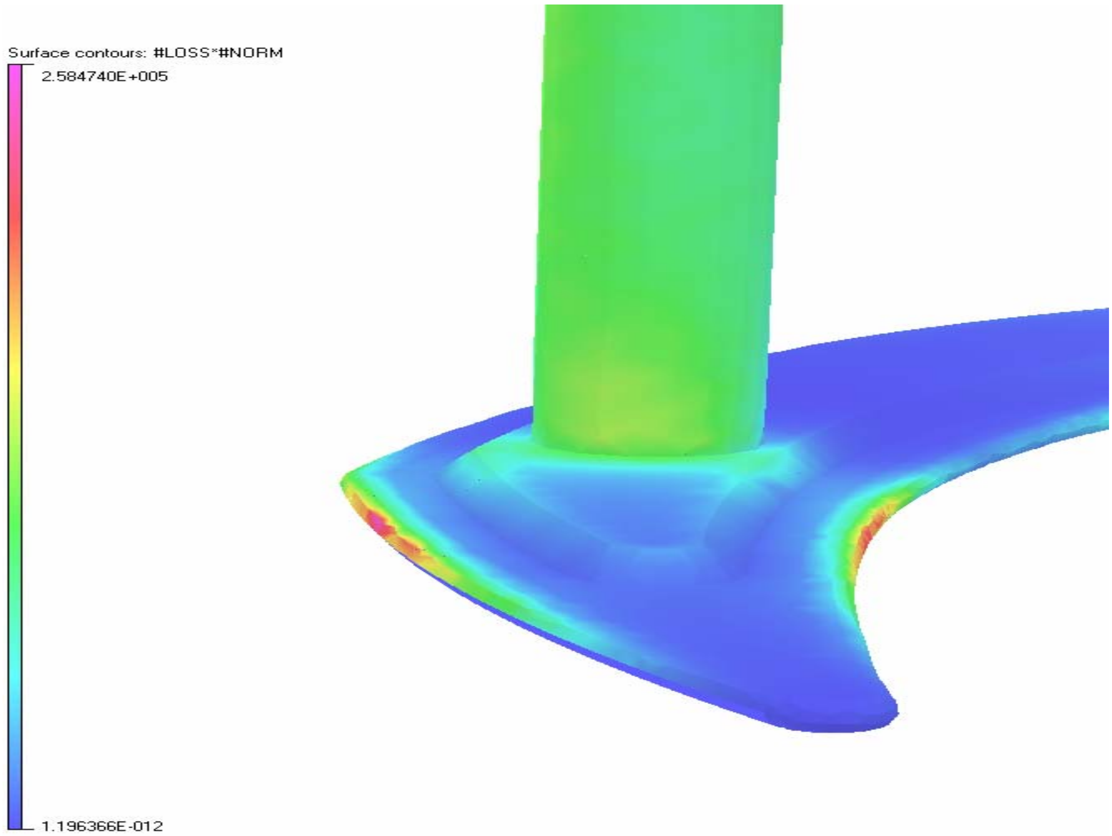

Fig. 4.4.3: Power density distribution (W/m^2) for 150 kV of peak voltage. The peak value is 25 W/cm^2.

4.5 Frequency tuning system

A trimmer capacitor with 3D EM code CST MWS has been investigated to compensate for a frequency variation of 100 kHz at most. The trimmer capacitor consists of a fixed cylinder 250 mm long, 110 mm in diameter, and with a moveable 100 mm diameter cylinder with a 50 mm stroke. The trimming capacitor is located symmetrically to the coupler in the lower half cavity to compensate for possible field variations.

Considering the elongation of the hot copper cavity part, we have estimated the variation of the main resonance frequency. Due to the cavity geometry, only the Dee must feel the effect of the copper elongation because the stems are fixed at its ends to the liner and to the Dee. So we have only considered a transversal expansion of the Dee, in accordance with the thermal expansion law $l' = l(1+\alpha\Delta T)$ where α is the copper thermal coefficient ($\alpha = 17\cdot10^{-7}\ K^{-1}$), l is the length of the copper piece and ΔT is the temperature variation. With a hypothetical ΔT of 20 K, we have calculated a 50 kHz variation in the main resonance frequency.

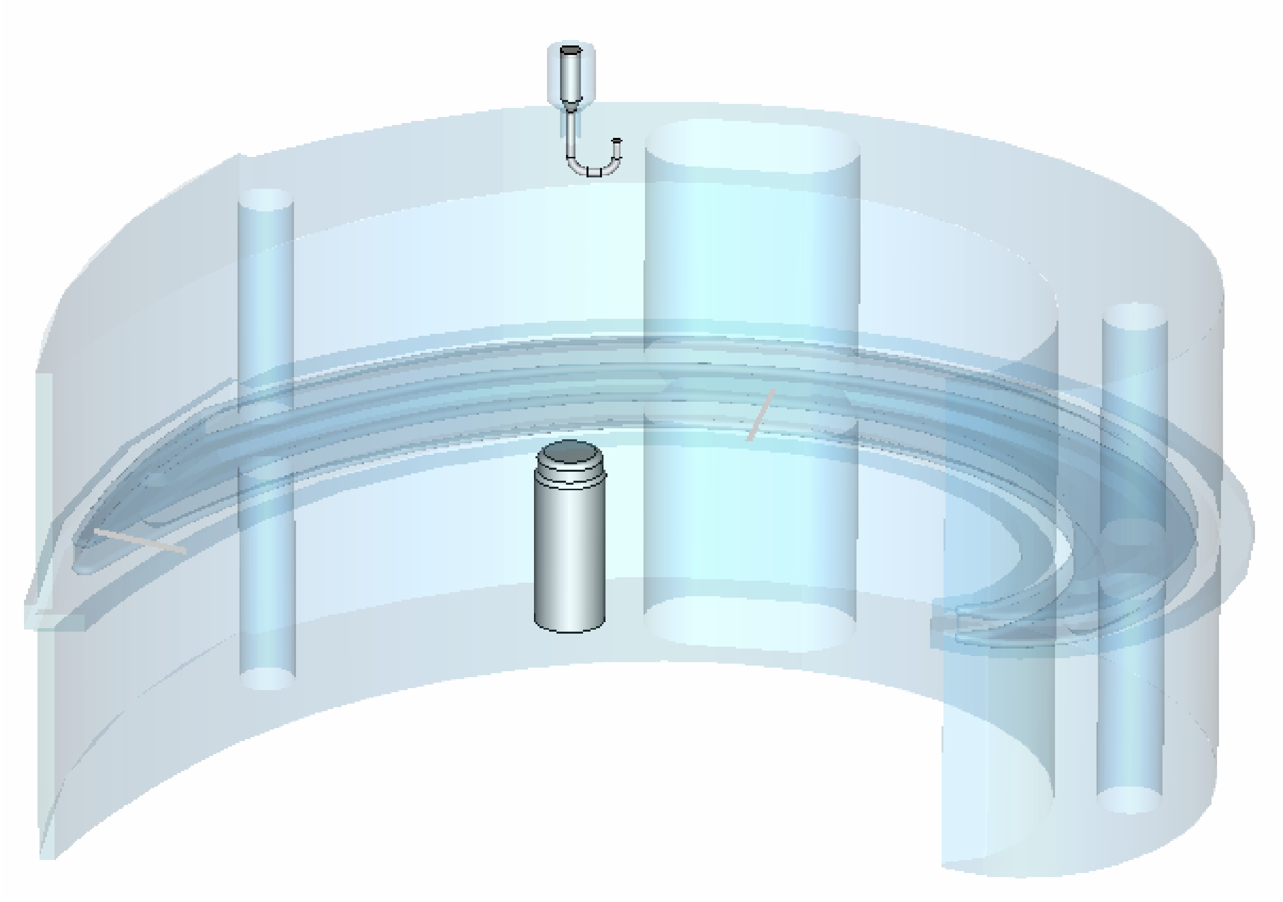

Fig. 4.5.1: Trimming capacitor and coupler layout.

4.6 Coupler design

To feed the power from the RF amplifier into the cavities, we have chosen an inductive coupling, placing a coupler at the top of the liner, near one of the stems.

We have chosen these areas as they are easily accessible from the outside and have a high magnetic field. In fact inductive coupling is achieved by perturbing an elevated magnetic field area of the desired mode with a current coil (loop). The interaction of such field with the coil, allows the transfer of power from the source to the cavity. The dimensioning of the loop has been performed with the aid of electromagnetic codes CST MWS and ANSOFT HFSS [5], varying the loop's area; in fact, varying the section of the loop, the interaction of the magnetic field with the coupler and therefore the transfer of power. In short, the efficiency of the coupler varies.

By studying Scattering parameters by means of Eigenmode – Driver Modal simulations, we get critical coupling in terms of minimal reflection at the coupler's port by studying

VSWR, impedance adaptation by analyzing Smith chart and critical coupling by comparing the cavity's quality factors such as Q_o and Q_{ext}. Critical coupling is achieved if the cavity is excited from a source whose inner impedance is equal to the characteristic impedance of the cavity. This condition implies that the energy supplied from the generator, is evenly distributed between source and cavity, with the consequent equality of the values of Q_o and Q_{ext}. We evaluated the values of Q_o and Q_{ext} applying a numerical method on the S_{11} parameter obtained from the simulations and obtained the curves shown in Fig. 4.6.1.

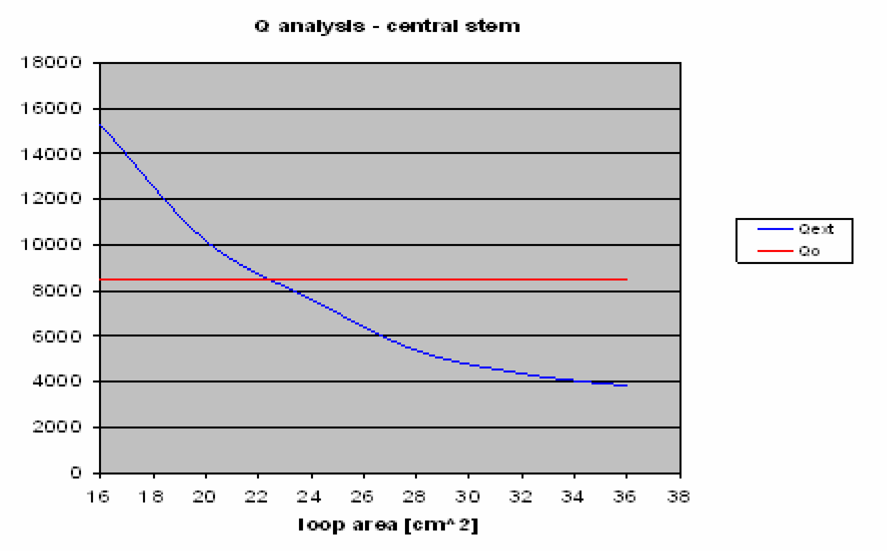

Fig. 4.6.1: Inductive loop Q analysis.

We can get critical coupling by positioning a 22 cm^2 area loop near the main stem and, with a similar analysis, by positioning a 6 cm^2 loop near the external stem. The picture in Fig. 4.6.2 shows the simulated loop configuration near the central stem.

A power amplifier prototype able to deliver up to 50 kW in the frequency range 60-110 MHz has been built over the past few years at LNS to feed our Chopper-500, and has been successfully tested. So the cavities could be driven by four independent RF amplifiers similar to our inexpensive prototype. According to our experience the use of four amplifiers instead of one allows us to operate with medium size RF transmission lines and feasible and reliable couplers.

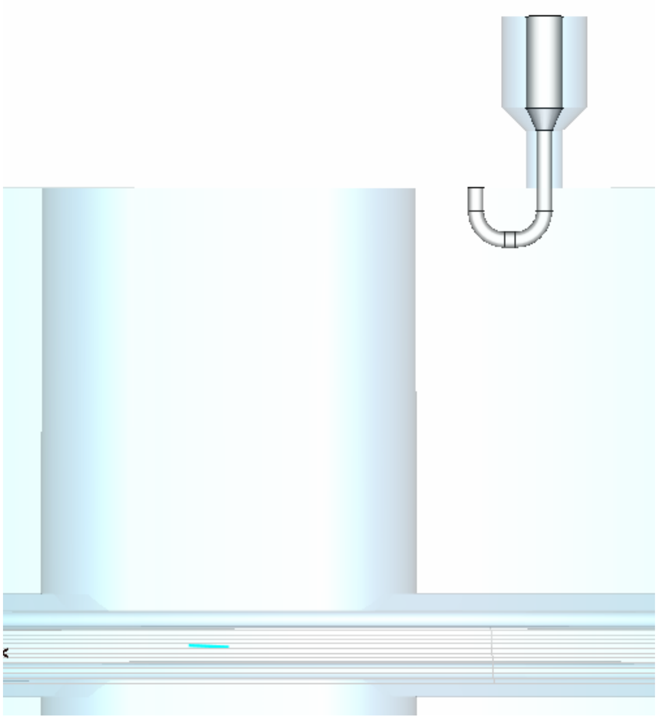

Fig. 4.6.2: Inductive loop layout.

4.7 Power amplifiers

The system analyzed in this work consists of 4 independent amplifiers, one per cavity, which will provide the power to drive up the cavities. This solution allows us to operate with medium-size RF transmission lines and feasible, reliable couplers. Each power amplifier must be able to deliver 50 kW, as confirmed by electromagnetic simulations.

Up to now we have not found commercial products that are cheap enough to meet our requirements. Since 2000, the INFN-LNS Radio Frequency Group has developed and successfully tested a tetrode amplifier prototype, able to deliver up to 100 kW at 100 MHz maximum with the following technical specifications of the RF final stage amplifier circuit:

- Tetrode: TH535 – Thompson Tubes Electroniques.
- Output power: >=50 kW.
- Bandwidth: 65 – 110 MHz.
- Cooling: by forced air and water.
- Efficiency: >=60%.
- Gain: 16 dB.

- Input/output impedance: 50 Ohm.
- Weight: 70 kg.
- Input RF connector: N-type.
- Output RF connector: 4”.
- Maximum pressure at the water inlet: 5 Bar.
- Minimum anode cooling water flow for 50 kW operation: 50 lit/min.

Hence we think that it is possible to build the required amplifiers on our own.

4.8 Cooling RF cavity

According to the cavity geometry and to the power lost inside it, a cavity model was developed to evaluate the temperature achieved at regime conditions.

The goal of the simulations was to achieve preliminary evaluations for the proper sizes, shape and paths of the cooling networks.

The temperature reached at stationary conditions was evaluated by the ANSYS code. This code allows for cavity simulation and the evaluation of heat transmission in the different parts of the cavity due to the conduction coefficient only.

In Table 4.8.1 the main characteristics of the copper used in the simulation are reported.

Table 4.8.1: Physical properties of cavity copper.

Thermal conductivity	386	W/mK
Thermal dilatation coefficient	$1{,}7\cdot10^{-5}$	1/K
Melting point	1083	°C

The simulations have demonstrated that assuming a fixed room temperature of 298 K on the lower surface of the Dee, the power lost inside the cavity could increase the temperature of the cavity’s surfaces by up to 2400 K, if thermal heat is not removed (see Fig. 4.8.1).

Due to the symmetry of the cavity with respect to the median plane, we present the cooling networks of just half the cavity in the following.

Six independent cooling piping were designed, each one for a different part of the cavity. Two networks are dedicated to the inner and outer liner surfaces, the other 3 to the 3 stem surfaces, and one for the Dee.

The temperature difference ΔT between the inlet and outlet water was fixed at 10 K.

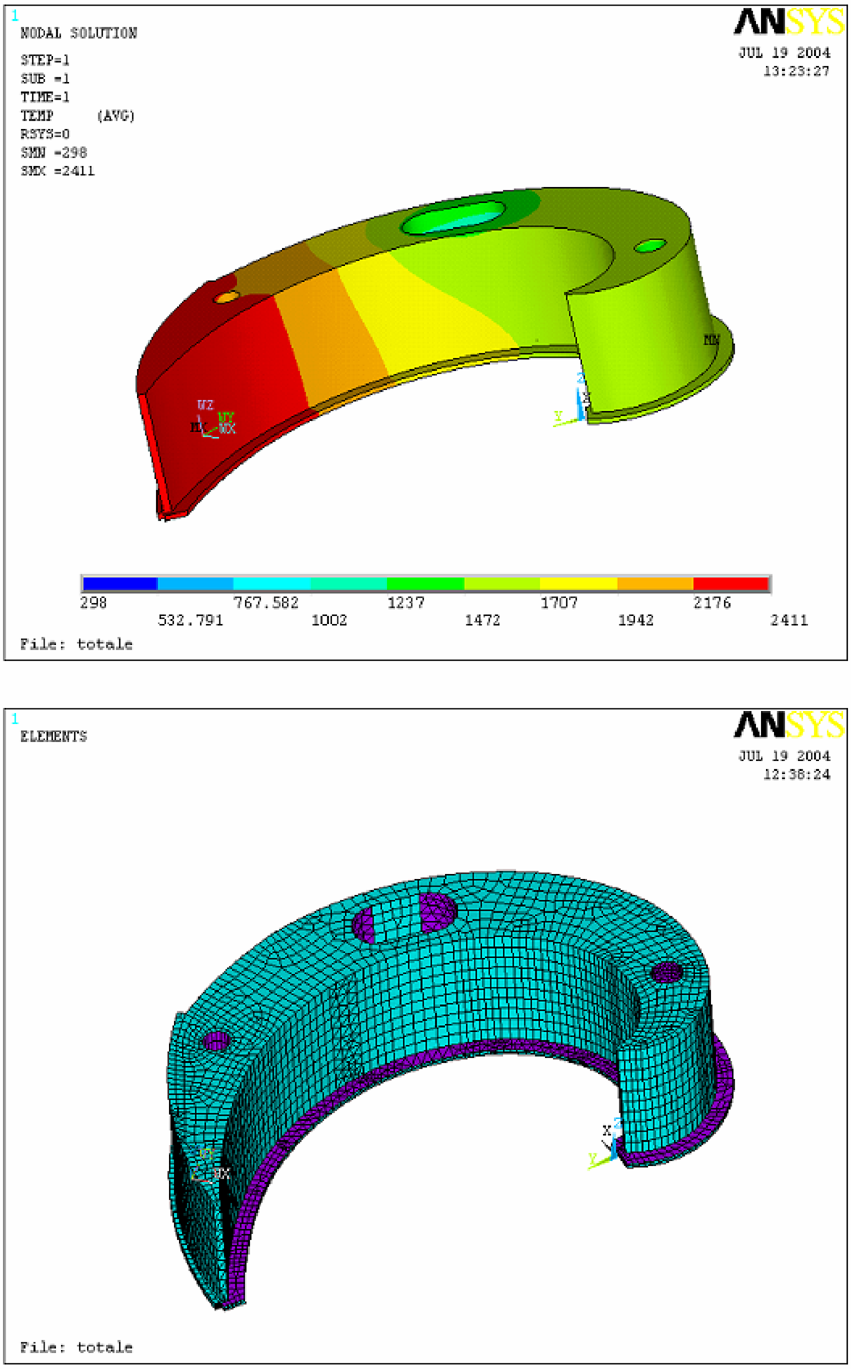
1
NODAL SOLUTION
STEP=1
SUB =1
TIME=1
TEMP (AVG)
RSYS=0
SMN =298
SMX =2411
ANSYS
JUL 19 2004
13:23:27
298
532.791
767.582
1002
1237
1472
1707
1942
2176
2411
File: totale
1
ELEMENTS
ANSYS
JUL 19 2004
12:38:24
File: totale

Fig. 4.8.1

The constraint of a temperature difference lower than 20 K between the hottest part of the copper and the coldest part, near the cooling pipeline, was imposed. The distances between the different pipeline arms of the cooling network were adjusted to achieve this constraint.

The Tables 4.8.2a and b show the results achieved for each arm of the networks, for the amount of water and also for the drop in pressure due to friction. The lengths of each network are reported too.

The inner diameter of all the pipelines is assumed to be 6 mm. Only for the external stem were two different solutions, one with a pipe diameter of 8 mm and another with 10 mm respectively, also evaluated. The full power removed is 28 kW on half cavity, 25% more than the expected 22-23 kW power lost inside the RF Cavity.

Table 4.8.3 shows the water speed and the drops in pressure vs. the difference in temperature ΔT of inlet/outlet water, the diameter of all the pipelines being 6 mm.

The only critical network is that of the external stem. Tables 4.8.4a and b show the parameters for the "External stem" assuming a pipeline diameter of 10 and 8 mm respectively.

Table 4.8.2a

Inner liner, yellow		
Pipeline length	7,76	m
Full power removed	3379,8	W
Water flow	0,081	kg/s
ΔT of cooling water	10	K
Water speed inside the cooling pipeline	2,86	m/s
Reynolds number	17510	
Number of network's bends	10	
Pressure drop along the pipeline	25	m
ΔP	2,5	atm
Outer liner, green		
Pipeline length	4,81	m
Full power removed	3305	W
Water flow	0,079	kg/s
ΔT of cooling water	10	K
Water speed inside the cooling pipeline	2,79	m/s
Reynolds number	17120	
Number of network's bends	10	
Pressure drop along the pipeline	16	m
ΔP	1,6	atm
External stem, blue		
Pipeline length	4,8	m
Full power removed	8052	W
Water flow	0,193	kg/s
ΔT of cooling water	10	K
Water speed inside the cooling pipeline	6,8	m/s
Reynolds number	41710	
Number of network's bends	10	
Pressure drop along the pipeline	90	m
ΔP	9	atm
Inner Stem, blue		
Pipeline length	5,76	m
Full power removed	3309	W
Water flow	0,079	kg/s
ΔT of cooling water	10	K
Water speed inside the cooling pipeline	2,8	m/s
Reynolds number	1714	
Number of network's bends	10	
Pressure drop along the pipeline	18	m
ΔP	1,8	atm

Table 4.8.2b

External Liner, Black		
Pipeline length	10,27	m
Full power removed	3287	W
Water flow	0,079	kg/s
ΔT of cooling water	10	K
Water speed inside the cooling pipeline	2,78	m/s
Reynolds number	17030	
Number of network's bends	14	
Pressure drop along the pipeline	7,11	m
ΔP	3,1	atm
Main Electrode or Dee, Black		
Pipeline length	4,46	m
Full power removed	7357	W
Water flow	0,176	kg/s
ΔT of cooling water	10	K
Water speed inside the cooling pipeline	6	m/s
Reynolds number	38110	
Number of network's bends	2	
Pressure drop along the pipeline	58,9	m
ΔP	5	atm
Central Stem, Black		
Pipeline length	4,34	m
Full power removed	2793	W
Water flow	0,066	kg/s
ΔT of cooling water	10	K
Water speed inside the cooling pipeline	2,37	m/s
Reynolds number	14510	
Number of network's bends	5	
Pressure drop along the pipeline	10,6	m
ΔP	1	atm

Table 4.8.3

Cooling water, ΔT	10 K		20 K		15 K	
	Velocity [m/s]	ΔP	Velocity [m/s]	ΔP	Velocity [m/s]	ΔP
Inner liner yellow	2,86	2,5	1,4	0,6	1,9	1,2
Outer liner green	2,79	1,6	1,4	0,4	1,8	0,7
External stem blue	6,8	9	3,4	2	4,5	4
Inner Stem blue	2,8	1,8	1,4	0,5	1,86	0,85
External liner black	2,78	3,1	1,4	0,8	1,85	1,4
Dee black	6	5	3,1	1,6	4,1	2,6

Table 4.8.4a

External Stem, pipeline $\phi 10$		
Pipeline length	4,8	m
Full power removed	8052	W
Water flow	0,193	kg/s
ΔT of cooling water	10	K
Water speed inside the cooling pipeline	2,5	m/s
Reynolds number	25510	
Number of network's bends	10	
Pressure drop along the pipeline	30	m
ΔP	3	atm

Table 4.8.4b

External Stem, pipeline $\phi 8$		
Pipeline length	4,8	m
Full power removed	8052	W
Water flow	0,193	kg/s
ΔT of cooling water	10	K
Water speed inside the cooling pipeline	3,8	m/s
Reynolds number	31020	
Number of network's bends	10	
Pressure drop along the pipeline	5,9	m
ΔP	6	atm

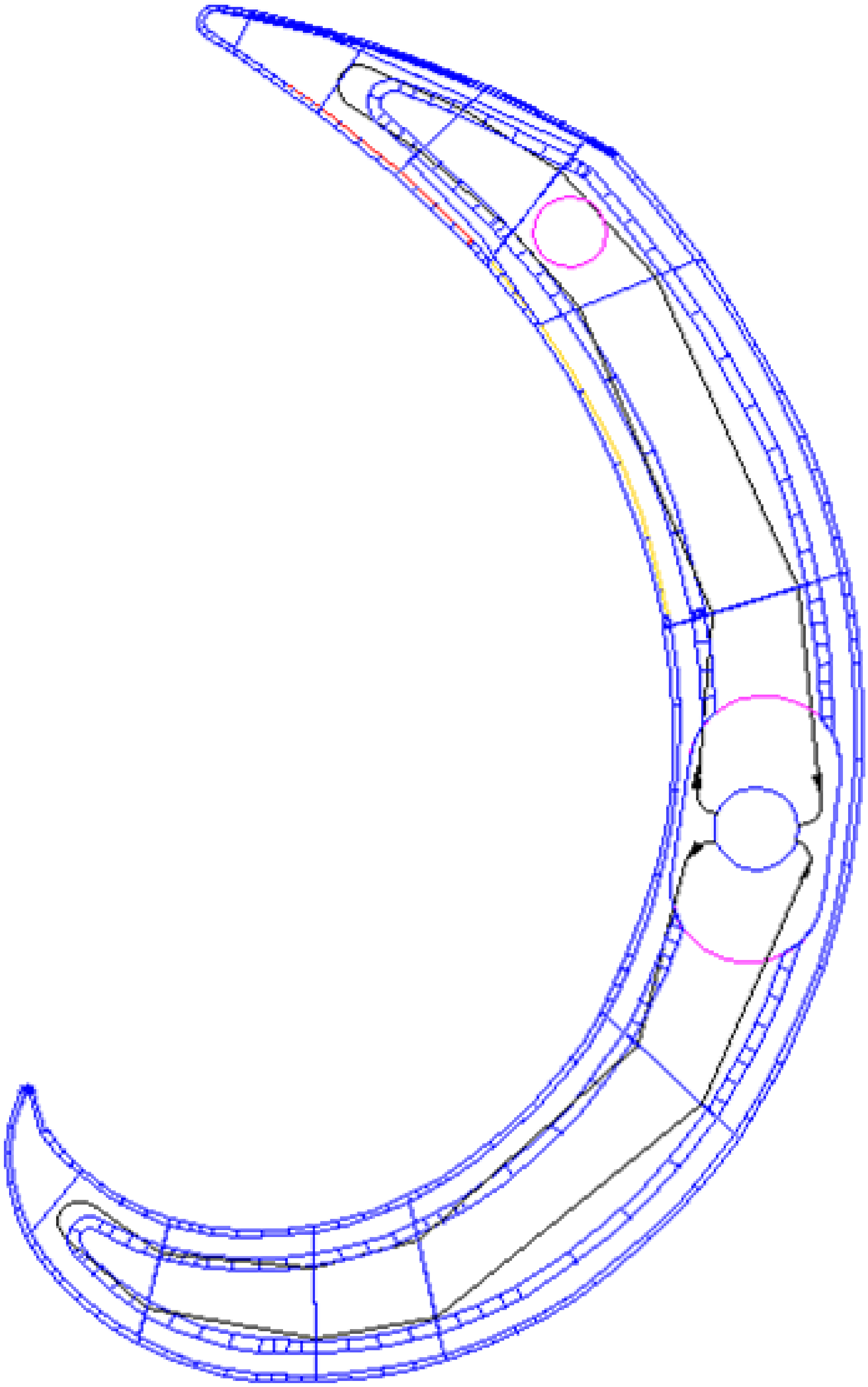

Fig. 4.8.1: Dee's cooling network.

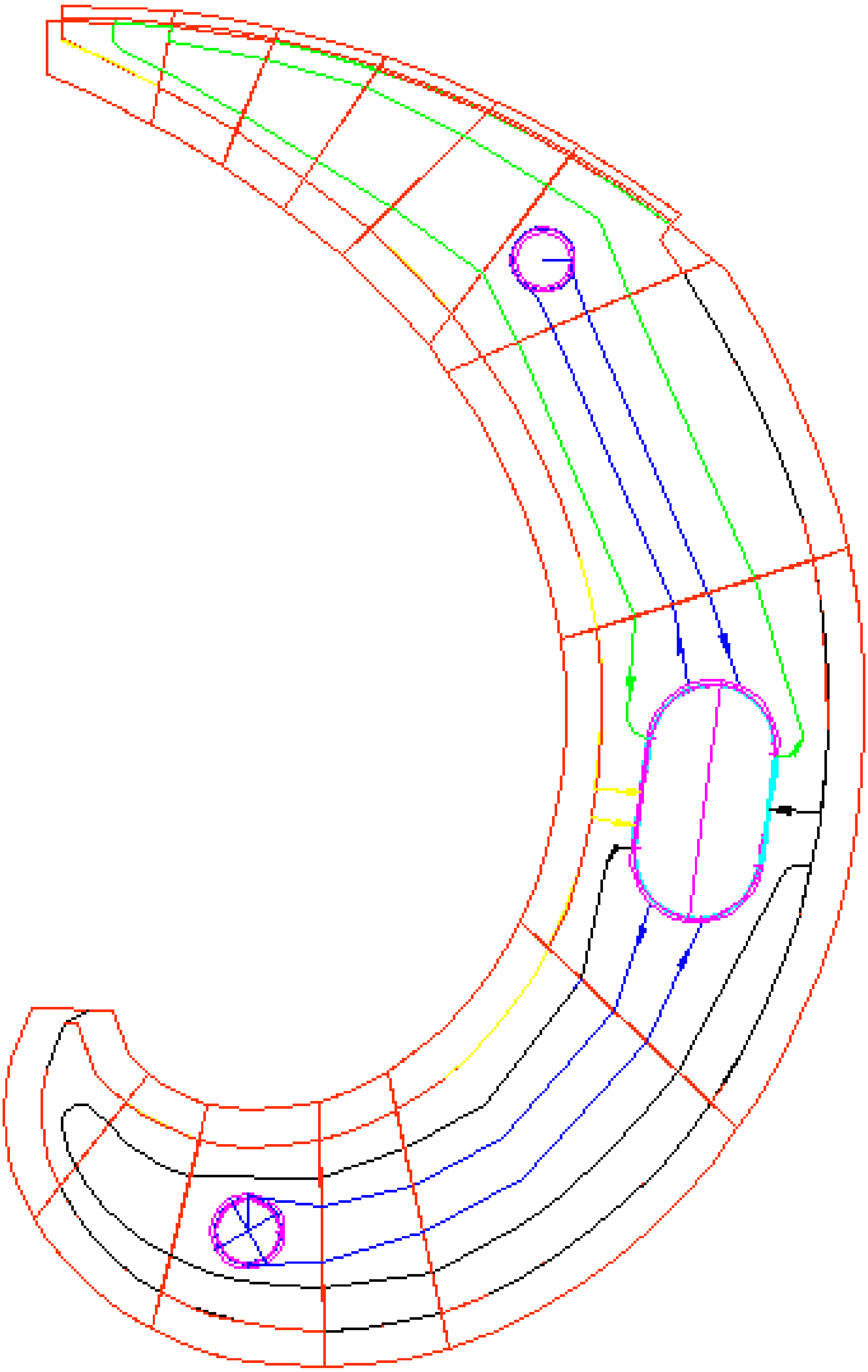

Fig. 4.8.2: Cooling path on the top side of the RF liner. Yellow is the cooling network for the inner liner; green for the outer part of liner; blue for the inner part of the liner and for the outer stem, black for the Dee, the external liner and central stem.

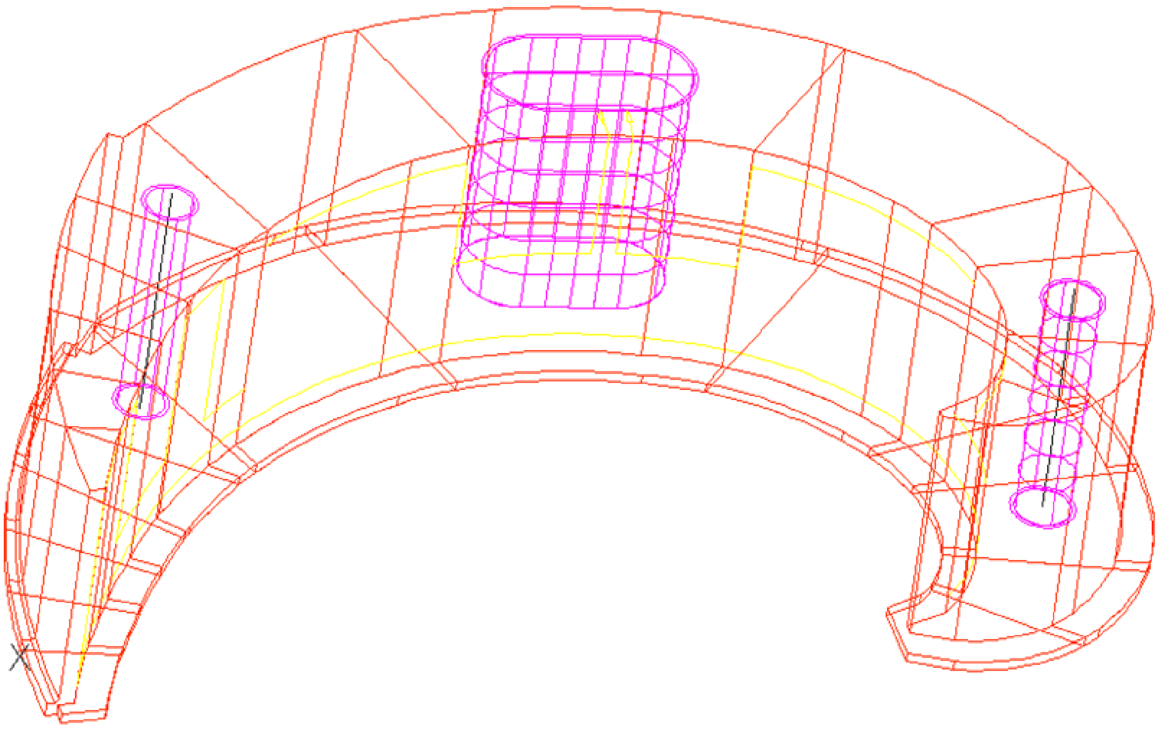

Fig. 4.8.3: Cooling networks on inner side of the liner, yellow, and of the three stems, pink.

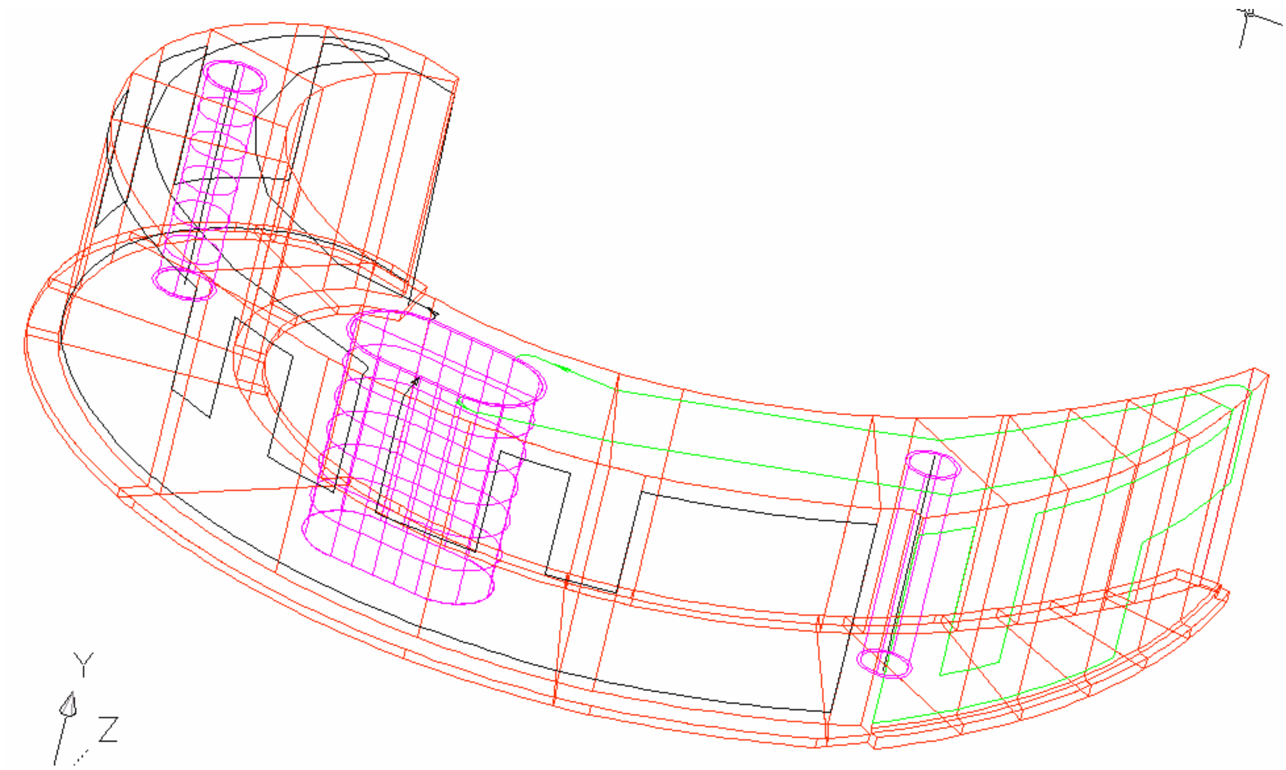

Fig. 4.8.4: Cooling networks on the liner, top side (black and green), external side (black) outer side (green).

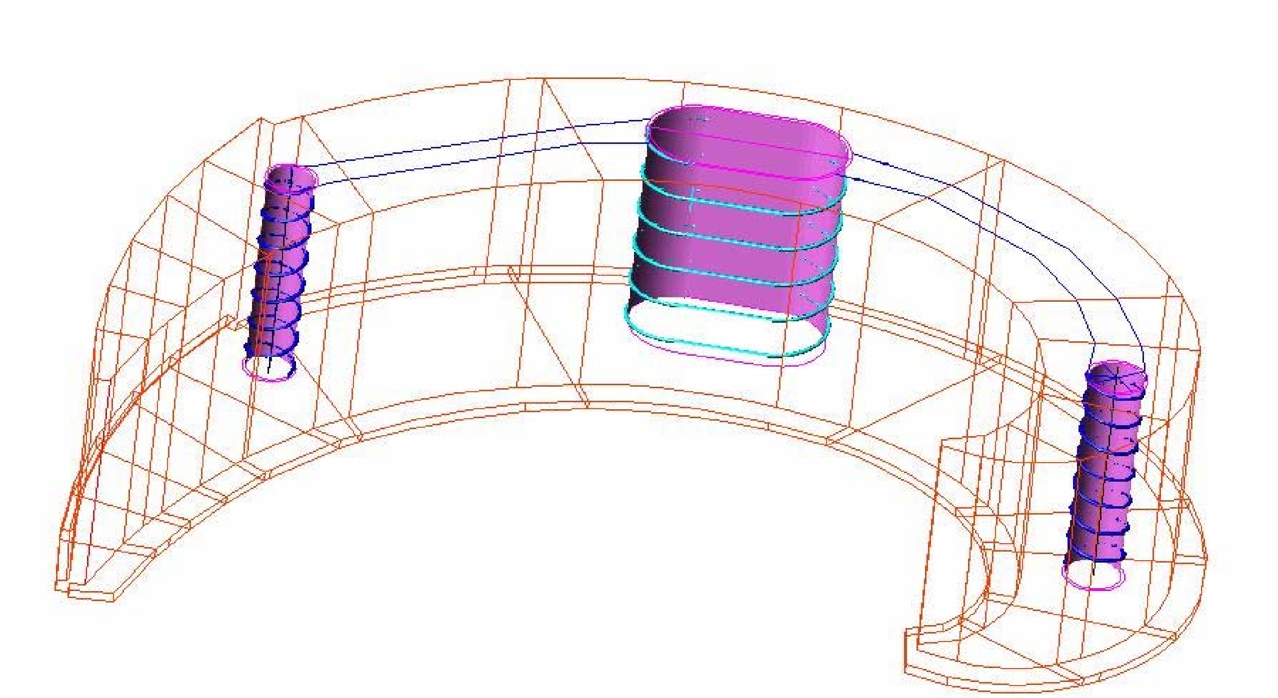

Fig. 4.8.5: Cooling networks for the stems.

4.9 Conclusions

Multi-stem cavities are a good solution for the design of fixed frequency cyclotron resonators with challenging Dee shapes and dimensions. Although the degrees of freedom of the structure grow with the number of stems, the RF design can be approached with some simple but realistic approximations which with the help of modern 3D EM codes, lead to a quick definition of the stem diameters and positions. Moreover, multi-stem cavities can easily be designed to provide the voltage distribution needed to optimize the power consumption, to reach high resonant frequencies in spite of the Dee dimensions, and to reduce the current densities and the total losses. Last but not the least, using more stems will also help to increase the mechanical stability of the structure and allow us to provide an easier path for the Dee cooling pipes.

4.10 References

[1] E. Acerbi et al., *"Design of the RF cavity for a 200 MeV PSC"*, 14th ICCA (1995), South Africa.

[2] C. Bieth et al., *"A very compact proton therapy facility based on use of HTS"*, 15th ICCA (1998), Caen, June.

[3] MWS by CST, www.cst.de.

[4] SOPRANO by Vector Fields, www.vectorfields.com.

[5] HFSS by Ansoft corp.,Pittsburgh PA, USA, www.ansoft.com/products/hf/hfss/.

Chapter 5. Beam extraction

The standard methods to extract the beam out from a cyclotron are two:

- one is based on the use of electrostatic deflectors to produce an electric field which push the beam towards the outer radii until the beam reaches the region where the magnetic field falls off, and the beam can escape from the pole;
- the second is the so-called stripping method used in all the latest commercial cyclotrons which accelerate negative ions.

The stripping method consists in the use of a thin stripper foil placed on the last orbit inside the cyclotron to remove one or more electrons from the ions of the beam. In this way, the ion crossing the stripper abruptly changes its charge state and then the curvature radius of its orbit changes too. The sudden change in the curvature radius allows us to bring the beam out from the pole cyclotron, if the stripper is properly placed.

It is evident that the stripper method can be used to extract the H_2^+, which is a molecule of H_2 ionised and is made up of two protons bound by one electron, but that it cannot be used to extract light ions fully stripped like $^{12}C^{6+}$. Alternatively, the electrostatic deflectors allow us to extract any kind of beam particle.

To extract the light ion beam from SCENT, a couple of Electrostatic Deflectors, E.D.1 and E.D.2 are used. Of course, these electrostatic deflectors also allow us to extract the H_2^+ beam. However, SCENT has been designed to allow the extraction of H_2^+ by the stripping method, which is very convenient because it allows us to extract the beam with an efficiency of 100%. Therefore, it is very useful when high intensity beams have to be extracted. Moreover, the stripping extraction allows us to extract the beam at different energies just by changing the radial position of the stripper, or the extraction radius. This feature is very interesting with a view to upgrading the SCENT design to 300 AMeV. Despite the fact it is advantageous to have light ions with higher energies to increase the maximum depth of treatable tumours, the range of protons with an energy of 250 MeV is already about 300 mm in water, which is enough to treat any tumours located inside the human body. Therefore, using a proton beam with an energy higher than 250 MeV is necessary in order to decrease its energy. Despite the fact it is quite simple to decrease beam energy using a degrader with the proper thickness (e.g. 63 mm Aluminium or 13 mm Tungsten can decrease the energy beam of a proton from 300 MeV to 250 MeV) during the deceleration process, a lot of neutron and gamma rays are produced and these particles induce radioactivity on all the devices inside the accelerator room and on the concrete walls which shield the accelerator.

Below we describe, in subsections 5.1 and 5.2, the solution for extraction by electrostatic deflectors and in subsection 5.3, the stripping extraction. In subsection 5.4, the compensation of the magnetic channel field by a compensating bar is discussed while, in subsection 5.5, the conclusion and the work to be carried out in the future are summarised.

5.1 Extraction by electrostatic deflectors, solution 1.

As already mentioned, the main devices used to extract the beam are two Electrostatic Deflectors (E.D.). The cross section of the E.D. with the electrode and the housing is shown in figure 5.1.1. This shape is similar to the existing deflector in our cyclotron K800; the main difference being the height: 60 mm in the K800 as opposed to 50 mm in SCENT. The reduction is feasible because the K800 original device was designed for a nominal gap of 8 mm between the electrode and the septum. For SCENT, the nominal gap is only 5 mm. This reduction allows us to reduce the height of the device by 6 mm. A further reduction of 4 mm was achieved, reducing the height of the electrode (2 mm) and by reducing the thickness of the upper and bottom face of the liner housing (2 mm). Actually in our cyclotron [1] and also at MSU, E.D.s with a 6 mm gap are used. Moreover, both our and the MSU cyclotrons deliver ions of different types and energies, so both the position and the radial curvature of the E.D. have to be adjusted and this requires a slightly larger gap to fit all the different beam trajectories. There is also another advantage of SCENT over our and the MSU cyclotron, which is due to the higher energy of SCENT and its larger extraction radius. These two differences produce a smaller beam emittance and a larger bending shape of the E.D. respectively. Consequently, we expect a larger extraction efficiency for SCENT even if a 5 mm gap is used.

The length of the two deflectors has to be as long as possible to reduce the maximum voltage to be applied to the electrodes. The angular width available for the E.D. is the angular width of the hill plus the thickness of the RF liner, which shields the iron pole from the RF field of the cavities' electrodes (see subsection 6.2). The hill width at outer radii is 44°. Looking at the equilibrium orbit for a Carbon beam at 250 AMeV (see subsection 3.4) we see that the mean radius is 127 cm. Despite the RF liner having a thickness of 10 mm along the perpendicular direction to the hill boundary (2 mm due the copper thickness, whilst 8 mm are due to the diameter of the cooling water pipeline) due to the spiral shape of the hill, the RF liner thickness along the beam trajectory is about 3.5 cm for each side. So the useful width for the E.D. and its housing is 44°+3.5°=47.5°.

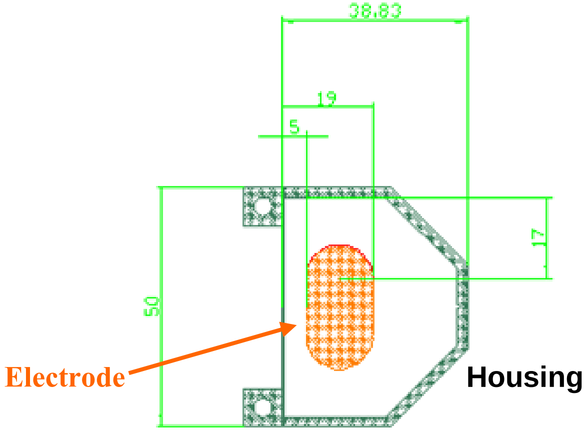

Fig. 5.1.1: Cross section of SCENT electrostatic deflector.

Despite the fact that the useful angular length for the E.D. is roughly 47°, the following simulations have been evaluated assuming an electrode length of 36° for both E.D.s. The positions of both the devices are shown in Table 5.1.1. In the following section, the results achieved by using an electrode length of 40° will be presented too.

Table 5.1.1: Position of the two E.D.s inside the cyclotron.

	Electrode Deflector 1	**Electrode Deflector 2**
Radii entrance side	128,46 [cm]	129,17 [cm]
Angle entrance side	112°	202°
Maximum R	129,568 [cm]	130,554 [cm]
Angle of Max. R	130°	222
Radii exit side	128,34 [cm]	129,73 [cm]
Angle exit side	148°	238°
Electric Field	84 kV/cm	84 kV/cm

For the present case, we are assuming a distance from the RF liner boundary to the E.D. electrode of about 11 cm, see figure 5.1.2. So the maximum angular length of each device is 37.5°. According to Fig. 5.1.2 and for all the following simulations, the length of the E.D. is 36°. Our computer code allows us to insert the angular length only as an integer number.

The electric field of the two E.D.s steers the beam towards the outer radii. The distance between the last accelerated orbit and the extracted trajectory depends, of course, on the electric field applied to the E.D. and also on the position along the trajectory. This is well illustrated in the Figs. 5.1.2a and 5.1.2b.

These electric fields can be achieved with a voltage lower than 45 kV applied to a gap of 5 mm. These values are consistent with our experience at K800 [1], where a voltage of 50-55 kV is usually applied on a gap of 6 mm.

To achieve a beam extracted from the cyclotron, the use of a magnetic channel with a double function is also mandatory. Magnetic channels have two functions: one is to reduce the magnetic field locally to allow the beam to escape the magnetic pole of the cyclotron; the second is to produce a field gradient to radially focus the beam. Indeed, along the extraction path the field strongly decreases and this produces an axial focusing, but also a strong radial defocusing. The field gradients produced by the magnetic channel are used to counterbalance this effect and to maintain the beam envelope acceptable along the extraction path.

It is important to place a magnetic channel as quickly as possible to achieve the shortest possible extraction path and cross the fringing field region suddenly. On the other hand, a magnetic channel has a thickness that means it can only be installed where the distance between the last accelerated orbit and the extraction trajectory is at least 18 mm. This value has been used to design the extraction path of the COMET cyclotron [2]. Moreover, in Fig 6.1.4 the cross section of a typical magnetic channel and the position of the beam extracted (inside the channel) and of the last accelerated orbit (on the left of the channel) are shown. A conservative beam size of 4 mm in diameter was assumed, the true values being around 2-3 mm. Apart from the figure, the minimum separation could be one of 17 mm and even less if the bar size of the magnetic channel is thinner than 10 mm - some millimetres of extra separation are useful in guaranteeing a good first harmonic compensation (see subsection 5.4, compensation bars). In our cyclotron design we chose a design value of 20 mm for this parameter. According to this choice and looking at Fig. 5.1.3, the best position in which to install the first magnetic channel is at about 170°, but at this position there is an RF cavity.

Although it should be possible to install a magnetic channel on the boundary of the cavity, we prefer not to use this innovative solution for SCENT, because we would like to have a conservative and reliable design. So the position in which to install the first magnetic channel was that of 214°, approximately in the middle of the hill following the E.D.2.

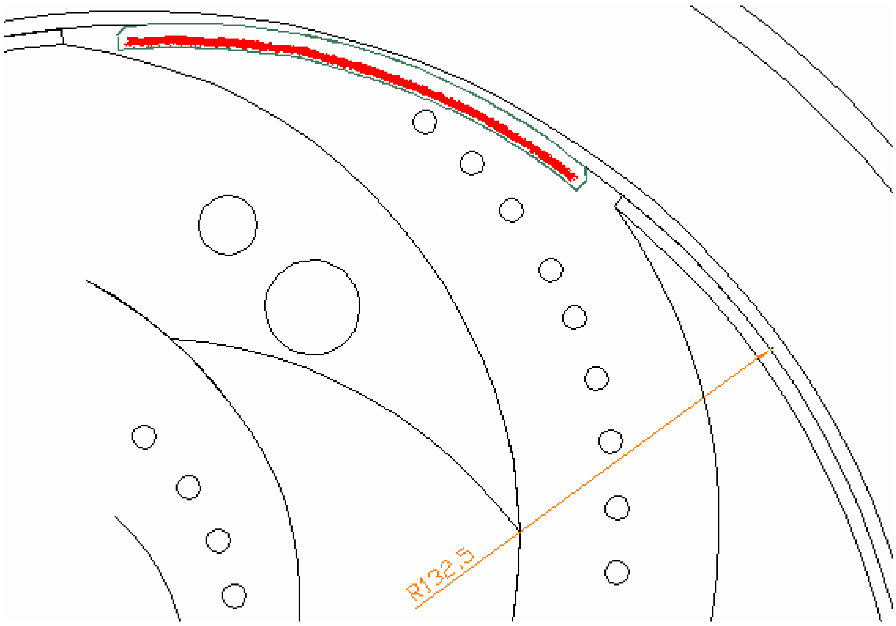

Fig. 5.1.2a

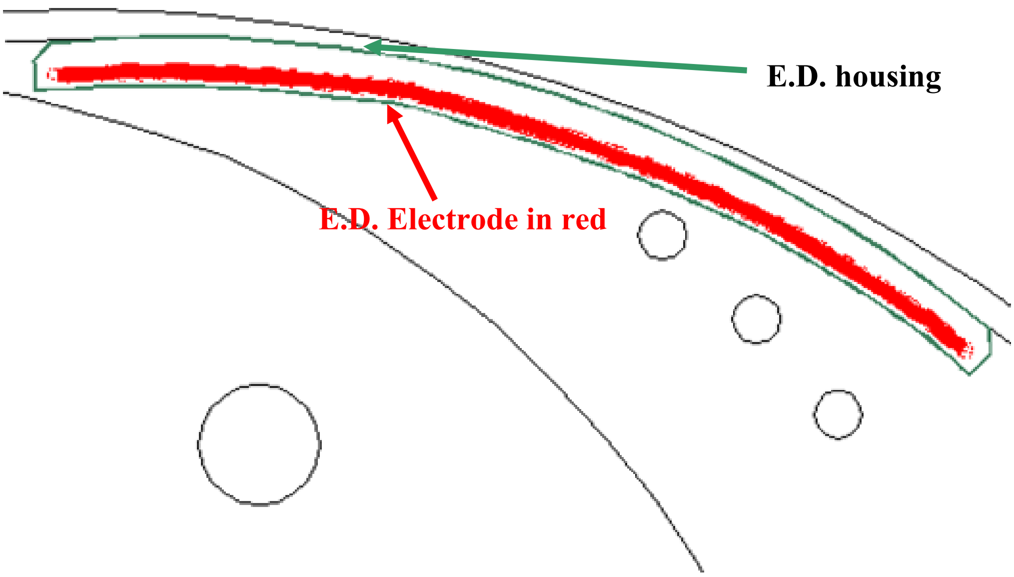

Fig. 5.1.2b. Layout of the Electrostatic Deflector, complete with housing and electrode, placed on the hill of the cyclotron. It is quite evident that the present angular length of the E.D. is very conservative.

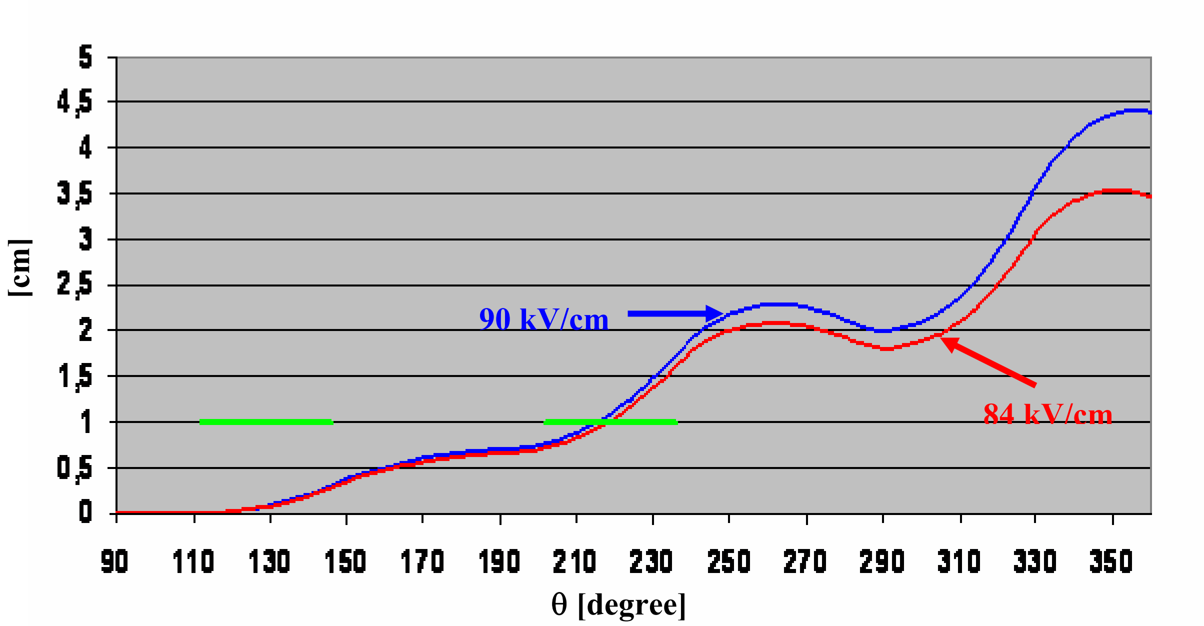

Fig. 5.1.3: Distance between accelerated orbit and extracted trajectory for two cases, one with an electric field of 84 kV/cm and the other of 90 kV/cm.

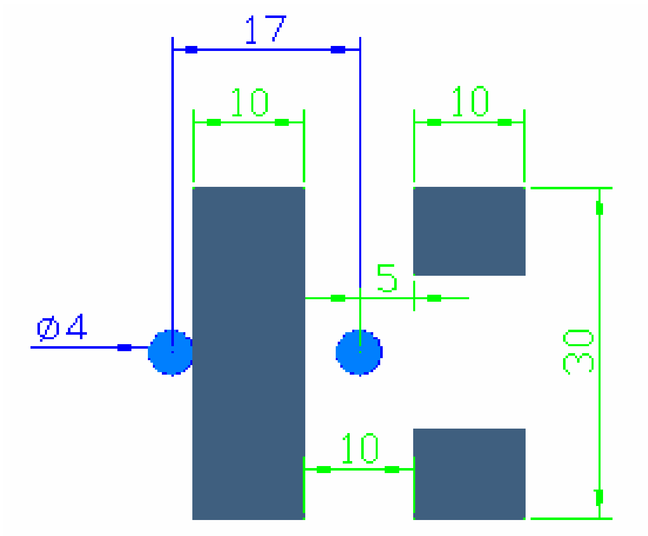

Fig. 5.1.4: Layout of usual magnetic channel, dimensions are in mm. The blue spots represent the size of the last accelerated orbit, on the left side, and the extracted beam on the right.

In Figure 5.1.4 the radial beam envelope along the extraction path and also the angular position of the magnetic channel are shown. In table 5.1.2 the angular and radial positions of each magnetic channel and their magnetic field and gradient are also reported. The radial beam envelope was evaluated transporting 8 particles with (*x,x'*) values corresponding to the boundary of an ellipse having an emittance of 4 π mm.mrad rms. The proper orientation of the ellipse at the starting point of integration was evaluated by the code GENSPE [3]. The simulation along the extraction path was performed with the MSU code extraction.

We will now try to explain what beam emittance we expect to achieve at the extraction radius; the starting point being the rms emittance of the source supernanogan, which is about 30 π mm.mrad at extraction voltage of 30kV. This is equivalent to a value of 0.2 π for the normalised emittance ε_n ($\varepsilon_n=\beta\gamma\varepsilon$).

We assume we will have the same value also for the upgraded source with an extraction voltage of 40 kV. The effective area of the emittance can be increased by many effects:

- the spiral inflector, about a factor 1.5 (see subsection 2.5);
- the mismatch of injected beam emittance with the acceptance of the cyclotron, about a factor 2;
- the magnetic field is non linearity along the injection line and the cyclotron, and also by the multiple scattering of the beam particles with the residual gases.

All these effects produce an increase in the effective emittance for an amount that can be expected as a factor 4. So the expected effective normalised emittance at a maximum energy of 250 AMeV will be about 0.8 π and then the value of the rms emittance should be 1 π mm.mrad. Because the expected beam emittance is about 1 π mm.mrad, our simulations' extractions which assume an rms emittance of 4 π mm.mrad are truly conservative. The vertical beam envelope is not here shown because it is quite regular and well focused, see section 5.2.

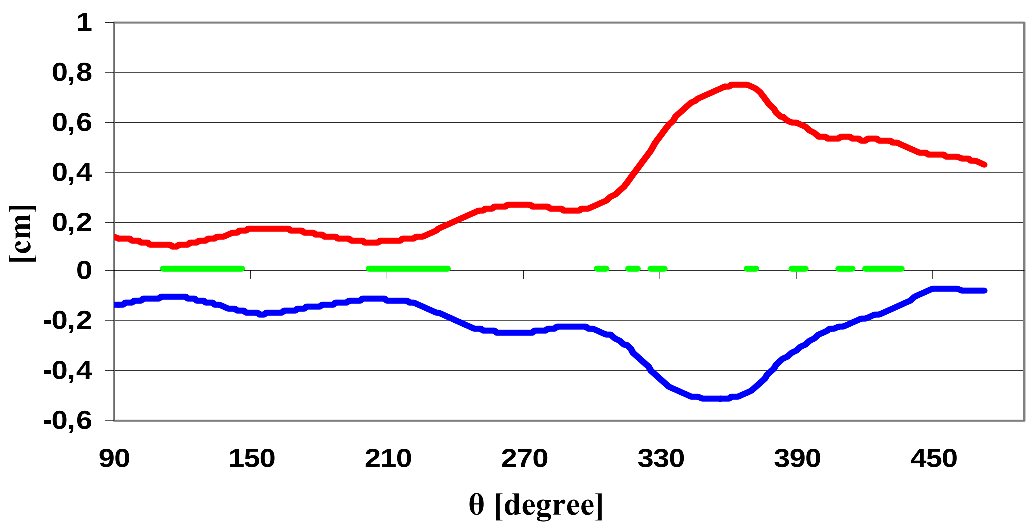

Figure 5.1.5: The radial beam envelope along the extraction path and the position of the magnetic channel are shown; emittance ε=2 π mm.mrad.

The first magnetic channel is supposed to be placed at 304°. According to Fig. 5.1.3, at this position the distance between the last accelerated orbit and the extracted orbit is more than 20 mm. This distance is enough to insert a magnetic channel without destroying the beam on the inner orbit. According to Fig. 5.1.3, the request minimum value is of 16-18 mm.

In figure 5.1.6 the trajectory along the median plane of the cyclotron is shown. According to our goal, the extraction is made in just one turn; the starting point being at angle 110° and the end at angle 382° and R=268 cm.

Table 5.1.2: Parameter of the magnetic channels.

Magnetic Channel	**R** [cm]	**θ_{in}** [deg]	**θ_{out}** [deg]	**B** [kG]	**ΔB/ΔR** [kG/cm]
M1	131,37	304	308	2	-1
M2	131,65	318	322	3	-2
M3	131,41	326	334	3	-2
M4	131,90	368	374	3	-2
M5	135,11	388	396	1	-2
M6	139,72	408	416	1	-2
M7	144,07	420	438	1	-2

In figure 5.1.6 the position of the magnetic channels is also shown, none compensating bar is shown. Indeed, the compensating bars are necessary to cancel at least the first harmonic component produced by the magnetic bar on the magnetic field at inner radii. The simplest solution is to evaluate the first harmonic component produced by a group of magnetic channels and then to insert an iron bar, which has the same effect at the opposite position (at 180°). It is quite evident that the magnetic channels at inner radii have more effect on the accelerated beam than the magnetic channels at outer radii. So it is very important to achieve a good 1st harmonic compensation for the inner magnetic channels from M1 to M4. It is also evident that the compensation bars for the M1-M3 channels have to be placed just on the same hill where the E.D.1 is installed and as near as possible to the E.D.1. Therefore, this compensation bar must be carefully designed and developed, see subsection 5.4.

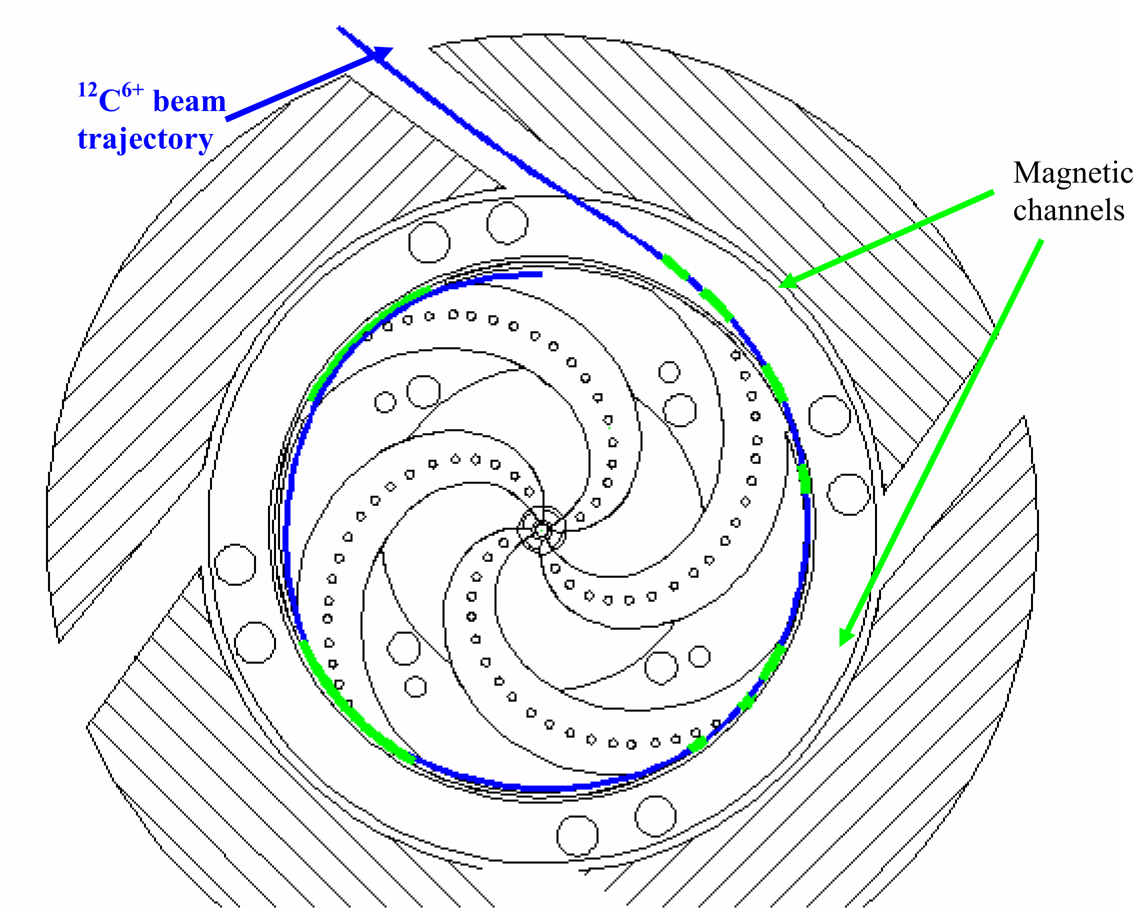

Figure 5.1.6: Extraction trajectory along the median plane of the SCENT cyclotron median plane. The positions of the magnetic channels are also shown in green.

The efficiency of the extraction process is related to the feasibility of single turn extraction, which requires separated turns and good beam quality in terms of energy spread, bunch length and beam halo. According to [4], the orbits separation at the extraction radius is given by:

$$\frac{dR}{dN} = \frac{R \cdot E_g}{E} \cdot \frac{\gamma}{\gamma + 1} \cdot \frac{1}{\nu_r^2} \qquad (5.1)$$

where R=1.27 m is the average orbit radius at extraction, E_g/E the ratio of the average energy gain per turn to the kinetic energy at extraction, γ=1.268 and ν_r=0.85, the relativistic factor and the frequency of radial betatron oscillations respectively. So according to the (5.1) the expected interturn separation is 1.6 mm.

On the other hand, the width of the beam is given by the emittance and the intrinsic energy spread:

$$\Delta x = \sqrt{\frac{4R}{\beta\gamma\nu_r} \cdot \frac{\varepsilon_x}{\pi} \left(\frac{dR}{dN} \cdot \frac{\Delta E}{E_g} \right)^2} \qquad (5.2)$$

where ε_x=0.8 is the normalised horizontal emittance, β=v/c and ΔE the full energy spread.

The term ΔE is in general due to three terms, the energy spread of the injected beam, the energy spread due to the bunch length and the spread due to the space charge effect:

$$\Delta E = \sqrt{\Delta E_i^2 + \Delta E(\phi) + \Delta E_{SC}^2} \qquad (5.3)$$

Due to the excellent beam emittance provided by the modern sources and to the high energy gain, the first term can be neglected with respect to the second. The contribution of the space charge effect ΔE_{sc} can also be neglected due to the moderate beam intensity.

The value of the term ΔE(ϕ) depends on the acceptance phase which is usually 40° then ΔE(ϕ)=0.15 AMeV; hence according to the (5.2) the expected value of Δx is 0.9 mm. The beam size shown in Fig. 5.1.5 has a minimum of about 2 mm at the entrance of the electrostatic deflector. If we divide this value for a factor $\sqrt{2}$ to take account of the emittance doubled in size (2 π mm.mrad) used to evaluate the beam envelope in the figure, we achieve a beam size of 1.4 mm in good agreement with the value achieved by formula (5.2).

So the interturn separation is larger than the beam size and the single turn separation then seems feasible. Moreover it should be possible to excite a 1st harmonic precession of the beam just to increase the separation between the orbits. This simulation was not accomplished for the present study.

However, the simulation of the beam envelope along the extraction path for beams with energy that is a little different to the nominal, have also been performed simply to verify that the multiturn extraction is also feasible. In Fig. 5.1.7, similar to Fig. 5.1.5, the envelopes of beams with energies corresponding to half a turn before and half a turn after the nominal are shown. These envelopes were evaluated assuming the same emittance as the nominal beam, 4 π mm.mrad, but they have an energy lower and higher than ΔE=0.25 AMeV respectively.

All the extraction simulation paths and beam envelopes have been evaluated using a magnetic field map with a perfect four-fold symmetry. Only at the final stage when the overall cyclotron design will be completed, will a more refined simulation also be accomplished taking the influence of all the magnetic channels and of the compensating magnetic bars into account. As a result of our experience, the characteristic of the extraction system achieved by the four-fold symmetry field will be modified just a little by the use of a more realistic field (less than 3-5%) in the simulation.

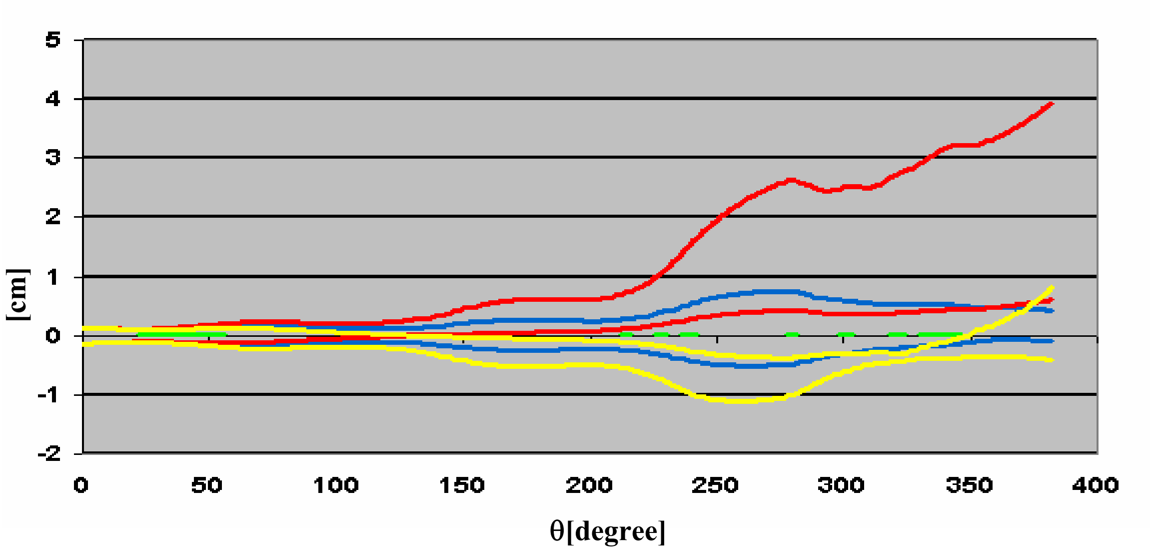

Fig. 5.1.7: Radial beam envelope for beam with an energy of 250 AMeV, blue colour. The red and yellow curves are the beam envelopes for an energy of ±ΔE=0.25 AMeV respectively. The position of each magnetic channels, green curve, is also shown.

5.2 Extraction by electrostatic deflectors, solution 2.

A slightly different extraction process was simulated assuming the two electrostatic deflectors have an effective length of 40°, about 10% longer than the previous simulation. As shown in figure 5.2.1, the extra cover due to the RF liner allows us to install electrostatic deflectors with a length of 40°, including a magnetic channel with 4° length. The extra push due to the 10% longer electrode allows us to install the first magnetic channel just at the end of the deflector E.D.2. Indeed, according to Fig. 5.2.2, the distance between the last accelerated orbit and the extracted trajectory at 150° means the position of the first magnetic channel is just 20 mm. Moreover, because the first magnetic channel position allows us to install compensating channels to achieve an exact four-fold symmetry, this solution will allow us to reduce the distance between the extraction path and the last accelerated orbit to 18 mm. This will also allow us to reduce the electric field and/or the length of the electrostatic deflectors E.D.1 and E.D.2.

In Tables 5.2.1 and 5.2.2 the parameters of the two electrostatic deflectors and of the magnetic channels used for this simulation are shown. In Fig. 5.2.3 the extraction path of the beam along the median plane of the cyclotron is shown. It is quite evident that it is shorter than the path shown in Fig. 5.1.6.

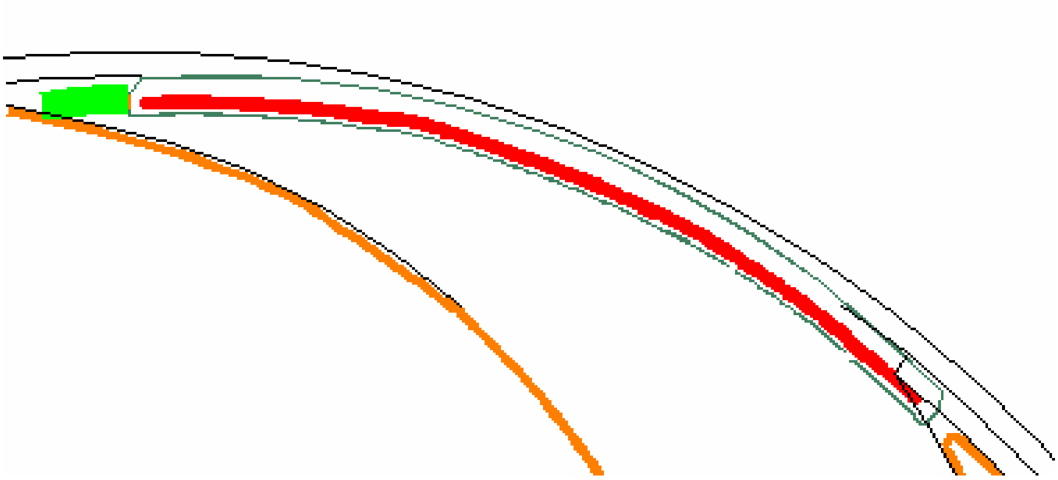

Fig. 5.2.1: Layout of the Electrostatic Deflector, complete with housing and electrode, placed on the hill of the cyclotron. This solution needs to extend the E.D. on the cover liner but allows us to install the first magnetic channel after the E.D.2.

Table 5.2.1: Position of E.D.1 and E.D.2 inside the cyclotron.

	Electrode Deflector 1	**Electrode Deflector 2**
Radii entrance side	127,92 [cm]	128,68 [cm]
Angle entrance side	108°	198°
Maximum R	129,60 [cm]	130,69[cm]
Angle of Max. R	130°	222
Radii exit side	128,42 [cm]	129,95[cm]
Angle exit side	148°	238°
Electric Field	84 kV/cm	84 kV/cm

Table 5.2.2: Parameter of the magnetic channels.

Magnetic Channel	R_{in} [cm]	θ_{in} [deg.]	θ_{out} [deg.]	**B** [kG]	$\Delta B/\Delta R$ [kG/cm]
M1	129,75	240	244	3	-1.5
M2	130,51	288	292	3	-1.5
M3	132,99	308	312	3	-3.
M4	134,92	330	346	2	-4.
M5	141,45	362	372	2	-3.
M6	154.69	386	394	2	-2.7

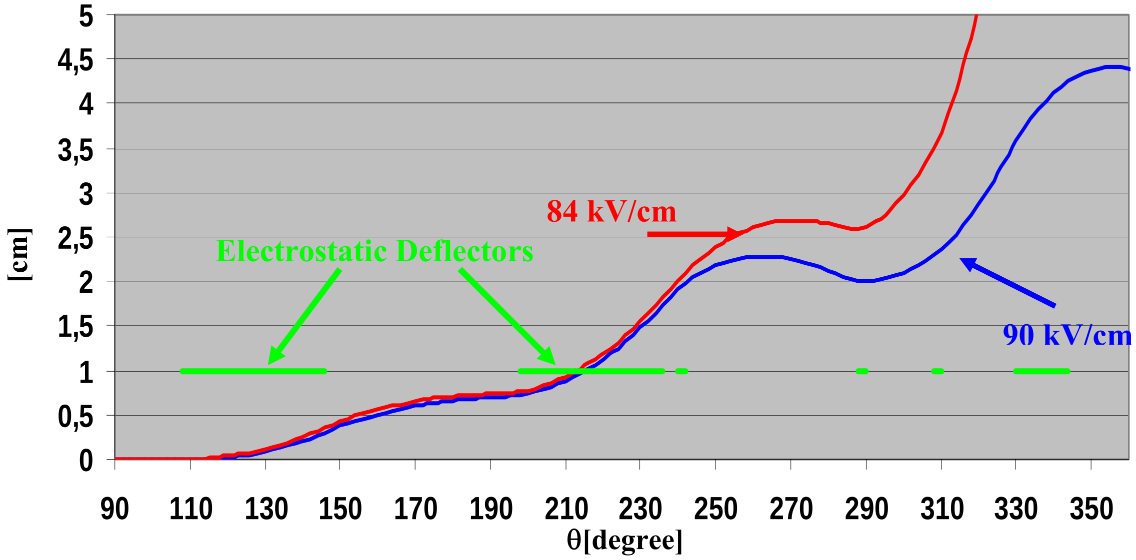

Fig. 5.2.2: Distance between accelerated orbit and extracted trajectory for two cases, one with electric field of 84 kV/cm, E.D. length 40° and with magnetic channels, the other with 90 kV/cm, E.D. length 36° and without magnetic channels.

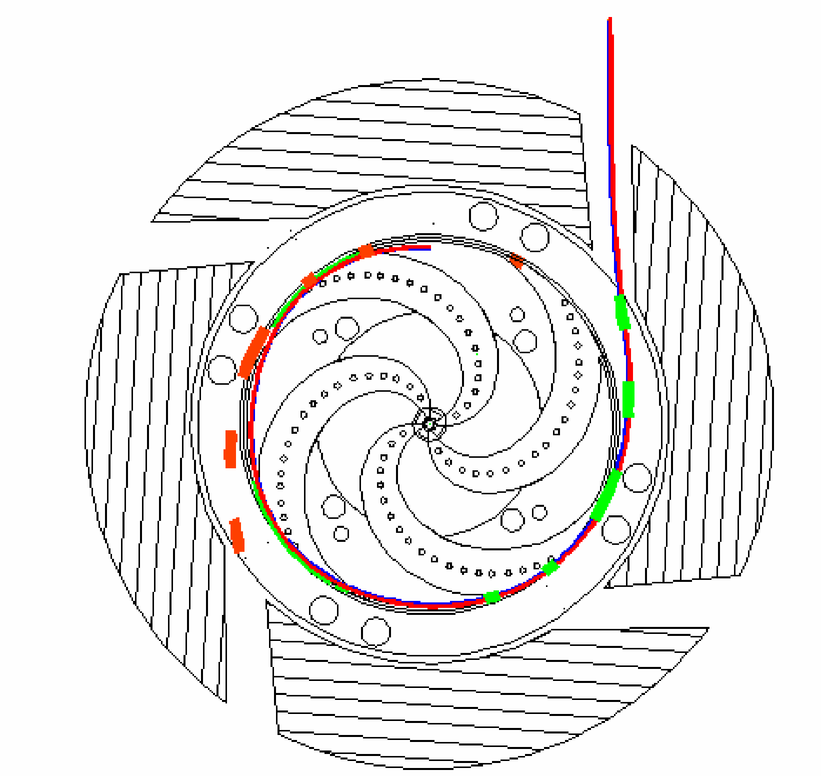

Figure 5.2.3: Extraction trajectory along the median plane of SCENT Cyclotron. The positions of the 6 magnetic channels are shown in green while the positions of the compensation bars are shown, in brown.

As shown in Fig. 5.2.4 the beam envelope for this simulation is also smaller and more symmetrical than for the previous one. This is related to the shorter length of the extraction path or, in other words, as the beam crosses the radial defocusing region in a shorter time, the extraction is more rapid. The rapid crossing of the magnetic fringing field of the cyclotron also produces a lower energy dispersion. This is well illustrated by a comparison of Fig. 5.2.6, in which the beam envelope of three beams with different energies is plotted, with the similar Fig. 5.1.7 of the previous simulation.

It is quite evident that this last extraction simulation is better than the previous one because the beam envelope is smaller everywhere and uses the same electric field as the E.D. in the previous solution. What we need is just a longer electrode and the first magnetic channel to have a dipole component of 3 kGauss. Both these conditions seem feasible and consistent with the present cyclotron design. Moreover, this solution allows us to compensate the first harmonic for the magnetic channel M1 more simply, by adding another M1 channel to the opposite hill, which is completely free. In addition, the compensation of the magnetic channel from M2 to M4 is simplified, the centre of this channel being at least 25 mm from the last accelerated orbit. In Fig. 5.2.6 the vertical beam envelope is shown. Although the vertical beam size is generally small at the end of the extraction, the beam size becomes slightly bigger.

Hence, further simulation studies are essential to find a better solution.

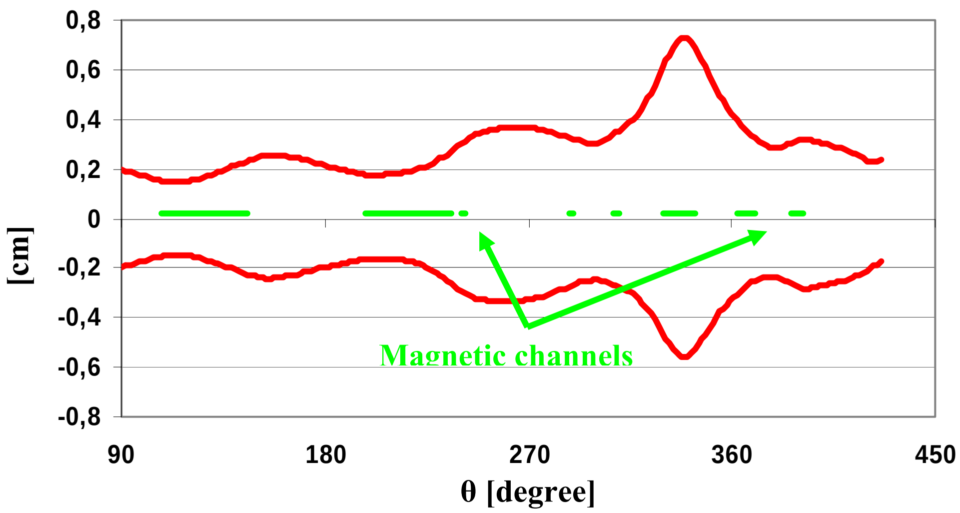

Figure 5.2.4: Radial beam envelope along the extraction path. The angular position of the magnetic channels are shown too. ε=2 π mm.mrad.

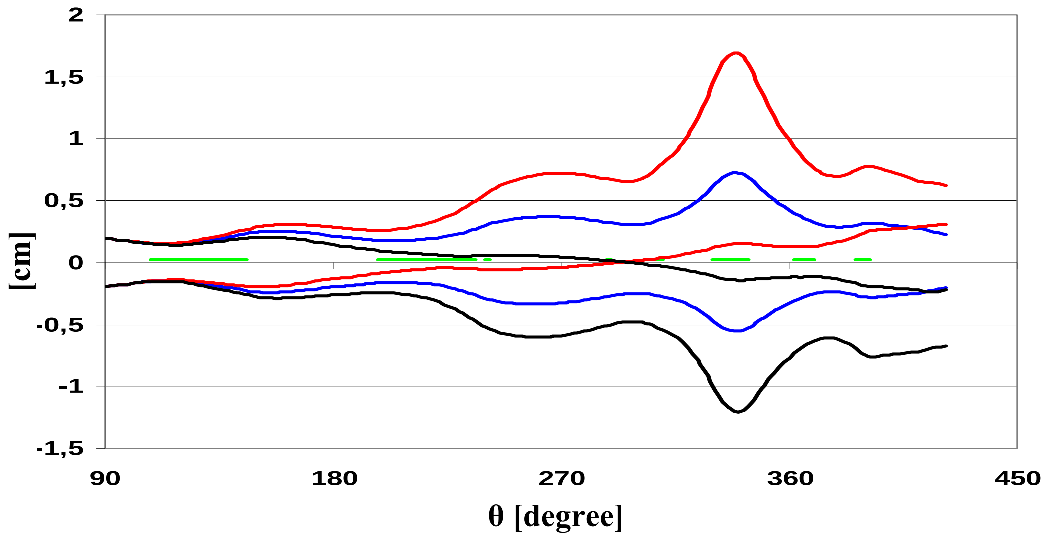

Figure 5.2.5: Radial beam envelope of three beams with different energies. The blue envelope is the nominal beam while the red and black envelopes are for energies +0.250 AMeV and –0.250 AMeV respectively.

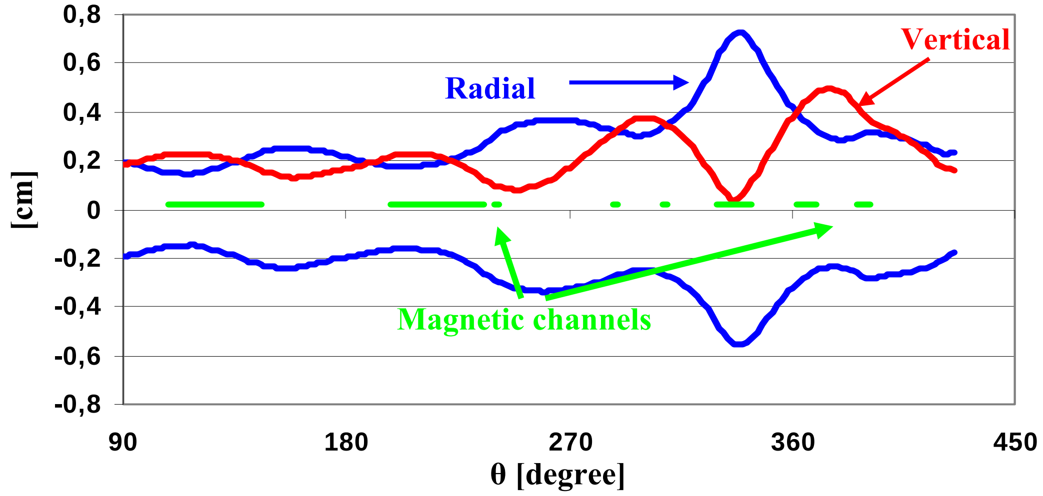

Figure 5.2.6: Radial and vertical beam envelope along the extraction path, blue and red lines respectively, emittance value 4 π mm.mrad.

5.3 Stripper extraction

The aim of the stripper extraction is to find out the radial and angular positions of the stripper, which allows us to deliver the proton beam outside the cyclotron in the same direction as the beam extracted by the E.D. Fig. 5.3.1 shows the extraction path of a 250 AMeV beam of H_2^+, which in its final part is very similar to the trajectory extracted by the electrostatic deflectors described in subsection 5.2. This trajectory is achieved by placing the stripper at the angular position of -48°. The best position for the stripper foil was found by moving the stripper along the equilibrium orbit of the particle with an energy of 250 AMeV. Despite our computer code only allowing us to change the stripper position with a step of 2°, the result achieved and shown in Fig. 5.3.1 is very good. In the simulation, the fine tuning is accomplished only by adjusting the length and the strength of the two magnetic channels, which are also used to focus the beam. Yet in reality, the radial and angular positions of the stripper can also be used to tune the position of the extraction trajectory.

The beam envelope along this trajectory is shown in Fig. 5.3.2 and the beam size shows an initial bump inside the area limited by the extraction radius, which is due to the radial defocusing magnetic field crossed by the beam in the inner region of the cyclotron.

Although it is not possible to focus the beam in the region inside the extraction radius, the beam size is acceptable. The two magnetic channels are also able to maintain the beam size at small values using moderate gradients too. The main parameters for this extraction trajectory are given in Table 5.3.1.

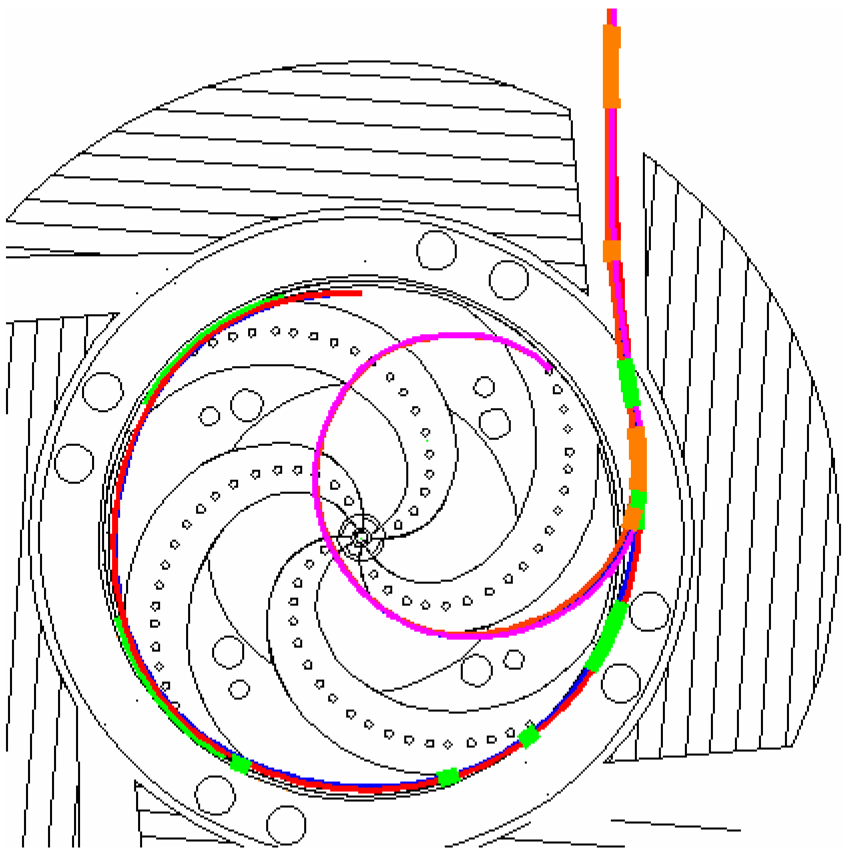

Figure 5.3.1: Stripping extraction of a proton beam with an energy of 250 AMeV. The final direction of the proton beam is put in the same direction as the E.D. extraction solution 2. The magnetic channels to steer and to focus the beam along the stripper direction are also shown.

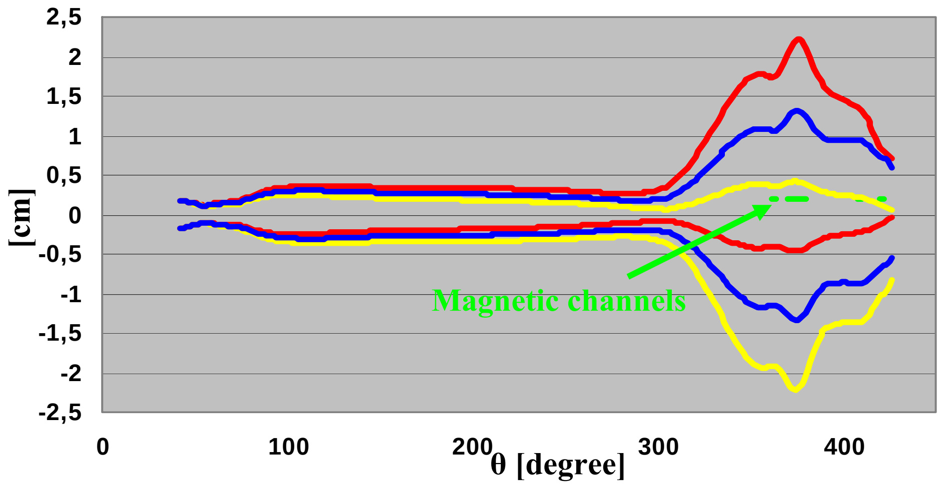

Fig. 5.3.2: Radial beam envelope of three beams with different energies along the stripping extraction. The blue envelope is the nominal beam whilst the red and yellow envelopes are for energies +/-0.25 AMeV respectively.

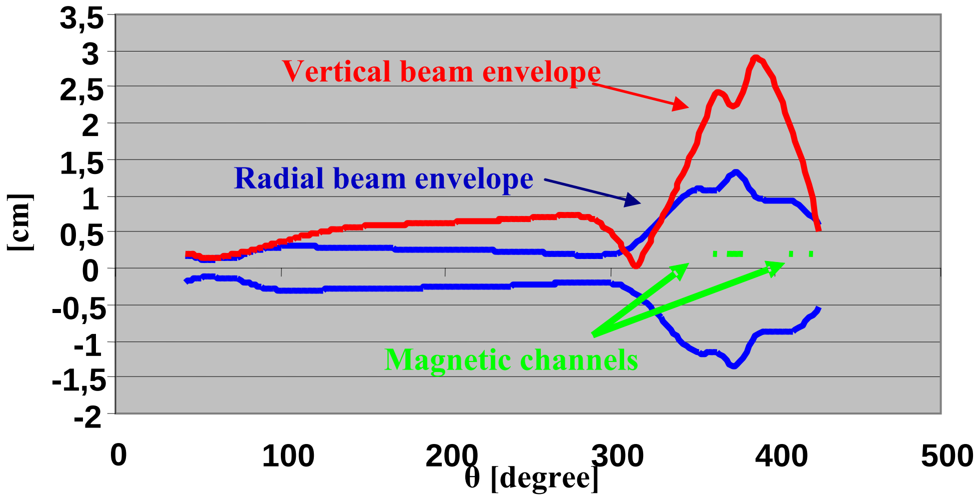

Fig. 5.3.3: Radial (blue lines) and vertical (red line) beam envelopes along the extraction path matching E.D. extraction solution 2, ε=4 π mm.mrad.

Table 5.3.1: Parameters of the magnetic channels and stripper.

Magnetic Channel	**R** [cm]	θ_{in} [deg.]	θ_{out} [deg.]	**B** [kG]	**ΔB/ΔR** [kG/cm]
M1	137.25	272	276	-1.62	1.5
M2	143.55	280	292	0.0	-3.4
M3	192.14	318	320	0.0	-0.7
M4	247.74	330	334	-3.55	0.0
Stripper	129,44	312			

To demonstrate the flexibility of the stripper extraction, the stripping extraction trajectory of H_2^+ for three cases is also reported here:

- extraction of H_2^+ beam at 250 AMeV placed in the same directions as the Carbon extraction solution 2, Fig. 5.3.1;
- extraction of H_2^+ beam at 208 AMeV placed in the same directions as the Carbon extraction solution 2, Fig. 5.3.4;
- extraction of H_2^+ beam at 208 AMeV, with final direction in the same direction as the Carbon extraction solution 1, Fig. 5.3.5.

The radial beam envelopes for the stripping extraction at 208 AMeV are also shown respectively in Fig. 5.3.6 and 5.3.8. While in Fig. 5.3.7 the vertical beam size of the beam along the stripping extraction path matching E.D. extraction solution 2 is also shown. In this case too, the vertical beam size is generally small except at the end of the extraction path. A comparison with Fig. 5.3.4 shows that the vertical beam envelope along the stripping extraction path for the 208 AMeV is smaller than for the 250 AMeV. This is probably due to the different focusing properties of the magnetic channels used in the two simulations, look at tables 5.3.1 and 5.3.2. It is evident that further simulation studies are necessary to find a better solution which will maintain the vertical beam size at acceptable values. The main difference between the stripping extraction at 250 AMeV and the extraction at 208 AMeV is that for the maximum energy an angular range for the stripper position exists, which allows the proton trajectories to escape from the cyclotron pole, whereas for the lower energy like 208, there is no stripper position which allows the trajectory to leave the pole cyclotron. In this case it is absolutely essential to use a magnetic channel to push the trajectory toward the outer radii.

Table 5.3.2: Parameters of the magnetic channels and stripper for extraction at 208 AMeV.

Magnetic Channel	**R** [cm]	**θ_{in}** [deg.]	**θ_{out}** [deg.]	**B** [kG]	**ΔB/ΔR** [kG/cm]
M1	140.81	264	272	1.75	-3.0
M2	158.40	296	306	-2.8	-2.9
M3	190.87	316	324	-3.2	1.3
Stripper	121.08	300			

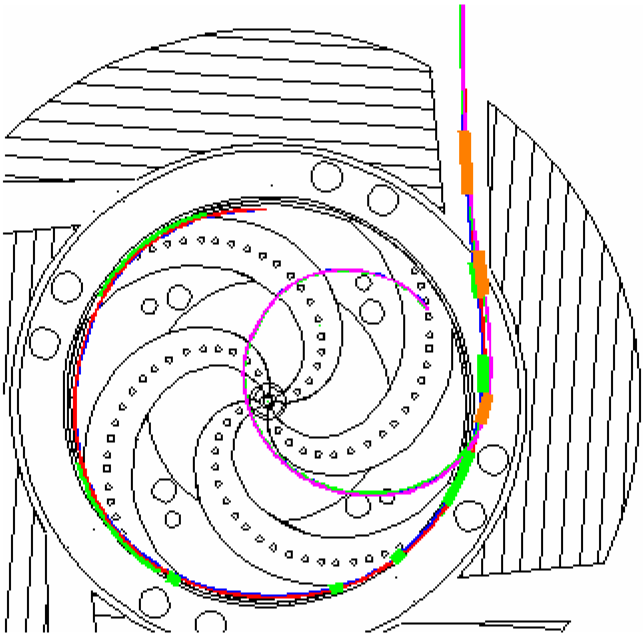

Figure 5.3.4: Stripping extraction of proton beam with energy of 208 AMeV. The final direction of the proton beam is put in the same direction as E.D. extraction solution 2.

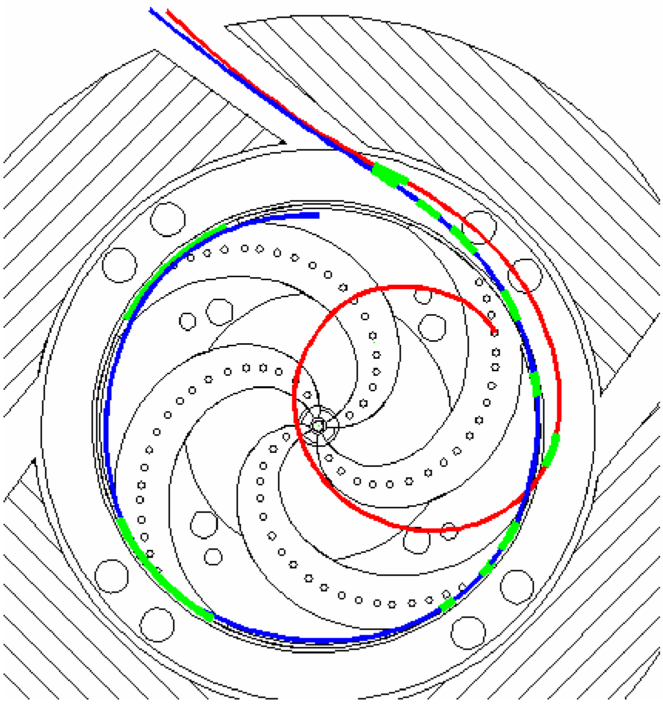

Fig 5.3.5: Stripping extraction of proton beam with an energy of 208 AMeV. The final direction of the proton beam is put in the same direction as E.D. extraction solution 1.

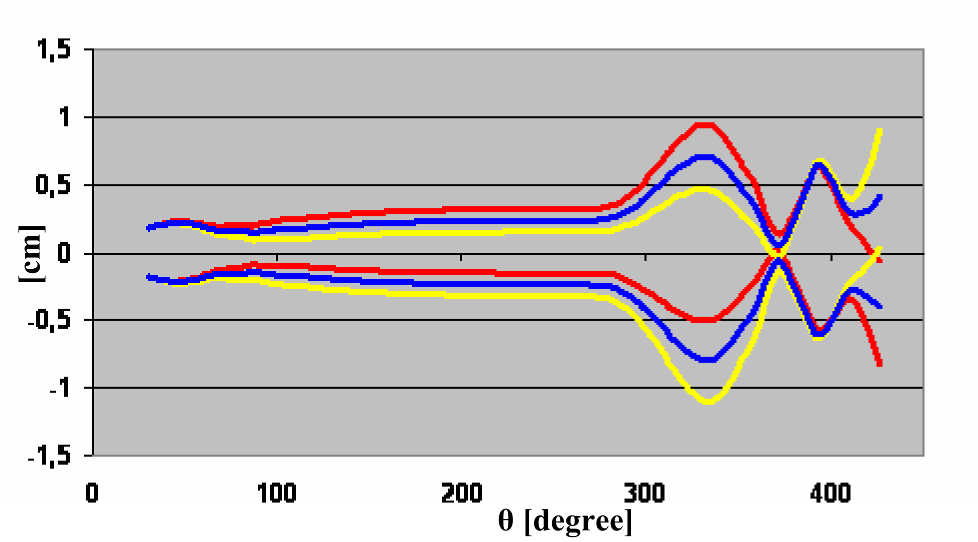

Fig. 5.3.6: Radial beam envelope of three beams with energies 208 ±0.250 AMeV along the stripping extraction which matches the E.D. extraction solution 2. The blue envelope is the nominal beam while the red and yellow envelopes are for energies ±0.250 AMeV respectively.

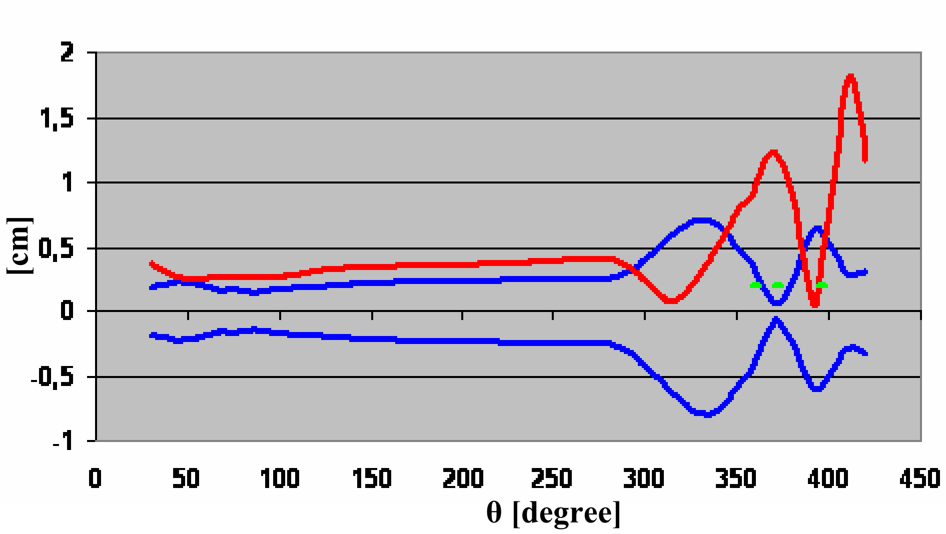

Fig. 5.3.7: Radial and vertical beam envelopes along the stripping extraction path which matches the E.D. extraction solution 2, ε=4 π mm.mrad.

With the help of the magnetic channel, it is then possible to extract the beam with energy as low as 200 AMeV. Extracting the beam with energy lower than 200 AMeV is not feasible if trajectories like those shown in Figs. 5.3.3-5.3.5 are desired. Y. Jongen [5] has recently shown that stripper extraction of a beam with lower energies is also feasible if the extraction trajectory runs for two or more turns inside the cyclotron pole.

The stripping extraction at 208 AMeV was performed to show that if the present cyclotron design is scaled up to a maximum energy of 300 AMeV, the extraction of a proton beam with an energy of 250 AMeV is feasible.

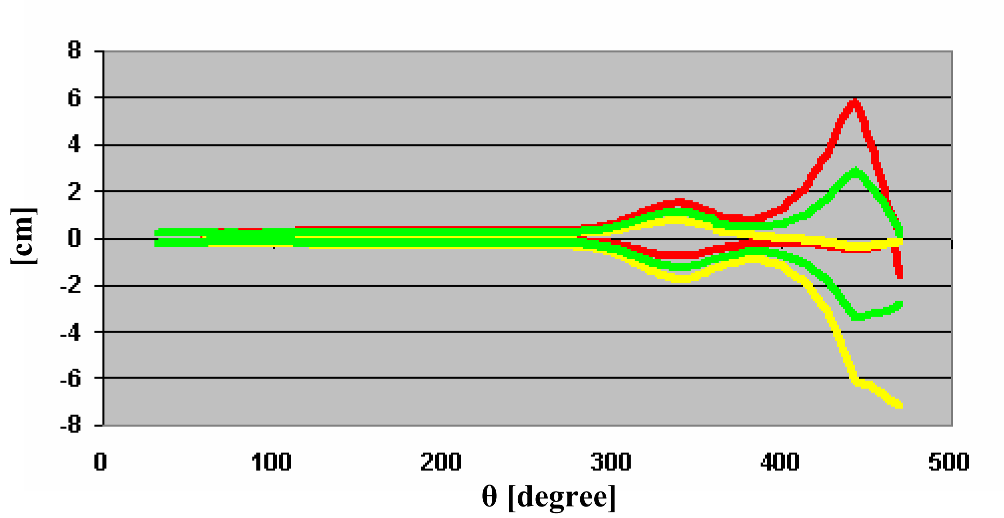

Fig. 5.3.8: Beam envelope of three beams with different energies along the stripping extraction which matches the E.D. extraction solution 1. The blue envelope is the nominal beam while the red and yellow envelopes are for energies +0.250 AMeV and –0.250 AMeV respectively.

5.4 Magnetic channel

For beam extraction, the use of electrostatic deflectors has been chosen. In high energy cyclotrons, passive magnetic channels are also used in addition to such deflectors. These channels use uniformly saturated iron bars, which modify the magnetic field in the extraction region: the beam passes through the channels. They provide a double effect. Firstly, they help the beam extraction by modifying the magnetic field shield with a step that kicks the beam; secondly, they provide a radial focusing force generated by their positive field gradient that contrasts with the main defocusing fringe field [6-9].

The field properties in the beam aperture have been analysed using a multipole expansion of the magnetic field in a 2D approximation on a longitudinal section of the cyclotron. Assuming that the iron bars are uniformly magnetized (the magnetic saturation is a must because the bars are immersed in the cyclotron's main magnetic field), then the magnetic field on the median plane due to a single iron bar of thickness *t* and height *2h*, placed at a distance *d* from the origin, can be written as:

$$B_z(x,y) = A\left[arctg\left(\frac{h-y}{d-x}\right) - arctg\left(\frac{h-y}{d+t-x}\right) + arctg\left(\frac{h+y}{d-x}\right) - arctg\left(\frac{h+y}{d+t+x}\right)\right] \quad (5.4.1)$$

where A=-3.375 kGauss in the case of iron saturated to 21.4 kGauss [6] and the origin coincides with the centre of the beam.

The magnetic field gradient Gz(x,y) is simply derived by (5.4.1).

By considering a magnetic channel made up of three iron bars as shown in Fig. 5.4.1 (x is the cyclotron radius), we have evaluated the magnetic field with the three iron bars as the superposition of (5.4.1), each term with correct values.

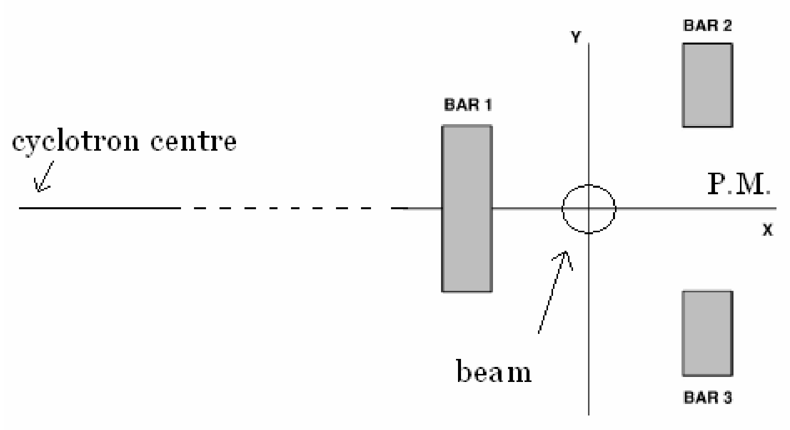

Fig. 5.4.1: Typical magnetic channel design.

Then we have dimensioned the bars to obtain a magnetic field in the origin of -3 kGauss with a gradient of about 1.5 kGauss/cm (these values are extracted to compensate for the cyclotron's main magnetic field).

The bar #1 will be 3.6 cm high, 0.6 cm wide, located 0.5 cm on the left of the origin symmetric on the median plane.

The bars #2 and #3 will be 0.2 cm high, 0.4 cm wide, located 0.5 cm on the right of the origin and +/-1.8 cm from the median plane.

Figures 5.4.2 and 5.4.3 show the magnetic field and the gradient of the magnetic channel with the chosen parameters.

To maintain the symmetry of the total magnetic field of the cyclotron, it is necessary to balance the field generated by the magnetic channel with another passive element that is located symmetrically with respect to the centre of the cyclotron and to the magnetic channel. In that region, the presence of an electrostatic deflector forces the position of the magnetic channel 0.51 cm outwards, as shown in Fig. 5.4.4.

Systems made up of 3 iron bars or a single iron bar have been analysed as solutions that will compensate for the magnetic field generated by the magnetic channel. Figures 5.4.5 and 5.4.6 show the two magnetic fields around the cyclotron radius and the difference between them, in the case of 3 iron bars.

Both solutions provide a difference between the magnetic field generated by the magnetic channel and the compensation magnetic field of ±30 Gauss, the acceptable value.

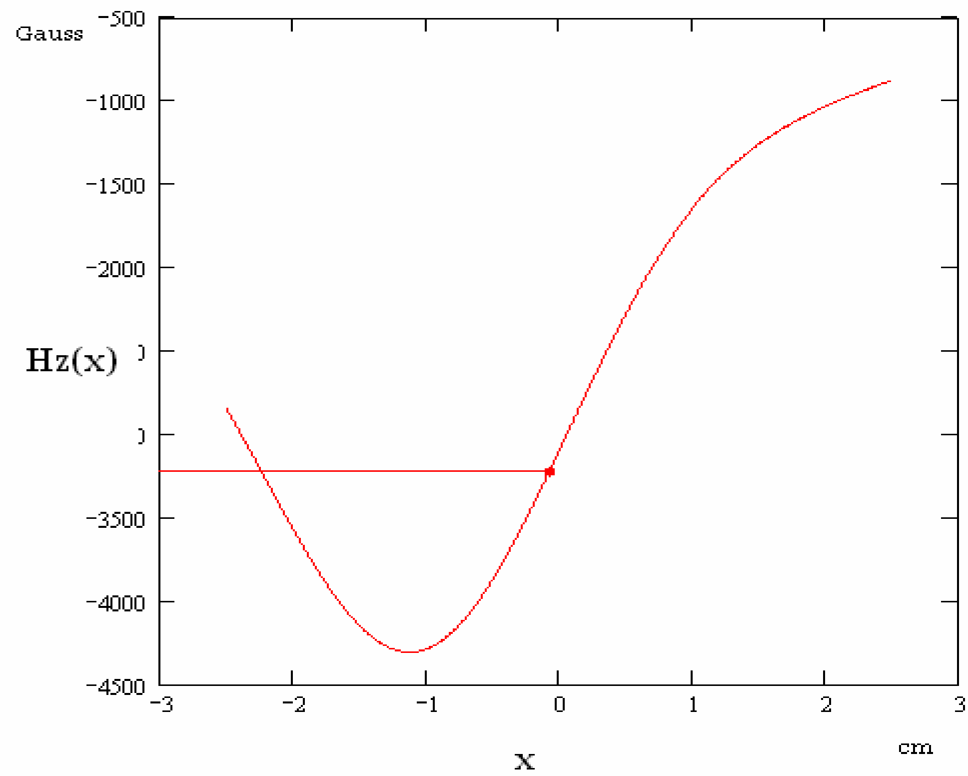

Fig. 5.4.2: Magnetic field around the radius on the median plane.

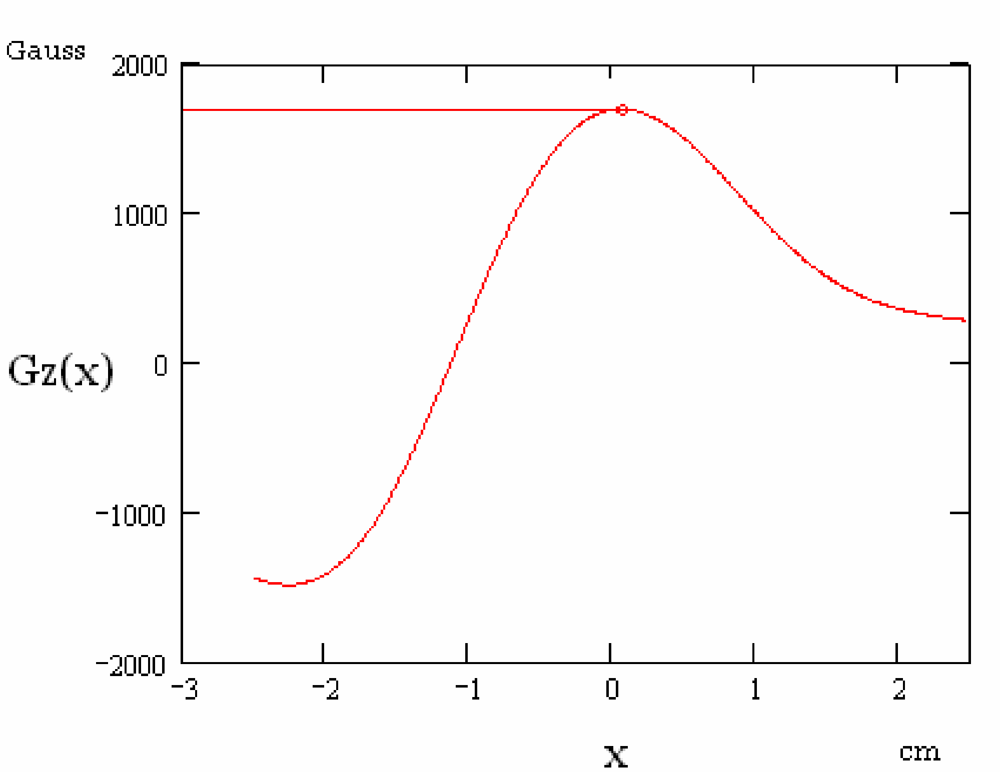

Fig. 5.4.3: Magnetic field gradient around the radius on the median plane.

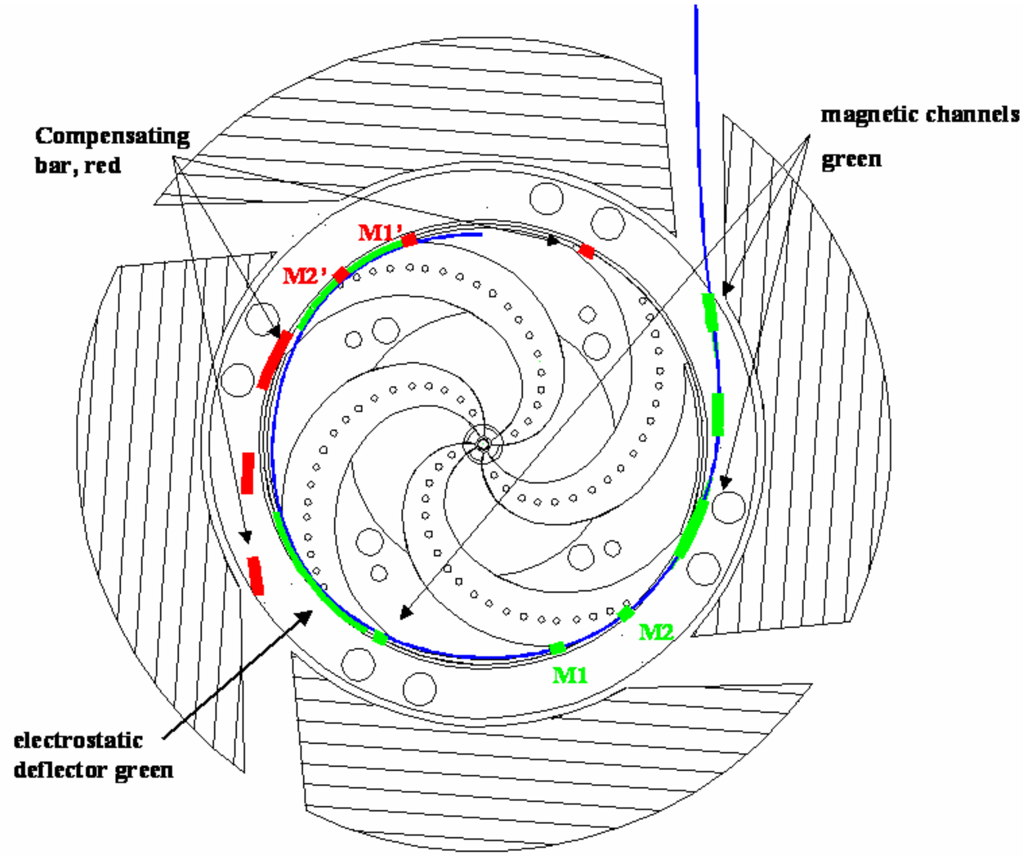

Fig. 5.4.4: Layout of the cyclotron: the compensation elements M1’ and M2’ (red, on the left) are symmetric with respect to the cyclotron centre to the magnetic channels (green, on the right), but located 5.1 mm towards the outside.

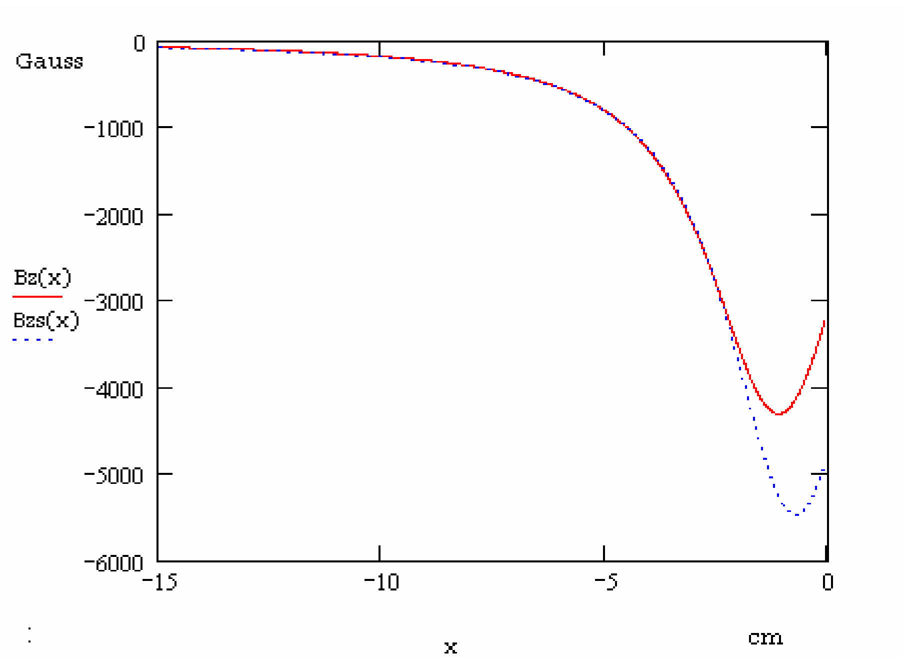

Fig. 5.4.5: Magnetic fields around the radius on the median plane.

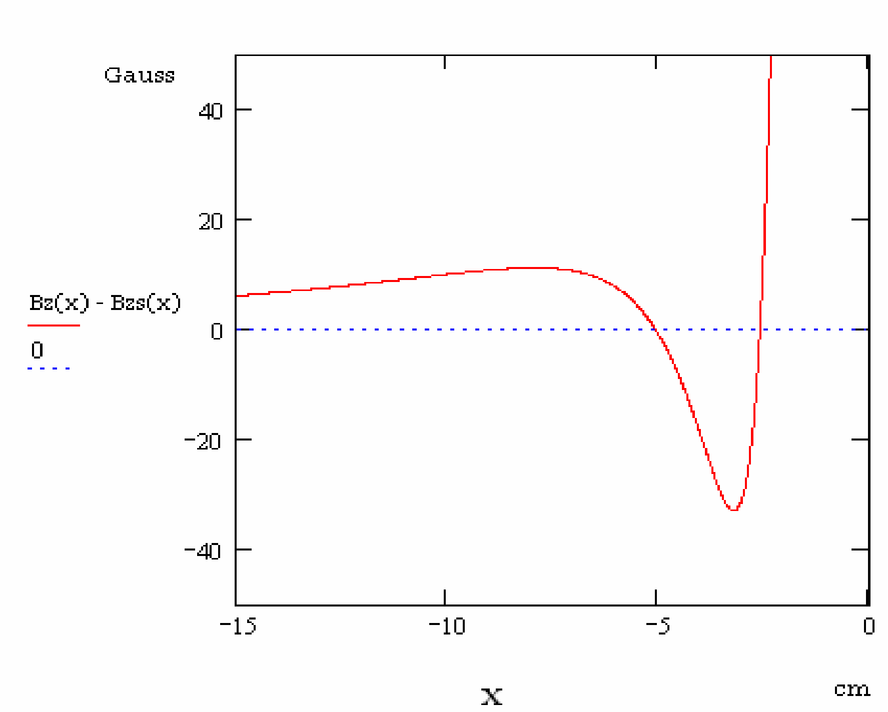

Fig. 5.4.6: Difference between the two magnetic fields around the radius on the median plane.

5.5 References

[1] D. Rifuggiato et al., *"Ten Years of Operations with the LNS Superconducting Cyclotron"*, XVII ICCA, Tokyo (2004) p. 118.

[2] ACCEL, private communication.

[3] GENSPE Code, NSCL-MSU.

[4] Th. Stambach et al., Nucl. Instr. & Meth. in Phys. Res. B113(1996) 1.

[5] W. Kleeven et al., *"Design of a K=1600 compact superconducting cyclotron for therapy by Carbon beams"*, XXXIV European Cyclotron Progress Meeting, Belgrade (2005).

[6] P. R. Sarma, *"Improvement of field quality in passive magntic channels by using linear programming technique"*. NIM A 455 (2000) pp. 539-544.

[7] B. Carbonel, *"Calculation of the geometry f magnetic channels for synchrocyclotrons and cyclotrons"*. NIM 84 (1970) 144-146.

[8] G. Bellomo,*"Design of passive magnetic channels"*. Proceedings of Cyclotrons 1994.

[9] M. M. Gordon, "*The Z4 orbit code and the focusing bar fields used in beam extraction calculations for superconducting cyclotrons*". NIM A 247 (1986), pp. 423-430.

Chapter 6. Losses and vacuum requirements

6.1 Introduction

The acceleration of molecular beam like H_2^+ needs to work with a good vacuum. Despite, due to the high binding energy of the H_2^+ molecule, ≈16.3 eV vs. 0.7 eV of H^-, it is possible to use magnetic fields as high as 10 T even at energies as high as 1 AGeV without any beam losses due to electromagnetic dissociation. Beam losses along the acceleration path are can be large due to the interactions of the H_2^+ ionized molecule with residual gases. These may produce stripping of the electron of H_2^+. In general, for a molecule this probability is higher than for a simple ion. The fraction of lost beam particles was evaluated according to the Betz-Bohr model [1] that takes into account the beam cross section for electrons lost versus the beam energy. It is summarized by the following formula:

$$Losses = 1 - \frac{N}{N_0} = 1 - e^{-\frac{P}{KT}\int \sigma(E)d\ell} \qquad (6.1)$$

where P is the pressure (Pa), ℓ is the path length (m), $\sigma(E)$ is the cross section of electron loss. The formula to evaluate $\sigma(E)$ is:

$$\sigma(E) \approx 4\pi a_0^2 (v_0 / v)^2 \left(Z_t^2 + Z_t\right) / Z_i^2 \qquad (6.2)$$

where a_0 and v_0 are the orbital radius and the speed of the electron, Z_i and Z_t are the number of electrons of the incident H_2^+ and of the residual gases respectively, v is the velocity of the accelerated H_2^+.

When reading the historical proceedings of the ICCA, we found a nice picture in H. Steimel's paper [2] which shows the measured current of a H_2^+ beam vs. radius. To check the formula (6.1) and the value of the parameter a_0 we evaluated the beam losses for the Karlsrhue cyclotron and compared them with the experimental results. Although our simulation overestimates the losses at inner radii and underestimates them at outer radii, the agreement was quite satisfactory, see Fig. 6.1.1. Perhaps the differences are due to our assumption of constant accelerating voltage at all radii (240 kV/turn) and of a uniform pressure of $2 \cdot 10^{-6}$ Torr, as reported by the authors. On the contrary, if the pressure is better in the central region than in the outer and/or if the accelerating voltage is higher at the inner radii, this could give a reasonable explanation for the slight differences.

Hence we used the previous formula to evaluate the beam losses for the present cyclotron design. We assumed an accelerating mean voltage of 800 kV per turn and a pressure value of 10^{-7} mBar. Most of the beam current is lost at small radii along the initial orbits where the beam has low speed, whilst a large amount of the power is lost at outer radii where the beam is more energetic.

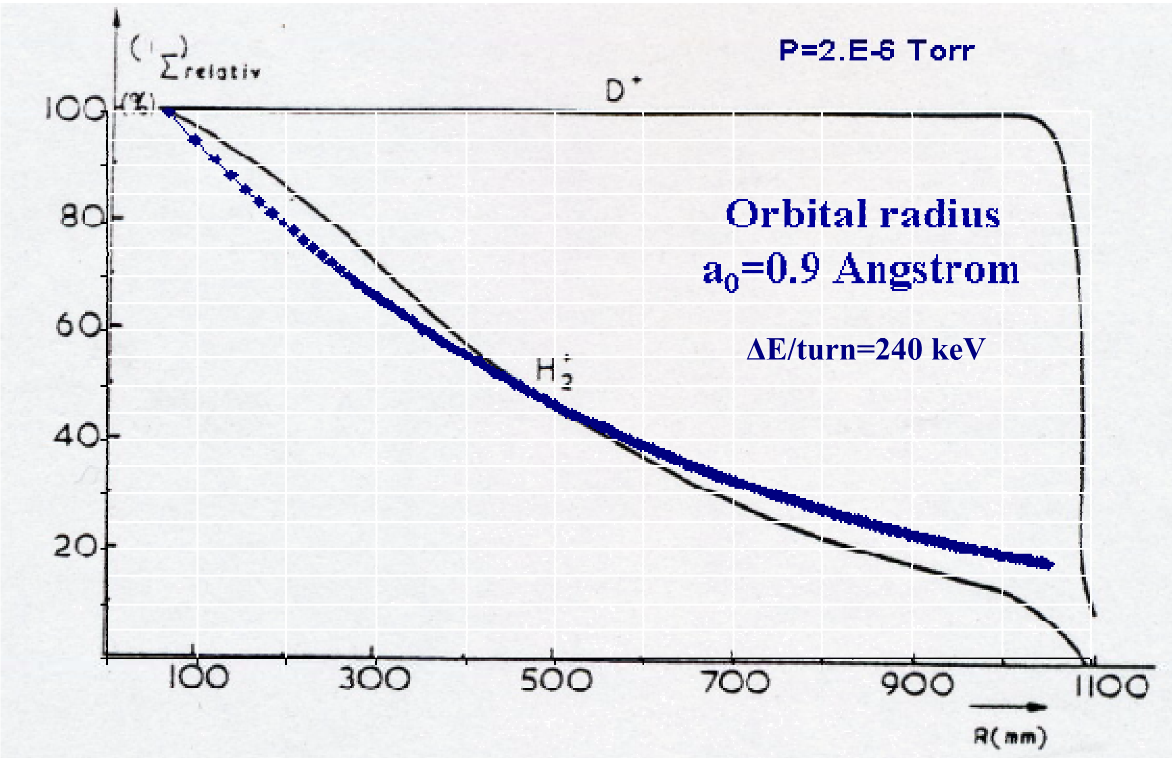

Fig. 6.1.1 Total current vs. radius for the H_2^+ and D^+ inside the Karlsruhe cyclotron. The blue dots are evaluated according to the formula (6.1) reported in the text (Int. Conf. On Sect. Foc. Cyc. And Meson Factories, Geneva (1963), p. 24).

We evaluated both the intensity and power losses by integrating formula (6.1) turn by turn. The expected beam loss right along the machine should be 2.8%, while the total power loss amounts to 100 W for an accelerating beam of 10 kW, see Fig. 6.1.2. These power losses are quite small and acceptable for the proposed cyclotron.

According to the Fig. 6.1.2, it is quite evident that most beam power is lost at the end of the acceleration or at outer radii. Consequently, a higher accelerating voltage at outer radii could significantly decrease the power beam lost inside the cyclotron.

Of course, a better vacuum could also significantly reduce the losses, see Fig. 6.1.3. If lower beam current have to be delivered, as for instance to accomplish therapy treatment or during the cyclotron commissioning, the vacuum pressure could be also higher, up to $5 \cdot 10^{-7}$ or 10^{-6} mBar if H_2^+ or C^{6+} are respectively accelerated.

For totally stripped Carbon the beam loss is due to electronic capture. At a pressure of 10^{-7} mBar, the lost beam is about 0.05% during the first 15 turns of acceleration. Moreover, when it gains higher energy (6 AMeV), its loss is about 4-5 order of magnitude lower, if compared with the calculated value for H_2^+.

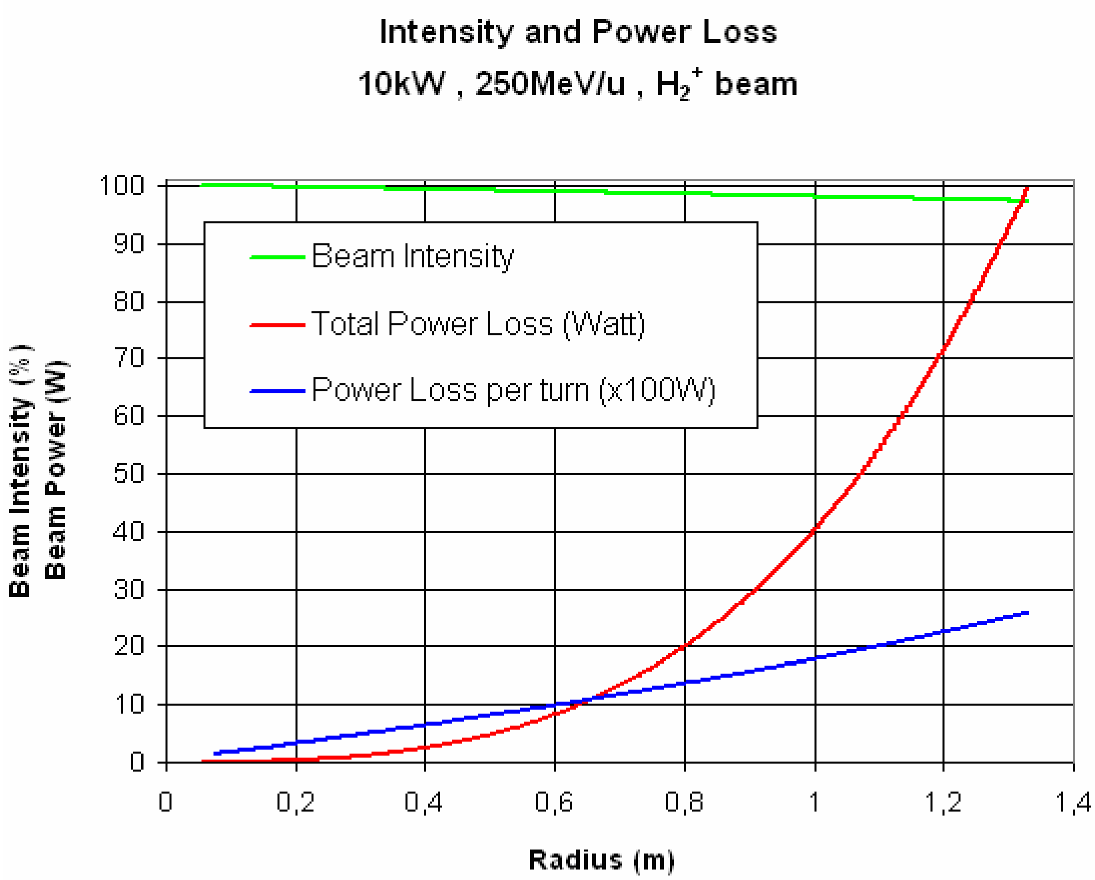

Fig. 6.1.2: The H_2^+ beam intensity, the power loss per turn and the integral power loss vs. radius of the orbit. The vacuum pressure being 10^{-7} mbar.

This analysis shows that a pressure of 10^{-7} mbar is indicated as operational pressure with acceptable beam losses when a beam power of 10-20 kW have to be delivered.

In the case of therapy treatment the maximum delivered beam power being of 125 W [3,4] the operational pressure can be increased up to 10^{-6} with an expected beam loss for H_2^+ of about 27%, corresponding to 12.5 W. These power losses are acceptable for the accelerator and for the cryogenic plant. Our experience with the K800 superconducting cyclotron also shows that with beam power higher than 100 W, lost at the extraction radius (very close to the cryostat), there are no detectable effects on the cryogenic parameters of the cryostat or other devices of the machine.

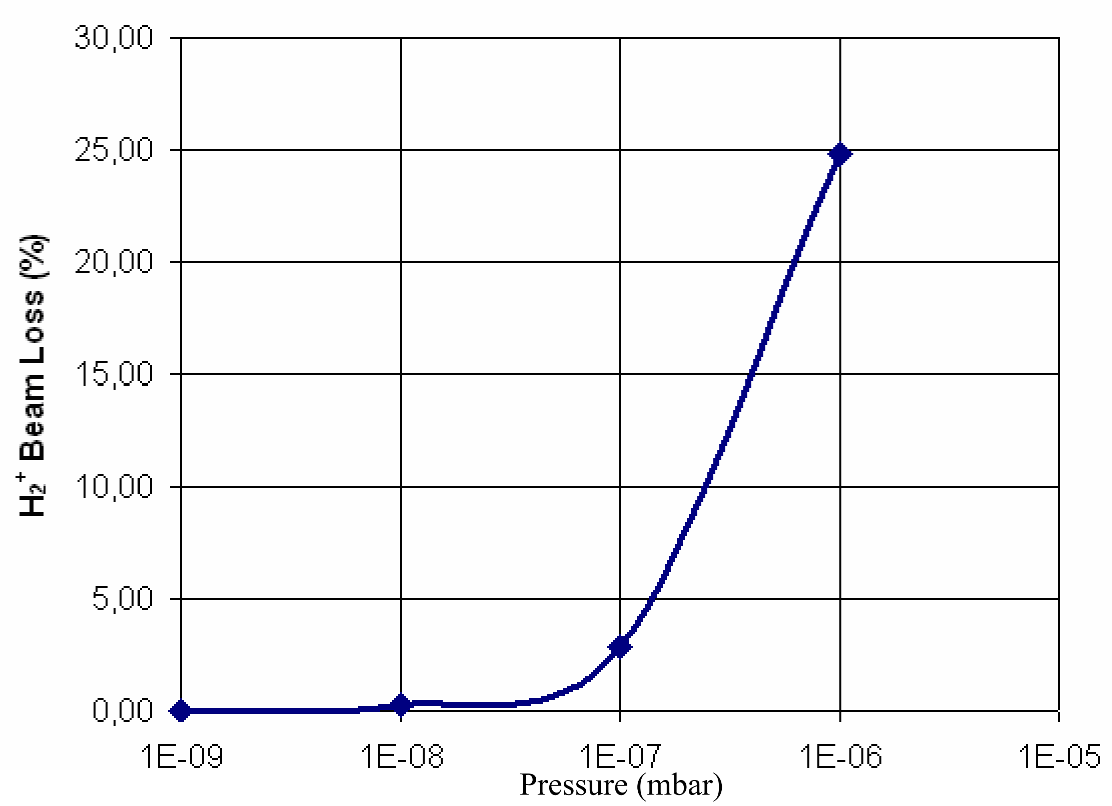

Fig. 6.1.3: Integral H_2^+ beam loss along the acceleration inside the cyclotron vs. vacuum pressure.

As far as the cyclotron liner is concerned, some unconventional alternatives were investigated about the possibility of eliminating the liner and replacing it with a 20 μm thick coating applied by a physical deposition, which would be situated on the pole of the magnet. Although this solution has several constructional good points, there are many technical disadvantages both in the planning stage of the cavities and in the operation, because the heat dissipation of the cavities influences the ironic temperature so that the magnetic characteristics are modified.

6.2 Layout of the vacuum chamber

In Fig. 6.2.1 the vertical cross section of only the cyclotron's main components is shown. A lot of the vertical holes drilled through the yoke are not shown for the sake of simplicity. The yellow line, shown in Fig. 6.2.1, is the RF liner.

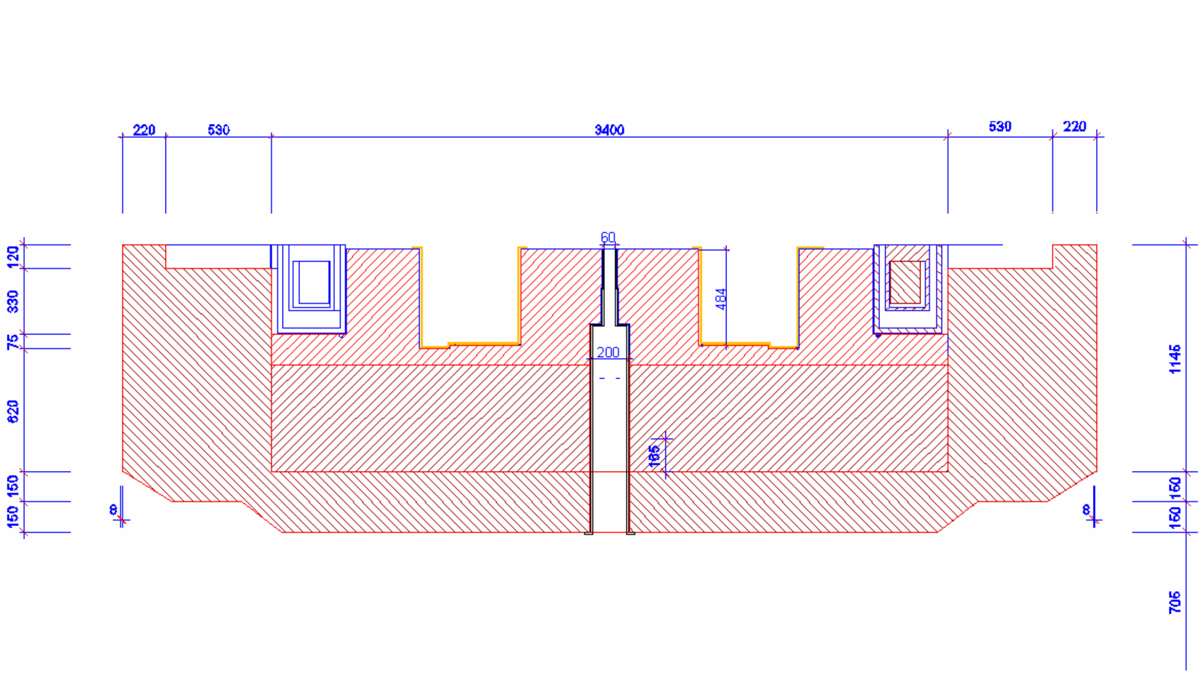

Fig. 6.2.1: Vertical cross section of half cyclotron.

In figure 6.2.2 a vertical cross section of the inner side of the cyclotron indicating the position of the main O'rings is shown. The boundaries of the vacuum chamber are:

- the surface of the cryostate inner ferrule (A), see Fig. 6.2.1;
- the iron pole surface, except the surface of the valley (B);
- the inner surface of the liner (C);
- the outer surface of the liner which is in front of the iron hill (D);
- the surface of the RF cavity Dee;
- the inner and outer surfaces of the 3 stems of each cavity;
- the surface of the extraction channel;
- the surface of 10 magnetic channels;
- the surface of 2 electrostatic deflectors;
- the surface of 4 couplers and 4 trimmers.

In Fig. 6.2.3, a top view of the cyclotron with the positions of the main O'ring are shown. In this last figure, the O'ring of the central axial hole is not shown. The vertical holes for the Trim Rods, which are drilled along the center of the hill, do not pass through the iron of the hill but end 10 mm before the inner pole surface, to reduce the number of O'rings and reduce the vacuum leaks. The top and bottom sides of the RF liner must be machined to host an

O’ring which seals each valley, up and down. The present design of the cyclotron valley plans to have a step, because the depth of the valley is not constant.

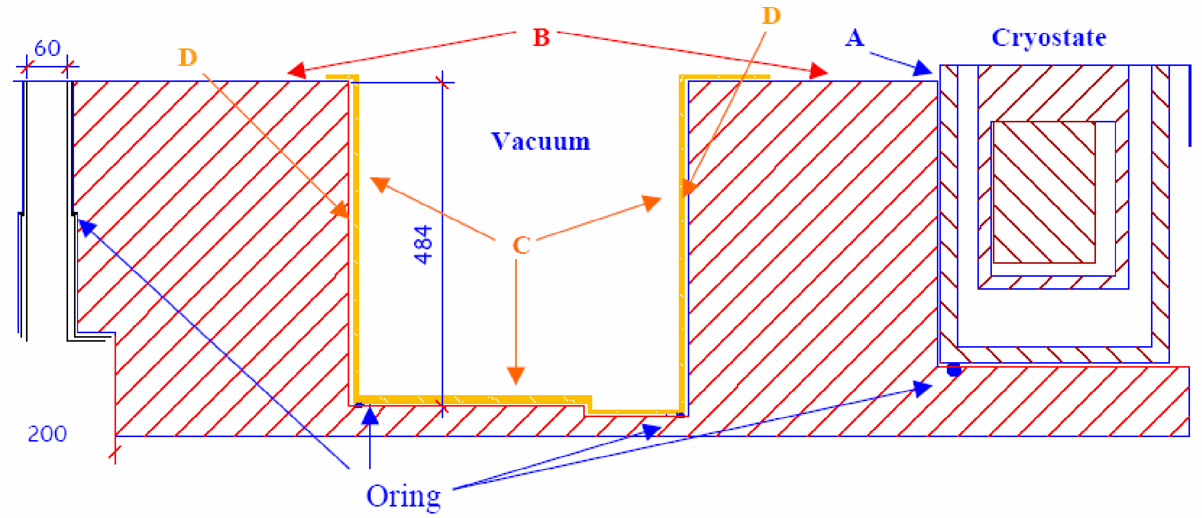

Fig. 6.2.2: Vertical cross section of a part of the cyclotron. The yellow part is the RF liner. The positions of the O’ring are also shown. The iron pole must be a single piece just to reduce the number of O’rings. The minimum diameter of this piece must be at least 2800 mm, just a little bigger than the O’ring placed below the cryostat. The letters indicate the surfaces in vacuum. See the text for more details.

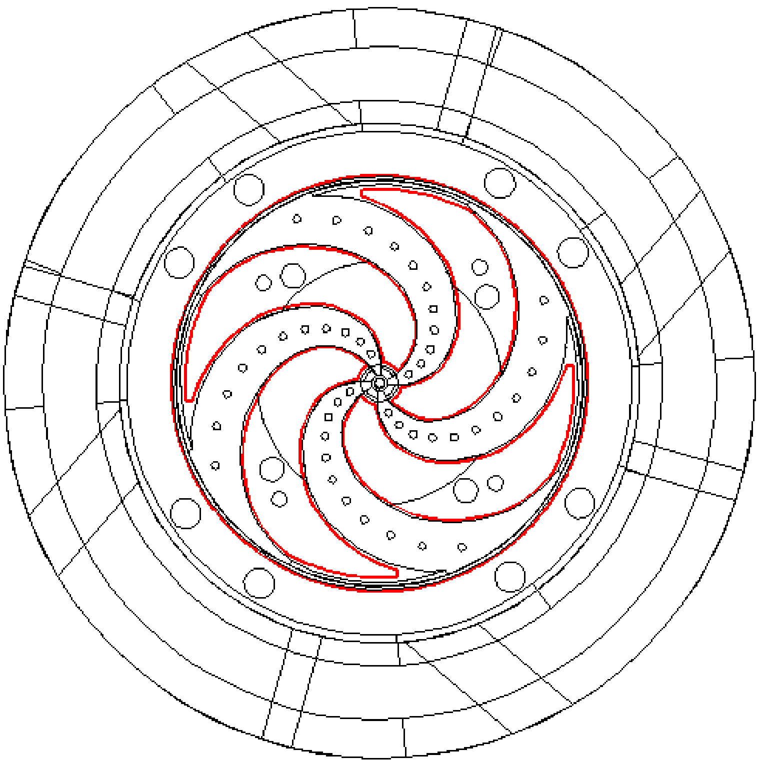

Fig. 6.2.3: View of the cyclotron from the median plane.

The valley region at inner radii is shallower than at outer radii so allowing us to increase the flutter at outer radii. This step produces a problem as regards the sealing by O'ring. A possible solution in overcoming this problem is to design all of the valley with the same depth, and to remove the iron from the outer radii below the iron plate which seals the valley. See Fig. 6.2.1 and Fig. 6.2.2.

In Fig. 6.2.3 a view of the cyclotron from the median plane is shown. The red lines are the paths of the main O'rings. The O'ring in the central axial hole is not shown. The Trim Rods hole, along the middle line of the hill, despite the picture, finishes 10 mm before the iron surface so they are in the air.

The vertical cross section of a part of the cyclotron is shown in Fig. 6.2.4. There is shown the tube of the RF, which allows to pump the vacuum chamber by turbo pump, from the bottom side of RF cavity, and if necessary to insert the cryo-pump's head from the top side. A piece of iron, just below the pole, has been removed to increase the flutter at outer radii. This solution is different respect the Fig. 6.2.2 and 6.2.3. We have to modify the pole design according to this figure to allow to use a single O'ring for each cavity to seals each valley. The actual design as already mentioned has a step in the valley and this prevent to place a single O'ring.

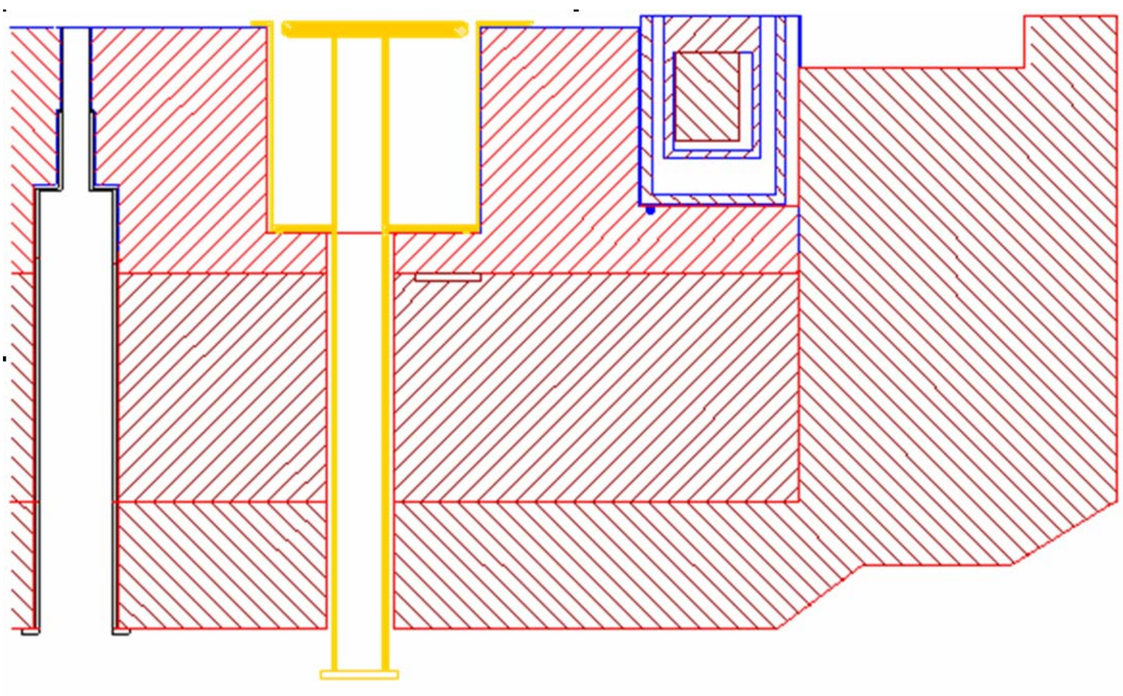

Fig. 6.2.4: Vertical cross section of a part of the cyclotron.

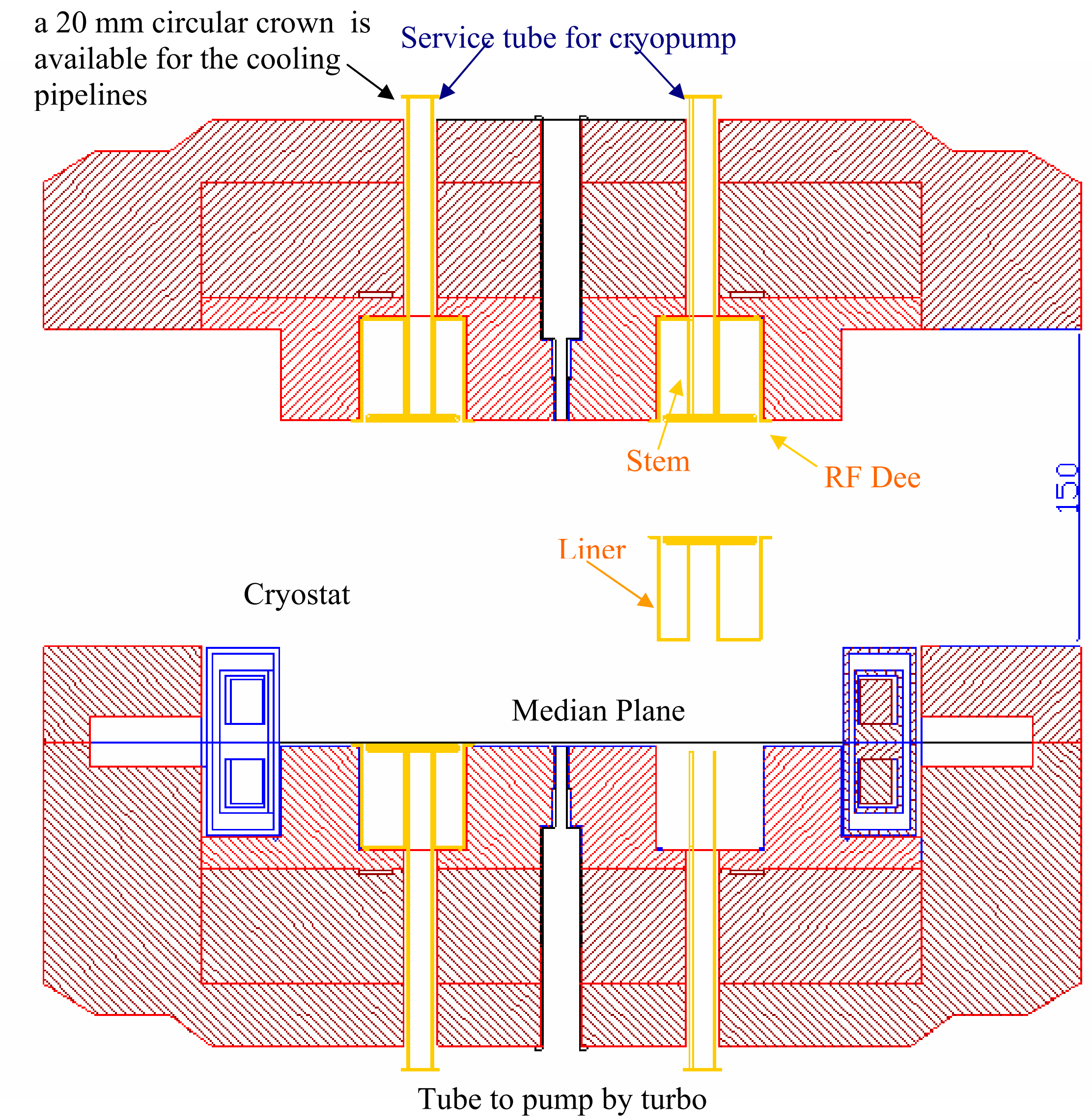

Fig. 6.2.5: View of open cyclotron, during the operation to mount/dis-mount the RF cavity complete of the Liner. The tube for pumping system is installed from the outside.

Fig. 6.2.6 shows a cross section of the RF cavity. In this figure, the tube for the pumping system and the cooling tubes are also shown.

The operation of connecting or disconnecting the cooling tube has to be described properly. Two solutions are feasible:

a) The pipelines are disconnected at the liner position inside the pole. In this case, the tube can be small and made out of copper, capable of working at a pressure of 10 bar. The geometry shown in the figure is not right. The rigid tube must be movable for half a meter, so the length of the tube must be at least half a meter longer than the length of the pole cap of iron yoke. In this way, all the tubes can have an extra length inside the valley of half a meter to allow for connection on the outer side of the liner. Then the cavity and the pipelines are shifted into their final position inside the valley. The tube then exceeds in length from the yoke side.

b) The pipelines are disconnected outside the iron yoke. In this case, the cable must be flexible to allow for insertion (or removal) from the internal side. This poses a problem for the availability of flexible cable capable of operating at 10 bar.

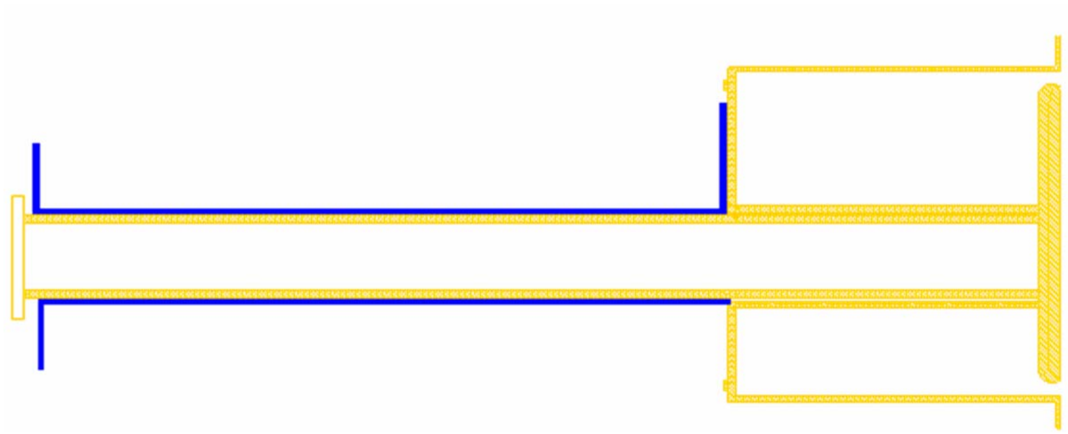

Fig. 6.2.6: Cross section of the RF cavity and its liner.

6.3 Calculations for the vacuum system

Although a vacuum of 10^{-7} Torr is also nowadays feasible in a cyclotron, to achieve this goal careful treatment of all the surfaces inside the vacuum chamber is required. We have evaluated [5-7] and compared some different solutions concerning the vacuum plant suitable for this cyclotron. We have taken into account three different solutions which are here illustrated and discussed:

- 4 turbo pumps and 4 "splitted" cryo-pumps;
- 4 turbo pumps and 4 diffusive pumps;
- 8 turbo pumps.

The materials exposed to the vacuum are mainly:

- Stainless STeel (SST) AISI 316, from the cryostat inner ferrule;
- soft Iron, chemically nickel plated (Ni/Fe), from the magnetic pole;
- OFHC Copper (Cu), from the cavity and the liner;

- Viton, from the o-ring of the cryostat (n. 2) and the sealing on the bottom of the cavities (n. 8).

From published data it is not possible to estimate with a high degree of accuracy the outgassing rate of each of these materials, since this value strongly depends on the production process of the raw materials and their treatments. The following data refers to materials that were cleaned (with tensio-active and organic solvents) and put for 20-30 hours under vacuum. In addition, for the Cu we also had to consider a dry abrasive surface treatment to remove the oxide layer. Moreover, since viton exhibits a strong outgassing rate (10^{-3} mbar l s^{-1} even after 24h under vacuum), it has to be vacuum backed in a separate chamber for about 12h at 150-200 °C. As a result of this treatment, the total outgassing rate is reduced to about 34% of the initial value, whilst the permeation will take the place of the main gas source from the o-ring. We wish to point out that if other viton sealing is needed in the cyclotron, the total outgassing rate (together with the permeation contribution) could be critical. In this case we suggest adopting a double O'ring system for the two main O'rings, where the volume in-between these two seals is differentially pumped to a pressure lower than 10 mbar. This will greatly reduce the gas permeation.

Taking both our operational experience and published data into consideration [6-9], we can establish with a good degree of confidence that the specific outgassing rates are:

- SST: $5 \cdot 10^{-10}$ mbar l s^{-1} cm^{-2}, composed of: 0% H_2O, 10% CO, 50% H_2.
- Ni/Fe: $5 \cdot 10^{-10}$ mbar l s^{-1} cm^{-2}, composed of: 40% H_2O, 10% CO, 50% H_2.
- Cu: $1 \cdot 10^{-10}$ mbar l s^{-1} cm^{-2}, composed of: 10% H_2O, 40% CO, 40% H_2.
- Viton: $1 \cdot 10^{-8}$ mbar l s^{-1} cm^{-1}, due to 34% outgassing and 66% permeation, composed of: 35 % of H_2O + 15% solvents and monomers, 10% of N_2 e 40% of O_2.

In order to get more precise values, it is strongly recommended to compare our operational data with that of the company supplying the materials, carrying out the treatments and building the vacuum chamber.

The outgassing rate is hence calculated by evaluating the exposed surfaces:

- 88000 cm^2 of SST $\rightarrow 4.4 \cdot 10^{-5}$ mbar l s^{-1};
- 380000 cm^2 of Ni/Fe $\rightarrow 1.9 \cdot 10^{-4}$ mbar l s^{-1};
- 583000 cm^2 of Cu $\rightarrow 5.8 \cdot 10^{-5}$ mbar l s^{-1};
- 6000 cm of Viton $\rightarrow 5.9 \cdot 10^{-5}$ mbar l s^{-1}.

From these values it is possible to estimate the total gas release rate after 24 hours under vacuum: $3.4 \cdot 10^{-4}$ mbar l s^{-1}, composed of 36% H_2O, 13 % CO, 2% N_2, 7% O_2, and 42% H_2.

The total leak rate from the welding parts is considered to be lower than 10^{-6} mbar l s^{-1}, since the standard leak rate for each welding on vacuum applications has to be lower than 10^{-9} mbar l s^{-1}. Therefore, this component is negligible compared to the total outgassing rate.

6.3.1 General considerations

The vacuum systems have been selected taking the operating pressure of $1 \cdot 10^{-7}$ mbar into account. The gap on the mid-plane is about 5 cm to consider this conductance, and the average pressure inside the acceleration chamber plus the equivalent pumping speed are reduced by a correction factor of 0.9. We must remind you that our estimations do not refer to the first vacuum procedure, but to an already outgassed system, vented with dry nitrogen and briefly exposed to the atmosphere.

Turbo pumps are not recommended for high magnetic field applications, therefore they must operate on a site where the dispersed magnetic field is lower than 500 Gauss, i.e. 3 m away from the mid-plane. The molecular conductance of a connection pipe from the acceleration chamber to the turbo pumps is about 150 l/s for air if we consider a DN150 tube. This value will limit the turbo pumping speed so that these pumps cannot be suited to the main pumping system of the cyclotron, unless the diameter of the tube is strongly increased, as described further on.

Though diffusive pumps can operate in a high magnetic field environment and exhibit a good pumping speed for H_2 and He, their use is not particularly recommended for this application. This is mainly due to some other technological drawbacks such as the resulting oil contamination, the high temperature of its body, the necessity to add a water-cooled (or rather a liquid-nitrogen-cooled) trap, and the requirement of a high vacuum gate valve for each pump. Nevertheless, this solution has been taken into consideration and will be illustrated further on. Getter pumps are also not recommended since the operational pressure for such pumps is quite high (their life would be strongly reduced). “Split” cryo-pumps have been in use in our cyclotron for 20 years [10]; the cold head is located inside the Dees with no reduction of the pumping speed especially for condensable gasses, and the He distribution system and compressor are far away from the high magnetic field area. Unfortunately, their main drawbacks are the length of time required to reach the working temperature (about 2h) and the cost.

To hold a good vacuum degree in the volume between the lateral wall of the Cu liner of the cavities and the front iron pole, it is necessary to foresee some apertures on the liner for a total equivalent normal area of 100 cm^2.

6.3.2 Solution 1: 4 turbomolecular pumps (DN150, 3 m) + 4 split cryogenic pumps

The split cryo-pumps exhibit a slightly higher pumping speed compared to the equivalent pump assembled in a flanged standard cylindrical container. On the other hand, they have a gas load capacity reduced by 50% due to their reduced exposed surface and the lower available refrigerating power. Their pumping speed for H_2 and He is quite low, therefore the contribution of the 4 turbo pumps also in the high vacuum regime is not negligible. Both the cryo and the turbo pumps are connected next to the Dees. Whilst the cryo-pumps are set inside the Dees, the turbo pumps are located 3 m away from the mid-plane. The contribution to the total pumping speed from the turbo pumps for H_2 and He amounts to about 800 l/s, whilst for the other gasses this only amounts to about 400 l/s. However, turbo pumps are needed to quickly reach the cryo crossover pressure of 10^{-4}-10^{-5} mbar. Since the turbo pumping speed is strongly limited by the DN150 connection tubes, the pumping speed at the cyclotron chamber does not depend on the size of the turbo pump. Therefore, it is not worth using DN150 turbo pumps. DN100 pumps will however exhibit the same final pumping speed. By this configuration the turbo pumps do not need any high vacuum gate valve, since the venting time will be determined only by the time that the cryo-pumps will need to reach room temperature again when heated by the resistance heater (typically 20 minutes). During this time, the turbo pumps will be at a complete stop and the venting with dry nitrogen will be permitted. This will reduce the costs of the vacuum system.

The total pumping speed for 4 cryo-pumps is: 10000 l/s for H_2O; 2500 l/s for N_2, O_2 and CO; 4000 l/s for H_2 and 1200 l/s for He. The introduction of a further cryo-pump next to the centre of the cyclotron (where a 70 mm aperture is available) will locally decrease the total pressure within a radius of 15 cm by one order of magnitude. This will reduce the beam intensity loss, but not appreciably reduce the total beam power loss.

The pre-vacuum procedure will be conducted through the DN 150 tubes, by 4 pre-vacuum pumps of 32 m^3/h that can also be used as primary pumps for the turbo. Depending on the pressure, a different flow regime will take place in the DN150 tubes, as reported below:

- from atmosphere to 500 mbar the flow will be turbulent (4600>Re>2300);
- from 500 to 250 mbar it is transitory viscous (2300>Re>1250);

- from 250 to 10^{-2} mbar it is laminar viscous (Kn<0.01);
- from 10^{-2} to 10^{-4} mbar it is transitory of Knudsen (1>Kn>0.01);
- from 10^{-4} to 10^{-7} mbar it is molecular (Kn>1).

In these conditions, this vacuum system needs about 14 minutes to reduce the pressure inside the acceleration chamber (3.2 m^3) from atmosphere to $1 \cdot 10^{-1}$ mbar. After 30 minutes the pressure will be $7 \cdot 10^{-5}$ mbar with the contribution of the 4 turbo. At this point, the 4 cryo-pumps can be switched on. They will reach the final temperature in about 2h when the pressure will be $6 \cdot 10^{-7}$ mbar. Because of the strong outgassing rate, the final pressure of $1 \cdot 10^{-7}$ mbar will be reached only after 20-30 hours. In order to reduce the venting time, we strongly recommend adopting a resistive heater on the cryogenic panels and monitoring the pressure during the heating procedure so that this never exceeds the water triple point (i.e. 6 mbar).

Figure 6.3.1 shows the pump-down line versus the time for this pumping system.

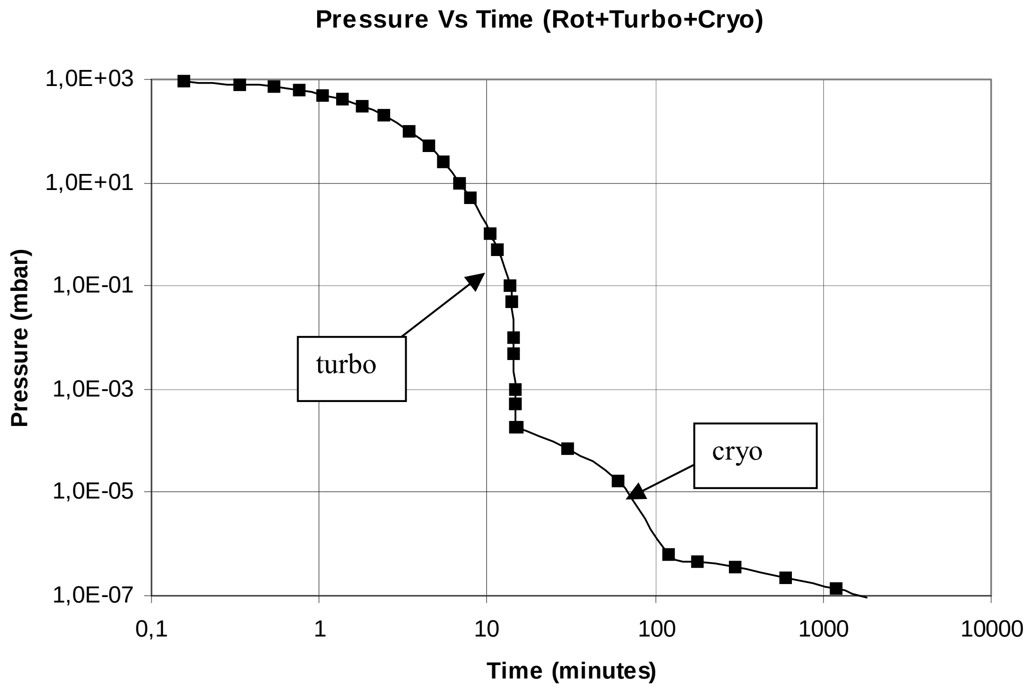

Fig. 6.3.1

Since the apertures in the Dees are elliptic, we could use elliptic-shaped pumps to maximise the size of the cryo-pumps. The pumping speed and the gas load capacity result increased by 15%, especially for H_2O, CO_2 and solvents. Unfortunately, the main drawback of this solution is that the heat load for the cryo-cooler will be higher and consequently, the time needed to reach the final temperature will be longer. This will completely compensate for the reduced time in obtaining the equilibrium final pressure.

6.3.3 Solution 2: 4 turbomolecular pumps (DN200, 3 m) + 4 diffusive pumps (DN200, 1.5 m)

The principal advantages of the diffusive pumps consist in their structural simplicity, their low cost, their possible use in a high magnetic field area, and their high pumping speed for light gasses (H_2 and He). On the other hand, these pumps need a high vacuum gate valve each and a trap to stop the oil vapour contamination from the pumps to the acceleration chamber. Therefore, either water-cooled baffles or liquid-nitrogen (LN_2) cryo-traps can be applied. While both will reduce the pumping speed for non condensable gasses, the latter exhibit an intrinsically high pumping speed for H_2O and solvents. The main drawback consists in the use of the LN_2. Finally, we must note that the introduction of these components (valve and baffle) will increase the costs of the vacuum plant itself and its maintenance.

Though the introduction of the diffusive pumps can avoid us using the cryo-pumps, the turbo pumps must be applied anyway. They are actually necessary to reach the crossover pressure of the diffusive pumps of 10^{-3} mbar quickly. Figure 6.3.2 shows the pressure drop vs. time for the cyclotron evacuated only by 4 pre-vacuum pumps of 32 m^3/h each. From this figure we can see that the pressure value of $5 \cdot 10^{-3}$ mbar is reached after 3 hours. This will consequently increase the time needed to reach $1 \cdot 10^{-7}$ mbar by +15%.

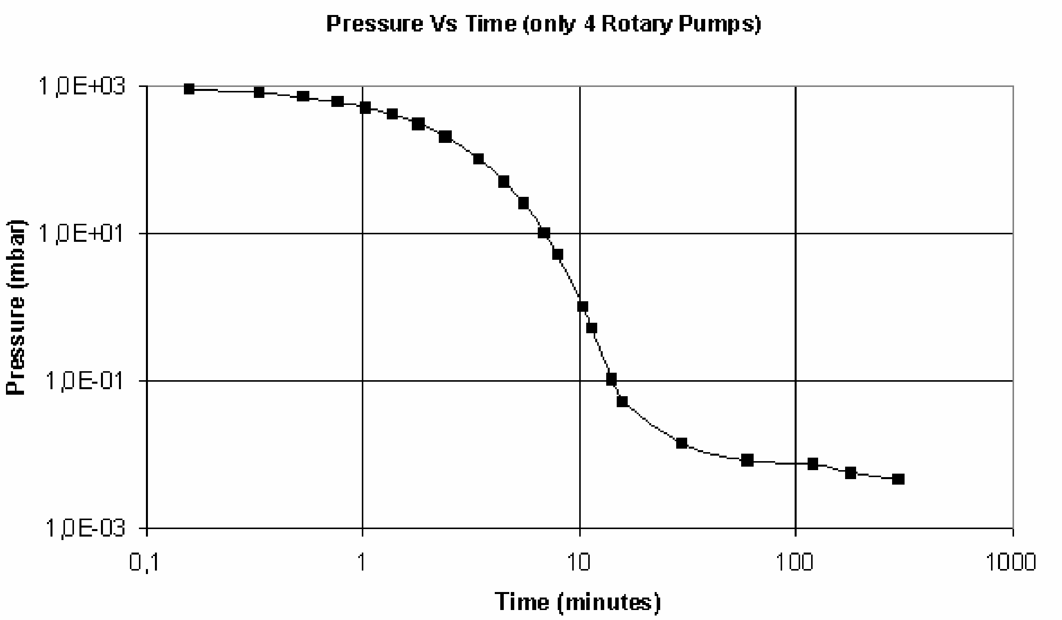

Fig. 6.3.2

To overcome this problem, 1 or 2 Roots Pumps with high pumping speed could be added to reach the diffusive pump crossover pressure in a shorter time. However, the solution of 4 turbo and 4 diffusive pumps is preferable because of the significant contribution to the pumping speed of the turbo pumps in the high vacuum regime of 700 l/s for air, and about 900 l/s for the gas composition after 30 hours.

For this solution we considered DN200 tubes. The turbo ones are located 3 m away from the mid-plane, while the diffusive ones are located just at the end of the pole expansion (1.5 m from the mid-plane) with a water-cooled baffle and a gate valve. The diffusive pumps are flanged DN200 and the turbo pumps are DN150, since their pumping speed is mainly limited by the conductance of the connection tube that is about 280 l/s for air in the molecular regime. The total pumping speed for the diffusive pumps is initially about 1250 l/s (H_2O and air), whilst after 30 hours it is about 1800 l/s (mainly due to the increased H_2 fraction in the gas composition).

The pre-vacuum procedure will be conducted through the DN 200 tubes, by 4 pre-vacuum pumps of 32 m^3/h that can also be used as primary pumps for the turbo. Depending on the pressure, a different flow regime will take place in the DN200 tubes, as here reported:

- from atmosphere to 600 mbar the flow will be turbulent (4600>Re>2300);
- from 600 to 300 mbar it is transitory viscous (2300>Re>1250);
- from 300 to $5\cdot10^{-2}$ mbar it is laminar viscous (Kn<0.01);
- from $5\cdot10^{-2}$ to $5\cdot10^{-4}$ mbar it is transitory of Knudsen (1>Kn>0.01);
- from 5 10^{-4} to 10^{-7} mbar it is molecular (Kn>1).

In these conditions, the vacuum system needs about 13 minutes to reduce the pressure inside the acceleration chamber (3.2 m^3) from atmosphere to $1\cdot10^{-3}$ mbar, when the gate valve of the diffusive pump can be opened. Then the pressure drops very quickly to $4\cdot10^{-5}$ mbar. From this point the outgassing rate will determine the equilibrium pressure that will reach the required value of $1\cdot10^{-7}$ mbar after 30 hours, while the value of $1\cdot10^{-6}$ mbar is reached after 5 hours.

By using this system the pressure vs. time line is show in Fig. 6.3.3.

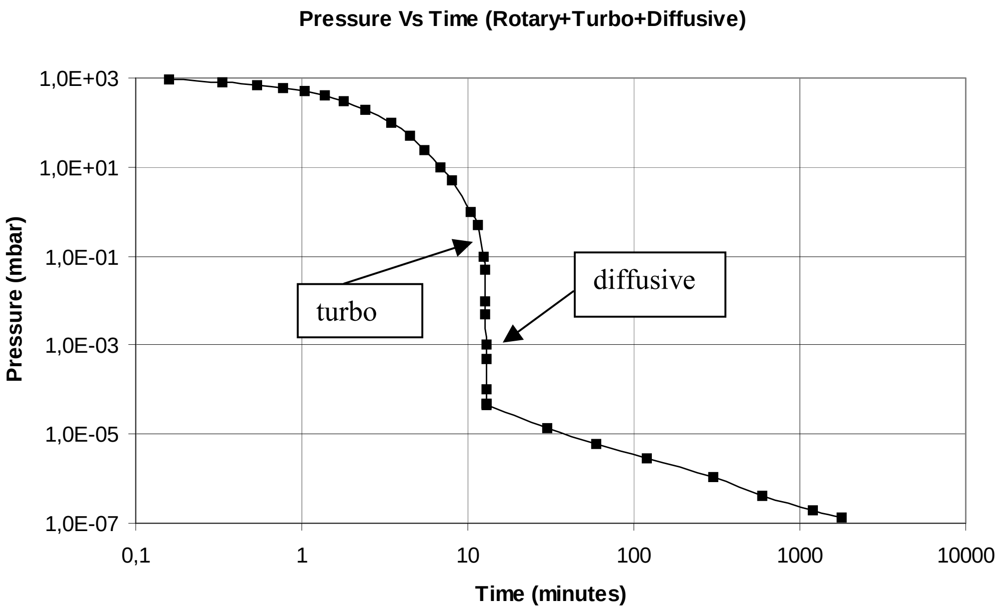

Fig. 6.3.3

6.3.4 Solution 3: 8 turbomolecular pumps (DN250, 1.7 m)

We have also considered the possibility of employing 8 turbo pumps to reach the required operating pressure. The appealing perspective of this solution is the use of a single vacuum configuration multiplied by 8, reducing the venting time and the maintenance costs. This evaluation has been carried out considering 8 large turbo pumps DN250, of 1950 l/s for air, operating in a horizontal position just at the end of the pole, at about 1.7 m from the mid-plane and connected to the acceleration chamber through a DN250 curve and a 1.5 m long DN250 tube. No gate valve is required. The pumps have to be shielded from the magnetic field in this working area. It is worth noting that such pumps are quite expensive and their life could be compromised by the horizontal working position.

The DN250 tube conductance is about 720 l/s for air, while the total equivalent pumping speed after 20 hours is about 5050 l/s for the gas composition at that time.

The pre-vacuum procedure will be conducted through the DN 250 tubes, by 8 pre-vacuum pumps of 32 m^3/h that can also be used as primary pumps for the turbo. Depending on the pressure, a different flow regime will take place in the DN250 tubes, as reported below:

- from atmosphere to 800 mbar the flow will be turbulent (4600>Re>2300);
- from 800 to 400 mbar it is transitory viscous (2300>Re>1250);
- from 400 to $5 \cdot 10^{-2}$ mbar it is laminar viscous (Kn<0.01);

- from $5 \cdot 10^{-2}$ to $5 \cdot 10^{-4}$ mbar it is transitory of Knudsen (1>Kn>0.01);
- from $5 \cdot 10^{-4}$ to 10^{-7} mbar it is molecular (Kn>1).

In these conditions, the vacuum system needs about 10 minutes to reduce the pressure inside the acceleration chamber from atmosphere to $3 \cdot 10^{-5}$ mbar. From this point, the pressure will be determined by the outgassing rate, then the chamber will reach the required value of $1 \cdot 10^{-7}$ mbar after 20 hours, whilst the value of $1 \cdot 10^{-6}$ mbar is reached after 2.5 hours.

Figure 6.3.4 shows the pressure vs. time for this kind of pumping system.

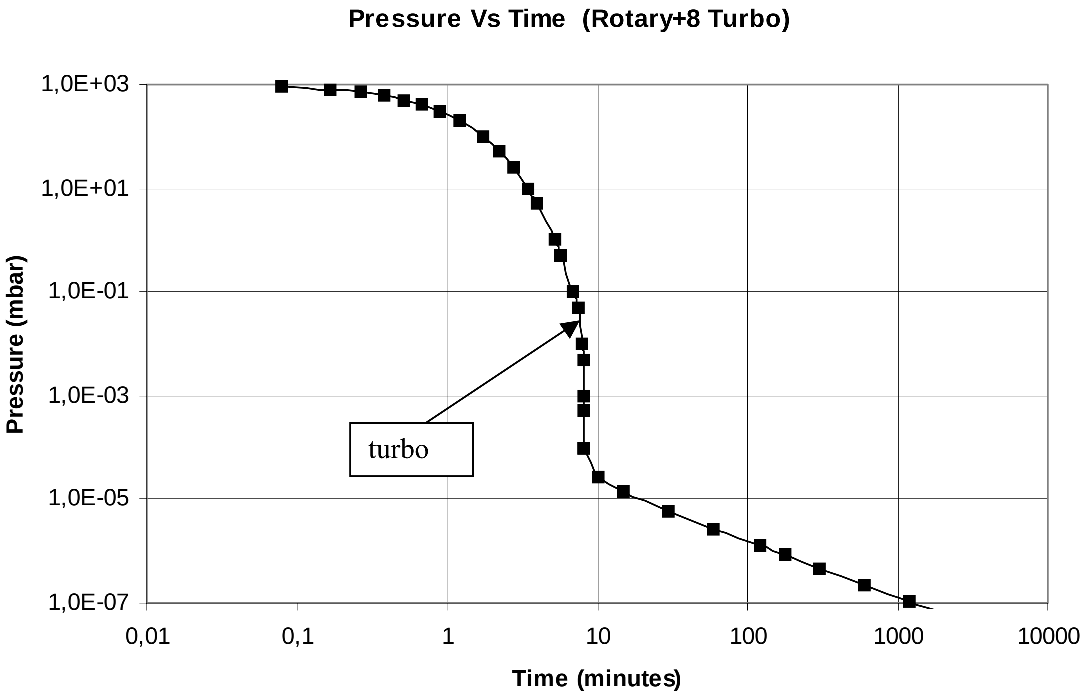

Figure 6.3.4

6.3.5 Systems comparison

In Fig. 6.3.5 the pump-down line for the comparison of the 3 pumping systems is reported. They exhibit nearly the same pump-down time (20-30 hours). The main difference is shown by the solution with the diffusive pumps for which we need longer (about 5 hours) to reach the operating pressure of 10^{-6} mbar, which is suitable during the commissioning of the cyclotron. Together with the other drawbacks of the diffusive pumps, we believe this to be the worst solution. The other two solutions can be better compared, but a definitive decision depends on the weight given to each item in the “pros” and “cons”. The Table 6.3.1 is a summary of the results.

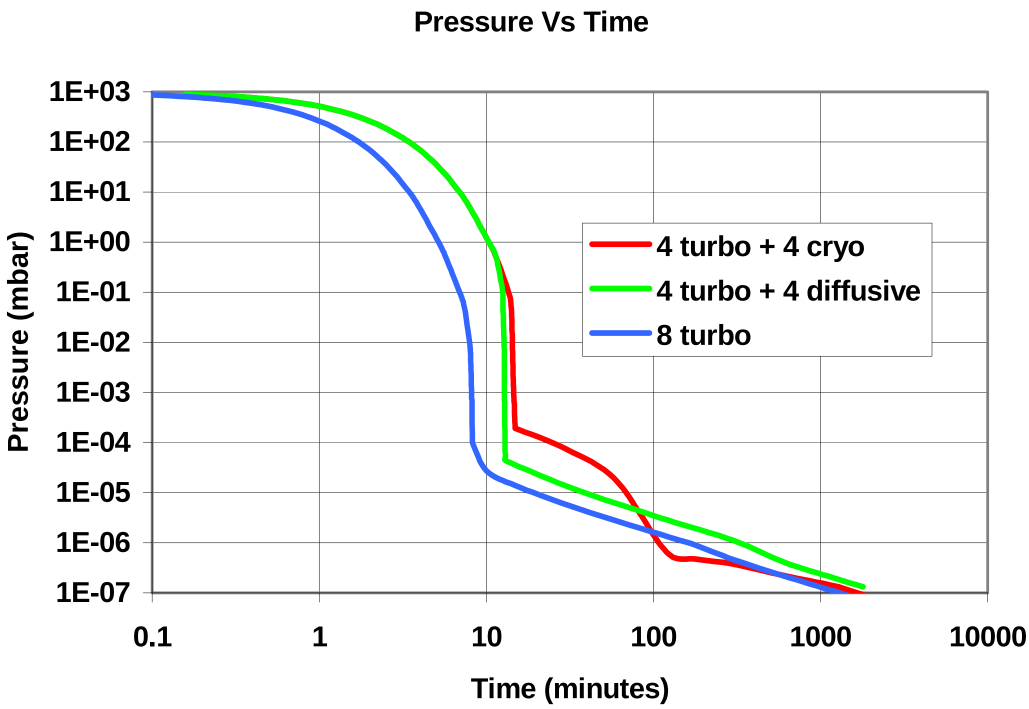

Figure 6.3.5

Table 6.3.1

4 turbo + 4 cryo		**8 turbo**	
Advantages	*Disadvantages*	*Advantages*	*Disadvantages*
Small turbo pumps	Expensive cryo-pumps	Short pump-down time	Expensive turbo pumps
High pumping speed for water	Higher maintenance costs	Single pumping configuration	Horizontal mounting
Small pole apertures (190 mm)	20 minutes for venting time	Short venting time (10 min)	Large pole aperture (290 mm)
10^{-6} in less than 2 h	10^{-7} in 24 h	10^{-7} in 20 h	10^{-6} in more than 2 h

6.4 References

[1] Betz, Rev. of Mod. Phys. Vol. 44, N° 3 (1972), p. 465.

[2] H. Steimel, *Int. Conf. On Sect. Foc. Cyc. and Meson Factories*, Geneva, CERN (1963) p. 24.

[3] A. Geisler et al., XVII ICCA, Tokyo (2004) p.178.

[4] Y. Jongen et al., XIV ICCA, Cape Town (1995) p.606.

[5] Leybold, *Vakuum Vademekum*.

[6] B. Ferrario, *"Introduzione alla tecnologia del Vuoto"*, Patron Editrice 1999, and references herein.

[7] J. F. O'Hanlon, *"A User Guide to Vacuum technology"*, and references herein.

[8] P. Michelato, C. Pagani, Proc. *11th Int. Conf. on Cycl. and their Appl.*, Tokyo (1987) p. 401.

[9] R. Schmaus, University of Alberta, *"Basic Vacuum Technologies Resources"*, and references herein.

[10] P. Michelato et al., Vacuum Vol. 38 (8-10) (1988) p. 831.

Chapter 7. Conclusion

The present design study verified the feasibility of the proposed superconducting cyclotron for the production of fully stripped light ions and proton beams at a maximum energy of 250 AMeV.

Despite the fact that a lot of work is required to produce the final design of the machine now, all the essential and useful information required to carry out an evaluation of the cost and time needed to build and to commission this cyclotron is available.

Here we would like to point out the main items that need further study and simulations:

- a fast tuning system to change from the isochronous magnetic field of ^{12}C to H_2^+. Despite the solution presented in subsection 3.3 being feasible and fast, it is not beautiful and it is probably not the cheapest. A study for a different technical solution is already in progress. It consists in moving three big sheets of iron of right thickness to change the main field profile from ^{12}C to H_2^+. This solution is quite similar to the technical solution used in the small cyclotron of 10-18 MeV to change the magnetic field to accelerate protons or deuterons. The final design will probably have two systems for field trimming. One system is the fine tuning of the field to optimise the isochronous field for the ^{12}C, and we suggest using the system similar to the ACCEL cyclotron [1], which consists of a set of trim rods placed on the pole's surface, which are adjusted from the inner side of the cyclotron. The fine setting of the position of these trim rods will only be performed during the commissioning of the cyclotron. The gross change of the isochronous magnetic field changing from ^{12}C to H_2^+, requires a change of about 0.7% of the main field, and will be performed by moving the three iron sheets from the outside yoke.
- the interference between the magnetic channels of the electrostatic deflector extraction and the magnetic channels for the stripper extraction. Further studies are necessary to find the best solution that will minimise the interference among the magnetic channels, but we expect that an interference-free solution does not exist. We are working on a simpler solution that allows us to move one set of magnet channels or the other into the working position. The simplest solution is based on the insertion of a radial mechanic bar which allows us to move the magnetic channels as for the K800 cyclotron [2].

- the central region has to be completed through further study to optimise the matching of the injected beam to the cyclotron acceptance;
- the cryostat design has to be done;
- an evaluation of the cryogenic consumption has to be carried out;
- optimisation of the magnetic yoke to reduce the magnetic stray field;
- optimisation of the vacuum plant.

An important result achieved by the present study is that the present cyclotron design has a significant margin in terms of axial focusing power, of maximum electric field on the electrostatic deflectors and on the maximum current density inside the coils. Consequently, it can be upgraded to allow us to achieve a maximum energy of about 300 AMeV.

The main limitation to the increase in the final energy over 300 AMeV is due to the injection energy of the beam and to the axial focusing.

Indeed, if we would like to upgrade the present cyclotron design without changing the size of the accelerator too much, we need to increase the magnetic field. Despite this being feasible, the adverse consequence on the radius of the first orbit means it becomes smaller. The present design of the central region is very small and a further reduction in size is not possible because it will produce a design that is unsafe. Therefore, the only alternative solution is to increase the injection energy.

The selected injection energy value for the cyclotron here presented is of 40 keV, so to increase the cyclotron final energy up to 300 AMeV it is necessary to increase the injection energy up to 50 keV. Despite the fact that the maximum injection energy has no intrinsic limitations, there are some constraints like the increasing cost of the injection system and also the safety of the injection system, and last but not least, the limit on the maximum voltage of the spiral inflector. The maximum voltage value chosen for the spiral inflector has been 7 kV up to now, and we do not want to increase this value because discharge becomes possible and consequently, the facility reliability would decrease.

Another limit to increasing the energy of the present cyclotron up to 400 AMeV is the vertical focusing. The higher mean magnetic field required to accelerate the beam up to 400 AMeV produces a reduction in the flutter value of the magnetic field and consequently, of the vertical focusing power. To compensate for the reduction in the flutter, the spiral angle should be increased at very high values [3].

These two considerations show that a cyclotron able to accelerate ^{12}C up to 400 AMeV should have an overall diameter which is about 1 m larger than the present design, and a weight of about 700 tons, according to the cyclotron design recently presented by Y. Jongen [4].

On the other hand, there is a real market for a 300 AMeV cyclotron as we will try to explain below. Fig.1. in the introduction of the present report, clearly shows that 72% of all the tumours treated at the CHIBA plant are less than 170 mm deep, in particular prostate and uterus tumours are the deepest.

In Fig. 7.1 the number of treatments vs. the treatment depth of the tumours in the head and neck areas treated at CHIBA (private communication Prof. J. Mizoe) are shown. It is evident from Fig. 7.1 that 95% off all those treatments are feasible with a 12C beam whose energy is lower than 300 AMeV.

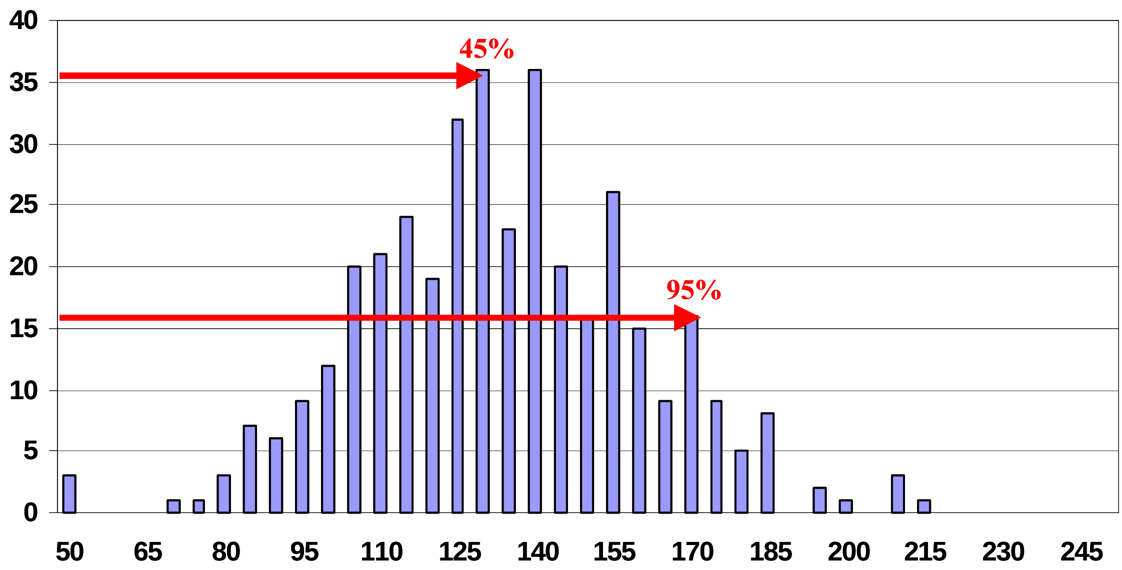

Fig. 7.1: Number of treatment vs. treatment depth. Data provided courtesy of Prof. J Mizoe of N.I.R.S.

We would like to remind that the treatment of tumours located at a depth of more than 170 mm has to take the physical problem of the dose deposited beyond the Carbon Bragg peak into account, see Fig. 7.2. Moreover, the dose beyond the Bragg peak is proportional to the depth of the tumour and it is produced by the different kind of light particles produced by the fragmentation of the ^{12}C, which each have a different RBE. Therefore, a careful evaluation of the actual damage produced on the surrounding tissue is very difficult.

For this reason, we believe treating the deeper tumours using proton or Lithium beams, which have a smaller amount of dose beyond the Bragg peak compared to the Carbon beam, to be more useful.

Another useful information to take in mind is that the range in water of a Lithium beam with an energy of 300 AMeV is 306 mm, which allows us to treat all the tumour at any location inside the human body using Lithium beam.

All these considerations urge us to develop further studies to fix the parameters for an upgraded version of the present design study; a superconducting cyclotron able to deliver light ions up to 300 AMeV.

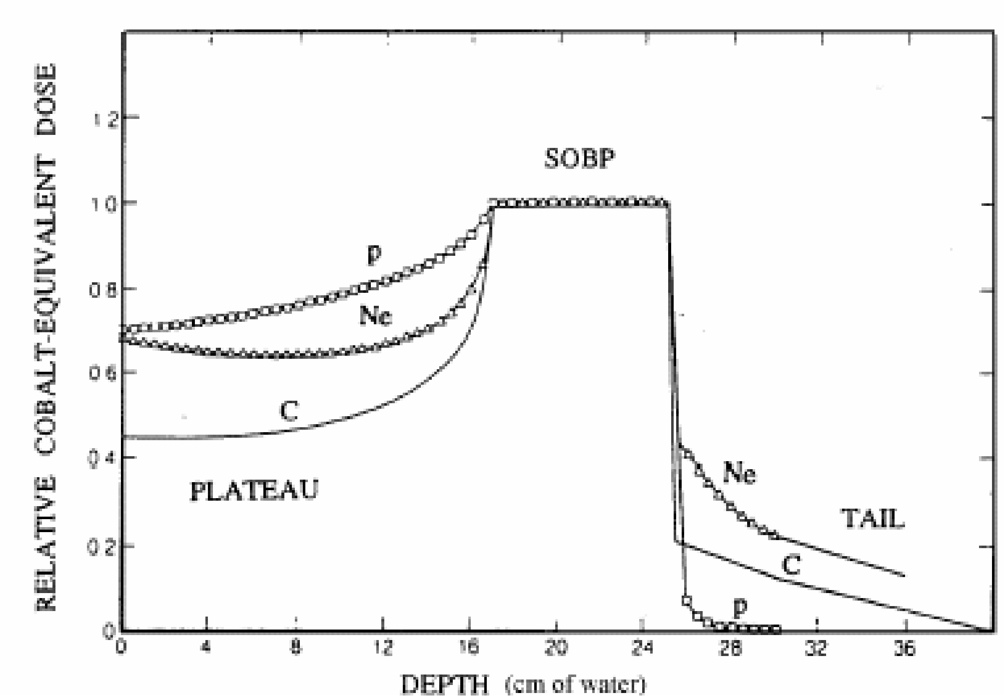

Fig. 7.2. : Spreaded Bragg Peak for Proton, Carbon and Neon beam. The released dose beyond the Bragg peak for the three cases is shown.

7.1 Scientific production of SCENT experiment

Graduate thesis

- D. Battaglia, *"Studio elettromagnetico delle cavità risonanti per un ciclotrone superconduttivo"*, electronic engineer degree thesis (2003).
- A. Calanna, *"Studio del circuito magnetico di un ciclotrone medicale da 250 AMeV"*, physics degree thesis (2003).
- L. Piazza, *"Eccitazione di cavità risonanti a radiofrequenza per la generazione di fasci pulsati di particelle cariche"*, electronic engineer degree thesis (2004).

- D. Campo, *"Studio dell'inflettore a spirale per il ciclotrone superconduttore del progetto SCENT"*, physics degree thesis (2005).

Ph.D. Thesis

- M. Maggiore, *"Design of a Superconducting Cyclotron for Exotic Nuclei production and Therapy"*, physics PhD. thesis (2005).

Articles published on international reviews

1. L. Calabretta, M. Maggiore, M. Re, D. Rifuggiato, S. Farinon, P. Fabbricatore, R. Musenich, *"A superconducting cyclotron as driver for radioactive beam facilities"*, Nuclear Physics A734 (C) (2004) pp. 378-381. Proceedings of the VIII International Conference on Nucleus-Nucleus Collisions (NN2003). Edited by: Y. Oganessian, R. Kalpakchieva.
2. M. Maggiore, L. Calabretta, M. Di Giacomo, D. Rifuggiato, D. Battaglia, L. Piazza, *"Conceptual design of the RF accelerating cavities for a superconducting cyclotron"*, Nuclear Inst. and Methods in Physics Research, A 557 (2006), pp. 414-420.
3. L. Calabretta, G. Cuttone, M. Maggiore, M. Re, D. Rifuggiato, *"A novel superconducting cyclotron for therapy and radioisotope production"*, to be published on Nuc. Inst. and Meth. A.

Articles published on Proceedings of International Conferences

1. L. Calabretta, G. Cuttone, M. Maggiore, M. Re, D. Rifuggiato, *"LNS Catania Project for Therapy and Radioisotope production",* Int. Conf. on Cyc. and their Appl., Tokyo, 18-22 Oct. 2004 Invited, p. 72.
2. M. Maggiore, L. Calabretta, M. Di Giacomo, *"Design of the RF system for a 250 AMeV Superconducting Cyclotron"*, Int. Conf. on Cyc. and their Appl., Tokyo, 18-22 Oct.-2004, p. 324.

Oral contributions at International Workshop and Meetings

1. L. Piazza, L. Calabretta, A. Caruso, F. Consoli, M. Maggiore, D. Rifuggiato and A. Spartà, *"Design of the flat-top acceleration system for the LNS K800 cyclotron"*, Belgrade 6-8 October, XXXIV-ECPM 2005 http://www.tesla-sc.org/ecpm/ecpm_program.htm.
2. D. Rifuggiato, L. Calabretta and G. Cuttone, *"Status and prospective at the Laboratorio Nazionale del Sud"*, Belgrade 6-8 October, XXXIV-ECPM 2005 http://www.tesla-sc.org/ecpm/ecpm_program.htm.
3. L. Calabretta, *"A Superconducting Cyclotron for Light Ion Beams"*, PTCOG 2003 http://www.ucsf.edu/radonc/ptcog/index.html.
4. L. Calabretta, *"A Novel Superconducting Cyclotron for Hadrontherapy"*, PTCOG 2005 http://www.ptcog43.com/program/monday.htm.

Patents

Patent n. RM2004A000408, title: *"Metodo di progettazione di una cavità a radiofrequenza, in particolare da utilizzare in un ciclotrone, cavità a radiofrequenza realizzata utilizzando tale metodo, e ciclotrone utilizzante tale cavità"*, registered since 11/08/2004. Inventors: Luciano Calabretta e Mario Maggiore.

7.2 References

[1] ACCEL, private communication.

[2] E. Acerbi et al., "*The beam diagnostic of the Milan K800 Cyclotron"*, XII Int. Conf. On Cyclotrons and Their Applications, Berlin (1989), p.283.

[3] J. Kim, F. Marti and H. Blosser, *"Design Study of a Superconducting Cyclotron for Heavy Ion Therapy"*, XVI Int. Conf. On Cyclotrons and Their Applications, East Lansing (2001), p.324.

[4] W. Kleeven et al., "Design of a K=1600 compact superconducting cyclotron for therapy by Carbon beams", XXXIV European Cyclotron Progress Meeting, Belgrade (2005).

Document version: 1.1
Printed in Catania on July 2006